Ministry of Education and Science of the Russian Federation
Saint Petersburg National Research University of Information
Technologies, Mechanics, and Optics

NANOSYSTEMS:
PHYSICS, CHEMISTRY, MATHEMATICS

2019, volume 10(6)

Наносистемы: физика, химия, математика

2019, том 10, № 6

NANOSYSTEMS:

PHYSICS, CHEMISTRY, MATHEMATICS

ADVISORY BOARD MEMBERS

Chairman: V.N. Vasiliev *(St. Petersburg, Russia),*
V.M. Buznik *(Moscow, Russia)*; V.M. Ievlev *(Voronezh, Russia),* P.S. Kop'ev*(St. Petersburg, Russia),* N.F. Morozov *(St. Petersburg, Russia),* V.N. Parmon *(Novosibirsk, Russia),* A.I. Rusanov *(St. Petersburg, Russia),*

EDITORIAL BOARD

Editor-in-Chief: I.Yu. Popov *(St. Petersburg, Russia)*

Section Co-Editors:
Physics – V.M. Uzdin *(St. Petersburg, Russia),*
Chemistry, material science –V.V. Gusarov *(St. Petersburg, Russia),*
Mathematics – I.Yu. Popov *(St. Petersburg, Russia).*

Editorial Board Members:
V.M. Adamyan *(Odessa, Ukraine)*; O.V. Al'myasheva *(St. Petersburg, Russia)*; A.P. Alodjants *(Vladimir, Russia)*; S. Bechta *(Stockholm, Sweden)*; J. Behrndt *(Graz, Austria)*; M.B. Belonenko *(Volgograd, Russia)*; A. Chatterjee (*Hyderabad, India)*; S.A. Chivilikhin *(St. Petersburg, Russia)*; A.V. Chizhov *(Dubna, Russia)*; A.N. Enyashin *(Ekaterinburg, Russia),* P.P. Fedorov *(Moscow, Russia)*; E.A. Gudilin *(Moscow, Russia)*; V.K. Ivanov *(Moscow, Russia),* H. Jónsson *(Reykjavik, Iceland)*; A.A. Kiselev *(Durham, USA)*; Yu.S. Kivshar *(Canberra, Australia)*; S.A. Kozlov *(St. Petersburg, Russia)*; P.A. Kurasov *(Stockholm, Sweden)*; A.V. Lukashin *(Moscow, Russia)*; I.V. Melikhov *(Moscow, Russia)*; G.P. Miroshnichenko *(St. Petersburg, Russia)*; I.Ya. Mittova *(Voronezh, Russia)*; V.V. Pankov *(Minsk, Belagus)*; K. Pankrashkin *(Orsay, France)*; A.V. Ragulya *(Kiev, Ukraine)*; V. Rajendran *(Tamil Nadu, India)*; A.A. Rempel *(Ekaterinburg, Russia)*; V.Ya. Rudyak *(Novosibirsk, Russia)*; D Shoikhet *(Karmiel, Israel)*; P Stovicek *(Prague, Czech Republic)*; V.M. Talanov *(Novocherkassk, Russia)*; A.Ya. Vul' *(St. Petersburg, Russia)*; A.V. Yakimansky (*St. Petersburg, Russia*), V.A. Zagrebnov *(Marseille, France).*

Editors:
I.V. Blinova; A.I. Popov; A.I. Trifanov; E.S. Trifanova *(St. Petersburg, Russia),*
R. Simoneaux *(Philadelphia, Pennsylvania, USA).*

Address: University ITMO, Kronverkskiy pr., 49, St. Petersburg 197101, Russia.
Phone: +7(812)312-61-31, **Journal site:** http://nanojournal.ifmo.ru/,
E-mail: popov1955@gmail.com

AIM AND SCOPE

The scope of the journal includes all areas of nano-sciences. Papers devoted to basic problems of physics, chemistry, material science and mathematics inspired by nanosystems investigations are welcomed. Both theoretical and experimental works concerning the properties and behavior of nanosystems, problems of its creation and application, mathematical methods of nanosystem studies are considered.

The journal publishes scientific reviews (up to 30 journal pages), research papers (up to 15 pages) and letters (up to 5 pages). All manuscripts are peer-reviewed. Authors are informed about the referee opinion and the Editorial decision.

CONTENT

The Editorial Board of the Journal congratulates Andrei Andreyevich Rempel, a member of our editorial board, on his election to the prestigious role of Academician of the Russian Academy of Sciences. We wish him continued success in his academic career.

NANOSYSTEMS: PHYSICS, CHEMISTRY, MATHEMATICS, 2019, 10 (6), P. 608–615

Exact calculation of the trace of the Birman–Schwinger operator of the one-dimensional harmonic oscillator perturbed by an attractive Gaussian potential

S. Fassari[1,2,3], F. Rinaldi[2,3,4]
[1]Department of Higher Mathematics, ITMO University, St. Petersburg, Russia
[2]CERFIM, PO Box 1132, CH-6601 Locarno, Switzerland
[3]Dipartimento di Fisica Nucleare, Subnucleare e delle Radiazioni,
Univ. degli Studi Guglielmo Marconi,Via Plinio 44, I-00193 Rome, Italy
[4]Istituto Nazionale di Fisica Nucleare, Sezione di Napoli, Naples, Italy
silvestro.fassari@uva.es, f.rinaldi@unimarconi.it

DOI 10.17586/2220-8054-2019-10-6-608-615

By taking advantage of Wang's results on the scalar product of four eigenfunctions of the 1D harmonic oscillator, we explicitly calculate the trace of the Birman–Schwinger operator of the one-dimensional harmonic oscillator perturbed by a Gaussian potential, showing that it can be written as a ratio of Gamma functions.

Keywords: Gaussian potential, Birman–Schwinger operator, trace class operator, harmonic oscillator.

Received: 4 November 2019

1. Introduction

As is well known, the harmonic oscillator is one of the very few solvable quantum models, that is to say its eigenfunctions and eigenvalues can be expressed analytically. As a consequence, one of the most fundamental chapters in any quantum mechanics textbook, such as [1], is devoted to its detailed description.

This remarkable property has led theoretical physicists to study various types of models involving perturbations of the harmonic oscillator over many decades. In our inevitably limited summary of the related literature, we have chosen to restrict ourselves to time independent perturbations of the one-dimensional harmonic oscillator.

The numerous contributions spanning many decades can be essentially divided into the following groups:
i) polynomial perturbations;
ii) nonpolynomial perturbations;
iii) point perturbations.

The x^4-perturbation was the first polynomial perturbation to be extensively investigated also because of its connections with Quantum Field Theory. As the Hamiltonian $-\frac{d^2}{dx^2}+x^2+\beta x^4$ is one of the key topics in [2, 3], we refer the interested reader to those textbooks and the related references cited therein (see [4] in particular). We remind the reader that the non-analyticity of its eigenvalues as functions of β was a well-known thorny issue in the early days of quantum mechanics. However, it is possible to exploit the Borel summability method to get around this obstacle (see Theorems XII.19, XII.21 and Example 1 for both theorems in [3]). A modified Borel transform allows the extension of the method to Hamiltonians of the type $-\frac{d^2}{dx^2}+x^2+\beta x^{2m}, m \geq 3$ (see Example 3 for Theorems XII.20, XII.21 in [3]). Another noteworthy polynomial perturbation is the one leading to the double well oscillator whose Hamiltonian is given by $-\frac{d^2}{dx^2}+x^2+2\beta x^2+\beta^2 x^4 = -\frac{d^2}{dx^2}+x^2(1+\beta x)^2$. In particular, the analyticity of its eigenvalues is dealt with in Example 6 following Theorems XII.16.5 in [3] and the related references cited therein. Another important branch of polynomial perturbations is the one of the type $\beta x^{2m+1}, m \geq 0$, which had its origin in the early investigations on the Hamiltonian of the real cubic oscillator $-\frac{d^2}{dx^2}+x^2+\beta x^3$ (see, e.g., [5, 6]) and was initially studied in [7, 8]. Further interest has been drawn into the cubic anharmonic oscillator by the fact that the Hamiltonian $-\frac{d^2}{dx^2}+x^2+i\beta^{\frac{1}{2}}x^3, \beta > 0$ is *PT*-symmetric (see [9, 10]).

The most extensively studied nonpolynomial perturbation of the harmonic oscillator is certainly the potential $\frac{\lambda x^2}{1+gx^2}, \lambda, g > 0$ with the early works on this model dating back to the late seventies (see [11-20]). The functional analytic approach based on the Birman–Schwinger principle was used in [21] to analyze the behavior of the eigenvalues for small values of λ and large values of g. The same technique was exploited in [22] to further investigate this model assuming the coupling constant λ to be a function of g, in particular $\lambda(g) = g^{\frac{n}{2}}, n = 1, 2, 3$. In the last case $\lambda(g) = g^{\frac{3}{2}}$ the Hamiltonian behaves, apart from the constant term $g^{\frac{1}{2}}$, like that of the harmonic oscillator perturbed by a δ-sequence in the range of large values of g. More recent contributions to the study of this potential can be found in [23, 24].

The one-dimensional harmonic oscillator perturbed by a Dirac distribution centered at the origin was initially considered in [25] as a toy model for the top quark and later in [26] in relation to supersymmetry. It is worth pointing out that the potential $\frac{1}{2}x^2 - \lambda\delta(x), \lambda > 0$ can be regarded as a singular "funnel potential". The same model was subsequently investigated by means of the integral operator isospectral to the Birman–Schwinger operator in [27]. A renewed interest in this model, to a great extent motivated by its applications to Bose-Einstein condensates, has led to more recent contributions such as [28-36]. The case in which the Dirac distribution is not centered at the origin was analyzed in [37] (see also [28]) while the model with two identical deltas symmetrically situated about the origin was thoroughly investigated in [38] (see also [28]). The case of a *PT*-symmetric Hamiltonian for a one-dimensional harmonic oscillator potential decorated with an even number of Dirac delta functions located at symmetric points and complex conjugate strengths was first studied in [39] by means of ODE techniques and later in [40, 41]. As is well known, the Dirac distribution is not the only point interaction in one-dimensional Quantum Mechanics (see [42, 43]). Therefore, other types of point perturbations of the harmonic oscillator have been considered more recently, in particular the central δ'-potential (also called local δ' in the literature) and the central δ'-interaction (also called nonlocal δ' in the literature). The former has been investigated in [44, 45] while the latter has been considered in [46, 47] (see also [48]). A remarkable property of the latter model is given by the existence of infinitely many level crossings for a critical value of the coupling constant, which leads to a quantum phase transition since the ground state wave function becomes antisymmetric once the coupling constant falls below that critical value.

Although we have restricted our review to point perturbations of the one-dimensional harmonic oscillator, it is worth mentioning that a detailed comparison of the spectral properties of point perturbations of the n-dimensional harmonic oscillator, $n = 1, 2, 3$, stressing the role played by the dimension of the underlying space can be found in [50].

In this brief note, we have decided to start investigating the Hamiltonian $H_{-\lambda} = \frac{1}{2}(-\frac{d^2}{dx^2} + x^2) - \lambda e^{-x^2}, \lambda > 0$ since the latter Gaussian perturbation has the typical properties of short-range potentials but also those of the harmonic oscillator near the bottom of the well. To the best of our knowledge the only work on this model has been [49]. The combination of the harmonic potential with the attractive Gaussian gives rise to another type of funnel potential which, differently from the aforementioned one or the one analyzed in [51] with a central attractive point perturbation of the conic oscillator, has a finite minimum. The plot shown in Fig. 1 depicts this funnel potential for three different values of the coupling constant. It is rather evident that the Hamiltonian (with a singular funnel potential) $\frac{1}{2}(-\frac{d^2}{dx^2} + x^2) - \lambda\delta(x)$ is the limit in the norm resolvent sense (see [52]) of the sequence of Hamiltonians (with a finite funnel potential) $\frac{1}{2}(-\frac{d^2}{dx^2} + x^2) - \lambda n e^{-n^2x^2}, \lambda > 0$ as $n \to \infty$.

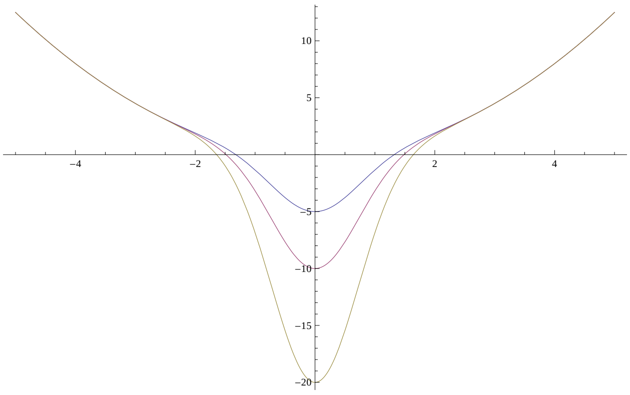

FIG. 1. The plot of $V_{-\lambda}(x) = \frac{1}{2}x^2 - \lambda e^{-x^2}, \lambda > 0$ for $\lambda = 5, 10, 20$

Although we are going to focus only on the attractive Gaussian potential $-\lambda e^{-x^2}$ in this note, it is clear that the integral operators to be investigated will also be relevant in the case of the repulsive perturbation λe^{-x^2} which, combined with the harmonic potential, produces the double well potential $V_{+\lambda}(x) = \frac{1}{2}x^2 + \lambda e^{-x^2}$, $\lambda > 0$, depicted in Fig. 2 for three different values of the coupling constant.

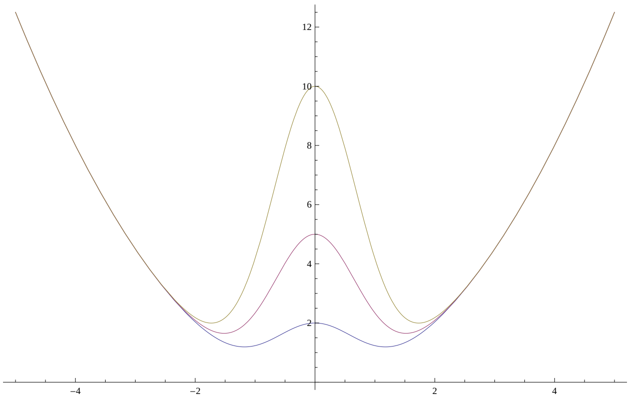

FIG. 2. The plot of $V_{+\lambda}(x) = \frac{1}{2}x^2 + \lambda e^{-x^2}$, $\lambda > 0$ for $\lambda = 2, 5, 10$

In particular, we carry out a detailed analysis of the two isospectral integral operators for this model that are at the heart of the renowned Birman–Schwinger principle, namely $\lambda e^{-x^2/2}\left[H_0 - E\right]^{-1} e^{-x^2/2}$ and $\lambda\left[H_0 - E\right]^{-\frac{1}{2}} e^{-x^2}\left[H_0 - E\right]^{-\frac{1}{2}}$. We show that the trace of these operators can be explicitly written in terms of a ratio of Gamma functions, a feature shared by point perturbations of the harmonic oscillator.

2. The Birman–Schwinger principle: recasting the Schrödinger equation into an integral equation

The Schrödinger Hamiltonian for the one-dimensional harmonic oscillator perturbed by an attractive central Gaussian potential reads:

$$H_\lambda = H_0 - \lambda V(x) = H_0 - \lambda e^{-x^2}, \quad \lambda > 0 \tag{2.1}$$

where

$$H_0 = \left(-\frac{1}{2}\frac{d^2}{dx^2} + \frac{x^2}{2}\right) \geq \frac{1}{2} \tag{2.2}$$

is the Hamiltonian of the unperturbed harmonic oscillator. Hence, the equation determining the lowest eigenvalue (ground state energy) is given by:

$$\left[H_0 - \lambda e^{-x^2}\right]\psi = E\psi, \quad E < \frac{1}{2}, \tag{2.3}$$

or equivalently,

$$\left[H_0 - E\right]\psi = \lambda e^{-x^2}\psi, \tag{2.4}$$

By setting $\chi = \left[H_0 - E\right]^{\frac{1}{2}}\psi$, the latter equation can be rewritten as:

$$\left[H_0 - E\right]^{\frac{1}{2}}\chi = \lambda e^{-x^2}\left[H_0 - E\right]^{-\frac{1}{2}}\chi, \tag{2.5}$$

which can finally be recast as the following integral equation

$$\chi = \lambda\left[H_0 - E\right]^{-\frac{1}{2}} e^{-x^2}\left[H_0 - E\right]^{-\frac{1}{2}}\chi, \tag{2.6}$$

taking account that the square root of the resolvent in x-space is a positive integral operator for any $E < \frac{1}{2}$.

Alternatively, one can set $\phi = e^{-x^2/2}\psi$, to get instead a different integral equation, namely:

$$\phi = \lambda e^{-x^2/2}\left[H_0 - E\right]^{-1} e^{-x^2/2}\phi, \tag{2.7}$$

the positive integral operator on the right hand side of the latter equation being the renowned Birman–Schwinger operator widely used in the literature on small perturbations of the Laplacian in the sense of quadratic forms. As is well known (see [55,56]), the two integral operators are isospectral.

Therefore, the Birman–Schwinger principle can be exploited in either integral equation to establish the one-to-one correspondence between the ground state energy of the original Hamiltonian and the value of the energy parameter in (2.6) or (2.7) for which the respective integral operator has an eigenvalue equal to one. We wish to remind the reader that the analog of the integral operator in (2.6) for $H_0 = -\frac{d^2}{dx^2}$ has been investigated in [53,54] to evaluate the lowest eigenvalues of the one-dimensional negative Laplacian perturbed by an attractive Gaussian potential. It is worth pointing out that in those works the p-space representation was chosen so that the square roots of the resolvent acted as multiplication operators and the potential as a convolution integral operator, thus taking advantage of the invariance of the Gaussian under the Fourier integral transform.

3. Exact calculation of the trace of $\lambda\,[H_0 - E]^{-\frac{1}{2}}\, e^{-x^2}\, [H_0 - E]^{-\frac{1}{2}}$

As the Gaussian potential is clearly absolutely summable, we could exploit the general estimate of the trace class norm of our positive integral operator given for any absolutely summable perturbing potential in [21] in terms of the $||\cdot||_1$-norm of the potential, that is to say:

$$\lambda\left|\left|[H_0 - E]^{-\frac{1}{2}}\, e^{-x^2}\, [H_0 - E]^{-\frac{1}{2}}\right|\right|_1 = \lambda\sum_{n=0}^{\infty}\frac{(\psi_n, e^{-x^2}\psi_n)}{n+\frac{1}{2}-E} \le \lambda\pi^{\frac{1}{2}}C \tag{3.1}$$

where $C = \sum_{n=0}^{\infty}\frac{||\psi_n||_\infty^2}{n+\frac{1}{2}-E} < \infty$, given that the numerator of the sequence inside the sum decays like $n^{-\frac{1}{6}}$ ([27,35,38]).

It is instructive, however, to take advantage of the unique properties of the Gaussian potential in order to obtain more detailed information on the trace of the operator. Given that $(\psi_n, e^{-x^2}\psi_n) = \pi^{\frac{1}{2}}(\psi_n, \psi_0\psi_0\psi_n) = \pi^{\frac{1}{2}}(\psi_n\psi_0, \psi_0\psi_n) = \left(\frac{\pi}{2}\right)^{\frac{1}{2}}\psi_{2n}^2(0)$ (having taken account of the fact that the eigenfunctions of the harmonic oscillator are real-valued functions), as follows from Wang's results on such scalar products of four eigenfunctions of the harmonic oscillator (see [57,58]), one gets:

$$\lambda\sum_{n=0}^{\infty}\frac{(\psi_n, e^{-x^2}\psi_n)}{n+\frac{1}{2}-E} = \lambda\left(\frac{\pi}{2}\right)^{\frac{1}{2}}\sum_{n=0}^{\infty}\frac{\psi_{2n}^2(0)}{n+\frac{1}{2}-E} = \lambda\,(2\pi)^{\frac{1}{2}}\sum_{n=0}^{\infty}\frac{\psi_{2n}^2(0)}{2n+1-2E} \tag{3.2}$$

The convergence of the latter series is faster than that of the series defining the constant C in (3.1) since $\psi_{2n}^2(0) \to 0$ like $n^{-\frac{1}{2}}$ (see [27,35,38]). Furthermore, it is possible to write the series in terms of special functions since:

$$\lambda\,(2\pi)^{\frac{1}{2}}\sum_{n=0}^{\infty}\frac{\psi_{2n}^2(0)}{2n+1-2E} = \lambda\,(2\pi)^{\frac{1}{2}}\left(H_0+\frac{1}{2}-2E\right)^{-1}(0,0), \tag{3.3}$$

the value of the Green function (the integral kernel of the resolvent operator) of the unperturbed harmonic oscillator evaluated at $x = y = 0$.

As is well known from the aforementioned papers on point perturbations of the one-dimensional harmonic oscillator ([27,37,38,46]), the right hand side of (3.3) can be expressed in integral form as:

$$\lambda\,(2\pi)^{\frac{1}{2}}\left(H_0+\frac{1}{2}-2E\right)^{-1}(0,0) = 2^{\frac{1}{2}}\lambda\int_0^{\infty}\frac{e^{(2E-1)t}}{(1-e^{-2t})^{\frac{1}{2}}}dt = 2^{\frac{1}{2}}\lambda\int_0^{1}\frac{s^{-2E}}{(1-s^2)^{\frac{1}{2}}}ds \tag{3.4}$$

As the latter integral can be written in terms of the beta function, which in turn can be expressed as a ratio of Gamma functions, the right hand side of (3.4) is simply given by:

$$\lambda\left(\frac{\pi}{2}\right)^{\frac{1}{2}}\frac{\Gamma\left(\frac{1}{2}-E\right)}{\Gamma\left(1-E\right)} \tag{3.5}$$

The result that has just been obtained can be summarized as follows:

Theorem 3.1. *For any $E < \dfrac{1}{2}$ the positive isospectral integral operators*

$$(H_0 - E)^{-1/2}\, e^{-x^2}\, (H_0 - E)^{-1/2} \quad \textit{and} \quad e^{-\frac{x^2}{2}}\, (H_0 - E)^{-1}\, e^{-\frac{x^2}{2}}$$

are trace class and their trace class norm is equal to

$$\left|\left|\lambda (H_0 - E)^{-1/2} e^{-x^2} (H_0 - E)^{-1/2}\right|\right|_1 = \lambda \left(\frac{\pi}{2}\right)^{\frac{1}{2}} \frac{\Gamma\left(\frac{1}{2} - E\right)}{\Gamma\left(1 - E\right)} \tag{3.6}$$

Of course, when $E > \dfrac{1}{2}$ but still in the resolvent set $\rho(H_0)$ ($E \neq n + \dfrac{1}{2}$), the Birman–Schwinger operator is no longer positive so that the right hand side of (3.6) is no longer its $||\cdot||_1$- norm but only its trace, that is to say the difference between the norm of its positive part and that of its negative part. The plot of the right hand side of (3.6) is shown in Fig. 3.

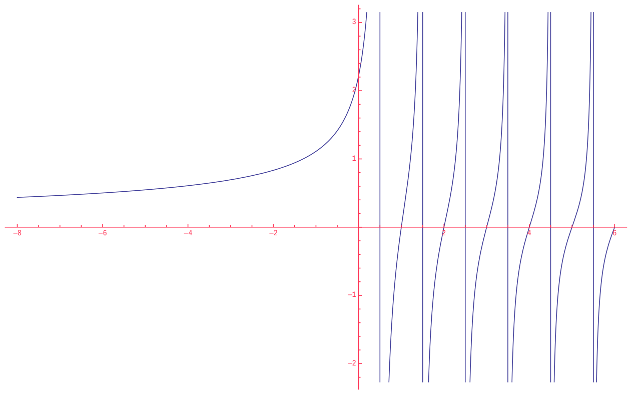

FIG. 3. The plot of the trace of the Birman–Schwinger operator for the Gaussian perturbation as a function of E for $\lambda = 1$.

As is evident from the graph, the trace is positively (respectively negatively) divergent as E approaches an eigenvalue of H_0 from the left (resp. right) due to the positive (respectively negative) divergence of the corresponding rank one operator in the left (resp. right) neighbourhood of that eigenvalue.

The reader acquainted with the literature on point perturbations of the one-dimensional harmonic oscillator (see [25, 27, 37, 38, 46]) will certainly recall that, in the case of an attractive central δ-perturbation, the trace of the positive operator $\lambda(H_0 - E)^{-1/2}\delta(x)(H_0 - E)^{-1/2}$ can also be written in terms of a ratio of Gamma functions, namely

$$\left|\left|\lambda (H_0 - E)^{-1/2} \delta(x) (H_0 - E)^{-1/2}\right|\right|_1 = \lambda \frac{\Gamma\left(\frac{1}{4} - \frac{E}{2}\right)}{2\Gamma\left(\frac{3}{4} - \frac{E}{2}\right)} \tag{3.7}$$

The plot of the right hand side of (3.7) is provided in Fig. 4. As was to expected, while the trace corresponding to the Gaussian perturbation vanishes at $E = n, n = 1, 2, ..$ and diverges at $E = n + \dfrac{1}{2}, n = 0, 1, 2, ..$, the trace corresponding to the δ-perturbation vanishes at $E = 2n + \dfrac{3}{2}, n = 0, 1, 2, ..$ and diverges at $E = 2n + \dfrac{1}{2}, n = 0, 1, 2, ...$

However, a crucial difference between the two models is to be stressed with regard to the quest for the eigenvalues of the perturbed Hamiltonian: while in the latter case, the operator has rank equal to one, which implies that the right hand side of (3.7) determines completely the bound state equation, in the case of the Gaussian perturbation the right hand side of (3.6) represents only the linear term in the expansion of the Fredholm determinant appearing in the bound state equation, that is to say

$$\det\left[1 - \lambda\, (H_0 - E)^{-1/2}\, e^{-x^2}\, (H_0 - E)^{-1/2}\right] = 0, \tag{3.8}$$

so that the traces of all the other powers of the operator are needed in order to compute the new eigenvalues created by the perturbation. We remind the reader that, as a consequence of a well-known inequality for Fredholm determinants, for any $\lambda > 0$ and $E < \dfrac{1}{2}$, we get:

$$\left|\det\left[1 - \lambda\, (H_0 - E)^{-1/2}\, e^{-x^2}\, (H_0 - E)^{-1/2}\right]\right| \leq e^{\lambda \left|\left|(H_0 - E)^{-1/2} e^{-x^2} (H_0 - E)^{-1/2}\right|\right|_1}, \tag{3.9}$$

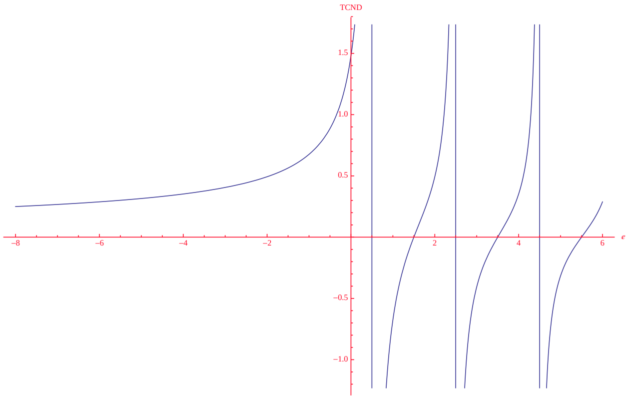

FIG. 4. The plot of the trace of the Birman–Schwinger operator for the δ-perturbation as a function of E for $\lambda = 1$.

which becomes

$$\left|\det\left[1-\lambda\left(H_0-E\right)^{-1/2}e^{-x^2}\left(H_0-E\right)^{-1/2}\right]\right| \le e^{\lambda\left(\frac{\pi}{2}\right)^{\frac{1}{2}}\frac{\Gamma\left(\frac{1}{2}-E\right)}{\Gamma(1-E)}}, \tag{3.10}$$

taking advantage of (3.6). In Fig. 5 the plot of the function on the right hand side of (3.10) is shown for $E < \dfrac{5}{2}$, even though it must be borne in mind that the function represents the upper bound of the absolute value of the determinant only up to $E < \dfrac{1}{2}$.

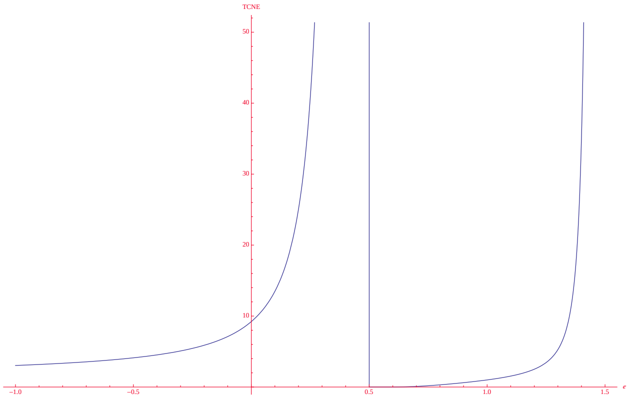

FIG. 5. The plot of $e^{\lambda\left(\frac{\pi}{2}\right)^{\frac{1}{2}}\frac{\Gamma\left(\frac{1}{2}-E\right)}{\Gamma(1-E)}}$ for $\lambda = 1$

Despite the far greater complexity of the determinant in our case, it might be possible to compute the eigenvalues of the Hamiltonian of the harmonic oscillator with an attractive Gaussian perturbation to a satisfactory degree of accuracy by exploiting the aforementioned fact that the integral operator $\lambda(H_0-E)^{-1/2}e^{-x^2}(H_0-E)^{-1/2}$ diverges only on a one-dimensional subspace in proximity of an eigenvalue of H_0, which was crucial in [21, 22] to investigate the discrete spectrum of the harmonic oscillator with the Lorentzian perturbation $\dfrac{\lambda}{1+gx^2}$. The latter issue will be dealt with in a separate publication.

Acknowledgements

The final part of S. Fassari's contribution to this work has been financially supported by the Government of the Russian Federation through the ITMO University Fellowship and Professorship Programme. S. Fassari would like to thank Prof. Igor Yu. Popov and the entire staff at the Departament of Higher Mathematics, ITMO University, St. Petersburg for their warm hospitality throughout his stay. F. Rinaldi wishes to thank Prof. Igor Yu. Popov for inviting him to the Pierre Duclos Workshop over the years as well as for his interest in our research work.

References

[1] Landau L.D. and Lifshits E.M., *Quantum Mechanics: Non-Relativistic Theory*, Pergamon Press.

[2] Reed M., Simon B. *Fourier Analysis*, Methods in Modern Mathematical Physics, Academic Press, New York, 1975.

[3] Reed M., Simon B. *Analysis of Operators*, Methods in Modern Mathematical Physics, Academic Press, New York, 1978.

[4] Loeffel J.J., Martin A., Simon B., Wightman A. *Padé approximants and the anharmonic oscillator*, Phys. Lett. B, 1969, **30**, P. 656–658.

[5] Davydov A.S. *Quantum Mechanics*, Oxford: Pergamon Press, 1965.

[6] Yaris R., Bendler J., Lovett R.A., Bender C.M. and Fedders P.A. *Resonance calculations for arbitrary potentials*, *Phys. Rev. A*, 1978, **18**, 1816.

[7] Caliceti E., Gra S., Maioli M. *Perturbation theory of odd anharmonic oscillators*, *Commun. Math. Phys.*, 1980, **75**, P. 51.

[8] Caliceti E., Maioli M. *Odd anharmonic oscillators and shape resonances* Ann. Inst. Henri Poincaré, 1983, **XXXVIII**(2), P. 175–186.

[9] Fernandez F.M., Guardiola R., Ros J. and Znojil M. Strong-coupling expansions for the PT-symmetric oscillators $V(x) = a(ix) + b(ix)^2 + c(ix)^3$. *J. Phys. A: Math. Gen.*, 1998, **31**, P. 10105.

[10] Grecchi V., Martinez A. The spectrum of the cubic oscillator. *Commun. Math. Phys.*, 2013, **319**, P. 479.

[11] Kaushal S.K. Small g and large λ solution of the Schrödinger equation for the interaction $\frac{\lambda x^2}{1+gx^2}$. *J. Phys. A Math. Gen.*, 1979, **12**, P. L253.

[12] Mitra A.K. On the interaction of the type $x^2 + \frac{\lambda x^2}{1+gx^2}$. *J. Math. Phys.*, 1979, **19**(10), P. 2018–2022.

[13] Bessis N., Bessis G. A note on the Schrödinger equation for the $x^2 + \frac{\lambda x^2}{1+gx^2}$ potential. *J. Math. Phys.*, 1980, **21**, P. 2780–2785.

[14] Bessis N., Bessis G., Hadinger G. Perturbed harmonic oscillator ladder operators: eigenenergies and eigenfunctions for the $x^2 + \frac{\lambda x^2}{1+gx^2}$ interaction. *J. Phys. A Math. Gen.*, 1980, **13**, P. 1651.

[15] Bhagwat K.V. A harmonic oscillator perturbed by the potential $\frac{\lambda x^2}{1+gx^2}$. *J. Phys. A: Math. Gen.*, 1981, **14**, P. 377.

[16] Bessis N., Bessis G. Perturbed factorization of the symmetric-anharmonic-oscillator eigenequation. *Phys. Rev A*, 1992, **46**, P. 6824.

[17] Hodgson R.J.W. High-precision calculation of the eigenvalues for the $x^2 + \frac{\lambda x^2}{1+gx^2}$ potential. *J. Phys. A: Math. Gen.*, 1988, **21**, P. 1563.

[18] Lai C.S., Lin H.E. On the Schrödinger equation for the $x^2 + \frac{\lambda x^2}{1+gx^2}$ interaction. *J. Phys. A: Math. Gen.*, 1982, **15**, P. 1495.

[19] Blecher M.H., Leach P.G.L. The Schrödinger equation for the $x^2 + \frac{\lambda x^2}{1+gx^2}$ interaction. *J. Phys. A: Math. Gen.*, 1987, **20**, P. 5923.

[20] Angeletti A., Castagnari C., Zirilli F. Asymptotic eigenvalue degeneracy for a class of one-dimensional Fokker-Planck operators. *J. Math. Phys.*, 1985, **26**, P. 678.

[21] Fassari S. A note on the eigenvalues of the Hamiltonian of the harmonic oscillator perturbed by the potential $\frac{\lambda x^2}{1+gx^2}$. *Rep. Math. Phys.*, 1996, **37**(2), P. 283–293.

[22] Fassari S., Inglese G. On the eigenvalues of the Hamiltonian of the harmonic oscillator with the interaction $\frac{\lambda x^2}{1+gx^2}$. II Rep. Math. Phys., 1997, **39**(1), P. 77–86.

[23] Cariñena J.F., Rañada M.F., Santander M. A quantum exactly solvable non-linear oscillator with quasi-harmonic behaviour. *Annals of Physics*, 2007, **322**(2), P. 434–459.

[24] Gadreau P., Safouhi H. Double exponential sinc-collocation method for solving the energy eigenvalues of harmonic oscillators perturbed by a rational function. *J. Math. Phys.*, 2017, **26**(10), P. 101509.

[25] Avakian M.P., Pogosyan G.S., Sissakian A.N., Ter-Antonyan V.M. Spectroscopy of a singular linear oscillator. *Physics Letters A*, 1987, **124**(4-5), P. 233–236.

[26] Goldstein J., Lebiedzik C., Robinett R.W. Supersymmetric quantum mechanics: Examples with Dirac δ-functions. *American Journal of Physics*, **62**(7), P. 612–618.

[27] Fassari S., Inglese G. On the spectrum of the harmonic oscillator with a $\delta-$type perturbation. *Helv. Phys. Acta*, 1994, **67**, P. 650–659.

[28] Demiralp E. Bound states of n-dimensional harmonic oscillator decorated with Dirac delta functions. *J. Phys. A: Math. Theor.*, 2005, **22**, P. 478393.

[29] Uncu H., Tarhan D., Demiralp E., Müstecaploğlu Ö.E. *Phys. Rev. A.*, 2007, **76**, P. 013618.

[30] Patil S.H. Harmonic oscillator with a δ-function potential. *Eur. J. Phys.*, 2006, **27**, P. 899.

[31] Goold J., ODonoghue D. and Busch Th. Low-density, one-dimensional quantum gases in the presence of a localized attractive potential. *J. Phys. B: At. Mol. Opt. Phys.*, 2008, **41**, P. 215301.

[32] Shea P., Van Zyl B.P. and Bhaduri R.K. The two-body problem of ultra-cold atoms in a harmonic trap. *Am. J. Phys.*, 2009, **77**, P. 5115.

[33] Filatova T.A. and Shafarevich A.I. Semiclassical spectral series of the Schrödinger operator with a delta-potential on a straight line and on a sphere. *Theor. Math. Phys.*, 2010, **164**, P. 106480.

[34] Mityagin B. The spectrum of a harmonic oscillator operator perturbed by point interactions. *Int. J. Theor. Phys.*, 2014, **53**, P. 118.

[35] Mityagin B.S., Siegl P. Root system of singular perturbations of the harmonic oscillator type operators. *Lett. Math. Phys.*, 2016, **106**, P. 147–167.

[36] Ferkous N., Boudjedaa T. Bound States Energies of a Harmonic Oscillator Perturbed by Point Interactions. *Commun. Theor. Phys.*, 2017, **67**, P 241.

[37] Fassari S., Inglese G. On the spectrum of the harmonic oscillator with a $\delta-$type perturbation. *II Helv. Phys. Acta*, 1997, **70**, P. 858–865.

[38] Fassari S., Rinaldi F. On the spectrum of the Schrödinger Hamiltonian of the one-dimensional harmonic oscillator perturbed by two identical attractive point interactions. *Rep. Math. Phys.*, 2012, **69**(3), P. 353–370.

[39] Demiralp E. Properties of a pseudo-Hermitian Hamiltonian for the harmonic oscillator decorated with Dirac delta interactions. *Czech. J. Phys.*, 2005, **55**, P. 10814.

[40] Haag D., Cartarius H. and Wunner G. A Bose-Einstein condensate with PT-symmetric double delta function loss and gain in a harmonic trap: a test of rigorous estimates. *Acta Polytech.*, 2014, **54**, P. 11621.

[41] Single F., Cartarius H., Wunner G. and Main J. Coupling approach for the realization of a PT-symmetric potential for a Bose-Einstein condensate in a double well. *Phys. Rev. A*, 2014, **90**, P. 042123.

[42] Albeverio S., Dabrowski L. and Kurasov P. Symmetries of Schrödinger operators with point interactions. *Lett. Math. Phys.*, 1998, **45**, P. 3347.

[43] Albeverio S. and Kurasov P. *Singular Perturbations of Differential Operators: Solvable Type Operators*. Cambridge, Cambridge University Press, 2000.

[44] Gadella M., Glasser M.L., Nieto L.M. One-dimensional models with a singular potential of the type $-\alpha\delta + \beta\delta'$. *Int. J. Theor. Phys.*, 2011, **50**, P. 2144–2152.

[45] Maldonado-Villamizar F.H. Semitransparent one-dimensional potential: a Green's function approach. *Phys. Scr.*, 2015, **90**, P. 065202.

[46] Albeverio S., Fassari S., Rinaldi F. A remarkable spectral feature of the Schrödinger Hamiltonian of the harmonic oscillator perturbed by an attractive δ'-interaction centred at the origin: double degeneracy and level crossing. *J. Phys. A: Math. Theor.*, 2013, **46**, P. 385305.

[47] Albeverio S., Fassari S., Rinaldi F. The Hamiltonian of the harmonic oscillator with an attractive δ'-interaction centred at the origin as approximated by the one with a triple of attractive interactions. *J. Phys. A: Math. Theor.*, 2016, **49**, P. 025302.

[48] Cheon T. and Shigehara T. Fermion-Boson duality of one-dimensional quantum particles with generalized contact interactions. *Phys. Rev. Lett.*, 1999, **82**, P. 2536.

[49] Nouicer K., Chetouani L. Variational treatment of Gaussian potentials. *Acta Physica Slovaca*, 1999, **49**(3), P. 309–318.

[50] Fassari S., Gadella M., Glasser M.L., Nieto L.M. and Rinaldi F. Level crossings of eigenvalues of the Schrödinger Hamiltonian of the isotropic harmonic oscillator perturbed by a central point interaction in different dimensions. *Nanosystems, Physics, Chemistry, Mathematics*, 2018, **9**(2), P. 179–186.

[51] Fassari S., Gadella M., Glasser M.L., Nieto L.M. Spectroscopy of a one-dimensional V-shaped quantum well with a point impurity. *Annals of Physics*, 2018, **389**, P. 48–62.

[52] Reed M., Simon B. *Functional Analysis, Methods in Modern Mathematical Physics*. Academic Press, New York, 1972.

[53] Muchatibaya G., Fassari S., Rinaldi F., Mushanyu J. A note on the discrete spectrum of Gaussian wells (I): the ground state energy in one dimension. *Adv. Math. Phys.*, 2016, Article ID 2125769.

[54] Fassari S., Gadella M., Nieto L.M., Rinaldi F. On the spectrum of the 1D Schrödinger Hamiltonian perturbed by an attractive Gaussian potential. *Acta Polytech.*, 2017, **57**, P. 385–390.

[55] Klaus M. A remark about weakly coupled one-dimensional Schrödinger operators. *Helv. Phys. Acta*, 1979, **52**, P. 223.

[56] Fassari S. An estimate regarding one-dimensional point interactions. *Helv. Phys. Acta*, 1995, **68**, P. 121–125.

[57] Wang W.-M. Pure Point Spectrum of the Floquet Hamiltonian for the Quantum Harmonic Oscillator Under Time Quasi-Periodic Perturbations. *Commun. Math. Phys.*, 2008, **277**, P. 459–496.

[58] Albeverio S., Fassari S., Gadella M., Nieto L.M. and Rinaldi F. The Birman–Schwinger Operator for a Parabolic Quantum Well in a Zero-Thickness Layer in the Presence of a Two-Dimensional Attractive Gaussian Impurity. *Front. Phys.*, 2019, **7**(102).

NANOSYSTEMS: PHYSICS, CHEMISTRY, MATHEMATICS, 2019, 10 (6), P. 616–622

Threshold analysis for a family of 2×2 operator matrices

T. H. Rasulov, E. B. Dilmurodov

Department of Mathematics, Faculty of Physics and Mathematics,
Bukhara State University, M. Ikbol str. 11, 200100 Bukhara, Uzbekistan

rth@mail.ru, elyor.dilmurodov@mail.ru

DOI 10.17586/2220-8054-2019-10-6-616-622

We consider a family of 2×2 operator matrices $\mathcal{A}_\mu(k)$, $k \in \mathbb{T}^3 := (-\pi, \pi]^3$, $\mu > 0$, acting in the direct sum of zero- and one-particle subspaces of a Fock space. It is associated with the Hamiltonian of a system consisting of at most two particles on a three-dimensional lattice $\mathbb{Z}^3$, interacting via annihilation and creation operators. We find a set $\Lambda := \{k^{(1)}, ..., k^{(8)}\} \subset \mathbb{T}^3$ and a critical value of the coupling constant μ to establish necessary and sufficient conditions for either $z = 0 = \min\limits_{k \in \mathbb{T}^3} \sigma_{\mathrm{ess}}(\mathcal{A}_\mu(k))$ (or $z = 27/2 = \max\limits_{k \in \mathbb{T}^3} \sigma_{\mathrm{ess}}(\mathcal{A}_\mu(k))$ is a threshold eigenvalue or a virtual level of $\mathcal{A}_\mu(k^{(i)})$ for some $k^{(i)} \in \Lambda$.

Keywords: operator matrices, Hamiltonian, generalized Friedrichs model, zero- and one-particle subspaces of a Fock space, threshold eigenvalues, virtual levels, annihilation and creation operators.

Received: 19 October 2019

Revised: 13 November 2019

1. Introduction

Operator matrices are matrices where the entries are linear operators between Banach or Hilbert spaces, see [1]. One special class of operator matrices are Hamiltonians associated with the systems of non-conserved number of quasi-particles on a lattice. In such systems the number of particles can be unbounded as in the case of spin-boson models [2,3] or bounded as in the case of "truncated" spin-boson models [4–7]. They arise, for example, in the theory of solid-state physics [8], quantum field theory [9] and statistical physics [4, 10].

The study of systems describing n particles in interaction, without conservation of the number of particles is reduced to the investigation of the spectral properties of self-adjoint operators acting in the *cut subspace* $\mathcal{H}^{(n)}$ of the Fock space, consisting of $r \leq n$ particles [4, 9, 10]. The perturbation of an operator (the generalized Friedrichs model which has a 2×2 operator matrix form acting in $\mathcal{H}^{(2)}$), with discrete and essential spectrum has played a considerable role in the study of spectral problems connected with the quantum theory of fields [9].

One of the most actively studied objects in operator theory, in many problems of mathematical physics and other related fields is the investigation of the threshold eigenvalues and virtual levels of block operator matrices, in particular, Hamiltonians on a Fock space associated with systems of non-conserved number of quasi-particles on a lattice. In the present paper, we consider a family of 2×2 operator matrices $\mathcal{A}_\mu(k)$, $k \in \mathbb{T}^3 := (-\pi, \pi]^3$, $\mu > 0$ (so - called generalized Friedrichs models) associated with the Hamiltonian of a system consisting of at most two particles on a three-dimensional lattice $\mathbb{Z}^3$, interacting via creation and annihilation operators. They are acting in the direct sum of zero-particle and one-particle subspaces of a Fock space. The main goal of the paper is to give a thorough mathematical treatment of the spectral properties of this family in three dimensions. More exactly, we find a set $\Lambda := \{k^{(1)}, ..., k^{(8)}\} \subset \mathbb{T}^3$ and prove that for a $i \in \{1, 2, \ldots, 8\}$ there is a value μ_i of the parameter μ such that only for $\mu = \mu_i$ the operator $\mathcal{A}_\mu(\bar{0})$ has a zero-energy resonance, here $0 = \min \sigma_{\mathrm{ess}}(\mathcal{A}_\mu(\bar{0}))$ and the operator $\mathcal{A}_\mu(k^{(i)})$ has a virtual level at the point $z = 27/2 = \max \sigma_{\mathrm{ess}}(\mathcal{A}_\mu(k^{(i)}))$, where $\bar{0} := (0, 0, 0) \in \mathbb{T}^3$ and $k^{(i)} \in \Lambda$. We point out that a part of the results is typical for lattice models; in fact, they do not have analogs in the continuous case (because its essential spectrum is half-line $[E; +\infty)$, see for example [4]).

We notice that threshold eigenvalue and virtual level (threshold energy resonance) of a generalized Friedrichs model have been studied in [11–14]. The paper [15] is devoted to the threshold analysis for a family of Friedrichs models under rank one perturbations. In [16] a wide class of two-body energy operators $h(k)$ on the d-dimensional lattice $\mathbb{Z}^{\mathrm{d}}$, $\mathrm{d} \geq 3$, is considered, where k is the two-particle quasi-momentum. If the two-particle Hamiltonian $h(0)$ has either an eigenvalue or a virtual level at the bottom of its essential spectrum and the one-particle free Hamiltonians in the coordinate representation generate positivity preserving semi-groups, then it is shown that for all nontrivial values k, $k \neq 0$, the discrete spectrum of $h(k)$ below its threshold is non-empty. These results have been applied to the proof of the existence of Efimov's effect and to obtain discrete spectrum asymptotics of the corresponding Hamiltonians. We note that above mentioned results are discussed only for the bottom of the essential spectrum. The threshold eigenvalues and virtual levels of a slightly simpler version of $\mathcal{A}_\mu(k)$ were investigated in [17], and the structure of the numerical range are studied using similar results. In [18], the essential spectrum of the family of 3×3 operator matrices $H(K)$ is described by the spectrum of the family of 2×2 operator matrices. The results of the present paper are play important role in the investigations of the operator $H(K)$, see [12].

The plan of this paper is as follows: Section 1 is an introduction to the whole work. In Section 2, a family of 2×2 operator matrices are described as bounded self-adjoint operators in the direct sum of two Hilbert spaces and its spectrum is described. In Section 3, we discuss some results concerning threshold analysis of a family of 2×2 operator matrices.

We adopt the following conventions throughout the present paper. Let $\mathbb{N}$, $\mathbb{Z}$, $\mathbb{R}$ and $\mathbb{C}$ be the set of all positive integers, integers, real and complex numbers, respectively. We denote by $\mathbb{T}^3$ the three-dimensional torus (the first Brillouin zone, i.e., dual group of $\mathbb{Z}^3$), the cube $(-\pi, \pi]^3$ with appropriately identified sides equipped with its Haar measure. The torus $\mathbb{T}^3$ will always be considered as an abelian group with respect to the addition and multiplication by real numbers regarded as operations on the three-dimensional space $\mathbb{R}^3$ modulo $(2\pi\mathbb{Z})^3$.

Denote by $\sigma(\cdot)$, $\sigma_{\text{ess}}(\cdot)$ and $\sigma_{\text{disc}}(\cdot)$, respectively, the spectrum, the essential spectrum, and the discrete spectrum of a bounded self-adjoint operator.

2. Family of 2×2 operator matrices and its spectrum

Let $L_2(\mathbb{T}^3)$ be the Hilbert space of square-integrable (complex-valued) functions defined on the three-dimensional torus $\mathbb{T}^3$. Denote $\mathcal{H}$ by the direct sum of spaces $\mathcal{H}_0 := \mathbb{C}$ and $\mathcal{H}_1 := L_2(\mathbb{T}^3)$, that is, $\mathcal{H} := \mathcal{H}_0 \oplus \mathcal{H}_1$. We write the elements f of the space $\mathcal{H}$ in the form $f = (f_0, f_1)$ with $f_0 \in \mathcal{H}_0$ and $f_1 \in \mathcal{H}_1$. Then for any two elements $f = (f_0, f_1)$ and $g = (g_0, g_1)$, their scalar product is defined by

$$(f, g) := f_0\overline{g_0} + \int\limits_{\mathbb{T}^3} f_1(t)\overline{g_1(t)}dt.$$

The Hilbert spaces $\mathcal{H}_0$ and $\mathcal{H}_1$ are zero- and one-particle subspaces of a Fock space $\mathcal{F}(L_2(\mathbb{T}^3))$ over $L_2(\mathbb{T}^3)$, respectively, where

$$\mathcal{F}(L_2(\mathbb{T}^3)) := \mathbb{C} \oplus L_2(\mathbb{T}^3) \oplus L_2((\mathbb{T}^3)^2) \oplus \cdots \oplus L_2((\mathbb{T}^3)^n) \oplus \cdots .$$

In the Hilbert space $\mathcal{H}$ we consider the following family of 2×2 operator matrices

$$\mathcal{A}_\mu(k) := \left(\begin{array}{cc} A_{00}(k) & \mu A_{01} \\ \mu A_{01}^* & A_{11}(k) \end{array} \right),$$

where $A_{ii}(k) : \mathcal{H}_i \to \mathcal{H}_i$, $i = 0, 1$, $k \in \mathbb{T}^3$ and $A_{01} : \mathcal{H}_1 \to \mathcal{H}_0$ are defined by the rules

$$A_{00}(k)f_0 = w_0(k)f_0, \quad A_{01}f_1 = \int\limits_{\mathbb{T}^3} v(t)f_1(t)dt, \quad (A_{11}(k)f_1)(p) = w_1(k, p)f_1(p).$$

Here $f_i \in \mathcal{H}_i$, $i = 0, 1$; $\mu > 0$ is a coupling constant, the function $v(\cdot)$ is a real-valued analytic function on $\mathbb{T}^3$, the functions $w_0(\cdot)$ and $w_1(\cdot, \cdot)$ have the form

$$w_0(k) := \varepsilon(k) + \gamma, \quad w_1(k, p) := \varepsilon(k) + \varepsilon(k + p) + \varepsilon(p)$$

with $\gamma \in \mathbb{R}$ and the dispersion function $\varepsilon(\cdot)$ is defined by

$$\varepsilon(k) := \sum_{i=1}^{3}(1 - \cos k_i), \; k = (k_1, k_2, k_3) \in \mathbb{T}^3. \tag{2.1}$$

Under these assumptions the operator matrix $\mathcal{A}_\mu(k)$ is a bounded and self-adjoint in $\mathcal{H}$.

We remark that the operators A_{01} and A_{01}^* are called annihilation and creation operators [9], respectively. In physics, an annihilation operator is an operator that lowers the number of particles in a given state by one, a creation operator is an operator that increases the number of particles in a given state by one, and it is the adjoint of the annihilation operator.

Let $\mathcal{A}_0(k) := \mathcal{A}_\mu(k)|_{\mu=0}$. The perturbation $\mathcal{A}_\mu(k) - \mathcal{A}_0(k)$ of the operator $\mathcal{A}_0(k)$ is a self-adjoint operator of rank 2. Therefore, in accordance with the invariance of the essential spectrum under the finite rank perturbations [19], the essential spectrum $\sigma_{\text{ess}}(\mathcal{A}_\mu(k))$ of $\mathcal{A}_\mu(k)$ fills the following interval on the real axis

$$\sigma_{\text{ess}}(\mathcal{A}_\mu(k)) = [m(k), M(k)],$$

where the numbers $m(k)$ and $M(k)$ are defined by

$$m(k) := \min_{p\in\mathbb{T}^3} w_1(k,p), \quad M(k) := \max_{p\in\mathbb{T}^3} w_1(k,p). \tag{2.2}$$

Remark 2.1. *We remark that the essential spectrum of $\mathcal{A}_\mu(\bar{\pi})$, $\bar{\pi} := (\pi,\pi,\pi) \in \mathbb{T}^3$ is degenerate to the set consisting of the unique point $\{12\}$ and hence we can not state that the essential spectrum of $\mathcal{A}_\mu(k)$ is absolutely continuous for any $k \in \mathbb{T}^3$.*

For any $\mu > 0$ and $k \in \mathbb{T}^3$ we define an analytic function $\Delta_\mu(k\,;\cdot)$ in $\mathbb{C} \setminus \sigma_{\rm ess}(\mathcal{A}_\mu(k))$ by

$$\Delta_\mu(k\,;z) := w_0(k) - z - \mu^2 \int\limits_{\mathbb{T}^3} \frac{v^2(t)dt}{w_1(k,t)-z}, \ z \in \mathbb{C} \setminus \sigma_{\rm ess}(\mathcal{A}_\mu(k)).$$

Usually the function $\Delta_\mu(k\,;\cdot)$ is called the Fredholm determinant associated to the operator matrix $\mathcal{A}_\mu(k)$.

The following statement establishes connection between the eigenvalues of the operator $\mathcal{A}_\mu(k)$ and zeros of the function $\Delta_\mu(k\,;\cdot)$, see [11, 14].

Lemma 2.2. *For any $\mu > 0$ and $k \in \mathbb{T}^3$ the operator $\mathcal{A}_\mu(k)$ has an eigenvalue $z_\mu(k) \in \mathbb{C} \setminus \sigma_{\rm ess}(\mathcal{A}_\mu(k))$ if and only if $\Delta_\mu(k\,;z_\mu(k)) = 0$.*

From Lemma 2.2 it follows that

$$\sigma_{\rm disc}(\mathcal{A}_\mu(k)) = \{z \in \mathbb{C} \setminus \sigma_{\rm ess}(\mathcal{A}_\mu(k)) :\ \Delta_\mu(k\,;z) = 0\}.$$

Since the function $\Delta_\mu(k\,;\cdot)$ is a monotonically decreasing function on $(-\infty;m(k))$ and $(M(k);+\infty)$, for $\mu > 0$ and $k \in \mathbb{T}^3$ the operator $\mathcal{A}_\mu(k)$ has no more than 1 simple eigenvalue in $(-\infty;m(k))$ and $(M(k);+\infty)$.

Let $\Lambda := \{k = (k_1,k_2,k_3) : k_i \in \{-2\pi/3, 2\pi/3\}, i = 1,2,3\}$. Since the set $\Lambda \subset \mathbb{T}^3$ consists 8 points for a convenience we rewrite the set Λ as $\Lambda = \{k^{(1)}, k^{(2)}, \ldots, k^{(8)}\}$.

It is easy to verify that the function $w_1(\cdot,\cdot)$ has a non-degenerate minimum at the point $(\bar{0},\bar{0}) \in (\mathbb{T}^3)^2$, $\bar{0} := (0,0,0)$ and has non-degenerate maximum at the points of the form $(k^{(i)},k^{(i)}) \in (\mathbb{T}^3)^2$, $i = 1,\ldots,8$, such that

$$\min_{k,p\in\mathbb{T}^3} w_1(k,p) = w_1(\bar{0},\bar{0}) = 0, \quad \max_{k,p\in\mathbb{T}^3} w_1(k,p) = w_2(k^{(i)},k^{(i)}) = 27/2, \quad i = 1,\ldots,8.$$

Simple calculations show that

$$\sigma_{\rm ess}(\mathcal{A}_\mu(\bar{0})) = [0;12];$$
$$\sigma_{\rm ess}(\mathcal{A}_\mu(k^{(i)})) = [\frac{15}{2};\frac{27}{2}], \quad i = 1,\ldots,8.$$

Therefore,

$$\min_{k\in\mathbb{T}^3} \sigma_{\rm ess}(\mathcal{A}_\mu(k)) = 0, \quad \max_{k\in\mathbb{T}^3} \sigma_{\rm ess}(\mathcal{A}_\mu(k)) = \frac{27}{2}.$$

3. Threshold eigenvalues and virtual levels

In this Section, we prove that for any $i \in \{1,\ldots,8\}$ there is a value μ_i of the parameter (coupling constant) μ such that only for $\mu = \mu_i$ the operator $\mathcal{A}_\mu(\bar{0})$ has a virtual level at the point $z = 0$ (zero-energy resonance) and the operator $\mathcal{A}_\mu(k^{(i)})$ has a virtual level at the point $z = 27/2$ under the assumption that $v(\bar{0}) \neq 0$ and $v(k^{(i)}) \neq 0$. For the case $v(\bar{0}) = 0$ and $v(k^{(i)}) = 0$ we show that the number $z = 0$ $(z = 27/2)$ is a threshold eigenvalue of $\mathcal{A}_\mu(\bar{0})$ $(\mathcal{A}_\mu(k^{(i)}))$.

Denote by $C(\mathbb{T}^3)$ and $L_1(\mathbb{T}^3)$ the Banach spaces of continuous and integrable functions on $\mathbb{T}^3$, respectively.

Definition 3.1. *Let $\gamma \neq 0$. The operator $\mathcal{A}_\mu(\bar{0})$ is said to have a virtual level at $z = 0$ (or zero-energy resonance), if the number 1 is an eigenvalue of the integral operator*

$$(G_\mu\psi)(p) = \frac{\mu^2 v(p)}{2\gamma} \int\limits_{\mathbb{T}^3} \frac{v(t)\psi(t)dt}{\varepsilon(t)}, \quad \psi \in C(\mathbb{T}^3)$$

and the associated eigenfunction $\psi(\cdot)$ (up to constant factor) satisfies the condition $\psi(\bar{0}) \neq 0$.

Definition 3.2. *Let* $\gamma \neq 9$ *and* $i \in \{1,\dots,8\}$*. The operator* $\mathcal{A}_\mu(k^{(i)})$ *is said to have a virtual level at* $z = 27/2$*, if the number* 1 *is an eigenvalue of the integral operator*

$$(G_\mu^{(i)}\varphi)(p) = \frac{\mu^2 v(p)}{\gamma - 9} \int\limits_{\mathbb{T}^3} \frac{v(t)\varphi(t)dt}{\varepsilon(k^{(i)}+t)+\varepsilon(t)-9}, \quad \varphi \in C(\mathbb{T}^3)$$

and the associated eigenfunction $\varphi(\cdot)$ $($*up to constant factor*$)$ *satisfies the condition* $\varphi(k^{(i)}) \neq 0$.

Using the extremal properties of the function $\varepsilon(\cdot)$, and the Lebesgue dominated convergence theorem, we obtain that there exist the positive finite limits

$$\lim_{z\to -0} \int\limits_{\mathbb{T}^3} \frac{v^2(t)dt}{\varepsilon(t)-z} = \int\limits_{\mathbb{T}^3} \frac{v^2(t)dt}{\varepsilon(t)};$$

$$\lim_{z\to 9+0} \int\limits_{\mathbb{T}^3} \frac{v^2(t)dt}{z-\varepsilon(k^{(i)}+t)-\varepsilon(t)} = \int\limits_{\mathbb{T}^3} \frac{v^2(t)dt}{9-\varepsilon(k^{(i)}+t)-\varepsilon(t)}.$$

For the next investigations, we define the following quantities

$$\mu_l(\gamma) := \sqrt{2\gamma} \left(\int\limits_{\mathbb{T}^3} \frac{v^2(t)dt}{\varepsilon(t)} \right)^{-1/2} \quad \text{for } \gamma > 0;$$

$$\mu_r^{(i)}(\gamma) := \sqrt{9-\gamma} \left(\int\limits_{\mathbb{T}^3} \frac{v^2(t)dt}{9-\varepsilon(k^{(i)}+t)-\varepsilon(t)} \right)^{-1/2} \quad \text{for } \gamma < 9, \ i = 1,\dots,8.$$

Let $\gamma_i \in (0;9)$ be an unique solution of $\mu_l(\gamma) = \mu_r^{(i)}(\gamma)$. It follows immediately that

$$\gamma_i := 9 \left(2\int\limits_{\mathbb{T}^3} \frac{v^2(t)dt}{9-\varepsilon(k^{(i)}+t)-\varepsilon(t)} + \int\limits_{\mathbb{T}^3} \frac{v^2(t)dt}{\varepsilon(t)} \right)^{-1} \int\limits_{\mathbb{T}^3} \frac{v^2(t)dt}{\varepsilon(t)}.$$

In the following, we compare the values of $\mu_l(\gamma)$ and $\mu_r(\gamma)$ depending on $\gamma \in (0;9)$.

Remark 3.3. *Let* $i \in \{1,\dots,8\}$*. By the definition of the quantities* $\mu_l(\gamma)$ *and* $\mu_r^{(i)}(\gamma)$ *one can conclude that*
if $\gamma \in (0;\gamma_i)$*, then* $\mu_l(\gamma) < \mu_r^{(i)}(\gamma)$;
if $\gamma = \gamma_i$*, then* $\mu_l(\gamma) = \mu_r^{(i)}(\gamma)$;
if $\gamma \in (\gamma_i;9)$*, then* $\mu_l(\gamma) > \mu_r^{(i)}(\gamma)$.

From the Definition 3.1 (resp. 3.2) we obtain that the number 1 is an eigenvalue of G_μ (resp. $G_\mu^{(i)}$) if and only if $\mu = \mu_l(\gamma)$ (resp. $\mu = \mu_r^{(i)}(\gamma)$).

We notice that in the Definition 3.2, the requirement of the presence of an eigenvalue 1 of $G_\mu^{(i)}$ corresponds to the existence of a solution of the equation $\mathcal{A}_\mu(k^{(i)})f = (27/2)f$ and the condition $\psi(k^{(i)}) \neq 0$ implies that the solution $f = (f_0, f_1)$ of this equation does not belong to $\mathcal{H}$. More exactly, if the operator $\mathcal{A}_\mu(k^{(i)})$ has a virtual level at $z = 27/2$, then the vector-function $f = (f_0, f_1)$, where

$$f_0 = \text{const} \neq 0, \quad f_1(q) = -\frac{\mu v(q) f_0}{\varepsilon(k^{(i)}+q)+\varepsilon(q)-9}, \tag{3.1}$$

satisfies the equation $\mathcal{A}_\mu(k^{(i)})f = (27/2)f$ and $f_1 \in L_1(\mathbb{T}^3) \setminus L_2(\mathbb{T}^3)$ (see assertion (i) of Theorem 3.4).

If the number $z = 27/2$ is an eigenvalue of the operator $\mathcal{A}_\mu(k^{(i)})$ then the vector-function $f = (f_0, f_1)$, where f_0 and f_1 are defined in (3.1), satisfies the equation $\mathcal{A}_\mu(k^{(i)})f = (27/2)f$ and $f_1 \in L_2(\mathbb{T}^3)$ (see assertion (ii) of Theorem 3.4).

The same assertions are true for the operator $\mathcal{A}_\mu(\bar{0})$ at the point $z = 0$.

Henceforth, we shall denote by C_1, C_2, C_3 different positive numbers and for each $\delta > 0$, the notation $U_\delta(p_0)$ is used for the $\delta-$neighborhood of the point $p_0 \in \mathbb{T}^3$:

$$U_\delta(p_0) := \{p \in \mathbb{T}^3 : |p - p_0| < \delta\}.$$

Now we formulate the first main result of the paper.

Theorem 3.4. *Let $\gamma < 9$ and $i \in \{1, \ldots, 8\}$.*
(i) *The number $z = 27/2$ is an eigenvalue of the operator $\mathcal{A}_\mu(k^{(i)})$ if and only if $\mu = \mu_r^{(i)}(\gamma)$ and $v(k^{(i)}) = 0$;*
(ii) *The operator $\mathcal{A}_\mu(k^{(i)})$ has a virtual level at the point $z = 27/2$ if and only if $\mu = \mu_r^{(i)}(\gamma)$ and $v(k^{(i)}) \neq 0$.*

Proof. Suppose $\gamma < 9$ and $i \in \{1, \ldots, 8\}$.

(i) "Only If Part". Let the number $z = 27/2$ be an eigenvalue of $\mathcal{A}_\mu(k^{(i)})$ and $f = (f_0, f_1) \in \mathcal{H}$ be an associated eigenvector. Then f_0 and f_1 are satisfy the system of equations

$$(\gamma - 9)f_0 + \mu \int\limits_{\mathbb{T}^3} v(t) f_1(t)dt = 0;$$

$$\mu v(p) f_0 + (\varepsilon(k^{(i)} + p) + \varepsilon(p) - 9) f_1(p) = 0. \tag{3.2}$$

This implies that f_0 and f_1 are of the form (3.1) and the first equation of system (3.2) yields $\Delta_\mu(k^{(i)}; 27/2) = 0$, therefore, $\mu = \mu_r^{(i)}(\gamma)$.

Now let us show that $f_1 \in L_2(\mathbb{T}^3)$ if and only if $v(k^{(i)}) = 0$. Indeed, if $v(k^{(i)}) = 0$ (resp. $v(k^{(i)}) \neq 0$), from analyticity of the function $v(\cdot)$ it follows that there exist $C_1, C_2, C_3 > 0$, $\theta_i \in \mathbb{N}$ and $\delta > 0$ such that

$$C_1 |p - k^{(i)}|^{\theta_i} \le |v(p)| \le C_2 |p - k^{(i)}|^{\theta_i}, \quad p \in U_\delta(k^{(i)}), \tag{3.3}$$

respectively

$$|v(p)| \ge C_3, \quad p \in \mathbb{T}^3 \setminus U_\delta(k^{(i)}). \tag{3.4}$$

Since the function $\varepsilon(k^{(i)} + p) + \varepsilon(p)$ has an unique non-degenerate maximum at the point $k^{(i)} \in \mathbb{T}^3$ there exist $C_1, C_2, C_3 > 0$ and $\delta > 0$ such that

$$C_1 |p - k^{(i)}|^2 \le |\varepsilon(k^{(i)} + p) + \varepsilon(p) - 9| \le C_2 |p - k^{(i)}|^2, \quad p \in U_\delta(k^{(i)}), \tag{3.5}$$

$$|\varepsilon(k^{(i)} + p) + \varepsilon(p) - 9| \ge C_3, \quad p \in \mathbb{T}^3 \setminus U_\delta(k^{(i)}). \tag{3.6}$$

We have

$$\int\limits_{\mathbb{T}^3} |f_1(t)|^2 dt = \mu^2 |f_0|^2 \int\limits_{U_\delta(k^{(i)})} \frac{v^2(t)dt}{(\varepsilon(k^{(i)} + t) + \varepsilon(t) - 9)^2}$$

$$+ \mu^2 |f_0|^2 \int\limits_{\mathbb{T}^3 \setminus U_\delta(k^{(i)})} \frac{v^2(t)dt}{(\varepsilon(k^{(i)} + t) + \varepsilon(t) - 9)^2}. \tag{3.7}$$

Let $v(k^{(i)}) = 0$. Then by (3.3) and (3.5) for the first summand on the right-hand side of (3.7) we have

$$\int\limits_{U_\delta(k^{(i)})} \frac{v^2(t)dt}{(\varepsilon(k^{(i)} + t) + \varepsilon(t) - 9)^2} \le C_1 \int\limits_{U_\delta(k^{(i)})} \frac{|t - k^{(i)}|^{2\theta_i} dt}{|t - k^{(i)}|^4} < +\infty.$$

It follows from the continuity of $v(\cdot)$ on a compact set $\mathbb{T}^3$ and (3.6) that

$$\int\limits_{\mathbb{T}^3 \setminus U_\delta(k^{(i)})} \frac{v^2(t)dt}{(\varepsilon(k^{(i)} + t) + \varepsilon(t) - 9)^2} \le C_1 \int\limits_{\mathbb{T}^3 \setminus U_\delta(k^{(i)})} dt < +\infty.$$

So, in this case $f_1 \in L_2(\mathbb{T}^3)$.

For the case $v(k^{(i)}) \neq 0$ there exsist the numbers $\delta > 0$ and $C_1 > 0$ such that $|v(p)| \ge C_1$ for any $p \in U_\delta(k^{(i)})$. Then from (3.5) we obtain

$$\int\limits_{\mathbb{T}^3} |f_1(t)|^2 dt \ge C_1 \int\limits_{U_\delta(k^{(i)})} \frac{dt}{|t - k^{(i)}|^4} = +\infty.$$

Therefore, $f_1 \in L_2(\mathbb{T}^3)$ if and only if $v(k^{(i)}) = 0$.

"If Part". Suppose that $\mu = \mu_r^{(i)}(\gamma)$ and $v(k^{(i)}) = 0$. It is easy to verify that the vector-function $f = (f_0, f_1)$ with f_0 and f_1 defined in (3.1) satisfies the equation $\mathcal{A}_\mu(k^{(i)}) f = (27/2) f$. We proved above that if $v(k^{(i)}) = 0$, then $f_1 \in L_2(\mathbb{T}^3)$.

(ii) "Only If Part". Suppose that the operator $\mathcal{A}_\mu(k^{(i)})$ has a virtual level at $z = 27/2$. Then by Definition 3.2 the equation

$$\varphi(p) = \frac{\mu^2 v(p)}{\gamma - 9} \int\limits_{\mathbb{T}^3} \frac{v(t)\varphi(t)dt}{\varepsilon(k^{(i)} + t) + \varepsilon(t) - 9}, \quad \varphi \in C(\mathbb{T}^3) \tag{3.8}$$

has a nontrivial solution $\varphi \in C(\mathbb{T}^3)$, which satisfies the condition $\varphi(k^{(i)}) \neq 0$.

This solution is equal to the function $v(p)$ (up to a constant factor) and hence

$$\Delta_\mu(k^{(i)}, 27/2) = \gamma - 9 - \mu^2 \int\limits_{\mathbb{T}^3} \frac{v^2(t)dt}{\varepsilon(k^{(i)}+t) + \varepsilon(t) - 9} = 0,$$

that is, $\mu = \mu_r^{(i)}(\gamma)$.

"If Part". Let now $\mu = \mu_r^{(i)}(\gamma)$ and $v(k^{(i)}) \neq 0$. Then the function $v \in C(\mathbb{T}^3)$ is a solution of (3.8), and consequently, by Definition 3.2 the operator $\mathcal{A}_\mu(k^{(i)})$ has a virtual level at $z = 27/2$. □

The following result may be proved in much the same way as Theorem 3.4.

Theorem 3.5. *Let* $\gamma > 0$.
(i) *The operator* $\mathcal{A}_\mu(\bar{0})$ *has an zero eigenvalue if and only if* $\mu = \mu_l(\gamma)$ *and* $v(\bar{0}) = 0$;
(ii) *The operator* $\mathcal{A}_\mu(\bar{0})$ *has a zero energy resonance if and only if* $\mu = \mu_l(\gamma)$ *and* $v(\bar{0}) \neq 0$.

Since $\mu_l(\gamma_i) = \mu_r^{(i)}(\gamma_i)$, setting $\mu_i := \mu_l(\gamma_i)$, from Theorems 3.4 and 3.5 we obtain the following

Corollary 3.6. *Let* $\gamma \in (0; 9)$ *and* $i \in \{1, \ldots, 8\}$.
(i) *The operator* $\mathcal{A}_\mu(\bar{0})$ *has a zero eigenvalue and the number* $z = 27/2$ *is an eigenvalue of* $\mathcal{A}_\mu(k^{(i)})$ *iff* $\mu = \mu_i$ *and* $v(\bar{0}) = v(k^{(i)}) = 0$;
(ii) *The operator* $\mathcal{A}_\mu(\bar{0})$ *has zero-energy resonance and the operator* $\mathcal{A}_\mu(k^{(i)})$ *has a virtual level at the point* $z = 27/2$ *iff* $\mu = \mu_i$, $v(\bar{0}) \neq 0$ *and* $v(k^{(i)}) \neq 0$;
(iii) *The operator* $\mathcal{A}_\mu(\bar{0})$ *has a zero eigenvalue and the operator* $\mathcal{A}_\mu(k^{(i)})$ *has a virtual level at the point* $z = 27/2$ *iff* $\mu = \mu_i$, $v(\bar{0}) = 0$ *and* $v(k^{(i)}) \neq 0$;
(iv) *The operator* $\mathcal{A}_\mu(\bar{0})$ *has a zero-energy resonance and the number* $z = 27/2$ *is an eigenvalue of* $\mathcal{A}_\mu(k^{(i)})$ *iff* $\mu = \mu_i$, $v(\bar{0}) \neq 0$ *and* $v(k^{(i)}) = 0$.

Next we will consider some applications of the results. Denote by $\mathcal{H}_2 := L_2^{\rm s}((\mathbb{T}^3)^2)$ the Hilbert space of square integrable (complex) symmetric functions defined on $(\mathbb{T}^3)^2$. In the Hilbert space $\mathcal{H}_1 \oplus \mathcal{H}_2$ we consider a 2×2 operator matrix

$$\mathcal{A}_\mu := \begin{pmatrix} A_{11} & \sqrt{2}\mu A_{12} \\ \sqrt{2}\mu A_{12}^* & A_{22} \end{pmatrix},$$

where $A_{ij} : \mathcal{H}_j \to \mathcal{H}_i$, $i = 1, 2$ are defined by the rules

$$(A_{11}f_1)(k) = w_1(k)f_1(k), \quad (A_{12}f_2)(k) = \int\limits_{\mathbb{T}^3} v(t)f_2(k,t)dt,$$

$$(A_{22}f_2)(k,p) = w_1(k,p)f_2(k,p) \quad f_i \in \mathcal{H}_i, \quad i = 1, 2.$$

Here $A_{12}^* : \mathcal{H}_1 \to \mathcal{H}_2$ denotes the adjoint operator to A_{12} and

$$(A_{12}^*f_1)(k,p) = \frac{1}{2}(v(k)f_1(p) + v(p)f_1(k)), \quad f_1 \in \mathcal{H}_1.$$

Under these assumptions the operator $\mathcal{A}_\mu$ is bounded and self-adjoint.

The main results of the present paper plays crucial role in the study of the spectral properties of the operator matrix $\mathcal{A}_\mu$. In particular, the essential spectrum of $\mathcal{A}_\mu$ can be described via the spectrum of $\mathcal{A}_\mu(k)$ the following equality holds

$$\sigma_{\rm ess}(\mathcal{A}_\mu) = [0; 27/2] \cup \bigcup_{k \in \mathbb{T}^3} \sigma_{\rm disc}(\mathcal{A}_\mu(k)).$$

Since the operator $\mathcal{A}_\mu(k)$ has at most 2 simple eigenvalues, the set $\sigma_{\rm ess}(\mathcal{A}_\mu)$ consists at least one and at most three bounded closed intervals, for similar results see [7].

Using Theorems 3.4 and 3.5 one can investigate [14] the number of eigenvalues of $\mathcal{A}_\mu$ and find its discrete spectrum asymptotics.

We note that the case

$$v(p) = \sqrt{\mu} = const, \quad w_1(k,p) = \varepsilon(k) + \varepsilon(\frac{1}{2}(k+p)) + \varepsilon(p)$$

is studied in [13], and it is shown that the bounds $\min\limits_{k \in \mathbb{T}^3} \sigma_{ess}(\mathcal{A}_\mu(\bar{0}))$ and $\max\limits_{k \in \mathbb{T}^3} \sigma_{ess}(\mathcal{A}_\mu(\bar{\pi}))$ are only virtual levels. This paper generalizes the results of the paper [13] and it is proved that these bounds are threshold eigenvalues or virtual levels depending on the values of the function $v(\cdot)$.

Acknowledgements

The authors thank the anonymous referee for reading the manuscript carefully and for making valuable suggestions.

References

[1] Tretter C. *Spectral Theory of Block Operator Matrices and Applications*. Imperial College Press, 2008.

[2] Huebner M.,Spohn H. Spectral properties of spin-boson Hamiltonian. *Annl. Inst. Poincare*, 1995, **62**(3), P. 289–323.

[3] Spohn H. Ground states of the spin-boson Hamiltonian. *Comm. Math. Phys.*, 1989, **123**, P. 277–304.

[4] Minlos R.A., Spohn H. The three-body problem in radioactive decay: the case of one atom and at most two photons. Topics in Statistical and Theoretical Physics. *Amer. Math. Soc. Transl.*, Ser. 2, **177**, AMS, Providence, RI, 1996, P. 159–193.

[5] Muminov M., Neidhardt H., Rasulov T. On the spectrum of the lattice spin-boson Hamiltonian for any coupling: 1D case. *Journal of Mathematical Physics*, 2015, **56**, P. 053507.

[6] Ibrogimov O.I. Spectral Analysis of the Spin-Boson Hamiltonian with Two Photons for Arbitrary Coupling. *Ann. Henri Poincaré*, 2018, **19**(11), P. 3561–3579.

[7] Rasulov T.Kh. Branches of the essential spectrum of the lattice spin-boson model with at most two photons. *Theoretical and Mathematical Physics*, 2016, **186**(2), P. 251–267.

[8] Mogilner A.I. Hamiltonians in solid state physics as multiparticle discrete Schrödinger operators: problems and results. *Advances in Sov. Math.*, 1991, **5**, P. 139–194.

[9] Friedrichs K.O. *Perturbation of spectra in Hilbert space*. Amer. Math. Soc., Providence, Rhole Island, 1965.

[10] Malishev V.A., Minlos R.A. *Linear infinite-particle operators*. Translations of Mathematical Monographs. 143, AMS, Providence, RI, 1995.

[11] Albeverio S., Lakaev S.N., Rasulov T.H. On the spectrum of an Hamiltonian in Fock space. Discrete spectrum asymptotics. *J. Stat. Phys.*, 2007, **127**(2), P. 191–220.

[12] Muminov M.I., Rasulov T.H. On the number of eigenvalues of the family of operator matrices. *Nanosystems: Physics, Chemistry, Mathematics*, 2014, **5**(5), P. 619–625.

[13] Rasulov T.H., Dilmurodov E.B. Eigenvalues and virtual levels of a family of 2×2 operator matrices. *Methods of Functional Analysis and Topology*, 2019, **25**(3), P. 273–281.

[14] Rasulov T.Kh. On the number of eigenvalues of a matrix operator. *Siberian Math. J.*, 2011, **52**(2), P. 316–328.

[15] Albeverio S., Lakaev S.N., Muminov Z.I. The threshold effects for a family of Friedrichs models under rank one perturbations. *J. Math. Anal. Appl.*, 2007, **330**, P. 1152–1168.

[16] Albeverio S., Lakaev S.N., Makarov K.A., Muminov Z.I. The threshold effects for the two-particle Hamiltonians on lattices. *Commun. Math. Phys.*, 2006, **262**, P. 91–115.

[17] Rasulov T.Kh., Dilmurodov E.B. Investigations of the numerical range of a operator matrix. *J. Samara State Tech. Univ., Ser. Phys. and Math. Sci.*, 2014, **35**(2), P. 50–63.

[18] Rasulov T.H., Tosheva N.A. Analytic description of the essential spectrum of a family of 3×3 operator matrices. *Nanosystems: Physics, Chemistry, Mathematics*, 2019, **10**(5), P. 511–519.

[19] Reed M., Simon B. *Methods of modern mathematical physics*. IV: Analysis of Operators. Academic Press, New York, 1979.

NANOSYSTEMS: PHYSICS, CHEMISTRY, MATHEMATICS, 2019, 10 (6), P. 623–626

Metric graph version of the FitzHugh–Nagumo model

E. G. Fedorov, A. I. Popov, I. Y. Popov

ITMO University, Kronverkskii, 49, St. Petersburg, 197101, Russia

fedevg95@mail.ru, popov239@gmail.com, popov1955@gmail.com

DOI 10.17586/2220-8054-2019-10-6-623-626

The FitzHugh–Nagumo model on a metric graph is studied. System of delayed differential equations is used to model a pair of FitzHugh- Nagumo excitable systems with time-delayed fast threshold modulation coupling. The model can be used for description of signal transmission in different nanostructures, microsystems or neural networks. The effect of time delay on the impulse transmission is studied.

Keywords: FitzHugh–Nagumo system, time-delayed coupling, travelling wave, metric graph, neural network.

Received: 27 July 2019

Revised: 30 November 2019

1. Introduction

Coupled oscillating systems with time delay are presented in many problems related to nano- and micro-systems: oscillation reactions, delay-sustained pattern formation in subexcitable media, coupled lasers, signal transmission through biological neurons [1–5]. The most bright example of such system is a biological neural network. The signal transmission in such a system is based on a number of physical-chemical reactions in complex molecular structures. An appropriate but rather complicated model for the process was suggested by A. L. Hodgkin and A. F. Huxley [6]. The model is widely used (see, e.g., [7, 8]) although it is complex for computations. To reduce the computational complexity, FitzHugh and Nagumo suggested a more simple model [9,10] created, initially, for electronics. It is, really, a modification of the well-known van der Pol model [11]. The approach has been intensively used last decade (see, e.g., [12–16]). The model possesses the main features of the Hodgkin-Huxley model and quite accurately describes the dynamics of a biological neuron and at the same time has a relatively small computational complexity. In this article, we suggest a metric graph type model of a simple neural network including three neurons forming a lasso graph. The model describes the actual movement of an impulse through axons from one neuron to another and vice versa. The delay time plays an important role in the dynamics of the system. The delay time, really, corresponds to the length of the axons. As shown, the types of system behavior fundamentally depend on these parameters. One can observe oscillation or relaxation regime. The corresponding critical values of the parameters was found numerically.

2. Metric graph model

We now consider the model of three neurons. The system is modelled as a metric graph with a loop shown in Fig. 1. At each edge of the graph, the FitzHugh–Nagumo partial differential equations are treated:

$$\begin{cases} \dfrac{\partial u_1}{\partial t} &= D\dfrac{\partial^2 u_1}{\partial x^2} - au_1 + (a+1)u_1^2 - u_1^3 - v_1, \\ \dfrac{\partial v_1}{\partial t} &= bu_1 - \gamma v_1, \\ \dfrac{\partial u_2}{\partial t} &= D\dfrac{\partial^2 u_2}{\partial x^2} - au_2 + (a+1)u_2^2 - u_2^3 - v_2, \\ \dfrac{\partial v_2}{\partial t} &= bu_2 - \gamma v_2, \\ \dfrac{\partial u_3}{\partial t} &= D\dfrac{\partial^2 u_3}{\partial x^2} - au_3 + (a+1)u_3^2 - u_3^3 - v_3, \\ \dfrac{\partial v_3}{\partial t} &= bu_3 - \gamma v_3, \end{cases} \tag{1}$$

where $i = 1, 2, 3$, functions $u_i(t, x)$ and $v_i(t, x)$ describe the states of the corresponding neurons at time t at the axon point x, a, b, γ and D are constant parameters. At the graph vertices, we pose the following conditions ensuring a proper coupling (namely, the transmission from the first neuron to the second neuron only, and from the third neuron to the second neuron only, see Fig. 1):

$$\begin{cases} u_2(t,0) &=& u_1(t,L)+u_3(t,L), \\ u_3(t,0) &=& u_2(t,L), \\ \dfrac{\partial u_1}{\partial x}(t,0) &=& 0,\ \dfrac{\partial v_1}{\partial x}(t,0)\ =\ 0, \\ \dfrac{\partial u_1}{\partial x}(t,L) &=& 0,\ \dfrac{\partial v_1}{\partial x}(t,L)\ =\ 0, \\ \dfrac{\partial u_2}{\partial x}(t,L) &=& 0,\ \dfrac{\partial v_2}{\partial x}(t,L)\ =\ 0, \\ \dfrac{\partial u_3}{\partial x}(t,L) &=& 0,\ \dfrac{\partial v_3}{\partial x}(t,L)\ =\ 0, \end{cases} \tag{2}$$

where L is the axon length (we assume that all axons have the same length, this assumption is not essential). These vertex coupling conditions differ from the conventional conditions for stationary and non-stationary metric graphs (see, e.g., [21,22]).

Thus, the system describes three neurons: the first is the start, the second and the third are tied to each other (see. Fig. 1).

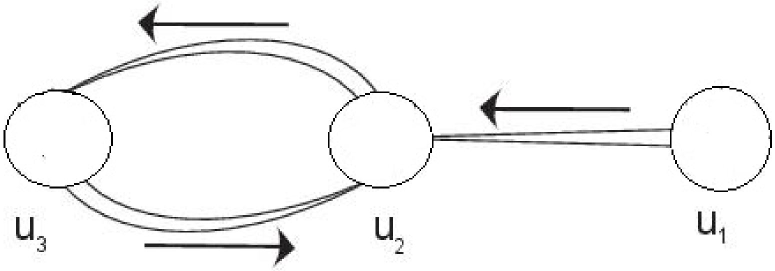

FIG. 1. Neuron connections

To numerically solve the system (1), the method described below was used. Consider the first neuron:

$$\begin{cases} \dfrac{\partial u_1}{\partial t}-D\dfrac{\partial^2 u_1}{\partial x^2} &=& f(u_1)-v_1; \\ \dfrac{\partial v_1}{\partial t} &=& bu_1-\gamma v_1; \\ \dfrac{\partial u_1}{\partial x}(t,0) &=& 0,\ \dfrac{\partial v_1}{\partial x}(t,0)\ =\ 0; \\ \dfrac{\partial u_1}{\partial x}(t,L) &=& 0,\ \dfrac{\partial v_1}{\partial x}(t,L)\ =\ 0. \end{cases}, \tag{3}$$

where, $f(x)=-ax+(a+1)x^2-x^3$. We divide the segment $[0,L]$ into n equal segments (with lengths $h=\dfrac{1}{n}$) by points $x_0=0, x_1=\dfrac{L}{n},\dots,x_{n-1}=\dfrac{L(n-1)}{n}, x_n=L$. We introduce a similar grid along the time axis with the step τ and the points $t_k=k\tau$. Next, we introduce the notation: $u_1^{(i,k)}=u_1(x_i,t_k)$. Now, system (3) can be rewritten in the form of the following difference equations:

$$\begin{cases} \dfrac{u_1^{(i,k)}-u_1^{(i,k-1)}}{\tau}-\dfrac{D}{2}\left(\dfrac{u_1^{(i+1,k)}-2u_1^{(i,k)}+u_1^{(i-1,k)}}{h^2}+\dfrac{u_1^{(i+1,k-1)}-2u_1^{(i,k-1)}+u_1^{(i-1,k-1)}}{h^2}\right)= \\ =f(u_1^{(i,k-1)})-v_1^{(i,k-1)}, \qquad i=1\dots n-1; \\ \dfrac{v_1^{(i,k)}-v_1^{(i,k-1)}}{\tau}=bu_1^{(i,k-1)}-\gamma v_1^{(i,k-1)}, \qquad i=1\dots n-1; \\ -3u_1^{(0,k)}+4u_1^{(1,k)}-u_1^{(2,k)}=0; \\ u_1^{(n-2,k)}-4u_1^{(n-1,k)}+3u_1^{(n,k)}=0; \\ -3v_1^{(0,k)}+4v_1^{(1,k)}-v_1^{(2,k)}=0; \\ v_1^{(n-2,k)}-4v_1^{(n-1,k)}+3v_1^{(n,k)}=0, \end{cases}. \tag{4}$$

Initial values $u_1^{i,0}, v_1^{i,0}, i = 0 \ldots n$ being given, the system can be solved by the three-diagonal matrix algorithm. Similarly, one can obtain solutions for the second and the third neurons.

This scheme was implemented in the Python programming language. Zero initial values were taken at all points, except for the vicinity of the beginning of the first axon, where the above-threshold disturbance was considered as the starting impulse of the system.

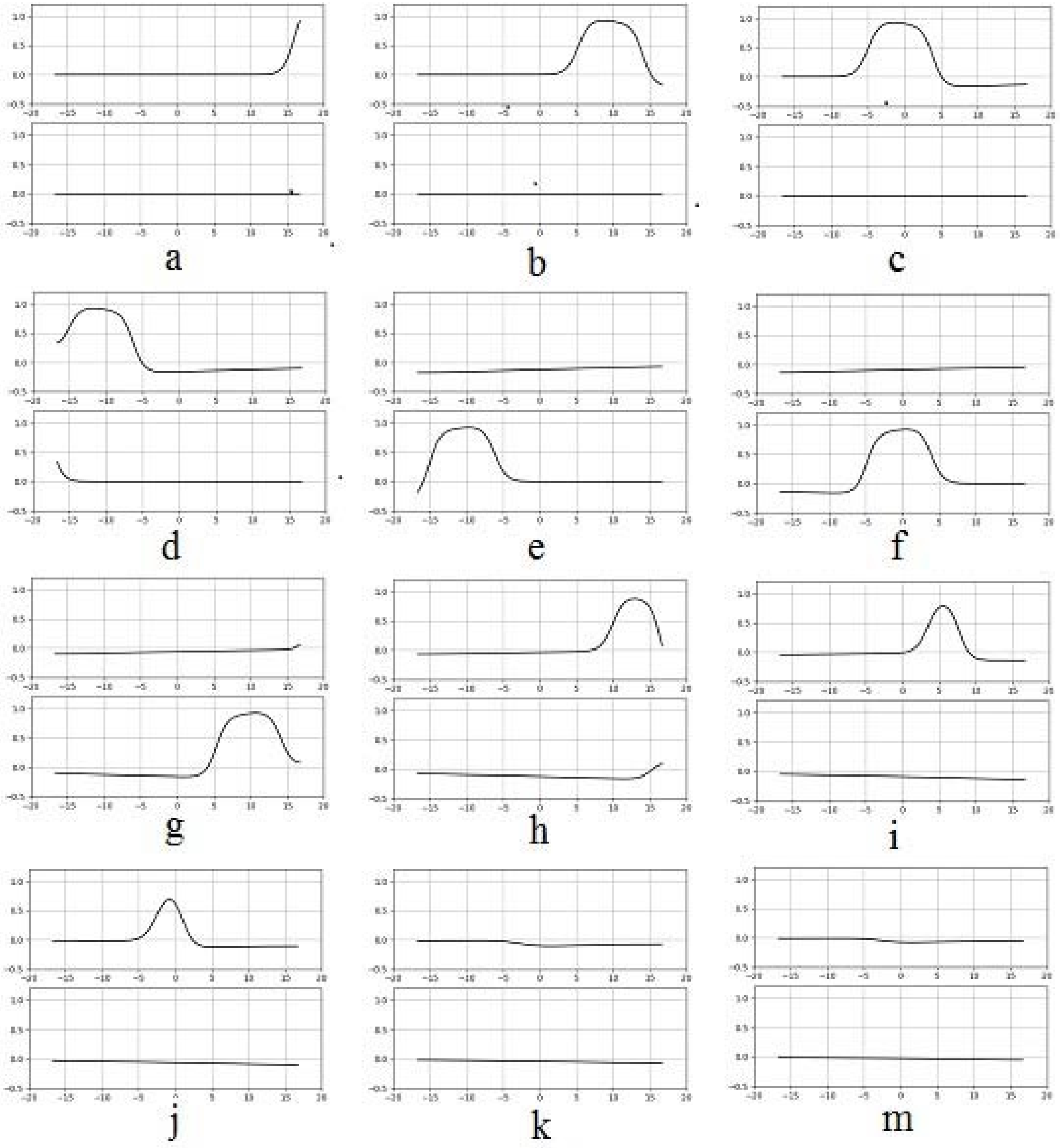

FIG. 2. Signal movement through neural system shown in Fig. 1. At each fragment, upper curve shows the signal in upper neuron from Fig. 1, lower curve corresponds to lower neuron. Different fragments correspond to different time moments (arbitrary units): a) $t = 5$, b) $t = 65$, c) $t = 125$, d) $t = 185$, e) $t = 245$, f) $t = 305$, g) $t = 365$, h) $t = 425$, i) $t = 485$, j) $t = 545$, k) $t = 605$, m) $t = 665$

Taking the following values of the parameters: $a = 0.25$, $b = 0.002$, $\gamma = 0.002$, $D = 0.3$ (as in [19]), we constructed several solutions for various axon lengths L. Fig. 2 shows several successive states of the system at different times for $L = 16.7$ (the upper part corresponds to the potential of the second axon, and the lower to the third). The figures show that, while returned to the second neuron, the signal decays. Numerical simulation shows that at $L = 16.8$, the attenuation does not occur. That is, the same situation is observed as in the discrete system, and the critical value lies between $L = 16.7$ and $L = 16.8$.

3. Conclusion

We suggest a mathematical model of graph type for the FitzHugh–Nagumo system. Particularly, it can be implemented to a neural network or to an invertible chemical or physical transformations spreading along a system of long molecules. The model showed a significant effect of the delay time on the impulse transfer and on the dynamics of the network as a whole. For the corresponding values of this parameter, one has a quick decay of the impulse or a periodic transmission. From a physical point of view, it turns out that small delays in the transmission of an impulse do not allow the impulse to pass through recursive systems. It is not essential why is the time delay small: because of short lengths of the graph edges or fast transmission speed along them. The main reason is simple. if the impulse comes to the next element of the system (e.g., a neuron) during the refractory period, it can not pass through it without an attenuation. It leads to a limitation in number of signals travelling inside the network.

Acknowledgement

This work was partially financially supported by the Government of the Russian Federation (grant 08-08), grant 16-11-10330 of Russian Science Foundation.

References

[1] Rosenblum M.G., Pikovsky A.S. Controlling synchronization in an ensemble of globally coupled oscillators. *Physical Review Letters*, 2004, **92**, P. 114102.

[2] Gassel M., Glatt E., Kaiser F. Delay-sustained pattern formation in subexcitable media. *Physical Review E*, 2008, **77**, P. 066220.

[3] Rankovic D. Bifurcations of FitzHugh–Nagumo excitable systems with chemical delayed coupling. *Matematicki Vesnik*, 2011, **63**, P. 103-114.

[4] Buric N., Todorovic D. Bifurcations due to small time-lag in coupled excitable systems. *International Journal of Bifurcation and Chaos*, 2005, **15**, P. 1775-1785.

[5] Domogo A.A., Collera J. Symmetric solutions to a system of mutually delay-coupled oscillators with conjugate coupling. *Journal of Physics: Conference Series*, 2018, **1123**(1), P. 012028.

[6] Hodgkin A.L., Huxley A.F. A quantitative description of membrane current and its application to conduction and excitation in nerve. *The Journal of Physiology*, 1952, **117**(4), P. 500–544.

[7] Izhikevich E.M. *Dynamical systems in neuroscience*, MIT Press, Cambridge, MA, 2007.

[8] Murray J.D., *Mathematical Biology. Biomathematics Vol. 19*, Springer-Verlag, Berlin, 1989.

[9] FitzHugh R. Impulses and physiological states in theoretical models of nerve membrane. *Biophysical journal*, 1961, **1**(6), P. 445–466.

[10] Nagumo J., Arimoto S. and Yoshizawa S. An active pulse transmission line simulating nerve axon. *Proceedings of the IRE*, 1962, **50**(10), P. 2061–2070.

[11] B. Van der Pol. On relaxation-oscillations. *The London, Edinburgh, and Dublin Philosophical Magazine and Journal of Science*, 1926, **1**(11), P. 978–992.

[12] Postnikov E.B., Titkova O.V. A Correspondence between the Models of Hodgkin-Huxley and FitzHugh–Nagumo Revised. *Eur. Phys. J. Plus*, 2016, **131**(11), P. 411.

[13] Saha A. and Feudel U. Extreme Events in FitzHugh–Nagumo Oscillators Coupled with Two Time Delays. *Phys. Rev. E*, 2017, **95**(6), P. 062219.

[14] Kudryashov N.A. Asymptotic and Exact Solutions of the FitzHughNagumo Model. *Regul. Chaotic Dyn.*, 2018, **23**(2), P. 152-160.

[15] D.-P. Li. Phase transition of oscillators and travelling waves in a class of relaxation systems. *Discrete and Continuous Dynamical Systems - B*, 2016, **21**(8), P. 2601–2614.

[16] Gu A., Wang B. Asymptotic behavior of random Fitzhugh-Nagumo systems driven by colored noise. *Discrete and Continuous Dynamical Systems - B*, 2018, **23**(4), P. 1689–1720.

[17] Bur N., Grozdanov I., and Vasov N. Type I vs. type II excitable systems with delayed coupling. *Chaos, Solitons and Fractals*, 2005, **23**(4), P. 1221–1233.

[18] Campbell S.A. Time delays in neural systems in *Handbook of brain connectivity*, Springer, Berlin, Heidelberg, 2007, P. 65–90.

[19] Rinzel J. Models in neurobiology in *Nonlinear phenomena in physics and biology*, Springer, Boston, MA, 1981, P. 345–367.

[20] Bur N. and Todorov D. Dynamics of FitzHugh–Nagumo excitable systems with delayed coupling. *Physical Review E*, 2003, **67**(6), P. 066222.

[21] Berkolaiko G., Kuchment P. *Introduction to Quantum Graphs*. AMS, Providence, 2012.

[22] Eremin D.A., Grishanov E.N., Nikiforov D.S., Popov I.Y. Wave dynamics on time-depending graph with Aharonov-Bohm ring. *Nanosystems: Physics, Chemistry, Mathematics*, 2018, **9**, P. 457–463.

NANOSYSTEMS: PHYSICS, CHEMISTRY, MATHEMATICS, 2019, 10 (6), P. 627–631

Modeling of linear optical controlled-z quantum gate with dimensional errors of passive components

F. D. Kiselev[1,2], E. Y. Samsonov[1], A. V. Gleim[1]

[1]ITMO University, Kronverkskiy, 49, St. Petersburg, 197101, Russia
[2]Corning Research & Development Corporation, Corning, NY

kiselevfd@corning.com, eduard.s1994@list.ru, aglejm@yandex.ru

PACS 42.00.00, 42.82.Gw **DOI 10.17586/2220-8054-2019-10-6-627-631**

Linear optical quantum computing can be realized using photonic integrate circuits (PICs). It is advantageous in comparison to other physical implementations of quantum computing due to simplicity of qubit encoding using photons and low decoherence times. Passive components like beamsplitters and phaseshifters are key elements for such PICs. In this article, we present modeling of linear optical controlled-Z gate with imperfections of beamsplitters and phaseshifters taken into account. Results showed that errors occur which cannot be detected by projection measurements and post-selection proposed by Knill, Laflamme and Milburn. We studied how these errors and success probability changes with the increase of dimensional errors using Monte-Carlo simulation. The obtained results can be used for design and calibration stages of chip manufacturing.

Keywords: quantum computing, linear optics.

Received: 2 April 2019

Revised: 6 November 2019

Final revision: 12 November 2019

1. Introduction

Quantum computing is a paradigm which considers usage of quantum mechanical effects in computation allowing massive parallelism and overall superiority relative toclassical computing for many important problems [1]. Quantum computing operates with unitary operations, called gates, which are building blocks of any quantum algorithm. Controlled-Z gate (or CZ-gate in short) is one of the basic 2-qubit gates which are considered to be a part of a universal set [2]. This is thus required for a quantum computer to be able to perform any unitary operation. For example, it is presented in Grover's [3] and Shor's [4] algorithms. There are several physical platforms for implementation of quantum computing. The most popular one being evaluated by IBM thatuses qubits based on superconductivity [5]. In this paper, we consider linear optical quantum computing (LOQC). Linear optical implementation of quantum computing has many advantages over superconducting alternatives, including: significantly longer decoherence times, simplicity of qubit encoding, as well as the benefits of using integrated photonic circuits as a physical platform. Typical LOQC chip is constructed from beamsplitters (or directional couplers) and phaseshifters. It was shown in [6] that any unitary operation can be constructed only with certain amount of these elements. Such simplicity might be attractive, however there are many issues in LOQC that need to be addressed. One of the main issues with linear optical quantum computing is probabilistic behavior of many-qubit gates [7]. It appears that every linear optical gate that has been proposed is capable of performing supposed operation only with certain probability due to the variation of basis states in the system which do not correspond to the right operation. Knill, Laflamme and Milburn [7] proposed using ancilla channels and projection measurements on them to force the system of the gate to collapse into a specific set of basis states, one of them corresponding to a desired operation. Such an approach does not solve the problem of non-determinacy, but at least gives us an ability to monitor whether the operation was performed correctly or not. Another featurewas proposed by the same authors to make near-deterministic operations by using multiple gates acting on the entangled set of qubits and using a teleportation protocol to extract the successfully applied gate and feed it forward to the computation. One can note that both approaches make the system more complex, introducing a significant numberof optical elements and increasing number of channels. Other issues include: probabilistic generation of single-photons, coupling losses, inefficiency of single-photon detectors, and different optical losses occurring inside the scheme. Most popular designs for LOQC systems use photonic integrated circuits (PIC's), as theyenablegood dimensional stability, compact sizes and integrability [8]. These circuits could be manufactured using ion exchange technology as was shown in [9]. But the most popular approach is to use silicon nanowires, as they have much more compact nanoscale sizes and also more components can be integrated in such chip [10]. However, there are manufacturing tolerances of such systems which need to be taken into account before designing any practical system. Even if a controllable Mach-Zehnder interferometer is used to mitigate these issues, it is important to know to what point MZIsneed to be calibrated [11].The topic of a quantum algorithm's performance on areal device was studied in [12], where the authors used IBM's superconducting quantum processor. In this paper, we present a modeling approach and resultsfor simulation of linear optical CZ-gate with dimensional imperfections of its passive components – beamsplitters and phaseshifters.

2. Modeling approach

A conventional approach to qubit encoding with photons is called dual-rail encoding. Thismeans that a qubit's state depends on the superposition of photon being in two optical modes. These modes can be spatial, polarization or even temporal. The KLM protocol considers spatial optical modes, and thus, our CZ-gate uses two optical channels to represent each of the 2 qubits. This correspondence can be written as

$$|0\rangle = |1\rangle_1 \otimes |0\rangle_2 = |1_1 0_2\rangle,$$
$$|1\rangle = |0\rangle_1 \otimes |1\rangle_2 = |0_1 1_2\rangle,$$

where left part represents qubit states, but the middle and right parts represent two different notations of a single photon existing in one of the two optical modes. The optical scheme of CZ-gate is taken from [7] and presented in Fig. 1. It consists of 4 logical optical modes, two of which are coupled to 4 ancilla modes. A single logical mode coupled to two ancilla ones with additional single-photon source and detectors form the so called nonlinear-sign (NS) gate (Fig. 2) which performs the following operation on Fock basis states:

$$|\Psi_{in}\rangle = \alpha|0\rangle + \beta|1\rangle + \gamma|2\rangle \to |\Psi_{out}\rangle = \alpha|0\rangle + \beta|1\rangle - \gamma|2\rangle.$$

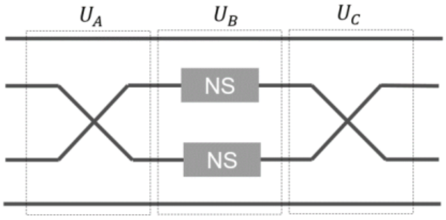

FIG. 1. Schematic of a KLM CZ-gate with 4 ancilla channels (right) and its representative matrix calculated using our modeling approach (left)

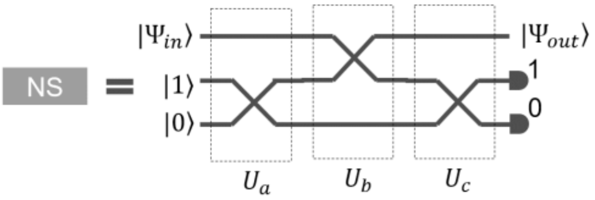

FIG. 2. Schematic of the nonlinear sign-flip gate consisting of one logical and two ancilla channels

The NS gate applies successfully when single photon is measured in the respective ancilla channel. Probability of that happening in the ideal case is $1/4$, which makes success probability of CZ gate equal to $1/16$. In our model, we divide the gate into parts each of which can be described by a single time-independent Hamiltonian. Passive components within these parts are described by following Hamiltonians:

$$\hat{H}_{BS} = \hat{a}_i^\dagger \hat{a}_j + \hat{a}_j^\dagger \hat{a}_i, \quad \hat{H}_{PS} = \hat{a}_i^\dagger \hat{a}_i,$$

where i, j are numbers of optical modes and $\widehat{a}_i$ are mode operators which act as annihilation operator on the channel with respective number. Transformation operators are then calculated via matrix exponential:

$$U = \exp(i\hat{H}_{BS/PS} z),$$

where propagation length **z** represents the effective interaction length of the directional coupler or the phase shift of the phaseshifter. Thus, dimensional errors can be introduced directly into equation shown above as random displacement Δz. We used Quantum Toolbox in Python (QuTiP) to setup and calculate our model.

In order to compute our model efficiently, we decided to split it into two steps. The first step is solving NS gate, which consists of 3 channels and operates with 3 photons. The two-photon state is taken as an input for the logical channel and an additional photon is taken as an input for the first ancilla channel. The important thing in this part is application of projection measurement operator, which corresponds to a successful performance of this gate:

$$P_{10} = (I \otimes |1\rangle\langle 1| \otimes |0\rangle\langle 0|).$$

The success probability of the NS gate can thenbe calculated as a norm of the output wave function. Second step is to solve CZ-gate itself. Here, we use matrices of NS-gates extracted from the previous calculation using partial trace.Two matrices are then included into a tensor multiplication, forming a transformation operator acting on 4 logical channels of CZ gate:

$$U_B = (I \otimes U^1_{NS} \otimes U^1_{NS} \otimes I).$$

The calculated CZ-gate is then applied to an input state of two photons being launched into second and third logical channels which logically correspond to $|11\rangle$ state. Here, we lay out the correspondence between optical basis states and computational once. Subsequently, we will only use computational notations:

$$\begin{aligned}
|00\rangle &= |1_1 0_2 0_3 1_4\rangle,\\
|10\rangle &= |0_1 1_2 0_3 1_4\rangle,\\
|01\rangle &= |1_1 0_2 1_3 0_4\rangle,\\
|11\rangle &= |0_1 1_2 1_3 0_4\rangle.
\end{aligned}$$

The success probability of this gate is calculated as multiplication of success probabilities of NS gates. Dimensions of these two problems are 3 channels, 3 photons and 4 channels, 2 photons, respectively. Such an approach appears to be significantly more efficient in comparison with the more straightforward approach that does not separate the problem and deals with 8 channels and 5 photons. One should note that we were able to divide the problem due to the presence of projection measurements in the NS gate. Projection measurement destroys entanglement between logical and ancilla channels. Thus, we can apply operation of partial trace without losing any important information.

As it was stated before, we can apply dimensional error of the phaseshifter or a beamsplitter as a random displacement of the propagation length. It is pretty straightforward for the characterization of phase shift. For the beamsplitter, however, it is more convenient to use value of splitting coefficient. Splitting coefficient of a beamsplitter is a ratio between input power and output power of the opposite channel. It can be calculated as:

$$C = \sin^2\left(\frac{\pi}{2}\frac{L_{int}}{l_c}\right),$$

where, L_{int} is an effective interaction length which in our case correspond to the value of z, l_c is the coupling length which corresponds to a values of interaction length required to fully couple light form one channel to another. The coupling length can be calculated for a given waveguide structure using overlap integrals and finite element method. In the initial simulation, we randomly choose errors for each component within boundaries of ± 0.05 for splitting coefficient and $\pm\pi/40$ for phase shift. These errors correspond to various dimensional errors which can occur in the manufacturing process of the component. For example silicon nitride-based directional couplers have such errors if the 400 nm separation between waveguides in the interaction region is displaced by 25 nm [13]. Other imperfections may occur in a value of interaction length and in a cross-section geometry of the waveguide. To observe the impact of these imperfections on the gate performance and to understand what it means, we considered diagonal elements of output wavefunction partial traces which basically gives us photon number distribution at given channels. In an ideal case, we should measure exactly one photon in the second and third channels for the input state $|11\rangle$. One can see in Fig. 3 that in the case of a dimensionally imperfect chip we are getting non-zero probabilities of 0 and 2 photons being measured at the output of respective logical modes. We want to point out that these errors occur if the projection measurement in both NS gates were successful thus they are not detectable by KLM-protocol and cannot be separated from the computation without some additional measures. In the next section of this article we investigate how this error depends on the amplitude of these imperfections.

3. Monte-Carlo simulations

Since dimensional errors of passive components are random in nature, we use the Monte-Carlo approach to study its effect on the performance of CZ-gate. At each step, we choose boundaries for splitting coefficient and phase errors. These boundaries are called dimensional error rate and defined by the relative change of splitting coefficient and phase shift with 0.5 and $\pi/2$ as references respectively. Then we run 1000 iterations randomly choosing errors of passive

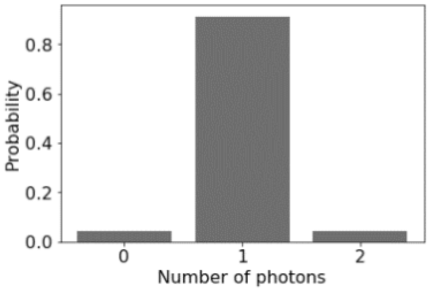

FIG. 3. Photon number probability distribution at the output of 2^{nd} and 3^{rd} logical optical modes. Probabilities at 0 and 2 photons correspond to the error caused by dimensional imperfections within ± 0.05 for splitting coefficient and $\pm\pi/40$ phase shift

components within defined boundaries. At the output we observe mean and maximum probability of error which is calculated as

$$P_{err} = 1 - \frac{1}{P_{succ}} \langle 11|\rho_{out}|11\rangle,$$

where ρ_{out} is the density matrix of the output state and P_{succ} is the success probability of CZ gate calculated as multiplication of success probabilities of two NS gates. This is basically probability of not measuring $|11\rangle$ state at the output even if both projection measurements were successful. It also corresponds to an imperfect photon number distribution showed in Fig. 3. Fig. 4 shows how probability of error grows with dimensional error rate being increased. One can readily see that the growth is nonlinear. Maximum error represents worst case scenario and it grows much faster than the mean error. This indicates that statistics of error probabilities spreads with the increase of error rate. From that, we conclude that larger dimensional errors not only introduce larger possibility of false computation, but also make performance of the chip less predictable. This also means that large enough dimensional errors won't allow us to separate its impact from other possible flaws in the experiment, unless dimensions of the device will be rigorously measured to calculate its exact impact with respect to our model, which could be complicated.

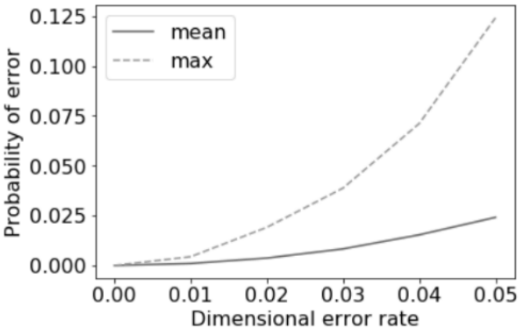

FIG. 4. Mean and maximum error probabilities obtained from Monte-Carlo simulation for different rates of dimensional errors

Another interesting thing to determine is the success probability of the gate (Fig. 5). Unlike the error probability, its mean value doesn't show a continuous decrease. However, maximum and minimum values spread around the ideal $1/16$. This again impacts the performance predictability of the device.

4. Conclusion

We proposed a modeling approach for KLM CZ-gate simulation with random dimensional imperfections of passive components taken into account. As a result, we observed errors – non-zero probabilities of 0 and 2 photons being measured at the output of optical modes which correspond to the basis state of $|11\rangle$. These errors cannot be detected by projection measurements. We used Monte-Carlo simulations to calculate mean and maximum error probabilities depending on the rate of dimensional errors. Our results show that maximum probability, which represents the worst case scenario for a given error rate, grows much faster than the mean one. Additionally, the success probability, which corresponds to a certain result of projection measurement, can significantly deviate from the ideal case in the presence

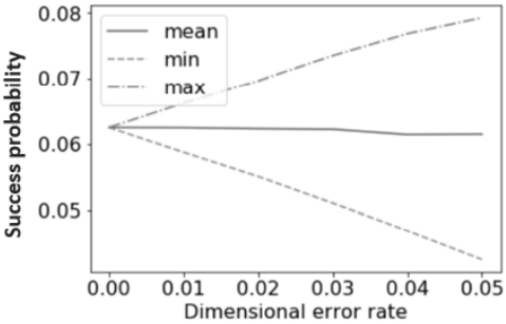

FIG. 5. Mean, minimum and maximum success probabilities of CZ-gate obtained from Monte-Carlo simulation for different rates of dimensional errors

of imperfections.These effects should be taken into account in the design stage of schemes with a large number of such gates. The proposed model can be used for calculation of gate matrix and then applied to performance simulation of quantum computational schemes based on LOQC.

References

[1] DiVincenzo D.P. Quantum computation. *Science*, 1995, **270** 5234), P. 255–261.

[2] Barenco A., Bennett C.H., et al. Elementary gates for quantum computation. *Phys. Rev. A*, 1995, **52**, P. 3457–3467

[3] Grover L.K. A fast quantum mechanical algorithm for database search. *Proceedings of Annual ACM symposium on Theory of Computing*, Philadelphia, Pennsylvania, USA, ACM, 1996, P. 212–219.

[4] Politi A., Matthews C.J., OBrien J. Shor's Quantum Factoring Algorithm on a Photonic Chip. *Science*, 2009, **325** (5945), P. 255–261.

[5] Devoret M.H., Schoelkopf R.J. Superconducting Circuits for Quantum Information: An Outlook. *Science*, 2013, **339** (6124), P. 1169–1174.

[6] Reck M., Zeilinger A., Bernsteim H.J., Bertani P. Experimental realization of any discrete unitary operator. *Phys. Rev. Lett.*, 1994, **73** (1) P. 58–61.

[7] Knill E., Laflamme R., Milburn G.J. A scheme for efficient quantum computation with linear optics. *Nature*, 2001, **409**, P. 46–52.

[8] Silverstone J.W., Bonneau D., OBrien J., Thompson M.G., Silicon Quantum Photonics. *IEEE Journal of Selected Topics in Quantum Electronics*, 2016, **22** (6), P. 390–402.

[9] Gerasimenko V., Gerasimenko N., et al. Numerical modeling of ion exchange waveguide for the tasks of quantum computations. *Nanosystems: Physics, Chemistry, Mathematics*, 2019. **10** (2), P. 147–153.

[10] Sun J., Timurdogan E., et al. Large-scale nanophotonic phased array. *Nature*, 2013, **493**, P. 195–199.

[11] Miller D.A. Perfect optics with imperfect components. *Optica*, 2015, **2** (8), P. 747–750.

[12] Gubaidullina K.V., Chivilikhin S.A. Stability of Grovers algorithm in respect to perturbations in quantum circuit. *Nanosystems: Physics, Chemistry, Mathematics*, 2017, **8** (2), P. 243–246.

[13] Poot M., Schuck C., et al. Design and characterization of integrated components for SiN photonic quantum circuits. *Optics Express*, 2016, **24** (7), P. 6843–6860.

NANOSYSTEMS: PHYSICS, CHEMISTRY, MATHEMATICS, 2019, 10 (6), P. 632–636

SiO_2 barrier layer influence on the glass composites with oxide nano films laser ablation destruction

V. G. Shemanin[1], E. V. Kolpakova[1], A. B. Atkarskaya[2], O. V. Mkrtychev[2]

[1]Novorossiysk Polytechnic Institute of Kuban State Technological University,
Karla Marksa street, 20, Novorossiysk, 353900, Russia
[2]Belgorod State Technological University named after V. G. Shukhov,
Novorossiysk branch, Myskhakskoe shosse, 75, Novorossiysk, 353919, Russia
vshemanin@yandex.ru, evge.kolpakova@yandex.ru, atkarsk06@mail.ru, oleg214@ya.ru

PACS 65.80.-g, 68.35.bj, 68.60.-p, 68.90.+g **DOI 10.17586/2220-8054-2019-10-6-632-636**

This study concerns the composites optical characteristics dependence on the chemical composition of the oxide nanofilms from TiO_2–Me_xO_y and on the existence of a SiO_2 barrier layer. The laser ablation destruction threshold energy density values decrease with the light transmission growth in the visible range of the composites for one- and double-layer nanofilms. These properties measurement results dependences for the composites with one- and double-layer nanofilms can be connected with various structure and composition of the complexes which were formed in the films.

Keywords: glass composites, nano film, laser ablation, threshold energy density, light transmission.

Received: 5 July 2018

Revised: 25 November 2019

1. Introduction

The nano dimensional oxide films using for the efficient change in the instrumental glass details properties allows one to considerably expand the range of application for modified glass composites [1–5]. Nano films are applied to change of the optical characteristics – the increasing in the light transmission by the optical details or giving of the reflecting properties [1, 4] to them. Such a film is obtained by the sol-gel technology including the contact of a film-forming solution with a glass substrate [3, 6–10]. The glass surface becomes covered by the oxide one- or multilayer nano films in this case. And, besides the basic functional purpose, the nano film will follow up provide the resistance to the surrounding medium influence [2, 11].

The influence of a SiO_2 barrier layer on the laser ablation destruction threshold energy density of the glass composites with the bicomponent oxide nano films of the TiO_2–Me_xO_y structure was studied after [3, 4]. The threshold density dependence on the composite other optical parameters – the light transmittance in the visible range, reflectivity coefficient at the 1064 nm laser radiation wavelength, an refractive index and a layer thickness were also investigated in detail.

This goal of these studies is the composites optical characteristics dependence on the chemical composition of the bicomponent oxide nano films from TiO_2–Me_xO_y and on the existence of a SiO_2 barrier layer. The knowledge of such a composite's properties will allow creation of new materials for nanophotonics with the new linear and non-linear optical properties.

2. Experimental samples and methods

The glass composites samples with the bicomponent oxide nanofilms with the structure of TiO_2–Me_xO_y have been received by the sol-gel technology. The alloying Me_xO_y oxide amount was 2 or 10 mass %. Starting materials were the titanium tetraethoxide and the copper, tin, zinc, cadmium and iron chlorides. The oxides sum mass content in the film-forming sol have been of 5 mass. %. The films were drawn on the float-glass substrate by the dipping method and the samples withdrawal rate from the sol was of 3.8 mm/s. The heat treatment in the microwave oven – the furnace was made within 30 minutes. The thickness, refractive index, film reflectivity have been measured by the Horiba Jobin Yvon type spectra ellipsometer as in [12] and the samples light transmittance by a FSD-8 type micro spectrometer (NCFO RAS).

The composites laser ablation destruction under the pulse laser radiation influence were studied at the experimental layout described in [10] and by the technique given in [4]. The YAG-Nd laser generated the radiation pulses at the 1064 nm wavelength of the 20 ns time duration and the pulse energy up to 0.15 J in the mode locking regime. The laser radiation was focused by the lens objective on the composite sample surface. The breakdown phenomenon was fixed on the existence of the laser plasma plume characteristic luminescence and was recorded by the FSD-8 type micro spectrometer with the fiber input. The laser pulse energy density changing in the range from 0.1 to 180 J/cm^2 was reached by the choice of this lens focal distance and the laser radiation weakening by the NS type calibrated neutral light filters. The photodiode with the glass light filter IKS-1 was used for the laser pulse energy monitoring. Management of duties of the spectrometer operation regimes controlling and the observed data processing were carried out in PC.

3. Experimental results

The film's thickness, refractive index and reflection coefficient at the 1064 nm wavelength have been measured by the Uvisel 2 type Horiba Jobin Yvon spectra ellipsometer. The experimental results were treated statistically and exhibited in Fig. 1 and Fig. 2.

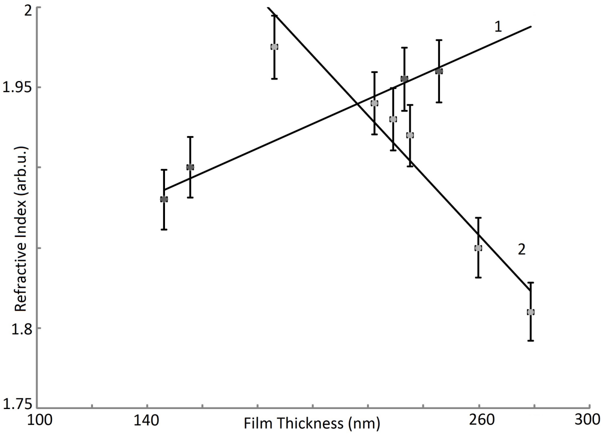

FIG. 1. The plot of the film refractive index n dependence on the film h thickness: 1 – the drawing speed of 3.8 mm/s, 2 – the drawing speed of 5.8 mm/s

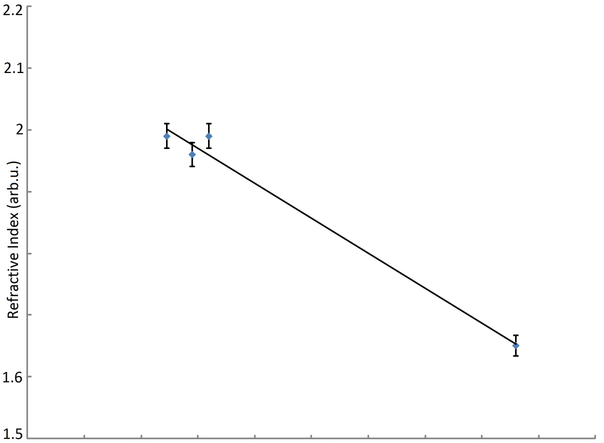

FIG. 2. The plot of the film refractive index n dependence on the film reflection coefficient at the 1064 nm wavelength and the drawing speed of 5.8 mm/s

The experimental straight lines of the trends in Fig. 1 shows that the drawing speed has significant effect on the film refractive index dependence on its thickness. This dependence is due to the sol particles packing density in a layer increases with the drawing speed from the sol particles diameter decreasing. Its increasing, probably, is connected with the influence of the light dispersion which is more, than more the film thickness for the film refractive index dependence on its thickness [12].

The films refractive index reduction with its reflection coefficient at the 1064 nm wavelength growth in Fig. 2 is explained by the same dispersion in the growth bulk of the film and the smaller size of sol particles and their more dense packing in the film layer [6].

At the next stage, the calibration experiments were executed at the target from a clear substrate – float glass and the threshold energy density at the breakdown probability of 0.5 was equal $F_{bn} = 143$ J/cm^2. It is necessary to make not less than 30 measurements at the given laser radiation pulse energy to generate the laser ablation destruction probability curve and to measure the ratio of the breakdown events number at the target surface to the total radiation pulses number. All range of the breakdown probability values from 1 to 0 were sequentially obtained over by changing the pulse energy value and repeating this process. The exact interpretation of this probability curve is important for the precise determination of the threshold energy density value of the composites laser destruction with the probability of 0.5. The calibration procedure allowed us to develop the threshold energy density measurement algorithm including the precise positioning and movement of the target about the laser beam.

Then, the breakdown probabilities curves for all samples, as well as in [9], have been obtained. The threshold energy density values of F_{bn} for all composites from these dependence at the probability level of $p = 0.5$ have been determined and such values of the laser ablation destruction threshold energy density of F_{bn} dependences on the composites light transmission in the visible range of T for the drawing speed of 3.8 mm/s for the one- and double-layer nanofilms are given in Fig. 3.

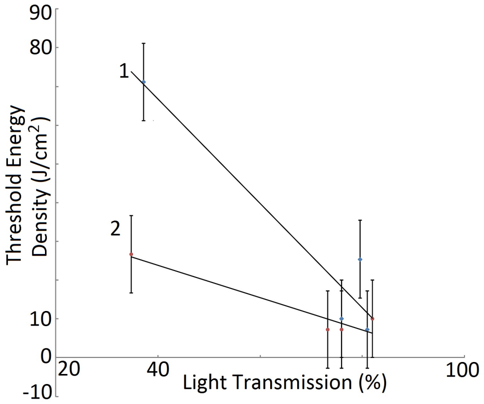

FIG. 3. The plots of the laser ablation destruction threshold energy density of F_{bn} dependence on the composites light transmission in the visible range of T. The line 1 – a one-layer film, line 2 – double-layers one. Drawing speed – 3.8 mm/s

The laser ablation threshold energy density values decrease with incresed light transmission as it appears from Fig. 3. It is possible to explain by the light losses decreasing in the composites volume due to the reflection and scattering on the particles in the film volume. This leads to decrease in the laser radiation ratio reflected at the composite surface with the high reflectivity coefficient and then the ablation destruction effectiveness increases.

It is also confirmed by the analysis of the laser ablation destruction threshold energy density of F_{bn} dependence on the reflectivity coefficient at the 1064 nm laser radiation wavelength of R_{1064} in Fig. 4.

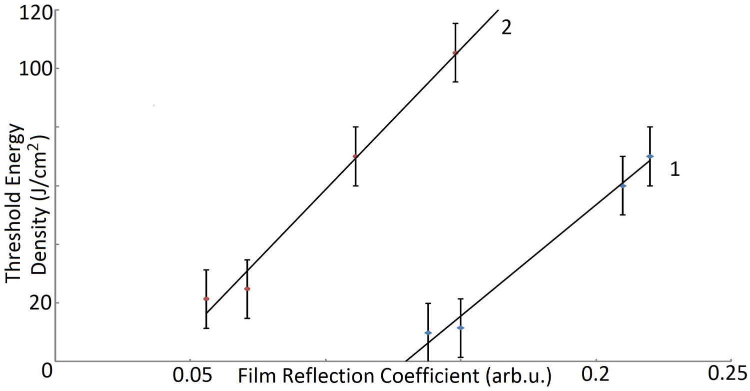

FIG. 4. The plots of the laser ablation destruction threshold energy density of F_{bn} dependence on the composites light transmission in the visible range of T. The line 1 – a one-layer film, line 2 – double-layers one. Drawing speed – 3.8 mm/s

It has been derived that the threshold energy density value increases with higher reflectivity coefficient values, which is explained by the ratio of the laser radiation reflected energy at the film surface increasing. The reflectivity coefficient decreasing in the double-layer films is bound to the film refractive index lowering due to the SiO_2 barrier layer as well as in [12].

The threshold energy density of the laser ablation destruction F_{bn} dependences on the film h thickness for all composites samples with single-layer film and the drawing speeds of 3.8 mm/s are given in Fig. 5.

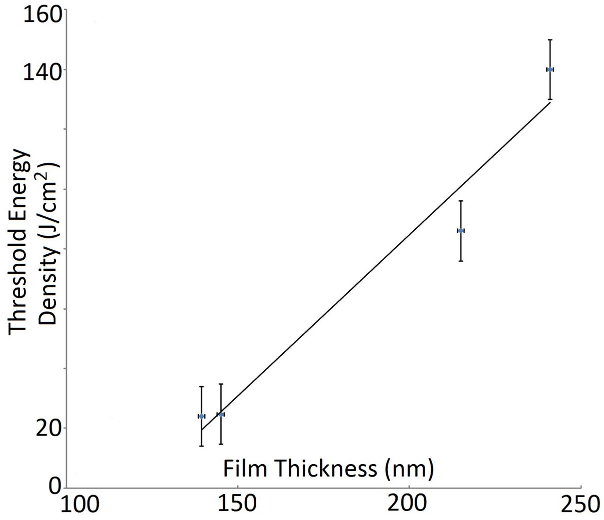

FIG. 5. The plot of the laser ablation destruction threshold energy density of F_{bn} dependence on the film h thickness. The drawing speed is 3.8 mm/s

As appears from a straight line in Fig. 5, the threshold energy density value is higher, than more thickness of the film. At the same time, this threshold energy density value for the double-layer film remains almost invariable with an accuracy of our measurements in this range of the films thickness.

As a result, the studied parameter properties of the composites with single-layer nanofilm changed in the following limits: the threshold energy density of the laser ablation destruction F_{bn} of 6.6 – 143 J/cm^2, light transmittance in the visible range of T of 36.8 – 84.3 %; film thickness h is 144.8 – 272.3 nm, an refractive index of n 1.6496 – 1.9926, and R_{1064} reflectivity coefficient at the 1064 nm wavelength – 0.041 – 0.286 arb. units. And for composites with double-layer film they changed in the following limits: the threshold energy density F_{bn} of 6.6 – 32.4 J/cm^2, light transmittance in the visible range of T of 34.8 – 85.8 %; film thickness h is 133.3 – 221.8 nm, an refractive index of n 1.6358 – 1.9952, and R_{1064} reflectivity coefficient – 0.042 – 0.184 arb. units.

Such the difference of these properties measurements result can be connected with various structure and composition of the complexes which are formed in these films [3, 4, 12].

4. Conclusion

The laser ablation destruction threshold energy density values decrease with the light transmission growth in the visible range of the composites for single- and double-layer nanofilms. This is explained by the decreasing in the light losses of the reflecting component.

The analysis of the threshold energy density of the laser ablation destruction dependence on the reflectivity coefficient at the 1064 nm laser radiation wavelength confirms this conclusion, and the reflectivity decreasing in the double-layer films is bound to the film's refractive index decrease due to the SiO_2 barrier layer.

The value of threshold energy density is higher, with increased thickness of the film. At the same time this threshold density value for a double-layer film, with the accuracy our measurements,remains almost invariable in this range of the film thickness.

In general, such difference of these properties measurement results for the composites with one- and double-layer nanofilms can be connected with various structure and composition of the complexes which were formed in the films.

Acknowledgements

This work was partially supported by the Basic part of State assignment of the Ministry of Education and Science of the Russian Federation, project No. 5.7721.2017/BC.

References

[1] Magnozzi M., Terreni S., et al. Optical properties of amorphous SiO_2–TiO_2 multi-nanolayered coatings for 1064-nm mirror technology. *Opt. Mat.*, 2018, **75**, P. 94–101.

[2] Sung Y., Malay R.E., et al. Anti-reflective coating with a conductive indium tin oxide layer on flexible glass substrates.*Appl. Opt.*, 2018,**57** (9), P. 2202–2207.

[3] Vytykáčová S., Mrázek J., et al. Sol-gel route to highly transparent $(Ho_{0.05}Y_{0.95})_2Ti_2O_7$thin films for active optical components operating at 2 μm. *Opt. Mat.*, 2018, **78**, P. 415–420.

[4] Shemanin V.G., Atkarskaya A.B. Breakdown of Glass Composites with a TiO_2 Nanodimensional Coating by Laser Ablation. *Technical Phys.*, 2016, **86** (2), P. 140–142.

[5] Lyubas G.A. Generation of laser radiation by nanostructured solid active elements with selective optical nanoresonators formed in nanoporous aluminum oxide films. *Nanosystems: Physics, Chemistry, Mathematics*, 2017, **8** (6), P. 793–797.

[6] Ottermann C.R., Bange K. Correlation between the density of TiO films and their properties. *Thin Sol. Films*, 1996, **286** (1–2), P. 32–34.

[7] Janicki V., Sancho-Parramon J., et al. Optical characterization of hybrid antireflective coatings using spectrophotometric and ellipsometric measurements. *Appl. Opt.*, 2007, **46** (24), P. 6084–6091.

[8] Atkarskaya A.B., Mkrtychev O.V., Privalov V.E., Shemanin V.G. Laser ablation of the glass nanocomposites studies. *Opt. Mem. Neural Networks*, 2014, **23** (4), P. 265–270.

[9] Cai Q.-Y., Zheng Y.-X., et al. Evolution of optical constants of silicon dioxide on silicon from ultrathin films to thick films. *J. Phys. D, Appl. Phys.*, 2010, **43**, 445302.

[10] Melikhov I.F., Popov I.Yu. Asymptotic analysis of thin viscous plate model. *Nanosystems: Physics, Chemistry, Mathematics*, 2018, **9** (4), P. 447–456.

[11] Privalov V.E., Shemanin V.G., Mkrtychev O.V. Method of assessing the optical resistance of an irradiated surface under laser ablation. *Meas. Tech.*, 2018, **61** (7), P. 694–698.

[12] Atkarskaya A.B., Shemanin V.G. Influence of the Interaction of Components in a Transient Layer of Oxide FilmGlass Substrate on Properties of the Composite Material. *Glass Physics and Chemistry*, 2015, **41** (5), P. 515–521.

NANOSYSTEMS: PHYSICS, CHEMISTRY, MATHEMATICS, 2019, 10 (6), P. 637–641

Pt nanoparticle-functionalized RGO counter electrode for efficient dye-sensitized solar cells

O. V. Alexeeva, S. S. Kozlov, L. L. Larina, O. I. Shevaleevskiy

Department of Solar Photovoltaics, Institute of Biochemical Physics RAS, Kosygin St. 4, Moscow, 119334, Russia
shevale2006@yahoo.com

PACS 73.63.Bd **DOI 10.17586/2220-8054-2019-10-6-637-641**

In this paper, we present a facile method for replacing conventional Pt-based counter electrode (CE) in dye-sensitized solar cells (DSCs) for the alternative low-cost nanostructured material containing reduced graphene oxide (RGO). Pt-NPs/RGO-based nanohybrid layers were synthesized at low temperature on a conductive glass substrate using microwave-assisted heating reduction strategy. The obtained material was characterized using XRD, SEM and TEM measurements and used for fabrication layered CEs on glass substrates. Photovoltaic characteristics of the DSCs based on Pt nanoparticle-functionalized RGO CEs were investigated under simulated AM1.5G solar illumination at an intensity of 1000 W/m^2. The obtained results have shown that Pt-NPs decorated RGO surfaces can be successfully used as CEs in high-efficiency DSCs and may be promising as low-cost electrodes in energy storage devices.

Keywords: nanostructures, reduced graphene oxide, thin films, semiconductors, solar photovoltaics, dye-sensitized solar cells.

Received: 1 December 2019

Revised: 4 December 2019

1. Introduction

In last few decades, dye-sensitized solar cells (DSCs), which reached over 12% power conversion efficiency, have attracted much attention as low cost alternatives to the conventional Si-based solid state solar cells (SCs) [1–3]. The main components of DSCs comprise a dye-sensitized mesoporous working photoelectrode (PE), redox electrolyte, and a counter electrode (CE) which plays a critical role in the reduction process of the dye-sensitized electrochemical cell processing.

Most studies so far have been focused on matching the device absorption characteristics to solar spectrum and the enhancement of the light collection ability of DSCs by the use of tandem systems, quantum dots, and new type of dyes [4–6]. However, much efforts have been also devoted in developing a new generation of more effective and low-cost PEs and CEs. Normally DSCs contain PEs based on a thin mesoscopic nanocrystalline titanium dioxide ($\mathrm{TiO_2}$) layer with a bandgap (E_g) of around 3 eV. Recently, it was shown that zirconia dioxide ($\mathrm{ZrO_2}$) with a very wide band-gap (E_g $\sim$5.7 eV) can be also successfully used as a PE in DSCs and perovskite SCs with an ability to reduce the recombination effects at the interface between photoactive layer and working electrode [7–9].

The conversion efficiency of DSCs is critically dependent on the CE materials and a number of factors including electrical conductivity and catalytic activity [10]. In DSCs platinum-based (Pt-based) CEs have been widely used as the catalyst due to its good conductivity, high chemical stability and outstanding catalytic property. However, the conventional Pt layers on the flat FTO glass surface sputtered from expensive Pt targets demonstrate poor charge exchange ability and possess limited surface area for redox reactions [11]. Thus, there is a strong need in development of the alternative materials for replacing expensive Pt in high performance DSCs.

Graphenes and reduced graphene oxide (RGO) produced by reduction of graphene oxide (GO) have emerged promising low-cost counter electrode catalytic materials for high efficiency DSCs [12–15]. Interesting results were obtained when using CVD grown graphene and RGO for this purpose [16].

In more advanced approaches, CEs were fabricated by decorating tracing amounts of Pt nanoparticles (Pt-NPs) on RGOs (Pt-NPs/RGO) prepared using laser- and plasma-based reduction of GO and Pt-NPs precursors [12]. However, the requirements for a two-step process and high temperature of around 350 °C for plasma reduction may limit the practical realization of these methods. High-performance DSCs were fabricated using CEs based on RGO functionalized with large (100 nm) Pt nanoparticles (L-Pt/RGO) which were prepared at ambient temperatures using γ-ray irradiation [17].

In this study, nanometer-size Pt-NPs-decorated RGO (Pt-NPs/RGO) were prepared under low temperatures using a facile synthesis via a microwave irradiation assisted method and used as a catalyst material for constructing efficient CEs. The structure and morphologies of CEs were characterized using XRD, SEM and TEM measurements. Using the developed Pt-NPs/RGO CEs, we have fabricated DSCs and provided the measurements of the main photovoltaic parameters under AM1.5G solar illumination.

2. Experimental

2.1. Synthesis and characterization of Pt-NPs/RGO CEs

Graphene nanoplatelets (grade C-500, 500 m^2/g) were purchased from Sigma-Aldrich GmbH. Pt NPs on RGO sheets were sensitized using the procedure described in [18]. Graphene oxide (GO) was added into a solution of benzyl alcohol and sonicated for 60 min to obtain a homogenous liquid GO suspension. Microwave pulsed irradiation reactor operated under 2.45 GHz (Energiya-K-1-2450, Russia) was used for treating the solution for 3 min at 150 °C. After cooling and washing of the obtained suspension the synthesis of RGO was fulfilled by drying in vacuum during 10 h. To obtain liquid RGO suspension the obtained RGO was added to a solution of ethylene and sonicated for 60 min. H_2PtCl_6 was added to RGO suspension and stirred for 1 h. The obtained solution was then subjected to pulsed microwave heating for 3 min in a microwave reactor operated at 150 °C. After microwave irradiation, the suspension was cooled down to room temperature and the solid product was isolated, washed and dried for 12 h.

The structure and composition of Pt-NPs/RGO hybrid was analyzed by X-ray diffraction (XRD) spectroscopy using Regaku D/MAX-RC diffractometer. The morphology of Pt-NPs/RGO was investigated using field-emission scanning electronic microscope (FESEM; Hitachi S-4800) without a preliminary covering of the samples with any conductive coatings. High-resolution TEM (HRTEM) measurements were provided using a JEOL 2100F (Japan). For TEM measurements a drop of diluted in an ethanol Pt/RGO dispersion ($\sim$0.5 μl) was deposited on a carbon grid. Two different CEs were prepared for comparison. GO coated CE was fabricated following the known procedure [19]. Pt nanoparticles-decorated RGO counter electrodes were fabricated as described in [20].

2.2. Fabrication and characterization of DSCs

The details of the fabrication process of DSCs can be found on our previous publications [3, 6]. Briefly, TiO_2 nanostructured layer deposited onto FTO coated conductive glass substrate was used as a PE. To perform the sensitization a TiO_2 PE, the FTO-coated glass electrodes were dipped in a 0.3mM of N719 dye solution in a mixture of acetonitrile and tert-butyl alcohol (1:1 volume ratio) for 24 h. Then the dye-sensitized PE was rinsed with ethanol to remove the residues and dried at room temperature. Finally, the counter and photo electrodes were assembled into a sandwich-type cell and sealed with ionomer film (Surlyn 1702). The commercially available 1,2-Dimethyl-3-propylimidazolium iodide electrolyte AN-50 (Solaronix) was used to fulfill the fabrication of a photovoltaic device. The active area of the fabricated DSCs was around 0.11 cm^2.

The measurements of the photovoltaic parameters of the DSCs were provided under simulated AM1.5G solar illumination with intensity P_{IN} = 1000 W/m^2. The current voltage characteristics (J–V) were recorded using Keithley 4200-SCS Parameter Analyzer (USA) and Abet Technologies Solar Simulator (Abet, USA) as a light source. The power conversion efficiency (η) of the DSC was calculated from the J–V data using the known formula:

$$\eta = \frac{J_{SC}V_{OC}FF}{P_{IN}} \times 100\%$$

where J_{SC} – short-circuit current density, V_{OC} – open-circuit voltage, *FF* – fill factor and P_{IN} – light intensity of solar radiation.

3. Results and discussion

The formation of Pt-NPs on RGO structures was confirmed by XRD. Fig. 1 shows XRD patterns of the Pt-NPs/RGO layer on a glass substrate. The broad diffraction peaks at around $2\theta = 39.8°$ and 46.2° match perfectly with the (111) and (200) crystalline planes respectively for the face centered Pt cubic structure.

High resolution scanning electron microscope (HRSEM) images of RGO and Pt-NPs/RGO CE structures are shown in Fig. 2. HRSEM plane images of RGO nanoplatelets (Fig. 2a) show that the RGO flakes are randomly and closely distributed with each other in a condensed layer. The surface morphology of CEs (Pt-NPs/RGO) presented in Fig. 2b shows that Pt NPs are immobilized on the RGO surface with a high surface coverage and high loading of NPs. Graphene nanoplatelets are clearly visible in the micrographs. The structure of RGO layers seen in Fig. 2 possesses high surface area and mesoporous-like volume structure which is favorable for the penetration of electrolyte ions thus improving the electrochemical catalytic activity of CE in DSCs.

The morphology of Pt-NPs immobilized on RGO surface as analyzed by HRTEM in different magnifications is presented in Fig. 3. It is seen that Pt nanoparticles with an average size of 30 nm are well attached to RGO nanoplatelets that suggests a perfect interaction between the functional groups of RGO and Pt nanoparticles.

Figure 4 shows a comparative view of the I–V curves recorded for the DSCs fabricated with Pt-NPs/RGO CE and with GO CE. Previously it was confirmed that the DSC performance is strongly affected by the CE parameters such as electrical conductivity and electrochemical catalytic activity for the iodide/triiodide redox couple [18]. PV

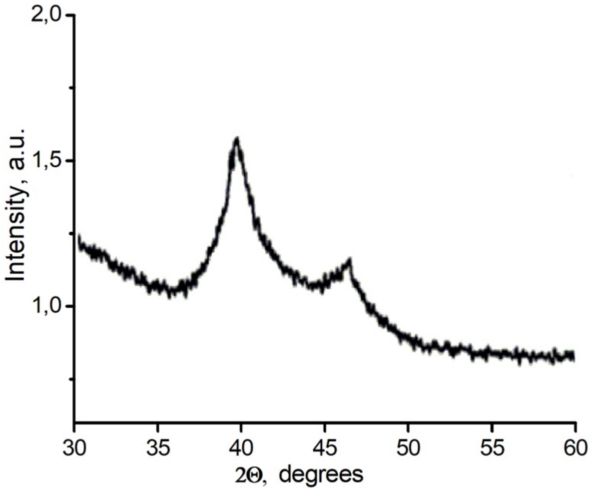

FIG. 1. XRD patterns of Pt-NPs/RGO composite

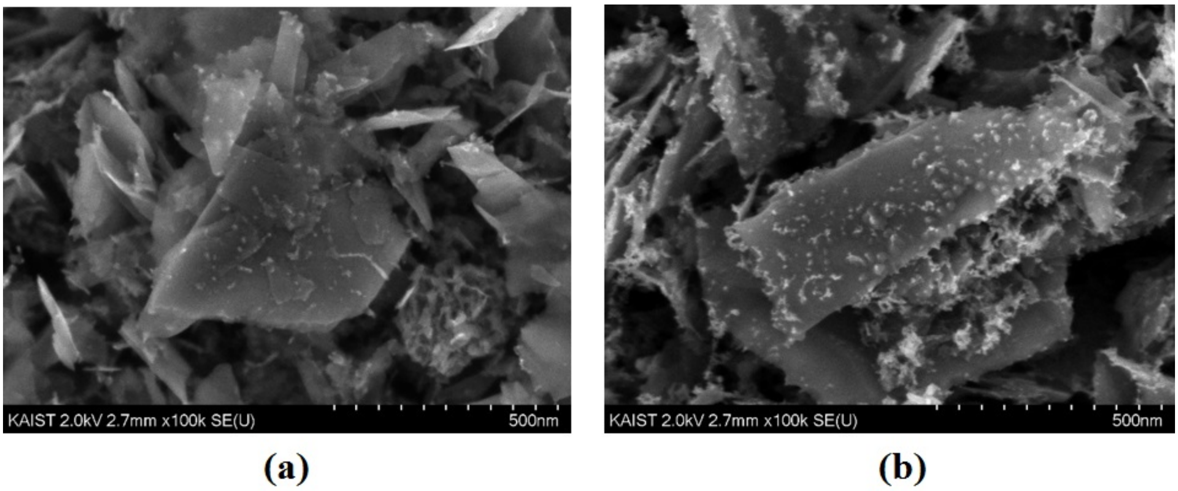

FIG. 2. HRSEM plane images of CE surface: (a) RGO nanoplatelets; (b) Pt-NPs immobilized on the RGO surface (Pt-NPs/RGO CE)

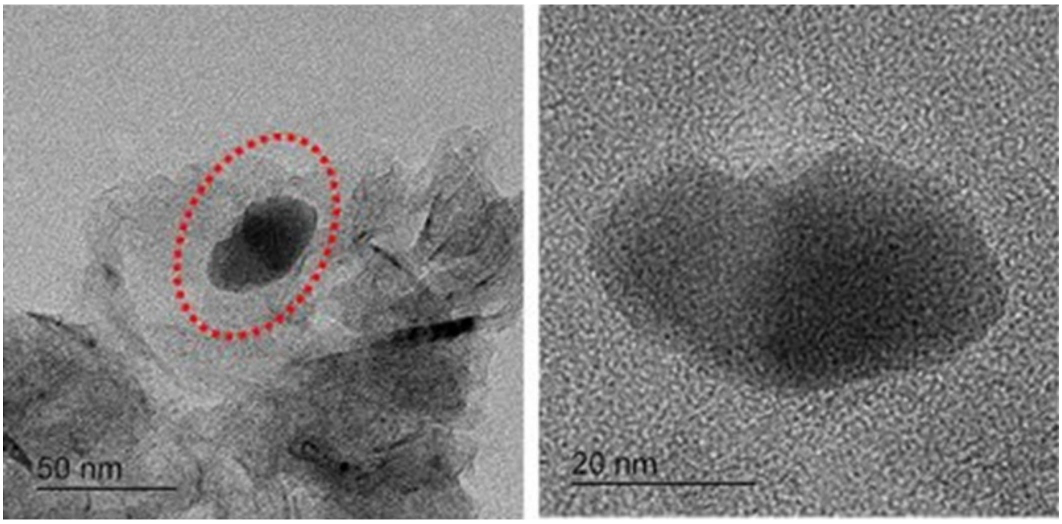

FIG. 3. Different magnification HRTEM images of Pt-NPs immobilized on RGO surface

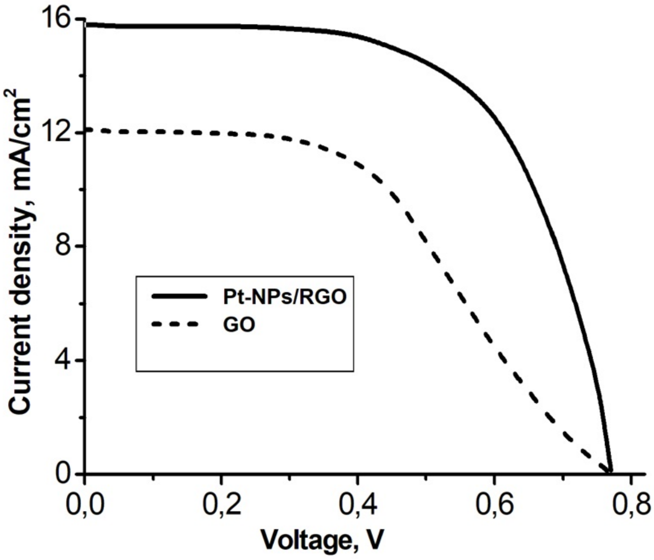

FIG. 4. J-V characteristics of DSCs with different CEs under simulated AM 1.5G solar illumination

measurements of the main DSC parameters clearly show the advantages of the Pt-NPs/RGO nanohybrids to provide perfect electrochemical catalytic activity when using as a CE in a photo electrochemical device. Fig. 4 shows that the DSC fabricated with Pt-NPs-decorated RGO counter electrode delivered the efficiency of 7.29% with $J_{SC} = 15.7$ mA/cm^2, $FF = 65.4$, and $V_{OC} = 0.71$ V. The alternative DSC configuration fabricated with a totally Pt-free GO CE has much poor performance and possesses non-typical I-V curve behavior. DSC based on GO counter electrode has shown the efficiency of 3.4% with $J_{SC} = 12.1$ mA/cm^2, $FF = 39.8$, and $V_{OC} = 0.7$ V. It should be noted that FF value in DSC based on GO CE was found to be nearly twice less than that obtained for Pt-NPs/RGO CE. As a result, the power conversion efficiency of the GO-based DSC was much decreased. We may propose that the observed poor behavior of the FF parameter may arise from factors including the poor catalytic activity of the GO electrode and high sheet resistance of the GO layer.

4. Conclusions

In summary, Pt-NPs/RGO-based nanohybrid layers were successfully synthesized at low temperature on a conductive glass substrate using microwave-assisted heating reduction method. SEM and TEM results have shown Pt NPs with a size of around 10 nm uniformly dispersed on the RGO surfaces. Pt-NPs/RGO-based layers were used as CEs for DSCs fabrication. The photovoltaic parameters of DSCs with nanohybrid CEs were achieved under simulated AM1.5G solar illumination and have shown long-term stability and high energy conversion performance of DSCs. The performance of 7.29%, with $J_{SC} = 15.7$ mA/cm^2, $FF = 65.4$, and $V_{OC} = 0.71$ V, was achieved for DSC fabricated with Pt-NPs-decorated RGO counter electrode. Thus, it was confirmed that small amounts of Pt nanoparticles decorated on RGO surfaces can be successfully used in low-cost electrodes for solar cells and energy storage devices such as lithium batteries and supercapacitors.

Acknowledgment

This research was supported by RFBR grant 16-29-06416.

References

[1] O'Regan B., Gratzel M. A low-cost, high-efficiency solar cell based on dye-sensitized colloidal TiO_2 films. *Nature*, 1991, **353**, P. 737–740.

[2] Shevaleevskiy O. The future of solar photovoltaics: from physics to chemistry. *Pure Appl. Chem.*, 2008, **80**, P. 2079–2089.

[3] Nikolay T., Larina, L., Shevaleevskiy O., Ahn B.T. Electronic structure study of lightly Nb-doped TiO_2 electrode for dye-sensitized solar cells. *Energ. Environ. Sci.*, 2011, **4**, P.1480–1486.

[4] Vildanova M.F., Nikolskaia A.B., Kozlov S.S., Shevaleevskiy O.I., Larina L.L. Novel types of dye-sensitized and perovskite-based tandem solar cells with a common counter electrode. *Tech. Phys. Lett.*, 2018, **44**(2), P. 126–129.

[5] Yum J., Jung I., Baik. C., Ko J., Nazeeruddin M.K., Gratzel M. High efficient donor–acceptor ruthenium complex for dye-sensitized solar cell application. *Energ. Environ. Sci.* 2009, **2**, P. 100–102.

[6] Dao V.D., Choi Y., Yong K., Larina L.L., Shevaleevskiy O., Choi H.-S. A facile synthesis of bimetallic AuPt nanoparticles as a new transparent counter electrode for quantum-dot-sensitized solar cells. *J. Power Sources*, 2015, **274**, P. 831–838.

[7] Larina L.L., Alexeeva O.V., Almjasheva O.V., Gusarov V.V., Kozlov S.S., Nikolskaia A.B., Vildanova M.F., Shevaleevskiy O.I. Very wide-bandgap nanostructured metal oxide materials for perovskite solar cells. *Nanosystems: Phys. Chem. Math.*, 2019, **10**(1), P. 70–75.

[8] Almjasheva O.V., Smirnov A.V., Fedorov B.A., Tomkovich M.V., Gusarov V.V. Structural features of ZrO_2–Y_2O_3 and ZrO_2–Gd_2O_3 nanoparticles formed under hydrothermal conditions. *Russ. J. Gen. Chem.*, 2014, **84**(5), P. 804–809.

[9] Bugrov A.N., Almjasheva O.V. Effect of hydrothermal synthesis conditions on the morphology of ZrO_2 nanoparticles. *Nanosystems: Phys. Chem. Math.*, 2013, **4**, P. 810–815.

[10] Kannan A.G., Zhao J., Jo S.G., Kang Y.S., Kim D.-W. Nitrogen and sulfur co-doped graphene counter electrodes with synergistically enhanced performance for dye-sensitized solar cells. *J. Mater. Chem.* A, 2014, **2**, P. 12232–12239.

[11] Somik M., Balavinayagam R., Griggs L., Hamm S., Baker G.A., Fraundorf P., Sengupta S., Gangopadhyay S. Ultrafine sputter-deposited Pt nanoparticles for triiodide reduction in dye-sensitized solar cells: impact of nanoparticle size, crystallinity and surface coverage on catalytic activity. *Nanotechnology*, 2012, **23**, P. 485405.

[12] Dao V.-D., Hoa N.T.Q., Larina L.L., Lee J.-K., Choi H.-S. Graphene-platinum nanohybrid as a robust and low-cost counter electrode for dye-sensitized solar cells. *Nanoscale*, 2013, **5**, P. 12237–12244.

[13] Chen J., Yao B., Li C., Shi G. An improved Hummers method for eco-friendly synthesis of graphene oxide. *Carbon*, 2013, **64**, P. 225–229.

[14] Gong F., Wang H., Wang Z.-S., Self-assembled monolayer of graphene/Pt as counter electrode for efficient dye-sensitized solar cell. *Phys. Chem. Chem. Phys.*, 2011, **13**, P. 17676–17682.

[15] Qui L., Zhang H., Wang W., Chen Y., Wang. R. Effects of Pt/RGO as counter electrode in dye-sensitized solar cells. *Appl. Surf. Sci.*, 2014, **319**, P. 339–343.

[16] Zhang D.W., Li X.D., Li H.B., Chen S., Sun Z., Yin X.J., Huang S.M. Graphene-based counter electrode for dye-sensitized solar cells. *Carbon*, 2011, **49**(15), P. 5382–5388.

[17] Ahn H.-J., Lee J.-S., Kim H.-S., Hwang I.-T., Hong J.-H., Shin J., Jung C.-H. Fabrication of large Pt nanoparticles-decorated rGO counter electrode for highly efficient DSSCs. *J. Ind, Eng. Chem.*, 2018, **65**, P. 318–324.

[18] Yoon S.-W., Dao V.-D., Larina L.L., Lee J.-K., Choi H.-S. Optimum strategy for designing PtCo alloy/reduced graphene oxide nanohybrid counter electrode for dye-sensitized solar cells. *Carbon*, 2016, **96**, P. 229–336.

[19] Dao V.-D., Ko S.H., Choi H.-S., Lee J.-K. Pt-NP–MWNT nanohybrid as a robust and low-cost counter electrode material for dye-sensitized solar cells. *J. Mater. Chem.*, 2012, **22**, P. 14023–14029.

[20] Dao V.-D., Tran C.Q., Ko S.-H., Choi H.-S. Dry plasma reduction to synthesize supported platinum nanoparticles for flexible dye-sensitized solar cells. *J. Mater. Chem. A*, 2013, **1**, P. 4436–4443.

NANOSYSTEMS: PHYSICS, CHEMISTRY, MATHEMATICS, 2019, 10 (6), P. 642–653

On the accuracy of the probe-sample contact stiffness measured by an atomic force microscope

A. V. Ankudinov

Ioffe Institute, 26 Politekhnicheskaya, Saint-Petersburg 194021, Russia

Alexander.ankudinov@mail.ioffe.ru

PACS 07.79.Lh **DOI 10.17586/2220-8054-2019-10-6-642-653**

To improve the accuracy of atomic force microscopy in nanomechanical experiments, an analytical model is proposed to study the static interaction of a cantilever in contact with a sample. The model takes into account: the cantilever probe is clamped by the sample or slides along its surface, the geometric and mechanical characteristics of the sample and the cantilever, their relative orientation. The cantilever console bending and torsion angles as functions of the sample displacements in three orthogonal directions have been measured by atomic force microscopy with an optical beam deflection scheme.The measurements are in good agreement with the simulation.

Keywords: AFM, cantilever, sliding and clamping probesample contact.

Received: 28 October 2019

1. Introduction

In atomic force microscopy (AFM) [1], local mechanical properties of a sample are studied using load–unloading dependencies of the indentation force on the sample deformation, force curves. They play a special role in the novel techniques [2] based on the so-called jumping mode AFM [3,4]: PeakForce QNM (Bruker), HybriD mode (NT–MDT SI), Fast force mapping mode (Asylum Research). The force curves are used to determine the height of the relief and serve as the basis for electrical, piezoelectric, magnetic, and thermal measurements [5].

A significant instrumental contribution to the shape of the force curve can be made by the friction in the AFM probe–sample contact. If the cantilever probe (the probe) slides over the surface, the force applied to the probe tip acts perpendicular to the sample and bends the cantilever beam (the console) so that the bending angle grows monotonously along the console [6, 7]. If the probe is clamped on the sample, a significant lateral friction force is added. This force buckles the console (the buckling angle varies non-monotonously along the console) [6, 7]. In the AFM device with an optical beam deflection system (OBD) [8], the deflection angle is monitored on the console locally, at the focus point of the OBD laser beam. Since the angle profile along the console is unknown, the AFM control system is not able to distinguish between the bending and the buckling of the console [9, 10], which leads to errors of the measured amplitude and direction of the indentation force. In principle, the OBD detects two parameters (bending and torsion angles of the console at the selected point), but both the contact point displacement vector and the concentrated force have three spatial components. Only recently a commercially available scheme for monitoring console deflections has appeared [11], combining the OBD with an interferometer [12] that allows measuring the missing third parameter – the console vertical displacement at the selected point.

In AFM, the normal stiffness of the probe–sample contact k_S is calculated from S, the force curve slope at the point of interest on the sample, S_0, this slope at the conditionally infinitely rigid and flat sample, and the console bending stiffness k_C, [13]:

$$k_S = \frac{k_C S}{S_0 - S}. \tag{1}$$

The equation (1) directly stems from the model of two springs, describing the AFM probe–sample contact interaction, see Fig. 1. This model does not take into account the following factors: the probe is clamped or slides over the sample, the deformation of the probe itself, the local sample inclination and the possible anisotropy of sample's mechanical properties, design features and location of the cantilever above the sample. It is more correct to think that expression (1) calculates a conditional, apparent stiffness k_A, instead of the k_S. As a result, this simple model may turn out to be a source of unreliable results in nanomechanical studies using AFM.

This work offers an analytical model of the mechanical system console–probe–sample, accounting the above mentioned factors. To describe the equilibrium states of the system, the minimum of its mechanical energy is determined. We analyze the deformation redistribution between three subsystems: the console with the non-deformable probe – the "ideal cantilever"; the deformable probe; and the sample. In each subsystem, the stiffness tensor linearly couples the concentrated force vector applied to the probe tip (at the contact point) with the deformation vector. General solutions are obtained for two types of holonomic constraints: the probe is clamped on the sample; the probe slides along the

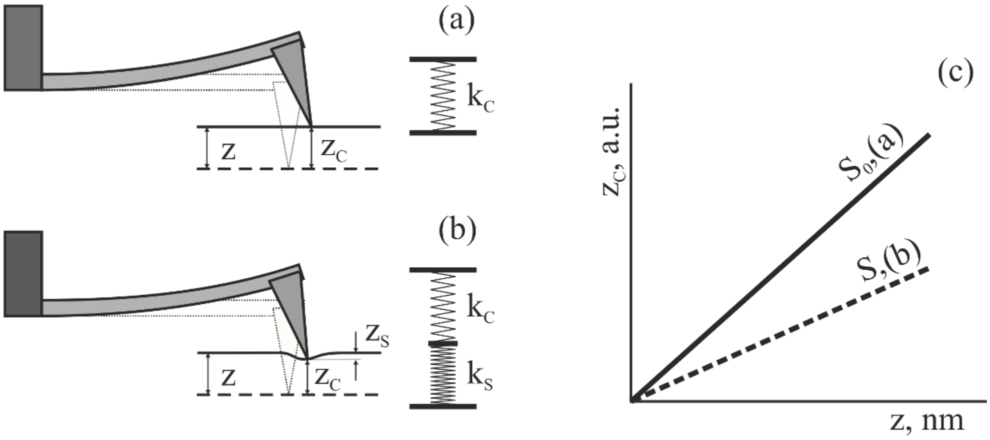

FIG. 1. Simple models of the AFM contact with a solid surface (a), with a soft sample (b). Cantilever and soft sample deformations are described using two springs: k_C and k_S. (c) Dependencies of the cantilever deviation Z^C on the sample vertical displacement Z: the solid sample, the calibration slope S_0,(a); the soft sample, the slope S,(b). Z^S on (b) denotes the sample deformation

sample selected plane. The contact of the so-called “real cantilever” (the console with the deform able probe) and the mechanically isotropic sample is examined in detail. Depending on the position of the OBD laser focus point on the console, the normalized sensitivities of its bending and torsion angles to the sample displacement along three orthogonal directions were calculated and as well measured. Good agreement between calculations and measurements is demonstrated.

2. Theoretical analysis

2.1. “Ideal cantilever”

First, consider the “ideal cantilever”, that is, one in which the applied force deforms only the console, but not the probe, Fig. 2. Let the Y axis of the YZ coordinate system be directed along the rectangular console, and the coordinate origin is at the console attachment line to the chip, Fig. 2(a). The console displacement profile due to the force $\mathbf{F}$ acting in the YZ plane is expressed as follows [6]:

$$Z\left(Y,\mathbf{F}\right)=\left(2/E_C w t^3\right)\left\{3l_T Y^2 F_Y+\left(3l_C Y^2-Y^3\right)F_Z\right\}, \tag{2}$$

where E_C is the Young’s modulus of the console; w, t and l_C its width, thickness and length; l_T is the probe height. We introduce the parameters: $\lambda=l_T/l_C$, the console stiffness $k_C=E_C w t^3/4l_C^3$, the normalized coordinate $\psi=Y/l_C$, – and rewrite (2) in a more concise form:

$$Z\left(\psi,\mathbf{F}\right)=\left(1/2k_C\right)\left\{3\lambda\psi^2 F_Y+\left(3\psi^2-\psi^3\right)F_Z\right\}. \tag{2a}$$

The displacement profile (2a) corresponds to the profile of the bending angle of the console of the ideal cantilever:

$$\alpha\left(\psi,\mathbf{F}\right)=l_C^{-1}\cdot dZ\left(\psi\right)/d\psi=\left(3/2k_C l_C\right)\left\{2\lambda\psi F_Y+\left(2\psi-\psi^2\right)F_Z\right\}. \tag{2b}$$

In AFM the console bending is small and the angle $\alpha\left(\psi,\mathbf{F}\right)\ll 1$. Therefore, the vector $\mathbf{r}^{\mathbf{C}}$ components of the “ideal cantilever”, the probe tip displacements, are quite accurately related linearly with the displacement and the angle corresponding to the console end ($\psi=1$):

$$Z^C=Z\left(1,\mathbf{F}\right),\quad Y^C=l_T\alpha\left(1,\mathbf{F}\right). \tag{3}$$

Using (2a), (2b), (3) and the substitution $l_T/l_C=\lambda$, we can determine the matrix elements of the compliance tensor, $\mathbf{C}^{-1}$, and the stiffness tensor, $\mathbf{C}$, of the “ideal cantilever” in the flat coordinate system YZ, see also [14]:

$$\mathbf{r}^{\mathbf{C}}=\mathbf{C}^{-1}\mathbf{F},\quad \mathbf{C}^{-1}=k_C^{-1}\begin{pmatrix}3\lambda^2 & 3\lambda/2\\ 3\lambda/2 & 1\end{pmatrix}, \tag{4a}$$

$$\mathbf{F}{=}\mathbf{C}\mathbf{r}^{\mathbf{C}},\quad \mathbf{C}{=}k_C\begin{pmatrix}4/3\lambda^2 & -2/\lambda\\ -2/\lambda & 4\end{pmatrix}. \tag{4b}$$

Using (4a) in (2a) and (2b), we can relate the bending angle and the displacement of the console measured by the OBD and interferometer methods with the probe tip displacements:

$$\alpha\left(\psi,\mathbf{r}^{\mathbf{C}}\right)=l_C^{-1}\left\{\psi\left(3\psi{-}2\right)Y^C/\lambda{+}6\psi\left(1{-}\psi\right)Z^C\right\}, \tag{5a}$$

$$Z\left(\psi,\mathbf{r}^{\mathbf{C}}\right)=\psi^2\left(\psi{-}1\right)Y^C/\lambda{+}\psi^2\left(3{-}2\psi\right)Z^C. \tag{5b}$$

Let the "ideal cantilever" be in contact with a flat, horizontal and non-deformable surface. If this surface is raised to a height of Z, the probe tip moves vertically by the same value, $Z^C{=}\ Z$. We can set the lateral displacement Y^C in two extreme cases: 1) the probe slides along the sample, $F_Y{=}\ 0$ (according to (4a), this is equivalent to $Y^C{=}3\lambda Z^C/2$); 2) the probe is clamped on the sample, $Y^C{=}\ 0$ ($F_Y{=}\ -F_Z/2\lambda$, according to (4b)), – and calculate using (5a) and (5b) the profiles of the console displacement and bending angle, see Table 1.

TABLE 1. "Ideal cantilever". Profiles of the console displacement and bending angle when the probe-sample contact moves to a height Z. The sample is horizontal, flat and non-deformable; the console is parallel to the sample

Contact	$Z\left(\psi\right)/Z$	$2l_C\alpha\left(\psi\right)/3Z$
Clamped ($Y^C=0$)	$\psi^2\left(3-2\psi\right)$	$4\psi\left(1-\psi\right)$
Sliding ($F_Y=0$)	$\psi^2\left(3-\psi\right)/2$	$\psi\left(2-\psi\right)$

Only when $\psi{=}1$, $Z\left(1\right)$ does not depend on Y^C. This point is the probe tip projection on the console plane, it may not coincide with the console edge. For the OBD method the special point is $\psi{=}2/3$, where $\alpha\left(\psi\right)$ depends only on Z^C. Since in AFM, the console deflection is regulated, for the "ideal cantilever" this point is optimal for OBD laser focusing. At $\psi{=}2/3$, in the controlled signal, the contribution from clamped state – sliding state transitions in the probe–sample contact (the main sources of instabilities during contact scanning) is suppressed, and the ratio $\alpha\left(\psi\right)/Z$, the sensitivity, is only $1/9$ less than the maximum. In AFM, the console is tilted from the horizontal line by a certain angle α_0. It can be shown that in this case the optimal focus will be almost at the same point: $\psi^*\cong 2\left(1{-}\lambda\tan^2\alpha_0+O\left(\lambda^2\right)\right)/3\cong 2/3$, since usually $\lambda\ll 1$.

In Fig. 2(b) the transverse force F_X twists the console at an angle β (measured by the OBD method) and additionally bends it and shifts its end by a distance $X^{C(b)}$. Such a bend leaves the console in the XY plane and it cannot be measured by the OBD or interferometer methods. By analogy with the F_Z component action considered in (2), we can write:

$$X^{C(b)}{=}\left(4l_C^3/E_Ctw^3\right)F_X{=}k_C^{-1}\delta^2F_X, \tag{4}$$

where $\delta{=}t/w$. The profile of the console torsion angle caused by the force moment F_Xl_T, responds to the relation, see details in [6, 14]:

$$\beta\left(\psi,\mathbf{F}\right)=-\psi\left(3l_C/G_Cwt^3\right)F_Xl_T, \tag{6a}$$

where the console shear modulus $G_C{=}E_C/(2+2\nu)$. For most materials, the Poisson's ratio $\nu\approx 1/3$; using the notation introduced earlier, we transform (6a):

$$\beta\left(\psi,\mathbf{F}\right)=-\left(2/k_Cl_C\right)\lambda\psi F_X. \tag{2c}$$

The action of the force F_X gives a superposition of the torsion and the in-plane bending. Using (6) and (2c), the total displacement of the probe tip is obtained:

$$X^C{=}X^{C(b)}{-}l_T\beta\left(1{,}\mathbf{F}\right)=k_C^{-1}\left(2\lambda^2{+}\delta^2\right)F_X. \tag{6b}$$

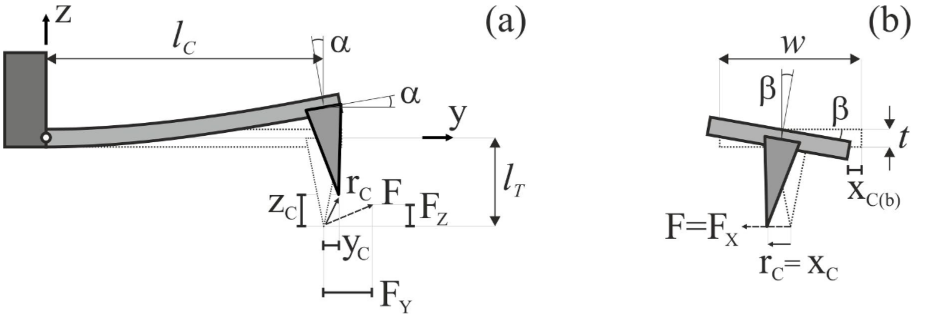

FIG. 2. “Ideal cantilever”. (a) The console bending by the force $\mathbf{F}$ with components F_Y, F_Z. Both the free end of the console and the non-deformable probe are deflected by a positive angle α. As a result, the probe tip moves along the vector $\mathbf{r^C}$ with the components Y^C, Z^C. (b) Torsion by a negative angle β and bending of the console to a distance $X^{C(b)}$ by the force $\mathbf{F}$ with a single, positive component F_X. The probe tip shifts in the direction of the force along the vector $\mathbf{r^C}$ with the component X^C. The console width w, thickness t and length l_C; the probe height l_T; the Y and Z axes of the coordinate system associated with the cantilever

Using (6b), (4a), and (4b), we write the matrix elements of the compliance tensors, $\mathbf{C}^{-1}$, and the stiffness tensor, $\mathbf{C}$, of the “ideal cantilever” in the XYZ coordinate system:

$$\mathbf{C}^{-1}{=}k_C^{-1}\begin{pmatrix} 2\lambda^2{+}\delta^2 & 0 & 0 \\ 0 & 3\lambda^2 & 3\lambda/2 \\ 0 & 3\lambda/2 & 1 \end{pmatrix},$$

$$\mathbf{C}{=}k_C\begin{pmatrix} \left(2\lambda^2{+}\delta^2\right)^{-1} & 0 & 0 \\ 0 & 4\lambda^{-2}/3 & -2\lambda^{-1} \\ 0 & -2\lambda^{-1} & 4 \end{pmatrix}. \tag{4c}$$

Dividing (2c) by (6b), we relate the console torsion angle measured by the OBD method to the displacement:

$$\beta\left(\psi,\mathbf{r^C}\right)=-l_C^{-1}\lambda\psi X^C/\left(2\lambda^2{+}\delta^2\right). \tag{5c}$$

When the laser focus is fixed, $\psi{=}\ const$, the equations (5a) – (5c) can be used to restore the displacement vector of the ideal cantilever from the three measured parameters, and the equations (2a) – (2c) to restore the force vector,see Table 2. The necessary three parameters can be obtained both in the combined OBD and interferometer scheme [11, 12], and using only the OBD method and two ψ values. In contrast to the restored force vector, the restored $\mathbf{r^C}$ describes only the probe tip displacements of the “ideal cantilever”.

TABLE 2. Profiles of the console vertical displacement, bending and torsion angles as functions of the displacement or of the force projections

Profile	$r^C=\left(X^C,Y^C,Z^C\right)$	$F=\left(F_X,F_Y,F_Z\right)$
$Z\left(\psi\right)$	$\psi^2\left(\psi-1\right)Y^C/\lambda+\psi^2\left(3-2\psi\right)Z^C$	$\left(1/2k_C\right)\left\{3\lambda\psi^2F_Y+\left(3\psi^2-\psi^3\right)F_Z\right\}$
$\alpha\left(\psi\right)$	$\left(1/l_C\right)\left\{\psi\left(3\psi-2\right)Y^C/\lambda+6\psi\left(1-\psi\right)Z^C\right\}$	$\left(3/2k_Cl_C\right)\left\{2\lambda\psi F_Y+\left(2\psi-\psi^2\right)F_Z\right\}$
$\beta\left(\psi\right)$	$-\left(2/l_C\right)\lambda\psi X^C/\left(2\lambda^2+\delta^2\right)$	$-\left(2/k_Cl_C\right)\lambda\psi F_X$

2.2. Deformation distribution in the console–probe–sample system

To calculate the profiles of the console displacements, bending and torsion angles for the "real cantilever", we consider the console–probe–sample system, see Fig. 3, and analyze how deformations are redistributed in it.

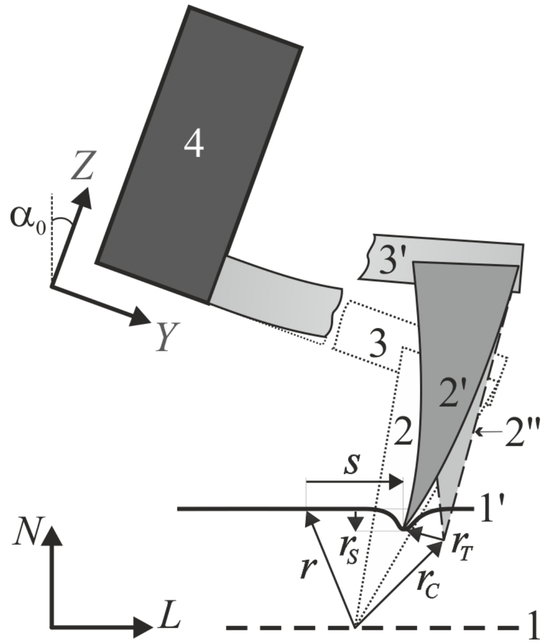

FIG. 3. Deformation of the sample and cantilever AFM in contact. Initial state: the sample (1) touches the probe (2), the interaction force is zero, the console (3) is not bent. Final state: the sample (1) moved along the vector **r**, deforms itself, the probe (2) and the console (3); the non-deformable holder (4) is stationary, the conditionally non-deformable probe is in the position (2"). Deformation vectors of: ideal cantilever (the conditional probe tip (2") displacements), $\mathbf{r}^C$; probe tip, $\mathbf{r}^T$; sample, $\mathbf{r}^S$. The sliding is along the vector **s**. The XLN coordinate system is associated with the scanner, XYZ – with the cantilever, the X axis is directed to the reader. The mounting angle of the cantilever holder, α_0, is deviated from the vertical: by 20° (NT-MDT microscopes) and by 12° (Bruker microscopes)

In each subsystem: console, "ideal cantilever", C, probe, T, sample, S, – the generalized Hooke's law is valid. Symmetric, positive definite stiffness tensors $C_{i,j}$, $T_{i,j}$, $S_{i,j}$ with nonzero determinants relate the force and associated vector components, $F_i^{C,T,S}$ and $r_j^{C,T,S}$, in the corresponding subsystem.E.g., for the "ideal cantilever": $F_i^{C,T,S}{=}C_{i,j}r_j^{C,T,S}$, see in Equation (4c) the matrix elements $C_{i,j}$ in the XYZ coordinate system. The quadratic forms of the tensors **C**, **T**, and **S** are expressions for the doubled elastic strain energy of the corresponding subsystem. The energy of the whole system is:

$$W{=}\frac{1}{2}\sum_{i,j}\left(C_{i,j}r_i^C r_j^C{+}T_{i,j}r_i^T r_j^T{+}S_{i,j}r_i^S r_j^S\right). \tag{5}$$

In the initial state $3/2/1$, Fig. 3, all coordinates are zero, there are no deformations, what minimizes the energy (7). When the sample holder moves along the vector $\mathbf{r}{=}\,(X, L, N)$ relative to the cantilever holder (this is done by the AFM scanner), then the deformation vectors appear in each subsystem: $\mathbf{r^C}{=}\left(X^C, Y^C, Z^C\right)$, $\mathbf{r^T}{=}\left(X^T, Y^T, Z^T\right)$ and $\mathbf{r^S}{=}\left(X^S, Y^S, Z^S\right)$. In the final equilibrium state $3'/2'/1'$, Fig. 3, the nine components of these vectors must be the coordinates of the conditional minimum of the energy.

Two cases are important, see also Fig. 3: a) the contact is clamped, $s\equiv 0$; b) the contact slides in some plane, $\mathbf{s}\neq 0$.

Case a). The system integrity is maintained, the deformation vectors obey the holonomic constraint:

$$\mathbf{r^C}{+}\mathbf{r^T}{-}\mathbf{r^S}{=}\mathbf{r}. \tag{7a}$$

The minimum energy is determined by zeroing the nine partial derivatives of W (7). Accounting for (7a), the minimum W is sought by solving a system of six equations for six unknown variables.

Case b). Let the contact slides in the XL plane, as in Fig. 3. Then the holonomic constraint will be only for the three vertical deformations:

$$N^C+N^T-N^S=N. \tag{7b}$$

The minimum W is sought by solving a system of eight equations for eight unknown variables.

Case a). According to the Newton's 3rd law, the forces $\mathbf{F^T}$ and $\mathbf{F^C}$, the action of the sample on the probe and the probe on the console, are equal to $-\mathbf{F^S}$, the counteraction of the probe on the sample. In each subsystem, the generalized Hooke's law is valid, e.g. $\mathbf{F^T}=\mathbf{Tr^T}$. This allows to relate the vectors $\mathbf{r^C}$, $\mathbf{r^T}$ and $\mathbf{r^S}$, and the vector $\mathbf{r}$:

$$\begin{cases}\mathbf{r^C}+\mathbf{r^T}-\mathbf{r^S}=\mathbf{r}\\ \mathbf{F^C}=\mathbf{F^T}=-\mathbf{F^S}\\ \mathbf{Cr^C}=\mathbf{Tr^T}=-\mathbf{Sr^S}\end{cases} \Rightarrow \begin{cases}\left(\mathbf{I}+\mathbf{T}^{-1}\mathbf{C}+\mathbf{S}^{-1}\mathbf{C}\right)\mathbf{r^C}=\mathbf{r}\\ \mathbf{r^T}=\mathbf{T}^{-1}\mathbf{Cr^C}\\ \mathbf{r^S}=-\mathbf{S}^{-1}\mathbf{Cr^C}\end{cases} \Rightarrow \begin{cases}\mathbf{r^C}=\mathbf{C}^{-1}\left(\mathbf{C}^{-1}+\mathbf{T}^{-1}+\mathbf{S}^{-1}\right)^{-1}\mathbf{r}\\ \mathbf{r^T}=\mathbf{T}^{-1}\left(\mathbf{C}^{-1}+\mathbf{T}^{-1}+\mathbf{S}^{-1}\right)^{-1}\mathbf{r}\\ \mathbf{r^S}=-\mathbf{S}^{-1}\left(\mathbf{C}^{-1}+\mathbf{T}^{-1}+\mathbf{S}^{-1}\right)^{-1}\mathbf{r}\end{cases} \tag{8a}$$

Where $\mathbf{I}$ is the unit matrix; $\mathbf{C}^{-1}$, $\mathbf{T}^{-1}$ and $\mathbf{S}^{-1}$ – the compliance (inverse stiffness) tensor of the corresponding subsystem. Unlike matrix elements, the solution form (8a) does not depend on the choice of the coordinate system. In the system, where the matrix elements of the tensors are the least bulky, calculations are simplified.

Case b). For the contact sliding in the XL plane, deformations of the "ideal cantilever" X^C, L^C, N^C, probe X^T, L^T, N^T, and sample X^S, L^S, N^S, will depend only on N, the vertical displacement of the scanner, although the latter moves the sample along the vector $\mathbf{r}=(X,L,N)$. We give this solution, omitting the cumbersome algebraic derivation:

$$\begin{pmatrix} X^C & X^T & X^S\\ L^C & L^T & Y^S\\ N^C & N^T & N^S\end{pmatrix} = \begin{pmatrix} C^{-1}_{NX} & T^{-1}_{NX} & -S^{-1}_{NX}\\ C^{-1}_{NL} & T^{-1}_{NL} & -S^{-1}_{NL}\\ C^{-1}_{NN} & T^{-1}_{NN} & -S^{-1}_{NN}\end{pmatrix} \frac{N}{C^{-1}_{NN}+T^{-1}_{NN}+S^{-1}_{NN}}, \tag{8b}$$

where e.g. C^{-1}_{NX} is the matrix element of the console compliance tensor in the XLN system associated with the scanner (or with the horizontally located flat sample), Fig. 3. The numerator in (8b) is proportional to N, the scanner displacement projection on the normal to the surface of sliding (the XL plane).

On the non-planar relief sample, the normal at the selected point on the sample may not coincide with the N axis. In this case, the local coordinate system xyz associated with the selected point is used, and the solution is obtained from (8b) by replacing: $X \to x,\ L \to y, N \to z$.

To calculate the bending and torsion angle profiles and the displacement profile, Table 2, the solution vector is taken in the coordinate system associated to the cantilever. For example in Fig. 3, the coordinate systems correspond to the following relation:

$$\begin{pmatrix} X^C\\ Y^C\\ Z^C\end{pmatrix} = \begin{pmatrix} 1 & 0 & 0\\ 0 & \cos\alpha_0 & -\sin\alpha_0\\ 0 & \sin\alpha_0 & \cos\alpha_0\end{pmatrix} \begin{pmatrix} X^C\\ L^C\\ N^C\end{pmatrix}. \tag{9}$$

2.3. "Real cantilever"

An AFM pyramidal probe can be modeled by a truncated elliptical cone. In the cantilever coordinate system, both the stiffness and the compliance tensors of such a model have three components:

$$\mathbf{T}=\begin{pmatrix} k_{T1} & 0 & 0\\ 0 & k_{T2} & 0\\ 0 & 0 & k_{T3}\end{pmatrix}, \quad \mathbf{T}^{-1}=\begin{pmatrix} k^{-1}_{T1} & 0 & 0\\ 0 & k^{-1}_{T2} & 0\\ 0 & 0 & k^{-1}_{T3}\end{pmatrix}, \tag{10}$$

where k_{T1} and k_{T2} are the bending stiffness along the mutually perpendicular ellipse axes, k_{T3} is the normal stiffness along the cone height.

For a simplified model of a truncated cone with an apex radius R_T and the apex half angle α_T, it is sufficiently to determine two stiffness values, e.g. in the framework of theories of small deflections of rods [15, 16] and contact mechanics [15, 17]:

$$k_{T1}{=}k_{T2}{=}k_{Tl} \cong (3\pi/4)\, E_T R_T (\tan\alpha_T\ )^3, \quad k_{T3}{=}k_{Tn} \cong 2E_T R_T. \tag{10a}$$

Si pyramidal probes e.g. on cantilevers HA_FM (NT–MDT SI) have the following parameters: Young's modulus: $E_T \approx 100$ GPa, $R_T \approx 10$ nm, $\alpha_T \approx 15°$. Using (10a) we get: $k_{Tl} \approx 50$ N/m, $k_{Tn} \approx 2000$ N/m.

For a more complex probe model, the truncated elliptical cone, let the semi axes of the ellipse lie along the X and Y directions, having dimensions c and d on the vertex. It can be shown that: $k_{T1}{=}q^{1/2}k_{Tl}$ and $k_{T2}{=}q^{5/2}k_{Tl}$, where the compression factor $q = d/c$, and the replacement $R_T{=}\sqrt{cd}$ is used in (10a) for k_{Tl} and k_{Tn}.

By analogy with the matrix elements (10), for the probe–sample contact we introduce the shear stiffness in the XLN coordinate system, $k_{S1}{=}k_{S2}{=}k_{Sl}$, and the normal stiffness, $k_{S3}{=}\ k_{Sn}$. Their values can be evaluated using the Hertz's contact mechanics, [17]:

$$\begin{gathered} k_{Sl}{=}\ 8G^*a, \quad k_{Sn}{=}\ 2E^*a{=}\sqrt[3]{6FR^*E^{*2}}, \\ a{=}\sqrt[3]{3FR^*/4E^*}, \quad R^*{=}R_T R_S/(R_T{+}R_S), \\ E^*{=}\left(\frac{1{-}\nu_T^2}{E_T}{+}\frac{1{-}\nu_S^2}{E_S}\right)^{-1}, \quad 4G^*{=}\left(\frac{(1{-}\nu_T/2)\,(1{+}\nu_T)}{E_T}{+}\frac{(1{-}\nu_S/2)\,(1{+}\nu_S)}{E_S}\right)^{-1}, \end{gathered} \tag{10b}$$

F – the interaction force, R_T and R_S – the tip curvature radius and the local curvature radius of the sample, E_T, ν_T and E_S, ν_S – Young's moduli and Poisson's ratios of the probe and sample, respectively.

Most materials have $\nu \approx 1/3$, therefore according (10b), $E^* \approx 4G^*$, and $k_{Sl} \approx k_{Sn}{=}k_S$. In this isotropic case, the sample local mechanical properties are modeled by one parameter k_S. Let both the probe with $R_T = 10$ nm and the flat, uniform sample be made of silicon, then for $F = 10$ nN we obtain: $k_S \approx 100$ N/m.

To use (8b), the tensor components of the sample, probe (10), console (4c) are converted using rotation matrices into values in the XLN coordinate system, see in particular (9). We give, for example, expressions for the components S^{-1}_{NN}, T^{-1}_{NN} and C^{-1}_{NN}:

$$\begin{aligned} C^{-1}_{NN} &= k_C^{-1}\left(3\lambda^2\sin^2\alpha_0 - 3\lambda\sin\alpha_0\,\cos\alpha_0 {+} \cos^2\alpha_0\ \right); \\ S^{-1}_{NN} &= k_C^{-1}\kappa_S^{-1}; \quad T^{-1}_{NN}{=}k_C^{-1}\left(\kappa_{T2}^{-1}\sin^2\alpha_0 + \kappa_{T3}^{-1}\cos^2\alpha_0\ \right). \end{aligned} \tag{11}$$

Here and further relative stiffness values are introduced: $\kappa_S{=}k_S/k_C$, $\kappa_{Ti}{=}k_{Ti}/k_C$, $i = 2, 3$.

To use (8a), we write $\mathbf{T}^{-1}{+}\mathbf{S}^{-1}$ by analogy with $\mathbf{T}^{-1}$ in (10), replacing k_{Ti}^{-1} with $k^{-1}\kappa_i^{-1}$, where $\kappa_i^{-1}{=}\kappa_{Ti}^{-1}{+}\kappa_S^{-1}$ and $i = 1, 2, 3$:

$$\mathbf{T}^{-1}{+}\mathbf{S}^{-1}{=}k_C^{-1}\begin{pmatrix} \kappa_1^{-1} & 0 & 0 \\ 0 & \kappa_2^{-1} & 0 \\ 0 & 0 & \kappa_3^{-1} \end{pmatrix}. \tag{12}$$

For the clamped contact, the proportionality coefficients between α or β and the displacement along the scanner selected axis can be obtained by substituting the matrix elements from (4c) and (12) into (8a), and using (9) and Table 2. For the sliding contact, to relate α and the scanner vertical displacement, one has to substitute in (8b) the matrix elements of the compliance tensors of the console, the sample, and the probe defined in the XLN coordinate system, see (11). Dependencies calculated in this way are shown in Table 3 as the normalized sensitivity profiles.

Using Table 3, we can significantly refine the equation (1). The ratio α/N is proportional to the force curve slope S; on the non-deformable sample ($\kappa_S^{-1}{=}\ 0$) it is proportional to S_0. For the sliding contact, using the profile 1 from Table 3, we can compose analytical expressions for S and S_0 and obtain a new formula for k_S, which differs from the equation (1) by the correcting γ-factor:

$$\begin{aligned} \gamma &= \left(\left(3\lambda^2{+}\kappa_{T2}^{-1}\right)\sin^2\alpha_0 - 3\lambda\sin\alpha_0\,\cos\alpha_0 + \left(1{+}\kappa_{T3}^{-1}\right)\cos^2\alpha_0\ \right)^{-1}, \\ k_S &= \gamma k_C S/(S_0{-}S). \end{aligned} \tag{1a}$$

With growing k_C, the relative compliances κ_{T2}^{-1} and κ_{T3}^{-1} increase, and the γ-factor can become less than unity. The γ-factor of a soft cantilever (κ_{T2}^{-1} and κ_{T3}^{-1} are small) is larger than unit, e.g. for $\lambda{=}\ 0.1$ and $\alpha_0{=}\ 20°$ the soft cantilever has $\gamma \approx 1.27$. If the γ-factor is neglected, the k_S will be overestimated in the first case, and in the second one it will be underestimated.

Earlier [18] it was reported, when calibrating the AFM cantilever stiffness the result is overestimated, in proportion $\cos^{-2}\alpha_0$ [19]. The expression (1a) for γ-factor substantially clarifies these remarks.

TABLE 3. "Real cantilever" in contact with the horizontal, deformable sample surface. Normalized profiles of the console bending and torsion angles (α and β) as functions of the scanner displacements (X, L, N)

No.	Normalized sensitivity profile
1	$\dfrac{2l_C\alpha_{b)}(\psi)}{3N}=\dfrac{(2-\psi)\cos\alpha_0-2\lambda\sin\alpha_0}{\left(3\lambda^2+\kappa_2^{-1}\right)\sin^2\alpha_0-3\lambda\sin\alpha_0\cos\alpha_0+\left(1+\kappa_3^{-1}\right)\cos^2\alpha_0}\psi$
2	$\dfrac{2l\alpha_{a)}(\psi)}{3N}=\dfrac{\left(4+4\kappa_3^{-1}\right)\lambda\sin\alpha_0+\left(12\lambda^2+8\kappa_2^{-1}\right)\cos\alpha_0-\left[6\lambda\sin\alpha_0+\left(12\lambda^2+4\kappa_2^{-1}\right)\cos\alpha_0\right]\psi}{3\lambda^2+12\lambda^2\kappa_3^{-1}+4\kappa_2^{-1}+4\kappa_2^{-1}\kappa_3^{-1}}\psi$
3	$\dfrac{2l\alpha_{a)}(\psi)}{3L}=\dfrac{\left(-4+8\kappa_3^{-1}\right)\lambda\cos\alpha_0+\left(12\lambda^2+8\kappa_2^{-1}\right)\sin\alpha_0+\left[6\lambda\cos\alpha_0-\left(12\lambda^2+4\kappa_2^{-1}\right)\sin\alpha_0\right]\psi}{3\lambda^2+12\lambda^2\kappa_3^{-1}+4\kappa_2^{-1}+4\kappa_2^{-1}\kappa_3^{-1}}\psi$
4	$\dfrac{2l\beta_{a)}(\psi)}{3X}=\dfrac{-4\lambda}{6\lambda^2+3\delta^2+3\kappa_1^{-1}}\psi$

Subscripts a) and b) refer to the clamped and sliding contacts. Relative compliances $\kappa_i^{-1}=\kappa_{Ti}^{-1}+\kappa_S^{-1}$, $i=1,2,3$ correspond to X,Y,Z axes. Mounting angle of the cantilever holder α_0; $\lambda=l_T/l_C$, $\delta=t/w$; see Fig. 2 and 3. At the line of the console attachment to the chip $\psi=0$, at the point of the probe tip projection to the console plane $\psi=1$.

If the probe–sample contact is clamped when calculating at least one of the slopes, S or S_0, the expression defining the k_S is significantly complicated, in particular by the dependence on ψ.

In this regard, it is important to determine in AFM whether the probe slides along the sample or not. E.g. for a homogeneous sample, the sliding probe should as a rule lead to reduced S values on the inclined surface areas compared to the horizontal ones [20]. In detail, using the analytical approach of this work, the question will be considered later.

When substituting $\kappa_i^{-1}=0$, the profiles in Table 3 describe the "ideal cantilever" on the non-deformable and horizontal sample. A special case when the console is parallel to the sample ($\alpha_0=0$) was considered in Table 1. The estimations made above for the probe and sample stiffness values may be used to conclude the following: 1) $\kappa_1^{-1}\cong\kappa_2^{-1}\gg\kappa_3^{-1}$, 2) $\kappa_i^{-1}\ll 1$ for soft cantilevers ($k_C<1N/m$). Thus on the solid and flat sample, the soft cantilevers should behave like the "ideal cantilever", some deviations from this behavior can be described using two small parameters, κ_1^{-1} and κ_2^{-1}.

3. Experimental verification of the theory and the results discussion

For the OBD method used in our AFM device, the console bending angle α is proportional to the DFL(deflection) signal, the photocurrent difference between the upper and lower halves of the photodetector; the console torsion angle β is proportional to the LF (lateral force) signal, the photocurrent difference between the right and left halves of the photodetector, [13]. The ratios α/N, α/L and β/X as functions of ψ were measured by analyzing the force dependencies $DFL(N)$ and the friction force loops $DFL(L)$ and $LF(X)$. In these measurements, an atomically smooth, freshly prepared n-type GaAs (110) cleaved surface (a doping level is 10^{18} cm^{-3}) was used as a flat and solid sample.

DFL and LF signals are measured in Amps or Volts, depending on the AFM model. To compare the measurement results with the calculations, it is necessary to convert the used units into radians.We use the AFM device Ntegra Aura (NT–MDT SI) in the configuration "scanning by sample". The screws that adjust the horizontal position of the photodetector along and across the console have a thread pitch of 0.35 mm. The angular size of the vector of the photodetector center displacement is inversely proportional to the optical arm, 25 mm. The light reflected in the photodetector is deflected by a double angle compared to the console deflection angle [21]. Given this and that in our AFM device the photodetector and console planes are parallel, one turn of the adjusting screw along the console corresponds to α=$\cos 20° \cdot 0.35\ /50 \cong 6.6 \cdot 10^{-3}$ rad, and one turn of the adjusting screw across the console to β=$0.35/50 = 7 \cdot 10^{-3}$ rad. This made it possible to quickly measure the necessary conversion factors for DFL and LF signals with an accuracy of about 5 % (1/24 turn).

Measurements of ψ, the focus point position of the OBD laser on the console, were carried out using the adjusting screw (0.35 mm thread pitch) moving a micropositioner table with the cantilever holder along the console. Given the length ($\approx$ 51 mm) of the lever of the force acting on the table, and the distance ($\approx$ 34 mm) from the cantilever to the table axis of rotation, one turn of the screw corresponds to the movement of $\approx$ 233 μm. Using this, it was possible to change the focus point position with an accuracy of about 10 μm (1/24 turn). The positions of the console attachment to the chip and of the free end of the console were determined by a 50 % reduction in the intensity of laser radiation reflected from the console to all four sections of the photodetector (a *Laser* signal).

Figure 4 presents the results of AFM measurements of the console bending and torsion angles caused by the movements of the GaAs (110) sample in three orthogonal directions. The cantilever fpS10 [22] with the following characteristics was studied. The console stiffness refined by the Sader method [23] was k_C= 51 mN/m. The geometric parameters of the console and probe, refined in an optical and scanning electron microscopes: l_C= 257 μm (the distance between the line of the console attachment to the chip and the point of the probe tip projection to the console plane), w = 34 μm and t = 1 μm; α_T= 10.5° and l_T= 12.5 μm.

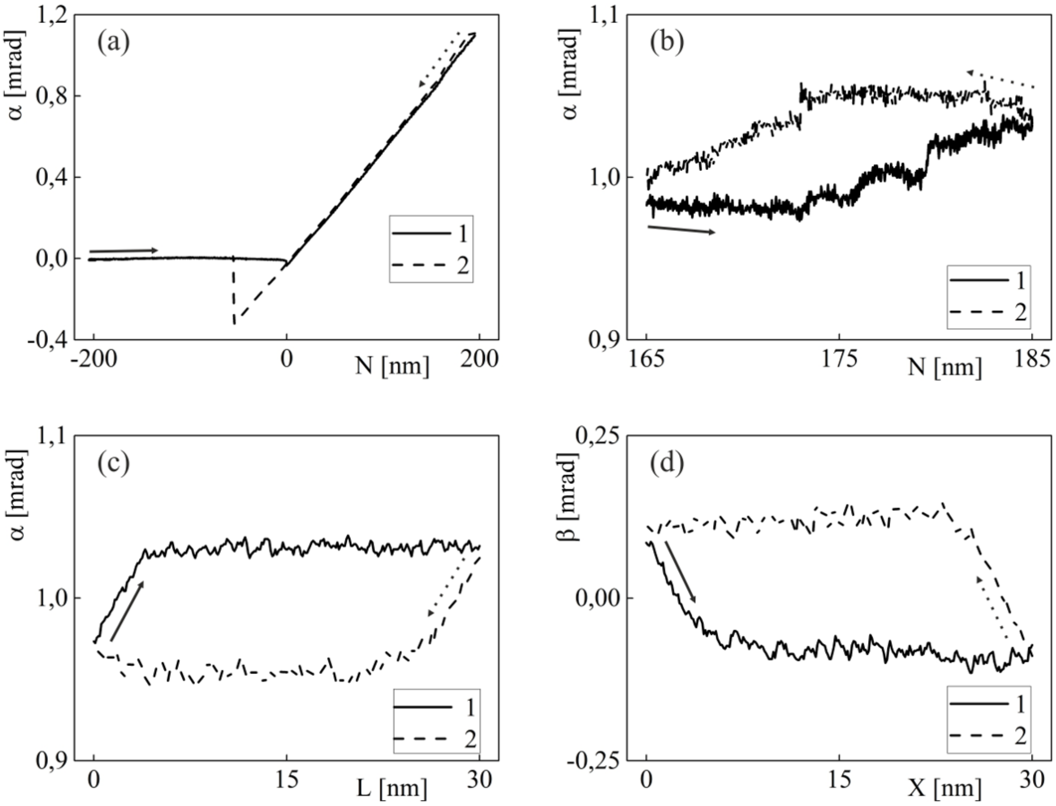

FIG. 4. (a) Force curves, $\alpha(N)$, DFL signal dependencies on the scanner vertical displacement: 1 loading; 2 unloading. Friction loops (hysteresis): (b) $\alpha(N)$, in the force curves; (c) $\alpha(L)$, in the DFL signal, the fast scanning direction is along the console; (d) $\beta(X)$, in the LF signal, the fast scanning direction is across the console. The scanning velocities both in positive 1 and negative 2 directions were: (a) 200 nm/s, (b) 10 nm/s, (c) and (d) 60 nm/s. (b–d) The interaction force, $F \approx 10$ nN. The OBD laser focus point coordinate on the console, $\psi = 0.95$

The experimental α/N ratio was determined for positive N as the average slope of the loading and unloading force curves. In particular it is 5.87 μrad/nm for the data in Fig. 4(a). The ratios α/L and β/X were determined on the left and right sides of the friction loops [18, 24], see arrows in Figs. 4(c) and 4(d) along the areas where the probe tip is clamped by the sample. To improve the accuracy of measurements, 32 friction loops were analyzed.

Using the data, as in Fig. 4, with different ψ, the profiles of the console torsion, buckling and bending angles were measured, see Fig. 5.

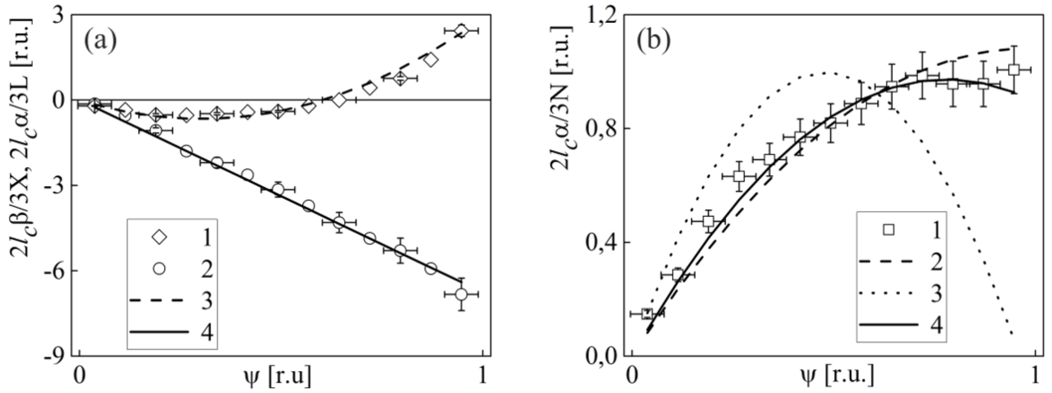

FIG. 5. Cantilever fpS10. (a) Measurement and approximation data for the buckling angle profile, 1 and 3, and torsion angle, 2 and 4, of the console. Model curves 3 and 4 are calculated according to the analytical dependencies 3 and 4 of Table 3 with the parameters, respectively: $k_2^{-1} = 0.007$ and $k_3^{-1} = 0$; $k_1^{-1} = 0.004$. (b) Measurement 1 and approximation 2–4 data for the bending angle profile of the console. Model curves 2 and 3 correspond to the dependencies 1 and 2 of Table 3 with the parameters $k_2^{-1} = 0.007$ and $k_3^{-1} = 0$. The curve 4 data are the sum of the 2 and 3 model profiles data with weights of 0.85 and 0.15

Measured torsion angle profile, Fig. 5(a), is well described by the ψ linear relationship 4 of Table 3 with a single fitting parameter $\kappa_1^{-1}= 0.004$. The fitting parameter value, see the discussion of expressions (10) and (11), corresponds to the bending stiffness of the probe $k_{T1} \cong 12.75$ N/m. Using (10a), we can estimate the tip radius $R_{T1} \cong 8.5$ nm, that is consistent with the supplier information [19].

At the console edge, the buckling angle in Fig. 5(a) is positive, and closer to the console fixing line on the chip it is negative. A zero angle value and, as a consequence, the disappearance of the friction loop were observed at $\psi = 0.64$; at lower ψ, the friction loop was inverted. In Fig. 4(d), the signal 1 (2) first decreases (increases), and then goes horizontally; after inversion, the signal 1 (2) first increased (decreased) and then saturated. In Fig. 5(a) the measured profile is consistent with the dependence 3 of Table 3 with a single fitting parameter $\kappa_2^{-1}= 0.007$, whence using (10a) we get: $k_{T2} \cong 7.3$ N/m and $R_{T2} \cong 5$ nm. The value $\kappa_2\kappa_1^{-1}$ differs from unity and corresponds to the probe vertex ellipticity, compression factor $q = \sqrt{4/7} \cong 0.76$.

The friction loop, hysteresis, is also observed in the force curves, i.e. in the bending angle signal, Fig. 4(b). In contrast to Fig. 4(c) and 4(d), the signal, associated with the probe–sample clamping, goes almost horizontally.The disappearance and subsequent inversion of the friction loop in the force curves were detected at the same values, $\psi \leq 0.64$, as for the buckling angle signal in Fig. 4(c). This observation directly shows the contribution of the clamped state of the contact to the console bending angle value.

The fitting parameter $\kappa_2^{-1}= 0.007$ of the data in Fig. 5(a) was used to calculate the normalized sensitivity profiles for bending angle in cases of sliding and clamped contacts, dashed, 2, and dotted, 3, curves, Fig. 5(b). The experiment is better described by the sliding contact model. However, for $\psi \leq 0.64$ this model underestimates somewhat, and for $\psi \geq 0.64$ it overestimates the experiment. The best agreement with the experiment shows the combined model (the sliding and clamped contacts profiles with corresponding contributions of 0.85 and 0.15), a solid curve in Fig. 5(b).

Note that when $\kappa_i^{-1}= 0$ the difference between dependencies 1 and 2 in Table 3 is maximum. When the variable ψ is close to unity, the clamped contact leads to a significantly decreasing slope of the force curve in comparison with the sliding contact, see also Fig. 5(b). As a consequence, in the first case, the sample may appear softer in the AFM measurement than in the second one. In this regard, simple experimental criteria are very important in distinguishing the sliding contact from the clamped one.

Thus, for the studied soft ($k_C \ll 1$ N/m) contact cantilever, all the three measured profiles agree well with the calculations. In each case, the fitting procedure used only one parameter. It turned out that $\kappa_2^{-1} \ll 1$, and the parameter κ_3^{-1} was not required.

The calculations were also consistent with measurements performed on stiff ($k_C \gg 1$ N/m) cantilevers: NSG11 and HA_NC (NT–MDT SI), RTESP-150 (Bruker). The fitting parameters κ_1^{-1} and κ_2^{-1} increased, and κ_3^{-1} was also used. It was found that the probes on these cantilevers are characterized by $k_{Tl}\sim 10$ N/m, which is close to the result for the fpS10 cantilever.

We define the values k_C for which the γ-factor in (1a) is less than unity. Assuming that κ_{T3}^{-1} and λ^2 are small and therefore neglecting them, we have the following condition: $k_C > k_{T2}\,(1+3\lambda\cot\alpha_0\,)$. Taking for estimation $k_{T2}=k_{Tl}=10$ N/m and $\lambda = 1/10$, for the mounting angle of the cantilever holder $\alpha_0 = 12^\circ$, we get: $k_C > 24$ N/m. The RTESP-300 cantilever (Bruker) has $k_C = 40$ N/m; when neglecting the γ-factor the AFM overestimate k_S by 7 %. In the case of RTESP-525, $k_C = 200$ N/m, k_S is overestimated by 75 % (and more than three times if $\alpha_0 = 20^\circ$).

Unlike the soft cantilever, no friction loops were observed in the force curves measured with the stiff cantilevers. This is due to both the force sensitivity decrease and the diminishing difference between the normalized sensitivity profiles of the sliding and clamped contacts (1 and 2 in Table 3) with increasing κ_2^{-1} and κ_3^{-1}. To illustrate this, it is enough to consider the case of a very soft sample, when $\kappa_S^{-1} \gg 1$. Since then $\kappa_i^{-1} \cong \kappa_S^{-1}$, it can be shown that with growing κ_S^{-1} the dependence 1 converges to $\psi\,[(2-\psi)\cos\alpha_0 - 2\lambda\sin\alpha_0\,]\,\kappa_S$ and the dependence 2, to $\psi\,[(2-\psi)\cos\alpha_0 + \lambda\sin\alpha_0\,]\,\kappa_S$. Since λ is small, both limits are very close to: $\psi\,(2-\psi)\,\kappa_S\cos\alpha_0$.

4. Conclusion

The results of modeling the contact static interaction of the AFM cantilever with the sample are presented. An analytical model was created to calculate the distribution of deformation between the sample, the probe and the console. The model takes into account the following factors: the probe is clamped by the sample or slides along its surface, the geometric and mechanical characteristics of the sample and cantilever and their relative orientation. A new expression is proposed to determine the probe–sample stiffness. The expression that differs from the generally accepted one by a correction factor is proven to be used when the probe–sample contact is sliding. Normalized sensitivity profiles were simulated for the console bending and torsion angles as functions of three dimensional displacements of the mechanically isotropic sample.The profiles were also measured using AFM. Good agreement between measured and simulated data is demonstrated.

It is interesting to adapt the analytical model of this work to increase the accuracy of AFM studies of mechanically anisotropic samples, for example, when measuring the Young's modulus of suspended nanometer scale objects [25]. It is also important to extend the results of this work to ways for proving the sliding of the AFM probe along the sample when measuring force curves.

Acknowledgements

The author thanks his colleagues, Dr. M. M. Khalisov and Dr. A. A. Krasilin for constructive criticism of the manuscript.

Thus work is financially supported by the Russian Scientific Foundation, grant No. 19-13-00151.

References

[1] Binnig G., Quate C.F., Gerber Ch. Atomic Force Microscope. *Physical Review Letters*, 1986, **56** (9), P. 930–933.

[2] Scanning probe based apparatus and methods for low-force profiling of sample surfaces and detection and mapping of local mechanical and electromagnetic properties in non-resonant oscillatory mode. Patent Number: US 9,110,092 B1, USA. Date of Patent: Aug. 18, 2015. Int. Cl.: GOIN I3/6 (2006.01), G0IB 5/28 (2006.01). Inventors: Magonov S., Belikov S., Alexander J.D., Wall C.G., Leesment S., and Bykov V. Assignee: NT-MDT Development Inc., Tempe, AZ (US). Appl. No.: 14/247,041. Filed: Apr. 7, 2014. 10 Claims, 34 Drawing Sheets.

[3] Jumping probe microscope. Patent Number: 5,229,606, USA. Date of Patent: Jul. 20, 1993. Int. Cl.: H01J 37/26. Inventors: Elings V., Gurley J. Assignee: Digital Instruments, Inc., Santa Barbara, Calif. Appl. No.: 361,545. Filed: Jun. 5, 1989. 30 Claims, 4 Drawing Sheets.

[4] de Pablo P.J., Colchero J., Gomez-Herrero J., and Baro A.M. Jumping mode scanning force microscopy. *Applied Physics Letters*, 1998, **73** (22), P. 3300–3302.

[5] Kalinin A.S. PhD thesis. National Research Center "Kurchatov Institute", Moscow, 2017, 102 p.

[6] Sarid D. *Exploring scanning probe microscopy with MATHEMATICA*. 2nd ed. Weinheim: WILEY-VCH Verlag, 2007, 310 p.

[7] Ankudinov A.V., Khalisov M.M., et al. The Probe Length Effect on the Cantilever of an Atomic Force Microscope in Measuring the Mechanical Properties of Living Neurons. *Tech. Phys. Lett.*, 2018, **44** (8), P. 671–674.

[8] Alexander S., Hellemans L., et al. An atomicresolution atomicforce microscope implemented using an optical lever. *J. of Appl. Phys.*, 1989, **65** (1), P. 164–167.

[9] Fujisawa S., Ohta M., et al. Difference between the forces measured by an optical lever deflection and by an optical interferometer in an atomic force microscope. *Rev. Sci. Instrum*, 1994, **65** (3), P. 644–647.

[10] Kawakatsu H., Bleuler H., Saito T., Hiroshi K. Dual Optical Levers for Atomic Force Microscopy. *Jpn. J. Appl. Phys.*, 1995, **34**, 1 (6B), P. 3400–3402.

[11] Asylum Research Quantifies the "Last Axis" in Atomic Force Microscopy, 2018, `URL: https://www.oxford-instruments.com`.

[12] Labuda A., Proksch R. Quantitative measurements of electromechanical response with a combined optical beam and interferometric atomic force microscope. *Appl. Phys. Lett.*, 2015, **106** (25), 253103.

[13] Mironov V.L. *Fundamentals of the Scanning Probe Microscopy*. The Russian Academy of Sciences Institute of Physics of Microsructures, Nizhniy Novgorod, 2004, 97 p.

[14] `URL: https://www.ntmdt-si.ru/resources/spm-theory/theoretical-background-of-spm`.

[15] Landau L.D., Lifshitz E.M. *Theory of Elasticity*. Oxford, Pergamon Press Ltd., 1970, 177 p.

[16] Dunaevskiy M., Geydt P., et al. Youngs Modulus of Wurtzite and Zinc Blende InP Nanowires. *Nano Letters*, 2017, **17** (6), P. 3441–3446.

[17] Popov V.L., Heß M., Willert E. Handbook of Contact Mechanics. Exact Solutions of Axisymmetric Contact Problems, 2019. Translation from the German Language edition: Popov et al: Handbuch der Kontaktmechanik. Springer-Verlag GmbH Deutschland, 2018, 347 p.

[18] Heim L.-O., Kappl M., Butt H.-J. Tilt of Atomic Force Microscope Cantilevers: Effect on Spring Constant and Adhesion Measurements. *Langmuir*, 2004, **20**, P. 2760–2764.

[19] Hutter J.L. Comment on Tilt of Atomic Force Microscope Cantilevers: Effect on Spring Constant and Adhesion Measurements. *Langmuir*, 2005, **21**, P. 2630–2632.

[20] Timoshchuk K.I., Khalisov M.M., et al. Mechanical characteristics of intact fibroblasts studied by atomic force microscopy. *Tech. Phys. Lett.*, 2019, **45** (9), P. 947–950.

[21] Bhushan B. (Ed.) *Nanotribology and Nanomechanics. An Introduction*. Springer-Verlag, Berlin, Heidelberg, 2005, 1148 p.

[22] `URL: http://nanoprobes.aist-nt.com`.

[23] Sader J.E., Chon J.W.M., Mulvaney P. Calibration of rectangular atomic force microscope cantilever. *Rev. Sci. Instrum.*, 1999, **70**, P. 3967–3969.

[24] Mate C.M., McClelland G.M., Erlandsson R., Chiang S. Atomic-scale friction of a tungsten tip on a graphite surface. *Phys. Rev. Lett.*, 1987, **59**, P. 1942–1945.

[25] Salvetat J.-P., Briggs G.A.D., et al. Elastic and Shear Moduli of Single-Walled Carbon Nanotube Ropes. *Phys. Rev. Lett.*, 1999, **82**, P. 944–947.

NANOSYSTEMS: PHYSICS, CHEMISTRY, MATHEMATICS, 2019, 10 (6), P. 654–665

Phosphors with different morphology, formed under hydrothermal conditions on the basis of ZrO_2:Eu^{3+} nanocrystallites

A. N.Bugrov[1,2], R. Yu.Smyslov[1,3], T. V. Khamova[4], D. A.Kirilenko[5,6], I. A.Rodionov[7]

[1]Institute of Macromolecular Compounds RAS, Bolshoy pr. 31, 199004 St. Petersburg, Russia
[2]Saint Petersburg Electrotechnical University "LETI", ul. Professora Popova 5, 197376 St. Petersburg, Russia
[3]Peter the Great St. Petersburg Polytechnic University, Polytechnicheskaya ul. 29, 195251 St. Petersburg, Russia
[4]Grebenshchikov Institute of Silicate Chemistry RAS, Makarova nab. 2., letter B, 199034 St. Petersburg, Russia
[5]Ioffe Institute RAS, Politekhnicheskaya ul. 26, 194021 St. Petersburg, Russia
[6]ITMO University, Kronverskii avenue 49, 197101 St. Petersburg, Russia
[7]Institute of Chemistry, Saint Petersburg State University,
Universitetskii prospect 26, Petergof, 198504 St. Petersburg, Russia

alexander.n.bugrov@gmail.com, urs1968@gmail.com, tamarakhamova@gmail.com,
demid.kirilenko@mail.ioffe.ru, i.rodionov@spbu.ru

PACS 78.67. n; 78.67.Bf **DOI 10.17586/2220-8054-2019-10-6-654-665**

Eu^{3+}-doped ZrO_2 nanostructures in the form of rods, stars, and hollow spheres were prepared by varying hydrothermal conditions. X-ray diffraction, transmission electron microscopy, ultraviolet-visible diffuse reflection spectroscopy, a low-temperature nitrogen adsorption method, Raman spectroscopy and photoluminescence spectra were used to characterize the polymorph modification, surface and optical properties of the $Zr_{0.98}Eu_{0.02}O_2$ nanophosphors. The Eu^{3+} content in a zirconia monoclinic lattice, remained constant for all types of obtained nanostructures in order to reveal the morphology influence on the efficiency of electronic excitation energy transfer from the host matrix to photoactive centers. The decrease of the average size of the coherent scattering regions in the series rods → stars → hollow spheres, is associated with increasing the specific surface area values. At that, in the photoluminescence spectrum, the splitting of the sublevels associated with the monoclinic lattice $^5D_0 \to {}^7F_1$ disappears.

Keywords: hydrothermal synthesis, monoclinic zirconia, europium, solid solution, rods, stars, hollow spheres, nanocrystals, energy gap, photoluminescence, lifetime.

Received: 17 June 2019

1. Introduction

Currently, metal-oxide semiconductors doped with lanthanide ions (Ln) are widely used in solid-state lighting technologies in the manufacture of LEDs, lasers, field emission and vacuum fluorescence displays, as well as in the medical field for the visualization of drug delivery systems and monitoring changes in implant structure [1–3].

The introduction of trivalent lanthanide ions into the crystal structure of semiconductor oxide leads to weakening of the selection rules for radiative transitions, which is accompanied by splitting of the 4f energy levels [4, 5]. In this case, the prohibition of intra-configuration transitions is weakened for Ln^{3+}, since such transitions can be partially resolved by vibronic interaction or by mixing higher configurations into 4f wave functions due to the crystal field effect. However, the luminescence lifetime is usually quite large compared to radiative recombination from other types of excited states [6, 7]. Such phosphors are characterized by narrow emission lines, high color purity, large anti-Stokes shifts, an acceptable quantum yield, and a significant luminescence lifetime [8–10]. Such signs are determined by the efficiency of electron excitation energy transfer from the host matrix to photoactive centers, which is determined by the band gap, the type of crystal structure, the size and morphology of the metal-oxide semiconductor particles, and also the local environment of Ln^{3+} ions in the lattice [11, 12]. For instance, the trivalent europium ion (Eu^{3+}) can be used as a spectroscopic probe for site symmetry determination [13].

Among p-type semiconductors, zirconia is the optimal optical medium for lanthanide ions, since it has photochemical stability, a high refractive index, a large band gap, transparency in the visible and near infrared regions of the spectrum, and low phonon energy, which helps to reduce the probability of nonradiative transitions due to multiphonon relaxation [14–16]. In turn, europium (III) ions possess intense luminescence in the red region of the visible spectrum and have an advantage over other lanthanides with an even number of 4f electrons, since their initial transition levels in both the absorption spectrum and the luminescence spectrum are non-degenerate ($J = 0$), which makes absorption and luminescence spectra interpretation easy. In addition, the contribution to the integrated luminescence intensity of the hypersensitive $^5D_0 \to {}^7F_2$ transition can be used to determine whether Eu^{3+} is located in the centers of symmetry of the crystal matrix [6].

Precipitation methods [17], combustion [18], sol-gel technology [19], template synthesis [20], hydrothermal treatment [21], aerosol pyrolysis [22], anodizing [23] and impregnation [24] are used to obtain nanostructures of various morphology based on ZrO_2 doped with europium (III) ions. Among the above synthetic approaches, the hydrothermal method is the most universal, since it allows one to obtain nanomaterials with a narrow particle size distribution, high crystallinity, controlled by morphology and microstructure. Varying the pH of the hydrothermal medium and introducing various mineralizers or surfactants can limit crystallite growth along certain crystallographic directions, contributing to the formation of nanostructures of different morphology based on monoclinic zirconia [25–27]. ZrO_2:Eu^{3+} nanophosphors with a baddeleyite structure, as far as we know, were obtained only in the form of rods under hydrothermal conditions. For example, Chen and colleagues obtained 1D nanostructures based on the $Zr_{0.98}Eu_{0.02}O_2$ solid solution by hydrothermal treatment a mixture of zirconium and europium hydroxides in the presence of cetyltrimethylammonium bromide [28].

The aim of this work was to synthesize nanostructures with different morphology based on monoclinic zirconia doped with Eu^{3+} by varying the hydrothermal treatment conditions. After that, it was necessary to study the influence of size, structural and surface characteristics of the obtained nanostructures (rods, stars, hollow spheres) on their optical and photoluminescent properties (excitation and emission spectrum profile, luminescence lifetime).

2. Experimental part

In this work, we synthesized nanorods, nanostars and hollow spheres of the ZrO_2–2 mol.% $EuO_{1.5}$ composition, which are represented by the monoclinic zirconia phase in order to study the features of their photoluminescence.

To synthesize nanorods, 2.54 g of $ZrOCl_2 \cdot 8H_2O$ and 0.06 g of $EuCl_3 \cdot 6H_2O$ were dis-solved in 15 ml of distilled water, after that a mixture of hydroxides of the corresponding metals was precipitated with continuous stirring, dropwise adding 5 M NaOH solution. The obtained precipitate was dehydrated under hydrothermal conditions at 240 °C and 15 MPa for 24 hours.

Four-pointed nanostars of a given composition were also formed from solutions of zirconium and europium chlorides in a hydrothermal medium under the conditions presented in [29].

In the case of hollow spheres, 1.22 g of zirconyl chloride and 0.03 g of europium (III) chloride were dissolved in 60 ml of a mixture of ethanol-hydrochloric acid, taken in a ratio of 3 to 2. Then, 0.75 g urea was added to the solution, and after its dissolution, all components were transferred to an autoclave. Subsequent hydrothermal treatment was carried out at a temperature of 160 °C, a pressure of 15 MPa and an isothermal exposure time of 24 hours.

At the end of hydrothermal synthesis, all the obtained suspensions of the above-described nanostructures were repeatedly washed with ethanol by centrifugation (8000 rpm) and dried in air to constant weight at 80 °C.

The elemental compositions of synthesized nanostructures were determined using a VEGA 3 SBH scanning electron microscope manufactured by Tescan (Czech Republic) with the Oxford Instruments AZtecOne Go X-ray energy dispersive microanalysis system.

X-ray diffraction (XRD) analysis of Eu^{3+}-doped ZrO_2 nanorods, nanostars and hollow spheres was performed using a Rigaku SmartLab diffractometer (Cu Kα radiation, Tokyo, Japan). The XRD patterns were recorded at a tube voltage of 40 kV, tube current of 40 mA, applying a scan rate of 0.5 °/min in a range of 2θ angles from 10 to 90°. The determination of zirconia crystalline phases was carried out in Crystallographica Search-Match software by comparing our experimental data with powder diffraction files from the ASTM database. The average size of the coherent scattering regions was calculated from XRD line broadening of ZrO_2–2 mol.% $EuO_{1.5}$ nanostructures in the PD-Win 4.0 program complex using the Scherrer equation.

The size, shape and phase composition of the ZrO_2:Eu^{3+} nanoaggregates and crystallites forming them were established using a JEM-2100F transmission electron microscope manufactured by JEOL (Tokyo, Japan) at an acceleration voltage of 90 kV.

The specific surface area of powders of the ZrO_2–2 mol.% $EuO_{1.5}$ composition in the form of rods, four-pointed stars and hollow spheres was measured by the low-temperature nitrogen adsorption method using a QuantaChrome Nova 4200V analyzer. Samples were degassed at 150 °C under vacuum for 16 hours before measurement. The specific surface area (S_{BET}) of samples was calculated based on the experimental data using the models: Brunauer–Emmett–Teller (BET) at 7 points in the range of partial pressures of nitrogen $P/P_0 = 0.07 \div 0.25$ and Langmuir. The pore size distribution was calculated based on nitrogen adsorption–desorption isotherms according to the Barrett–Joyner–Halenda (BJH) method.

Raman spectra were recorded in the backscattering geometry using a Jobin Yvon T64000 triple monochromator equipped with a liquid N_2-cooled charge-coupled device detector. The excitation wavelength λ was 488 nm from an Ar^+ laser with a typical laser power of $\sim$ 1 mW.

The photoluminescence emission spectra were recorded using a Horiba LabRAM HR Evolution system equipped with a He–Cd excitation laser emitting at 325 nm with a maximum power of 1 mW. Photoluminescence decay and excitation spectra were measured using the luminescence spectrophotometer LS-100 (PTIR®, Canada).

The optical absorption edge energy of nanostructures based on zirconia was determined using diffuse reflectance spectra (Shimadzu UV-2550 spectrophotometer equipped with an ISR-2200 integrating sphere) by the standard procedure from the cross point of linear sections of the Schuster–Kubelka–Munk function plot in the coordinates $(F(R) \times h\nu)^{1/2} = f(h\nu)$.

3. Results and discussion

The different morphology nanostructures based on ZrO_2 prepared in this study contained 2 at.% Eu^{3+} according to energy dispersive X-ray (EDX) spectroscopy (Table 1).

TABLE 1. EDX-analysis data of Eu^{3+}-doped ZrO_2 nanostructures with different morphology

Morphology	Zr	Eu	Hf	Na	Cl
	at., %				
Nanorods	96.8	2.1	0.6	0.5	—
Nanostars	96.7	2.0	0.6	0.7	—
Hollow spheres	96.1	2.1	0.8	—	1.0
	wt., %				
Nanorods	95.3	3.4	1.2	0.1	—
Nanostars	95.4	3.2	1.2	0.2	—
Hollow spheres	94.6	3.5	1.5	—	0.4

Phosphors in the form of nanorods were formed in a strongly alkaline medium under hydrothermal treatment of a $ZrO(OH)_2$–$Eu(OH)_3$ mixture precipitated from solutions of their chlorides. Qualitative phase analysis based on XRD of the ZrO_2–2 mol.% $EuO_{1.5}$ one-dimensional nanostructures using the PDWin 4.0 and Crystallographica Search-Match software packages showed their greatest correspondence to the baddeleyite structure (Card No. 24-1165 according to the ASTM database [30], Fig. 1, pattern 1). The average size of coherent scattering regions calculated by the Scherrer equation was 30 ± 5 nm. The length of the nanorods was about 150 nm, and the width was 50 nm, according to TEM micrographs (Fig. 2a, line 1). In addition to twin reflections of monoclinic (m) ZrO_2–2 mol.% $EuO_{1.5}$ rods elongated along the (100) plane, concentric rings indicating the presence of small crystallites with a tetragonal (t) structure were also observed in the electron microdiffraction image (Fig. 2b, line 1). Apparently, initially formed under hydrothermal conditions Eu^{3+}-stabilized t-ZrO_2 nanocrystals with an average size of $\sim 5 \pm 1$ nm (Fig. 3) gradually dissolve at high pH medium values and recrystallize along the crystallographic direction (100) with the formation of monoclinic rice-like structures.

Hydrothermal synthesis of ZrO_2–2 mol.% $EuO_{1.5}$ nanostars from the same precursors was carried out in the presence of sodium acetate. Its CH_3COO^- ions adsorbed on the surface of the germinal centers promoted the subsequent crystallization of zirconia along the direction perpendicular to the (101) planes. The resulting structures with a size of about 100 nm (Fig. 2a, line 2) have the shape of four-pointed stars with numerous outgrowth 7 nm wide according to TEM data. An electron diffraction pattern shows the presence of m-ZrO_2 with multiple twinning along the (100) plane (Fig. 2b, line 2). The observed diffraction maxima in the XRD pattern of ZrO_2–2 mol.% $EuO_{1.5}$ nanostars also refer exclusively to the monoclinic phase of zirconia, and the average size of the coherent scattering regions (CSR) for this sample is 12 ± 2 nm according to calculations (Fig. 1, pattern 2).

High-temperature hydrolysis of zirconyl and europium chlorides in the presence of urea produced nanostructures in the form of hollow microspheres (Fig. 2a, line 3) using a mixture of ethanol and hydrochloric acid in a ratio of 3:2 as a hydrothermal medium. In this case, the formation of the observed structures under hydrothermal conditions occurs by the mechanism of emulsion template synthesis. Ethanol in the presence of concentrated hydrochloric acid dehydrates with increasing temperature to form diethyl ether, which, due to its low solubility in water, can exist as droplets of oil in this solution [31]. The urea present in the initial mixture slowly reacts with water, forming NH_4OH

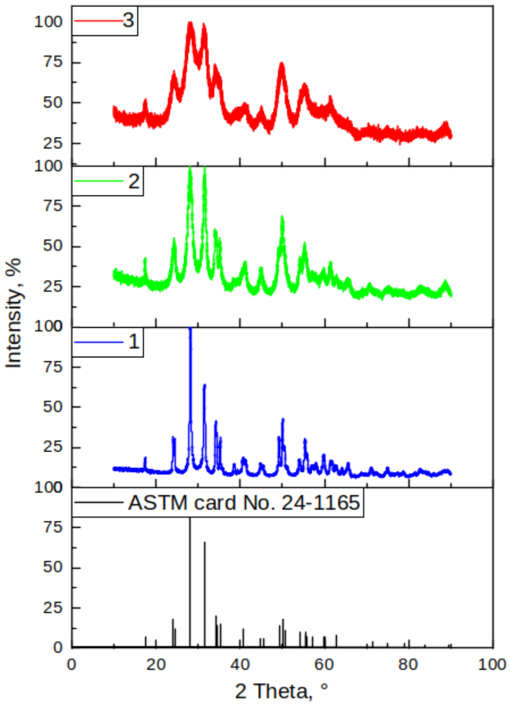

FIG. 1. XRD patterns of ZrO_2–2 mol.% $EuO_{1.5}$ nanostructures in the form of nanorods (1), nanostars (2) and hollow spheres (3)

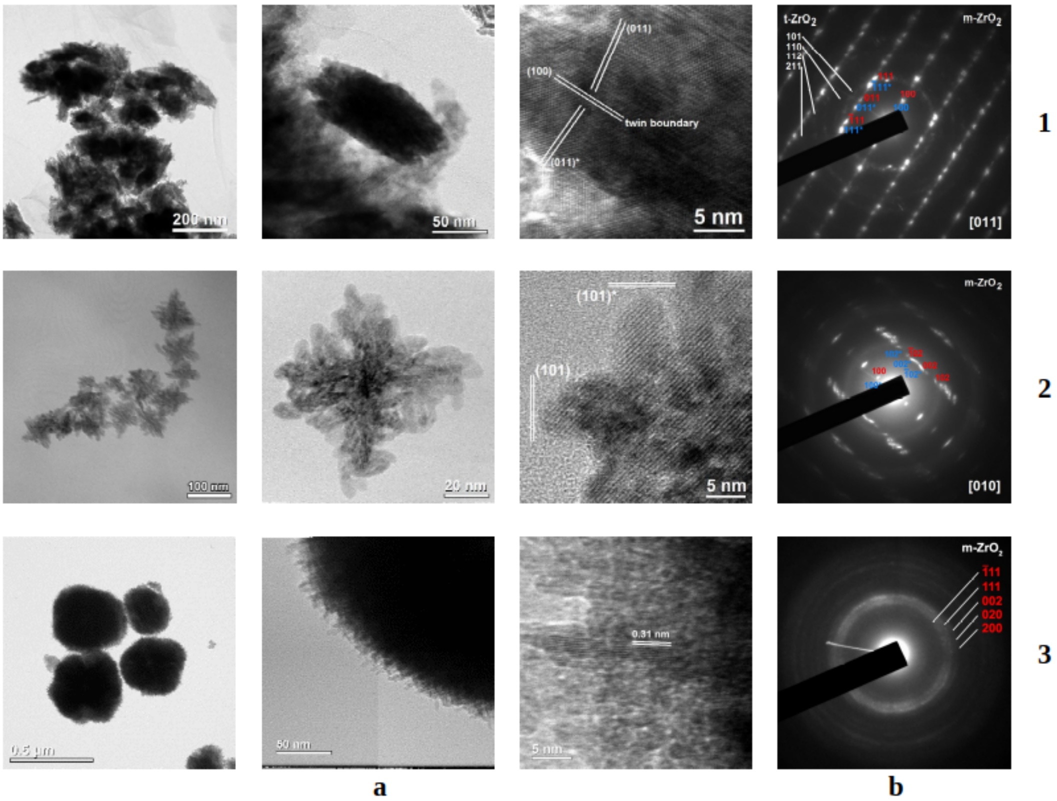

FIG. 2. TEM micrographs (a) and electron microdiffraction patterns (b) of ZrO_2–2 mol.% $EuO_{1.5}$ nanostructures in the form of nanorods (1), nanostars (2) and hollow spheres (3)

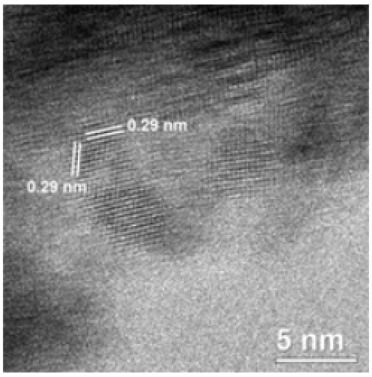

FIG. 3. TEM micrographs of quasispherical tetragonal zirconia nanoparticles of which rice-like ZrO_2–2 mol.% $EuO_{1.5}$ structures subsequently form under hydrothermal conditions

and CO_2, which leads to an increase in pH and, as a result, hydrolysis of $ZrOCl_2$ and $EuCl_3$ at the "oil drop – solution" interface. A shell of ZrO_2–2 mol.% $EuO_{1.5}$ crystallites is formed on the surface of ether drops in the process of hydroxide dehydration and subsequent isothermal exposure. In accordance with the powder XRD data, the hollow inorganic structures obtained in this way are an assembly of monoclinic zirconia crystallites with an average size of 5 ± 1 nm (Fig. 1, pattern 3). TEM images of microspheres show nanowires with a diameter of about 5 nm, assembled into spherical aggregates of submicron size ($\sim$ 400 nm, Fig. 2a, line 3). The structure of the aggregates corresponds to the monoclinic phase of zirconia (Fig. 2b, line 3).

According to the results of low-temperature nitrogen adsorption, nanocrystalline ZrO_2–2 mol.% $EuO_{1.5}$ powders of rods, stars, and hollow spheres are characterized by the specific surface area of 19.1, 92.3 and 151.1 m^2/g, respectively (Table 2). At the same time, the BET constant values for samples of nanoparticles collected in the form of rods and hollow spheres are equal to 508 and 745, respectively. This fact is indicative of the presence of a significant amount of micropores in these powders. Based on the foregoing, the assessment of the specific surface area for ZrO_2–2 mol.% $EuO_{1.5}$ powders with different morphology nanostructures was also carried out using the Langmuir model operating in the limit of monomolecular adsorption, i.e. adsorption on the surface of micropores (Table 2).

TABLE 2. The structure parameters determined using low-temperature nitrogen adsorption for powders consisting of ZrO_2–2 mol.% $EuO_{1.5}$ nanoaggregates with different morphology

Morphology	S_{BET}, m^2/g	$S_{Langmuir}$, m^2/g	D_1, nm	D_2, nm	$V_{pore}{}^*$, cm^3/g
Nanorods	19.1 ± 0.2	32	2.6	42.2	0.35
Nanostars	92.3 ± 1.8	—	2.2	13.4	0.22
Hollow spheres	151.1 ± 1.5	223.9	—	—	0.14

* The specific pore volume is determined by the maximum filling ($P/P_0 = 0.99$).

According to Fig. 4, the full adsorption-desorption isotherms for these powders substantially depend on their morphology. For example, the full isotherm for a powder consisting of ZrO_2–2 mol.% $EuO_{1.5}$ nanorods is close to type II, which is inherent in non-porous and macroporous samples. At the same time, the weak hysteresis and a high BET constant indicate the presence of a certain amount of micro and mesopores in this sample. This hysteresis can be classified as type H1 according to IUPAC, when the material has cylindrical pores open on both sides. Thus, the full isotherm can be attributed to the combined type (Fig. 4, isotherm 1).

The full isotherm of powder consisting of ZrO_2–2 mol.% $EuO_{1.5}$ nanostars clearly belongs to type IV, which is typical for mesoporous materials. Adsorption and capillary condensation can occur in the pores of such materials, which leads to the appearance of hysteresis between the adsorption–desorption isotherms (Fig. 4, isotherm 2). The course of the capillary-condensation hysteresis loop for a given nanopowder according to the IUPAC can be classified as type H2, which indicates the presence of bottle-shaped mesopores in it.

Finally, the full isotherm for a powder consisting of ZrO_2–2 mol.% $EuO_{1.5}$ hollow spheres is close to type I, which is mainly fixed in microporous samples (Fig. 4, isotherm 3). Moreover, the presence of a weakly expressed loop of capillary-condensation hysteresis on the full isotherm confirms the presence of a certain amount of mesopores

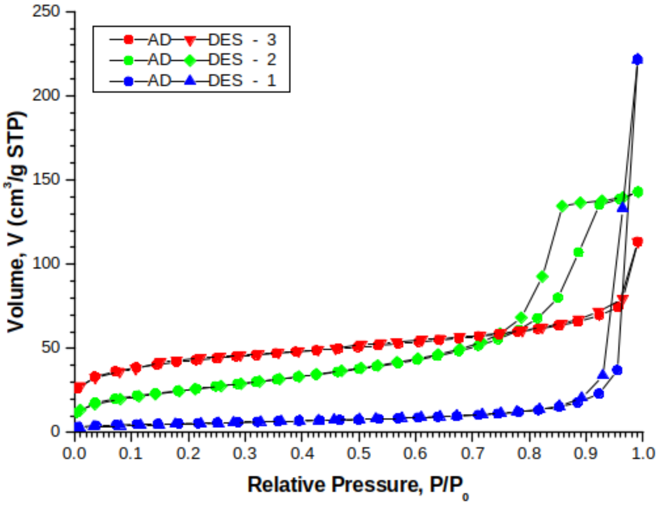

FIG. 4. Adsorption-desorption isotherms of powders consisting of ZrO_2–2 mol.% $EuO_{1.5}$ nanostructures with different morphology: rods (1), stars (2), hollow spheres (3)

in this sample. This type is the H4 hysteresis according to the IUPAC classification, which is characteristic of pore slit-like form.

Pore size distributions calculated for the desorption branch according to the BJH algorithm for powders consisting of ZrO_2–2 mol.% $EuO_{1.5}$ nanostructures with different morphology are shown in Fig. 5. Obviously, the porosity of these nanopowders substantially depends on morphology. A bimodal pore size distribution with maxima in the micro D_1 and mesopore D_2 regions is characteristic of powders containing nanostructures in the form of stars and rods (Table 2), respectively. In the case of the sample consisting of ZrO_2–2 mol.% $EuO_{1.5}$ hollow spheres, a uniformly decreasing pore size distribution in the range from 1.5 to 40 nm is observed, which confirms the presence of both micro- and mesopores in it.

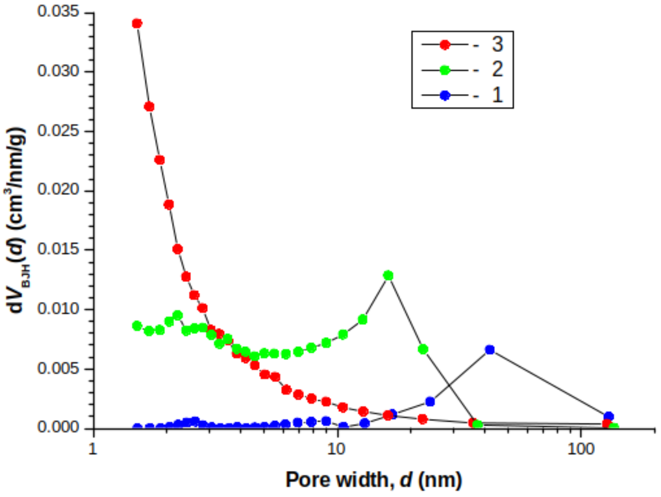

FIG. 5. Pore size distributions calculated according to the BJH algorithm for powders consisting of ZrO_2–2 mol.% $EuO_{1.5}$ nanostructures with different morphology: rods (1), stars (2), hollow spheres (3)

An intense peak at 614 nm is observed in the luminescence spectra of ZrO_2–2 mol.% $EuO_{1.5}$ nanostructures with different morphology and there is no component of the electric dipole transition in the region of 606 nm. This indicates the absence of cubic and tetragonal polymorphic modifications and localization of Eu^{3+} in the less symmetrical environment of the m-ZrO_2 for the synthesized phosphors (Fig. 6a). With an increase in the resolution of the luminescent equipment, one can see narrow peaks of fine splitting upon excitation at 325 nm not only in the spectral term $^7F_2$, but also in $^7F_4$ for Eu^{3+}. Such a splitting pattern allows us to conclude that the monoclinic phase is exceptionally prevalent for nanorods. At the same time, for nanostars and hollow spheres, the order of the monoclinic phase is disrupted due to internal stresses and a decrease in the size of crystallites. A similar violation of the long-range order also manifests itself in Raman spectra (Fig. 7) in the form of the contribution of the diffuse band in the range 400 – 700 cm^{-1}. Because of this, the fine splitting between 614 and 625 nm disappears in the luminescence spectra, which leads to an increase in the contribution to the luminescence band at 616 nm, as well as to the disappearance of the peak at 711 nm and a predominance of the contribution at 700 nm (compare spectrum 1 with spectra 2 and 3 in Fig. 6a).

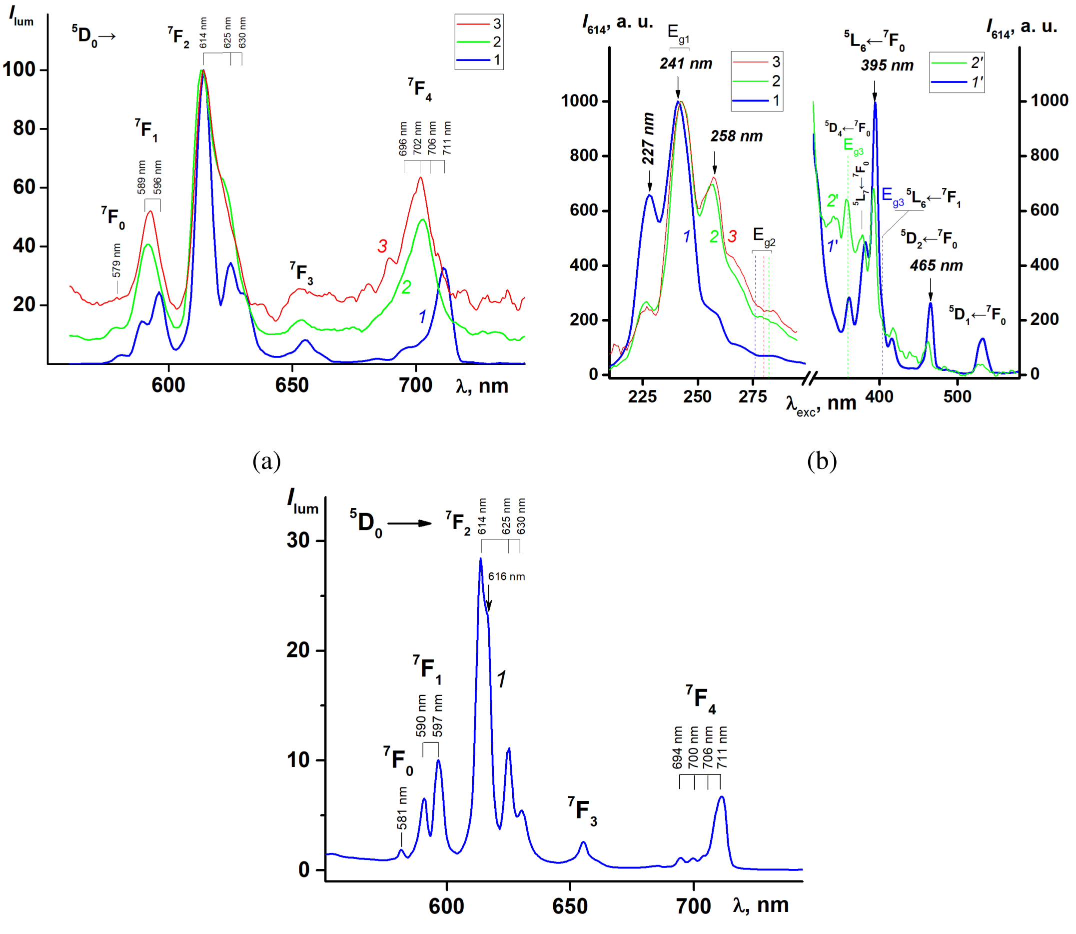

(a) (b)

(c)

FIG. 6. Emission spectra (a, c) and excitation spectra (b) of luminescence for nanorods (1, 1'), nanostars (2, 2'), and hollow spheres (3) of the ZrO_2–2 mol.% $EuO_{1.5}$, normalized at 614 and 241 nm, respectively. Excitation 242 (a) and 325 nm (c)

The luminescence excitation spectra of europium (III) ions in the structure of zirconia nanostars and hollow spheres are identical (Fig. 6b, spectra 2 and 3). In the case of nanorods, a more efficient absorption of electronic excitation energy is recorded in the region of hard ultraviolet, especially at wavelengths of 227 and 241 nm (Fig. 6b, spectrum 1). This excitation band with a maximum peak at 241 nm and several additional local extrema at 227 and 258 nm corresponds to the O^{2-}–Eu^{3+} charge transfer resulting from electron transitions from the 2p orbital of O^{2-} to the 4f orbital of Eu^{3+}.

In the Raman spectrum for ZrO_2–2 mol.% $EuO_{1.5}$ nanorods, the characteristic peaks correspond to the monoclinic crystal lattice at 178, 189, 305, 380, 474, 537, 556, 612 and 631 cm^{-1} (Fig. 7, spectrum 1). For nanostars and hollow spheres in the Raman spectra region of 400 – 700 cm^{-1}, a diffuse scattering band is detected, which is associated with the disappearance of long-range order due to internal stresses and twinning. A similar effect of the disappearance of the long-range order of the monoclinic phase was also found in the luminescence spectra (see Fig. 6 and in the text above).

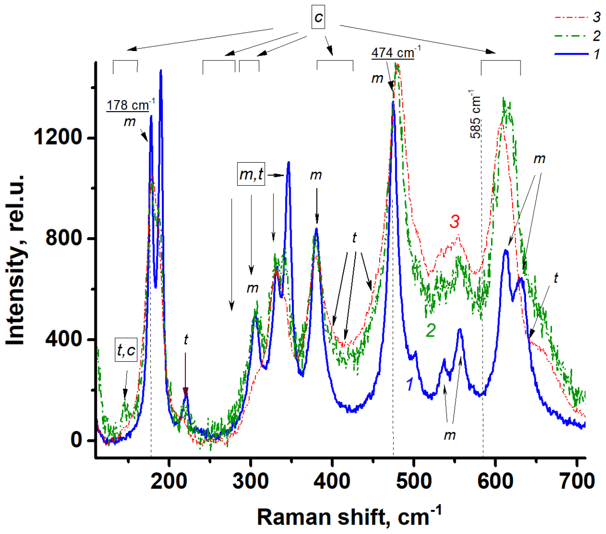

FIG. 7. Raman spectra for nanorods (1), nanostars (2) and hollow spheres (3) of ZrO_2–2 mol.% $EuO_{1.5}$, normalized at 474 cm^{-1}

Based on the diffuse reflectance spectra $R(\lambda)$ in the visible and ultraviolet range from 1.5 to 6 eV, one calculated the Schuster–Kubelka–Munk (SKM) or remission function [32]:

$$F\left(R_\infty\left(\lambda\right)\right) = \frac{\left(1 - R_\infty(\lambda)\right)^2}{2R_\infty(\lambda)} = \frac{K}{S} = \frac{2.303\varepsilon C}{S}, \qquad (1)$$

where K is the absorption coefficient (twice the Beer's law absorption coefficient); S is twice the scattering coefficient of the sample; ε is the absorptivity, and C is the analyte concentration.

Using the Tauc plot of $\left(F\left(R_\infty\right)h\nu\right)^{1/\eta}$ versus energy, $h\nu$, one estimated the energy gap, E_g, between the conduction band and the valence one in $Zr_{0.98}Eu_{0.02}O_{1.99}$ nanoparticles (Fig. 8).

In the region of the energy obtained from 2 to 6 eV, the indirect allowed absorption transitions turned out to manifest themselves because there are linear approximations at $\eta = 2$ for all the cases under investigation [33]. At that, the E_g values of the studied nanostructures are found from 3.07 to 5.13 eV (Table 3), which is consistent with work [34]. Analysis of the Tauc spectra showed that the widest absorption edge energy (E_{g1}) of *ca.* 5.1 eV clearly manifests itself for all the studied zirconia nanostructures containing Eu^{3+} [35]. There is no dependence of E_{g1} on the morphology of the nanoparticles. The absorption connected with it corresponds in the luminescence excitation spectra to a maximum of 241 nm (compare Fig. 6b and Table 3).

TABLE 3. Energy gap parameters as obtained from Tauc plots for $Zr_{0.98}Eu_{0.02}O_{1.99}$ nanoparticles with a different morphology

Morphology	Coherent scattering region, nm	Energy gap parameters, eV (wavelength, nm)[1]		
		$E_{g1}(\lambda_1)$	$E_{g2}(\lambda_2)$	$E_{g3}(\lambda_3)$
Nanorods	30 ± 5	5.10 (243)	4.49 (276)	3.07 (404)
Nanostars	12 ± 2	5.11 (243)	4.39 (282)	3.42 (362)
Hollow spheres	5 ± 1	5.13 (242)	4.42 (280)	3.57 (347)

[1] One uses the relationship between energy in eV and the corresponding wavelength in nm as $E \cdot \lambda = 1240$ eV·nm.

The presence in the band of the PL excitation spectrum for all synthesized nanostructural forms of maxima at 227 and 240 – 243 nm, as well as the E_{g1} values of 5.10 – 5.13 eV indicate the existence of inter-configuration transitions in m-ZrO_2 [36]. Besides, the largest contribution occurs at 258 nm for nanostars and hollow spheres

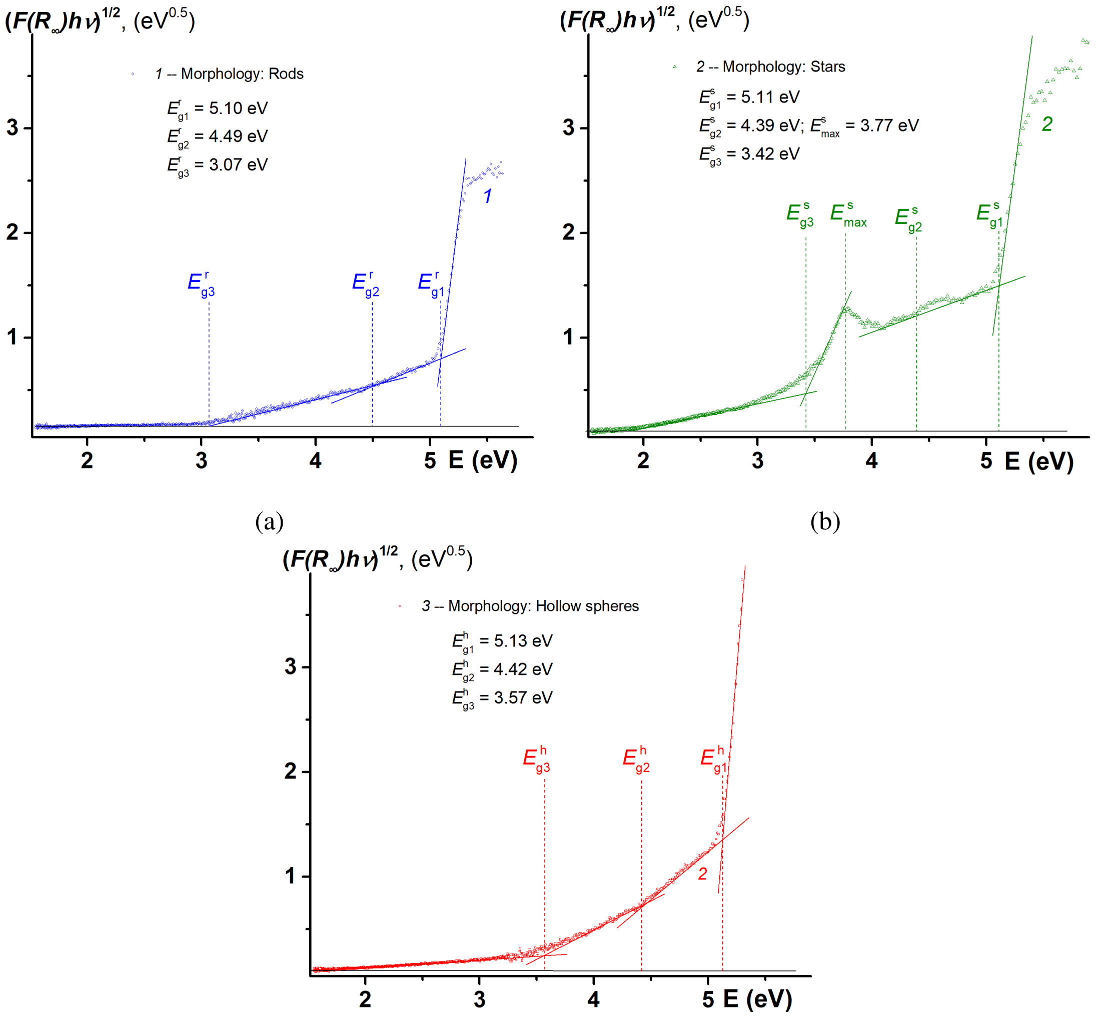

(a) (b)

(c)

FIG. 8. Tauc plot spectra for nanorods (a), nanostars (b) and hollow nanospheres (c) of ZrO_2–2 mol.% $EuO_{1.5}$

(compare normalized excitation spectra in Fig. 6b), which designates charge transfer ($Eu^{3+} \leftarrow O^{2-}$) for the type of Zr–O bond of 2.1297 Å in a monoclinic cell [35]. This indicates a perfect (with a large CSR) monoclinic phase in this case and is confirmed by other methods (XRD and RS). A change in the monoclinic modification and a decrease in its CSR (Table 3) is indicated by a shift in the excitation spectra from 241 to 243 nm during the transition to nanostars and hollow spheres. In addition, a diffuse band appears in the Raman spectra and the clear splitting of the monoclinic phase at 178 cm^{-1} disappears. As seen above, one can assume the formation of t,c-phase crystallites with a small CSR. The manifestation of the value of $E_{\max}$ 3.77 eV (Fig. 8b) for nanostars may indicate a low coordination of the bond with the t-ZrO_2 surface ($Zr^{4+} \leftarrow O^{2-}$) [36].

The decay of PL intensity ($I_{lum}(t)$) for nanoparticles can be approximated by a model of the dual exponential function:

$$I_{lum}(t) = A_1 \cdot \exp(-t/\tau_{PL1}) + A_2 \cdot \exp(-t/\tau_{PL2}) + B, \tag{2}$$

where τ_{PL1} and τ_{PL2} are the PL lifetime for the first and second emission processes; A_1 and A_2 are the first and second pre-exponential factors. Term B is a background contribution. Based on the obtained τ_{PL} and their contributions in the two-exponential approximation (Table 4), the weighted-average luminescence lifetimes, τ_{PLw}, are calculated according to the equation:

$$\tau_{PLw} = \frac{\sum_{i=1}^{2} A_i \tau_{PLi}^2}{\sum_{i=1}^{2} A_i \tau_{PLi}}. \tag{3}$$

TABLE 4. Photoluminescence lifetimes[1] of $Zr_{0.98}Eu_{0.02}O_{1.99}$ nanoparticles of a different morphology

Morphology	A_1	τ_{PL1}, ms	$A_2 = 1 - A_1$	τ_{PL2}, ms	χ^2	τ_{PLw}, ms[2]	DWP[3]
Nanorods	0.452(7)	0.455(8)	0.548(8)	1.31(1)	2.147	1.120	0.518
Nanostars	0.85(2)	0.248(7)	0.15(1)	0.69(6)	0.610	0.394	1.577
Hollow spheres	0.71(6)	0.064(9)	0.29(2)	0.49(3)	1.05	0.387	1.769

[1] PL lifetimes were fitted on the basis of the dual exponent decay (see Eq. 2) in minimizing a reduced χ^2-statistics.

[2] Note the mean-weighted PL lifetimes, τ_{PLw}, calculated upon Eq. 3.

[3] Darbin–Watson statistic parameter [37].

According to the data shown in Table 4, in a two-exponential approach both PL lifetimes τ_{PL1} and τ_{PL2} increase depending on morphology in series: hollow spheres to nanorods. Moreover, for the morphology of nanorods in the Raman spectra, a characteristic splitting of peaks corresponding to the monoclinic structure at 178 and 189 cm^{-1} is observed (Fig. 7). In the photoluminescence spectra for nanorods with Eu^{3+}, a fine splitting characteristic of m-ZrO_2 is observed in the spectral terms $^7F_2$ at 614, 625, 630 nm and $^7F_4$ at 694, 700, 706 and 711 nm (Fig. 6c). In these spectral terms, a characteristic intensity distribution pattern is observed with a maximum contribution at 614 nm in $^7F_2$ and 711 nm in $^7F_4$. The contributions to $^7F_4$ at 694, 700, and 706 nm are insignificant. In the $^7F_2$ term, the maximum of 614 nm has a shoulder at 616 nm. In nanorods, the formation of crystallites with a well-formed long-range order of the monoclinic phase (CSR ca. 30 nm) is also indicated by the manifestation of the $^5D_0 \rightarrow {}^7F_0$ optical transition in the luminescence spectrum. In addition, in this system, the $^5D_0 \rightarrow {}^7F_1$ magnetic dipole transition is characterized by splitting into two peaks at 590 and 597 nm. For nanostars, the optical transition $^5D_0 \rightarrow {}^7F_0$ manifests itself less, and for hollow spheres it practically disappears (Fig. 6a). For nanostars and hollow spheres in the optical term $^7F_1$, which is responsible for the magnetic dipole transition, fine splitting is not observed as for nanorods. The contribution at 625 nm compared to 614 nm grows in the order of nanorods → nanostars → hollow spheres, which leads to a greater "diffuseness" of the photoluminescence spectrum – the absence of pronounced fine splitting in the terms $^7F_1$, $^7F_2$ and $^7F_4$. This fact is consistent with Raman spectra, in which a diffuse scattering band appears during the transition from nanorods to nanostars (compare spectra 1 and 2 in Fig. 7). Moreover, the contribution of the diffuse band increases further during the transition from nanostars to hollow spheres (compare spectra 2 and 3 in Fig. 7). The appearance of a diffuse band in Raman spectra can be explained by CSR reduction in the series of nanorods → nanostars → hollow spheres (Table 3), and hence a decrease in the crystalline order in this series, as well as an increase in the amorphous component because of the growth of nanostructure surface area relating to volume (Table 2). This effect manifests itself if we compare the luminescence lifetimes in this order. The weighted-average luminescence lifetime decreases, indicating that the reduction in symmetry due to an increase in the contribution, which is more pronounced with a smaller CSR size and high S_{BET} values (Tables 2, 4). Thus, the most ordered monoclinic crystalline structure, in which the long-range order in the crystallite extends to 30 nm, is formed in nanorods. Disturbance of long-range order in nanostars is due to twinning, in hollow spheres – due to the presence of internal strains. The nanostar CSR is two to three times smaller than for nanorods, which is associated with the "splitting" of the crystallite into parts. In hollow spheres, the CSR is the lowest 6 nm, since the geometry of the sphere must have the strongest internal strains.

4. Conclusions

In this study, we examined the structure, morphology and emission properties of Eu^{3+}-doped zirconia nanophosphors using X-ray diffraction, Raman, UV-visible diffuse reflectance and photoluminescence spectroscopy. Earlier in [28], monoclinic $Zr_{0.98}Eu_{0.02}O_2$ nanorods with the lowered local site symmetry for photoactive centers were obtained by surfactant-assisted hydrothermal process. The authors observed the transformation of spherical particles of a tetragonal polymorphic modification with a size of less than 10 nm into lamellar structures of the same phase composition, which turned into m-ZrO_2nanorods, as basicity of the hydrothermal medium increases. In turn, we have obtained ZrO_2 nanostructures with a low content of Eu^{3+} (2 mol.%) in the form of rods, stars, and hollow spheres from the same precursors with varying hydrothermal conditions. Regardless of morphology, all synthesized nanoobjects are a monoclinic polymorphic modification of zirconia. A less defective structure of monoclinic zirconia was formed as the size of crystallites increased in a series of hollow spheres, stars and rods. Morphology is reflected in different luminescent properties. The more regular monoclinic structure, the longer luminescence lifetime: rods have 1.12 ms versus ~ 0.4 ms for stars and hollow spheres. A comparison of the Tauc plots for the SKM function and the photoluminescence excitation spectra shows (Zr–O–Eu) charge-transfer states and energy transfer to Eu^{3+} in the ZrO_2 matrix with an absorption edge energy of 4.80 – 5.13 eV. While decreasing the coherent scattering volume, the adsorption surface area in the series rods–stars–hollow spheres increases.

Acknowledgements

Alexander N. Bugrov appreciates the Russian Foundation for Basic Research (grant No. 16-33-60227) for the financial support.

Ruslan Smyslov is thankful for his funding received from the EU-H2020 research and innovation program under grant agreement No. 654360, having benefitted from the access provided by CEA/LETI in Grenoble within the framework of the NFFA-Europe Transnational Access Activity. X-ray diffraction experiments were performed on the Engineering Center equipment of the St. Petersburg State Technological Institute (Technical University). TEM studies were carried out in the Federal Joint Research Center “Material science and characterization in advanced technology” funded by the Ministry of Education and Science of the Russian Federation (id RFMEFI62117X0018).

References

[1] Dhoble S.J., Pawade V.B., Swart H.C., Chopra V. Spectroscopy of lanthanide doped oxide materials. Woodhead Publishing, 2019, 480 p.

[2] Cesaria M., Di Bartolo B. Nanophosphors-based white light sources. Nanomaterials, 2019, **9** (7), 1048.

[3] Gai S., Li C., Yang P., Lin J. Recent progress in rare earth micro/nanocrystals: Soft chemical synthesis, luminescent properties, and biomedical applications. Chemical Reviews, 2014, **114** (4), P. 2343–2389.

[4] Maciel G.S., Rakov N. Photon conversion in lanthanide-doped powder phosphors: concepts and applications. RSC Advances, 2015, **5**, P. 17283–17295.

[5] Ma C.-G., Brik M.G., et al. Spectroscopic and crystal-field analysis of energy levels of Eu^{3+} in SnO_2 in comparison with ZrO_2 and TiO_2. Journal of Alloys and Compounds, 2011, **509**, P. 3441–3451.

[6] Binnemans K. Interpretation of europium (III) spectra. Coordination Chemistry Reviews, 2015, **295**, P. 1–45.

[7] Nadort A., Zhao J., Goldys E.M. Lanthanide upconversion luminescence at a nanoscale: fundamentals and optical properties. Nanoscale, 2016, **8**, P. 13099–13130.

[8] Debashrita S., Sagar G., Tuhin S., Venkataramanan M. Design of lanthanide-doped colloidal nanoparticles: Applications as phosphors, sensors and photocatalysts. Langmuir, 2019, **35** (19), P. 6211–6230.

[9] Bugrov A.N., Smyslov R.Yu., et al. Soluble and insoluble polymer-inorganic systems based on poly(methyl methacrylate), modified with $ZrO_2–LnO_{1.5}$ (Ln = Eu, Tb) nanoparticles: Comparison of their photoluminescence. Journal of Luminescence, 2019, **207**, P. 157–168.

[10] Prakashbabu D., Ramalingam H.B., et al. Charge compensation assisted enhancement of photoluminescence in combustion derived Li^+ co-doped cubic $ZrO_2:Eu^{3+}$ nanophosphors. Phys. Chem. Chem. Phys., 2016, **18**, P. 29447–29457.

[11] Soares M.R., Rodrigues J., et al. Prospects on laser processed wide band gap oxides optical materials. Proceedings of SPIE, 2013, **8626**, 862607.

[12] Bugrov A.N., Smyslov R.Yu., et al. Phase composition and photoluminescence correlations in nanocrystalline $ZrO_2:Eu^{3+}$ phosphors synthesized under hydrothermal conditions. Nanosystems: Physics, Chemistry, Mathematics, 2018, **9** (3), P. 378–388.

[13] Tiseanu C., Cojocaru B., et al. Order and disorder effects in nano-ZrO_2 investigated by micro-Raman and spectrally and temporarily resolved photoluminescence. Phys. Chem. Chem. Phys., 2012, **14**, P. 12970–12981.

[14] Meetei S.D., Singh S.D. Effects of crystal size, structure and quenching on the photoluminescence emission intensity, lifetime and quantum yield of $ZrO_2:Eu^{3+}$ nanocrystals. Journal of Luminescence, 2014, **147**, P. 328–335.

[15] Bugrov A.N., Smyslov R.Yu., Zavialova A.Yu., Kopitsa G.P. The influence of chemical prehistory on the structure, photoluminescent properties, surface and biological characteristics of $Zr_{0.98}Eu_{0.02}O_{1.99}$ nanophosphors. Nanosystems: Physics, Chemistry, Mathematics, 2019, **10** (2), P. 164–175.

[16] De la Rosa E., Diaz-Torres L.A., Salas P., Rodriguez R.A. Visible light emission under UV and IR excitation of rare earth doped ZrO_2 nanophosphor. Optical Materials, 2005, **27**, P. 1320–1325.

[17] Marin R., Sponchia G., et al. Monitoring the $t \rightarrow m$ martensitic phase transformation by photoluminescence emission in Eu^{3+}-doped zirconia powders. J. Am. Ceram. Soc., 2013, **96** (8), P. 2628–2635.

[18] Manjunatha S., Dharmaprakash M.S. Eu^{3+} ion as a luminescent probe in $ZrO_2:Gd^{3+}$ co-doped nanophosphor. International Scholarly and Scientific Research & Innovation, 2017, **11** (1), P. 56–59.

[19] Ikeshita R., Hayakawa T., et al. Novel method to control initial crystallization of Eu^{3+} doped ZrO_2 nanophosphors derived from a Sol Gel route based on HNO_3 and their site-selective photoluminescence. Journal of the Ceramic Society of Japan, 2018, **126** (7), P. 551–556.

[20] Zhang M., Zuo W., et al. Synthesis and photoluminescence properties of Eu^{3+}-doped ZrO_2 hollow spheres. J. Mater. Res., 2015, **30** (24), P. 3740–3745.

[21] Bugrov A.N., Rodionov I.A., et al. Photocatalytic activity and luminescent properties of Y, Eu, Tb, Sm and Er-doped ZrO_2 nanoparticles obtained by hydrothermal method. Int. J. Nanotechnology, 2016, **13** (1/2/3), P. 147–157.

[22] Garcia-Hipolito M., Martinez E., et al. Preparation and characterization of Eu doped zirconia luminescent films synthesized by the pyrosol technique. Journal of Materials Science Letters, 2001, **20**, P. 1799–1801.

[23] Wang M., Wang X., et al. Preparation and photoluminescence properties of Eu^{3+}-doped ZrO_2 nanotube arrays. Ceramics International, 2015, **41** (7).

[24] Colbea C., Avram D., et al. Full tetragonal phase stabilization in ZrO_2 nanoparticles using wet impregnation: Interplay of host structure, dopant concentration and sensitivity of characterization technique. Nanomaterials, 2018, **8** (12), P. 988–1000.

[25] Chen Guo, Peng Wang, et al. Morphology-Controllable Hydrothermal Synthesis of Zirconia with the Assistance of a Rosin-Based Surfactant. Appl. Sci., 2019, **9**, 4145.

[26] Bugrov A.N., Almjasheva O.V. Effect of hydrothermal synthesis conditions on the morpholgy of ZrO_2 nanoparticles. Nanosystems: Physics, Chemistry, Mathematics, 2013, **4** (6), P. 810–815.

[27] Shu Z., Jiao X., Chen D. Synthesis and photocatalytic properties of flower-like zirconia nanostructures. Cryst. Eng. Comm., 2012, **14** (1122).

[28] Chen L., Liu Y., Li Y. Preparation and characterization of ZrO^2:Eu^{3+} phosphors. Journal of Alloys and Compounds, 2004, **381**, P. 266–271.

[29] Sokolova M.P., Smirnov M.A., et al. Structure of composite based on polyheteroarylene matrix and ZrO_2 nanostars investigated by quantitative nanomechanical mapping. Polymers, 2017, **9** (7), P. 268.

[30] Smith D., et al. Penn State University, University Park, Pennsylvania, USA, ICDD Grant-in-Aid, 1973.

[31] Lin F.Q., Dong W.S., et al. In situ source – template-interface reaction route to hollow ZrO_2 microspheres with mesoporous shells. Journal of Colloid and Interface Science, 2008, **323**, P. 365–371.

[32] Hecht H.G. The interpretation of diffuse reflectance spectra. Journal of Research of the National Bureau of Standards - A. Physics and Chemistry, 1976, **80A** (4), P. 567–583.

[33] Heine C., Girgsdies F., et al. The model oxidation catalyst α-V_2O_5: insights from contactless in situ microwave permittivity and conductivity measurements. Appl. Phys. A, 2013, **112** (2), P. 289–296.

[34] Gallino F., Di Valentin C., Pacchioni G. Band gap engineering of bulk ZrO_2 by Ti doping. Phys. Chem. Chem. Phys., 2011, **13**, P. 17667.

[35] Li L., Yang H.K., et al. Structure, charge transfer bands and photoluminescence of nanocrystals tetragonal and monoclinic ZrO_2:Eu. Journal of Nanoscience and Nanotechnology, 2011, **11**, P. 350–357.

[36] Rao G.R., Sahu H.R. XRD and UV-Vis diffuse reflectance analysis of CeO_2–ZrO_2 solid solutions synthesized by combustion method. Proc. Indian Acad. Sci. (Chem. Sci.), 2001, **113** (5, 6), P. 651–658.

[37] Bugrov A.N., Zavialova A.Yu., et al. Luminescence of Eu^{3+} ions in hybrid polymer-inorganic composites based on poly(methyl methacrylate) and zirconia nanoparticles. Luminescence, 2018, **33** (5), P. 837–849.

NANOSYSTEMS: PHYSICS, CHEMISTRY, MATHEMATICS, 2019, 10 (6), P. 666–673

Influence of nanoparticles of various types as fillers on resistance to hydrolysis of films of heat-resistant polyimide

E. N. Bykova[1], I. V. Gofman[1], E. M. Ivankova[1], A. L. Nikolaeva[1],
A. V. Yakimansky[1,2], O. S. Ivanova[3], A. E. Baranchikov[3], V. K. Ivanov[3,4]

[1]Institute of Macromolecular Compounds, Russian Academy of Sciences,
199004, Bolshoi prospect 31, Saint Petersburg, Russia
[2]Saint Petersburg State University, Institute of Chemistry,
198504, Universitetskii prospect 26, Peterhof, Saint Petersburg, Russia
[3]Kurnakov Institute of General and Inorganic Chemistry, Russian Academy of Sciences,
119991, Leninsky prospect 31, Moscow, Russia
[4]Lomonosov Moscow State University, Faculty of Materials Science,
119991, Leninskie gory 1, building 73, Moscow, Russia

bykova.elena.n@gmail.com, gofman@imc.macro.ru, ivelen@mail.ru, alexandra.l.nikolaeva@gmail.com,
yakimansky@yahoo.com, runetta05@mail.ru, a.baranchikov@yandex.ru, van@igic.ras.ru

DOI 10.17586/2220-8054-2019-10-6-666-673

Impact of nanoparticles of various types as fillers on the stability of the poly(pyromellitimide)-based nanocomposite films' properties in alkaline hydrolysis was studied. It was shown that the introduction of nanoparticles into the polymer can lead to an increase in excess free volume. This fact is evidenced by scanning electron microscopy and densitometric studies. The increase of the excess free volume was shown to provoke a rise of the diffusion intensity of the hydrolyzing agent in the films volume during their exposure to an alkaline medium. This effect leads to film swelling and, thereby, to increases of the intensity of the destructive action of hydrolysis on the material. Chemical surface pretreatment of the nanofiller allows one to obtain a composite with an increased packing density compared to that for a composite with unmodified nanoparticles. However, the hydrolytic stability of such a film still remains somewhat inferior to that of the pristine polyimide.

Keywords: polymer-inorganic nanocomposites, polyimides, hydrolysis, carbon nanoparticles, mechanical properties, thermal stability, packing density.

Received: 27 November 2019

Revised: 29 November 2019

1. Introduction

Progress in the field of polymer materials science is increasingly associated with the development of new polymer-inorganic nanocomposite materials [1,2]. This is due to the fact that the introduction of nanoparticles into the polymer matrix leads to the formation of the materials with improved characteristics owing to the unique properties of these nanofillers [1–4].

It is known that, depending on the geometric characteristics of the nanofiller used and the nature of its interaction with the polymer matrix, both the "physical" modification mechanism due to the reinforcement of the polymer by rigid particles with a high aspect ratio and the "chemical" modification due to the formation of additional chemical interactions in the material can take place [3–9].

Along with the aspect ratio, the extent of uniformity of nanoparticles distribution in the polymer volume is an important factor affecting the efficiency of modification the mechanical characteristics of a composite material. Most nanoparticles, due to the high surface energy, are prone to aggregation when introduced into polymer solutions and melts [4, 5]. An effective method of solving this problem is the chemical treatment of the surface of nanoparticles before they are introduced into the polymer matrix [5]. Such a modification allows us to prevent their aggregation, to ensure the uniform distribution of nanoparticles in the polymer volume, and to improve the extent of the compatibility of nanocomposite's components.

The improvement of the characteristics of different polymer materials caused by the introduction of different nanofillers in these matrices have beenthe subject of the extensive studies over the last decade. However, most of the information obtained in these works addresses physical properties of composites under study, viz., mechanical, electric, magnetic, optical, transport, etc., whereas issues pertaining to the impact of nanosized fillers on the chemical processes in polymer matrices, are, to the best of our knowledge, poorly elucidated.

The purpose of this work is the systematic study of the impact of a number of nanoparticles, which differ both in chemical composition and in shape, upon the resistance to hydrolysis of the materials based on one of the aromatic polyimides (PIs) – poly-4,4'-oxydiphenylene(pyromellitimide). Films of this PI combine high hydrolytic stability with extremely high mechanical and thermal characteristics. In practice, polymers of this type are used for the manufacture of parts of devices that can be subjected to prolonged exposure to hydrolyzing agents during operation [3, 10, 11]. Therefore, the problem of the stability of PI-based composite materials with regard to the action of aggressive hydrolyzing media is of great practical importance. The use of nanoparticles of various types introduced into the same polymer allowed us to consider a very topical issue on the influence of specific features of the nanofiller's geometry and chemical nature both on the mechanical properties and on the hydrolytic stability of the composite material.

2. Experimental

Poly-4,4'-oxydiphenylene(pyromellitimide) (polyimide PMDA-ODA) was chosen as a matrix polymer to prepare the nanocomposite films:

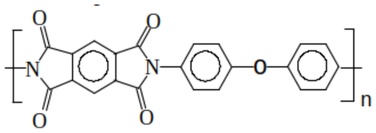

This is the most widely studied PI material, and is produced on an industrial scale (Kapton films [11] produced by DuPont and similar film materials from other producers).

Carbon nanocones/disks (CNCs), nanofibers (CNFs), multi-walled carbon nanotubes in both pristine (MWCNTs), and carboxylated (MWCNTs–COOH) states, as well as quasi-spherical cerium dioxide particles (CeO_2) were chosen as the active nano-sized fillers. CNCs, CNFs, and MWNTs are produced on an industrial scale and CeO_2 particles were synthesized at the Kurnakov Institute of General and Inorganic Chemistry, Russian Academy of Sciences.

To obtain the MWCNTs–COOH the MWCNTs were subjected to surface modification before use by carboxylation in a boiling concentrated solution of nitric acid for 30 hours, followed by washing the resulting product in water to a neutral pH and drying [5].

The characteristics of the nanoparticles used in this work are given in Table 1.

TABLE 1. Characteristics of the nanoparticles used in the work (size, density ρ, producer)

Nano-filler	Form	Size	ρ, g/cm^3	Aspect ratio	Producer
CNF	tubular	Diameters of 100 –150 nm, lengths of 6 –10 μm	2.0	$\sim 10^2$	Showa Denko Carbon Sales (USA–Japan) [13]
CNC	lamellar	Cone heights of 0.3 –0.8 μm; Diameter of cone base, disc diameter of 1 – 2 μm; Wall thickness of 20 – 50 nm	2.0	$\sim 10^2$	n-TEC AS (Norway) [14]
MWCNT	tubular	External diameter of 13 nm, intestine diameter of 4 nm, length of >1–20 μm	2.1	$\sim 10^3$	Bayer Material Science AG (Germany) [15]
CeO_2	Quasi-spherical	Mean diameter of 3.5 nm	7.65	~ 1	Kurnakov Institute of General and Inorganic Chemistry RAS (Russia)

The two-stage syntheticmethod was used to prepare both the nanocomposite films and control PI ones [10]. To prepare the nanocomposite films the nanoparticles of each type were introduced into the solutions of poly(amic acid) (PAA PMDA-ODA), the precursor of the PI. A solution of PAA PMDA-ODA in N,N-dimethylformamide (DMF) was provided by Sigma-Aldrich (catalog No. 575828). The nanoparticles were introduced into the polymer in the following concentrations: 3 vol.% for CNC and CNF, and 1 vol.% for MWCNT and MWCNT–COOH. It was shown in our previous studies [5, 12] being introduced into the polymer matrix in these concentrations the aforementioned nanoparticles can be uniformly distributed in the latter and thereby the increase in the Young's modulus value of the material at least by 20 % can be achieved. CeO_2 nanoparticles were used in the concentration of 0.55 vol.% only. Because of high density of these nanoparticles ($\sim$ 7.65 g/cm^3) further increase in ceria concentration leads to their precipitation in the PAA solution.

To prepare a nanocomposite solution, the calculated amount of nanoparticles was sonicated in DMF for 1 hour; the nanoparticles dispersion obtained was mixed with the required amount of PAA solution and the mixture was homogenized by a mechanical stirrer. The duration of homogenization was 24 hours.

Films of the obtained nanocomposites or of unfilled PAA were prepared by casting the flat layers of the corresponding solutions on glass substrates using a slit die with an adjustable working gap with the subsequent drying of the layers at 80 °C for 2 hours. To obtain PI and PI-based nanocomposite films, PAA and PAA-based films were cure by thermal treatment of the substrates with a heating rate of 3 °C/min up to 360 °C followed by treatment at this temperature for 30 min. The thickness of the films obtained was 30 – 35 microns.

The hydrolysis of the films was performed in concentrated (30 %) NaOH solution. After exposure to this solution at room temperature for different periods of time, the films were washed in distilled water to a neutral pH and dried.

Mechanical characteristics of the films were determined uniaxial extension using band-like samples which were 1 mm wide and 20 mm long. Experiments were carried out using AG-100kNX Plus universal mechanical tests system (Shimadzu, Japan) at the extension speed of 10 mm/min. The Young's modules E, yield stresses σ_y, tensile strengths σ_b, and ultimate strains ε_b were determined by these tests. Seven samples of each type were tested with the subsequent averaging of the results obtained.

Thermomechanical analysis (TMA) for determining the glass-transition point T_g was conducted on TMA 402 F1 Hyperion analyzer (Netzsch, Germany) with samples heated at a constant rate of 5 deg·min^{-1} under a stabilized tensile stress of 0.2 MPa.

Thermogravimetric analysis (TGA) of the films was performed to determine the heat resistance indices τ_5 and τ_{10} (the temperature values at which a polymer or a composite loses 5 % and 10 % of its initial weight, respectively, due to the thermal destruction processes). A DTG-60 thermal analyser (Shimadzu, Japan) was used for these tests. The samples were heated in an open crucible at a rate of 5 deg·min^{-1} in a self-generated atmosphere.

The density ρ values of the materials under study at a temperature of 20 °C were determined by the flotation method with small fragments of the samples in mixtures of carbon tetrachloride and toluene.

Microphotographs of the studied films surfaces were obtained using a Supra 55 VP scanning electron microscope (Carl Zeiss, Germany).

3. Results and discussion

The important problem to be solved while planning this investigation was to choose the criterion to be used to evaluate the intensity of the impact of hydrolyzing medium upon the materials studied.

This criterion that we have used in this work is the extent of the variation of the mechanical and thermal characteristics of the material caused by the exposure to an aqueous alkaline solution. During our preliminary investigations we have evidenced the very sensitive respond to these properties upon the hydrolytic degradation of both the pristine PI films and nanocomposite ones containing the nanofillers of different types.

First of all it was necessary to evaluate the starting level of the properties of the film materials under study. This evaluation makes it possible to compare the impact of different nanofillers upon the material's properties.

As it was repeatedly shown [1–9,12], the mechanical and thermal properties of the material are sensitive regarding to the introduction of active nanosized fillers into the polymer. Therefore, before studying the hydrolytic stability of PI-based composites, it was necessary to evaluate the degree of effectiveness of the fillers chosen as modifiers of the mechanical and thermal properties of the polymer.

The results of mechanical and thermal tests of the samples of the matrix PI film and composites based on it in the initial state are presented in the Table 2.

From the data presented it follows that not only the geometric characteristics of nanoparticles (shape, aspect ratio), but also the nature of their interaction with polymer matrix have a substantial influence on the degree of effectiveness of any filler.

CNCs were shown to be the most favourable modifier of the PI. The introduction of these nanoparticles into the material made it possible to increase the Young's modulus by 28 %. The introduction of two other nanofillers, namely CNF and MWCNT–COOH into PI led to a less pronounced increase in the stiffness of the material (by only 14 %). The least influence on the mechanical characteristics of PI is exerted by MWCNT and quasi-spherical nanoparticles – CeO_2. The introduction of CeO_2 nanoparticles into the PI matrix did not produce any positive effect on the mechanical properties of the material. This situation should be expected taking into account the geometric characteristics of these nanoparticles.

Aromatic PIs are widely known as heat-resistant polymeric materials [8]. For the matrix PI used in the work, the glass transition temperature T_g is 360 – 370 °C, and the process of intense thermal destruction of films begins at temperature range from 500 °C and above. Composite materials containing CNC, CNF and MWCNT in the initial state are characterized by the same values of heat resistance and glass transition temperature. Only for the composite

TABLE 2. Mechanical characteristics and glass transition temperatures of the matrix PI and nanocomposite films studied in the work

No	Filler	E, GPa	σ_y, MPa	σ_b, MPa	ε_b, %	T_g, °C
1	—	2.44 ± 0.07	101 ± 2	178 ± 3	93 ± 8	370
2	CNC	3.13 ± 0.07	112 ± 2	131 ± 5	29 ± 3	370
3	CNF	2.78 ± 0.07	104 ± 4	116 ± 3	30 ± 5	370
4	MWCNT	2.37 ± 0.11	101 ± 2	122 ± 11	33 ± 5	370
5	MWCNT–COOH	2.78 ± 0.08	98 ± 1	136 ± 4	62 ± 7	375
6	CeO_2	2.49 ± 0.05	88 ± 3	103 ± 5	29 ± 5	371

films containing CeO_2 and MWCNT–COOH the pronounced depression of the thermal stability and some increase of the glass transition temperature were registered. The former effect is inherent to ceria-containing PMDA–ODA-based films [9].

In our previous studies [16, 17], we have selected the extremely severe medium to investigate the hydrolysis of PI films taking into account high hydrolytic stability of these materials. These conditions results in a rather intensive process of hydrolytic destruction of PMDA–ODA control film just in the first hours of the experiment. A marked decrease in all the mechanical characteristics of the material was observed after 1 hour of exposure in alkaline medium, and after 40 hours of hydrolysis, the film completely degrades when removed from the hydrolytic bath (Fig. 1).

The introduction of nanoparticles into PI in all cases led to a marked decrease in hydrolytic stability (Fig. 1). Films of nanocomposites filled with MWCNT completely degrade even after 3 hours of hydrolysis. The introduction of CNC, CeO_2, and CNF into the polymer matrix made it possible to obtain films slightly more resistant to hydrolysis: the complete destruction of these materials was recorded after 4 – 5 hours of exposure in an alkaline solution. The film containing nanotubes subjected to a surface pretreatment, namely MWCNT–COOH is characterized by the highest resistance to hydrolytic destruction: only after 10 – 12 hours of hydrolysis the film began to break into fragments, which made further research difficult.

Note that exposure in an alkaline solution leads to a successive increase in the thickness (pronounced swelling) of the samples of both PI and composites based on it (Fig. 1e). Moreover, for the composite films a successive acceleration of this process along with the increase of the hydrolysis duration was registered. The thickness of the samples was measured after washing and removing water from their surface before mechanical testing.

The impact of the hydrolysis upon the surface morphology of both PI and nanocomposite films is presented in Fig. 2.

It is known that the swelling of a polymeric material during the sorption of some aggressive medium results in a decrease of the number of inter molecular interactions in this material,resulting in a decrease in the strength of polymer products [18]. These effects were registered while analyzing the kinetics of the process of hydrolytic destruction of the films under study. The formation of micro-cracks at the films' surface registered by SEM method (Fig. 2b), undoubtedly facilitates the propagation of the aggressive medium – alkaline solution into the polymer volume. The mechanical stresses caused by the incorporation of this solution into the cracks of the in homogeneously swollen material provoke the further destruction of the films [19]. The nanocomposite films, along with the aforementioned effect's tendency to accelerate the decomposition, the additional cracking at the boundaries "polymer–nanoparticles" with the formation of pores at these regions (the inferent SEM picture of the surface of nanocomposite containing CNCs exposed to hydrolysis during 3 h is presented in Fig. 2d). The micro- and nano-sized inhomogeneities formed at the phase boundaries during the nanocomposite films production because of the imperfect compatibility of the polymer and nanoparticles can give rise to these pores.

To elucidate the extent of the compatibility of the nanoparticles with the PI matrix, insured during the formation of composite films, the expected density values of the nanocomposite films under study were calculated by using the additive scheme of composite formation [7]:

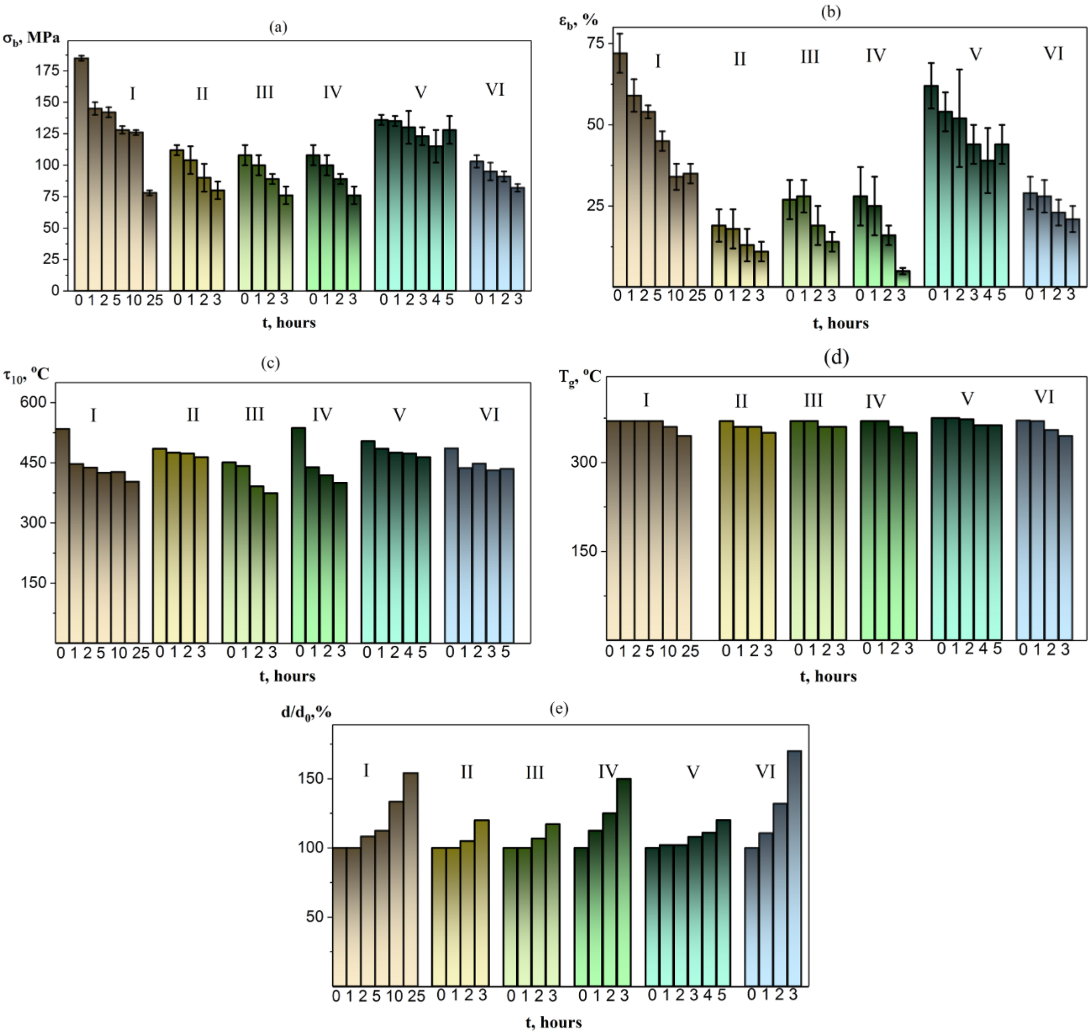

FIG. 1. (a) Tensile strength σ_b, (b) ultimate strain ε_b, (c) glass transition temperature T_g, (d) heat resistance index τ_{10}, (e) thickness d/d_0, of the films tested vs. the hydrolysis duration: (I) unfilled PI, (II) PI–CNC, (III) PI–CNF, (IV) PI–MWCNT, (V) PI–MWCNT–COOH, and (VI) PI–CeO_2; d_0 stands for the initial thickness if the film tested

$$\rho_{calc} = \rho_{PI} \times C_{PI} + \rho_{nano} \times C_{nano}, \tag{1}$$

where ρ_{calc} is the density of an“ideal” nanocomposite containing no pores; ρ_{PI} and ρ_{nano} denote the densities of the polymer and the nanoparticles introduced into it; whereas C_{PI} and C_{nano} denote their volume fractions in the nanocomposite, respectively.

As it was noted in [7], this calculation does not provide precise values of density of the nanocomposite materials under consideration because of the rather poor accuracy of the information concerning the nanoparticles' density values (producer's data). However, these results can give the reliable estimation of the tendency to the variation of free volume caused by the introduction of the nanoparticles into polymer.

The experimental density values of all studied nanocomposites were found to be inferior to calculated values (Table 4). This result testifies to the presence of a certain excess free volume in the composite films. Its value is sufficiently small: the ratio of the experimental density of the sample to the calculated one in all cases wasn't less than 0.994. The maximum value of this ratio corresponds to a composite containing carboxylated nanotubes ($\rho_{exp}/\rho_{calc} = 0.999$, Table 4). The composites containing CeO_2 ($\rho_{exp}/\rho_{calc} = 0.998$), CNC and CNF ($\rho_{exp}/\rho_{calc} = 0.996$) are characterized by slightly less dense packing. The highest value of the excess free volume was observed for the PI–MWCNT composite ($\rho_{exp}/\rho_{calc} = 0.994$).

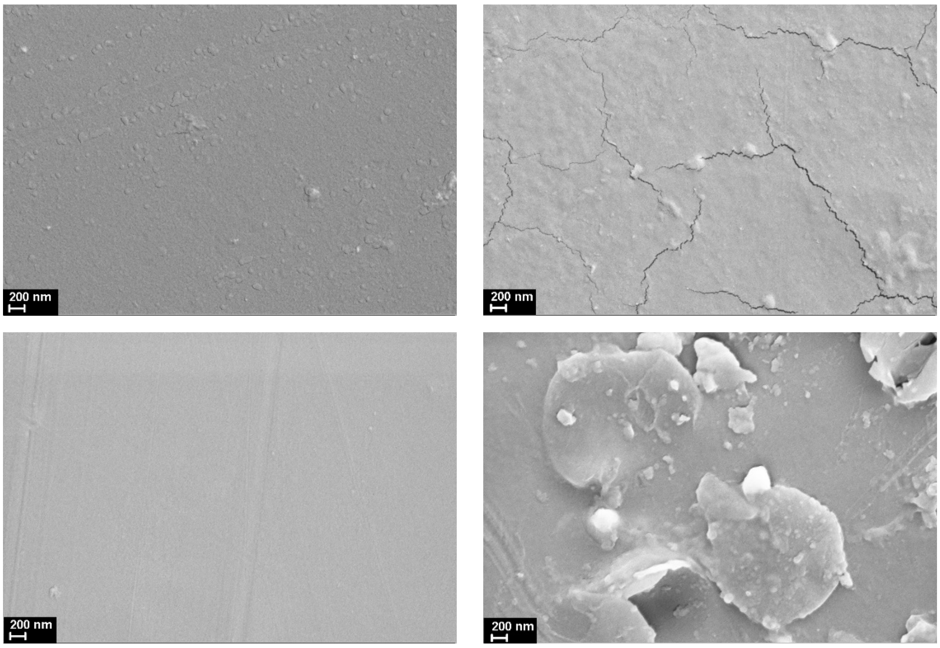

FIG. 2. SEM images of surfaces of the films: (a) PI in the initial state, and (b) after 25 hours of hydrolysis; (c) PI–CNC composite in the initial state, and (d) after 3 hours of hydrolysis

TABLE 3. Thermal stability of the matrix and nanocomposite films investigated in the work

No	Filler	τ_5, °C	τ_{10}, °C
1	—	505	534
2	CNC	506	529
3	CNF	497	524
4	MWCNT	506	537
5	MWCNT–COOH	470	504
6	CeO_2	370	425

TABLE 4. Experimental and calculated density values of the nanocomposite films studied in the work

Filler	ρ_{exp}, g/cm^3	ρ_{calc}, g/cm^3	ρ_{exp}/ρ_{calc}
CNC	1.423	1.428	0.996
CNF	1.423	1.428	0.996
MWCNT	1.408	1.417	0.994
MWCNT–COOH	1.416	1.417	0.999
CeO_2	1.441	1.444	0.998

As it was shown in previous studies [16, 17] and confirmed by the described work, a clear correlation is observed between the excess free volume determined in the densitometric experiment and extent of the hydrolytic stability of composites.

It would be interesting to trace such correlation by analysing the results obtained during the mechanical tests of the composite films. According to previously obtained data [7], the degree of intensity of the impact of nanoparticles introduced into the PI matrix upon the mechanical characteristics of the material (the difference between the properties of the nanocomposite and the initial PI) decreases along with the increase of the excess free volume formed during the formation of the nanocomposite material. Indeed, the main reason of the formation of excess free volume in a nanocomposite material is the incomplete compatibility of the nanoparticles with the polymer matrix. This lack of compatibility leads to a decrease in the local density of the material in the phase boundaries. The described effect naturally produces a negative influence on the mechanical characteristics of the material. However, the results of our tests are not entirely consistent with the above consideration. Indeed, it follows from the comparison of the calculated and experimental density values that a very dense and defect-free packing is realized in a nanocomposite film filled with cerium oxide (the ratio of the experimental density to the calculated one is 0.998). But the introduction of just these nanoparticles into the PI matrix led to a minimal increase in film stiffness (Table 4).

In fact, this apparent contradiction is caused by the well-known fact: the intensity of the variation of the mechanical properties of a matrix polymer caused by the introduction of some nanofilleris determined not only by the intensity of interaction of the composite's components, but also by ability of the nanoparticles used to create a rigid carcass inside the polymer volume. This frame can bear the mechanical load applied to the material and distribute it in the volume of the sample [1, 2]. The effectiveness of the impact of this framework on the properties of the material increases along with the increase in the aspect ratio of the nanoparticles introduced into the polymer [1, 2, 20]. For quasispherical cerium oxide nanoparticles, the value of the aspect ratio is close to 1, while for other nanofillers used in the work, it is 2 – 3 orders of magnitude higher. Given this circumstance, the result of mechanical tests of composites with cerium oxide should be treated as quite regular.

4. Conclusions

Based on the data presented, the following main conclusion can be drawn: the introduction of the nanoparticles of different types into the poly(pyromellitimide) matrix, regardless of their shapes and chemical nature, along with some positive effects, can provoke a decrease in the hydrolytic stability of the material. This effect is caused by the increase in the excess free volume in the process of the nanocomposite formation. The excessive free volume facilitates the diffusion of the hydrolyzing agent into the volume of the film during its aging in an alkaline medium (film swelling) that causes an increase in the extent of destructive action of the hydrolytic attack on the material. It is possible to increase the packing density of the composite due to the surface functionalization of the nanoparticles before their introduction into the polymermatrix. This enhancement of the material's density will insure the decrease in its permeability to hydrolyzing solution. In our work, this effect was realized by the chemical pretreatment (carboxylation) of MWCNT: while these nanoparticles were used as nanofiller the material was formed with the increased packing density as compared to that of a composite filled with the untreated MWCNT. However, even in this case, the hydrolytic stability of the composite film still remains somewhat lower than that of the initial PI.

Acknowledgements

The authors are grateful to M. Ya. Goikhman and I. V. Abalov (Institute of Macromolecular Compounds, Russian Academy of Sciences), who provided MWCNTs for this work.

This work was supported by the Russian Science Foundation (project No. 18-13-00305).

References

[1] Gogotsi Y. *Nanomaterials handbook*. Tailor and Francis, Boca Raton, London, New York, 2006, 779 p.

[2] Zaman I., Manshoor B., Khalid A., Araby S. From clay to graphene for polymer nanocomposites – a survey. *J. Polym. Res.*, 2014, **5** (21), P. 1–11.

[3] Kausar A. Progression from polyimide to polyimide composite in proton-exchange membrane fuel cell: a review. *Polymer-Plastics Technology and Engineering*, 2017, **56** (13), P. 1375–1390.

[4] Eletskii A.V., Knizhnik A.A., Potapkin B.V., Kenny J.M. Electrical characteristics of carbon nanotube-doped composites. *Physics-Uspekhi*, 2015, **58** (3), P. 209–251.

[5] Gofman I.V., Abalov I.V., et al. Comparative Evaluation of Different Methods of Carboxylation of Carbon Nanotubes as a Modifier of Mechanical Properties of Heat-Resistant Polyimide Based Nanocomposites. *Fibre Chemistry*, 2015, **47** (4), P. 236–243.

[6] Shang Z., Lu C., Lü X., Gao L. Studies on syntheses and properties of novel CeO_2/polyimide nanocomposite films from Ce(Phen)$_3$ complex. *Polymer*, 2007, **48** (14), P. 4041–4046.

[7] Gofman I.V., Ivankova E.M., et al. Effect of nanoparticles of various types as fillers on mechanical properties of block samples of a heat-resistant polyimide material: A comparative analysis. *Polymer Science Series A*, 2016, **58** (1), P. 87–94.

[8] Pandey R.P., Amit K.T., Shahi V.K. Sulfonated polyimide/acid-functionalized graphene oxide composite polymer electrolyte membranes with improved proton conductivity and water-retention properties. *ACS applied materials & interfaces*, 2014, **6** (19), P. 16993–17002.

[9] Gofman I., Nikolaeva A., et al. Unexpected selective enhancement of the thermal stability of aromatic polyimide materials by cerium dioxide nanoparticles. *Polymers for advanced technologies*, 2019, **30** (6), P. 1518–1524.

[10] Bessonov M.I., Koton M.M., Kudryavtsev V.V., Laius L.A. Polyimides – Thermally Stable Polymers. New York: Plenum Publishing Corp., 1987. 374 p.

[11] `URL: http://www.dupont.com/products-and-services/membranes-films/polyimide-films/brands/kapton-polyimide-film.html`.

[12] Gofman I.V., Abalov I.V., Tiranov V.G., Yudin V.E. Effect of carbon nanoparticles of different shapes on mechanical properties of aromatic polyimide-based composite films. *Polymer Science Series A*, 2013, **55** (5), P. 313–319.

[13] `URL: https://www.sdk.co.jp/english/products/126/132/2094.html`.

[14] `URL: https://www.strem.com/uploads/resources/documents/nanocones.pdf`.

[15] `URL: https://ru.scribd.com/document/59272724/Bay-Tubes`.

[16] Bykova E.N., Gofman I.V., Vlasova E.N. Hydrolytic stability of films of aromatic polyimides and composites on their basis, filled with carbon nanocones. *Russian Journal of Applied Chemistry*, 2018, **91** (9), P. 1460–1470.

[17] Bykova E.N., Gofman I.V. Effect of nanosized carbon fillers on the hydrolytic stability of films of a heat-resistant aromatic polyimide. *Russian Journal of Applied Chemistry*, 2017, **90** (1), P. 70–76.

[18] Rudakova T.E., Zaikov G.E. Degradation of polymers by mechanical forces and chemically active media. *Polymer degradation and stability*, 1988, **21** (1), P. 73–90.

[19] Malkin A.I. Regularities and mechanisms of the Rehbinders effect. *Colloid Journal*, 2012, **2** (74), P. 223–238.

[20] Garboczi E.J., Snyder K.A., Douglas J.F., Thorpe M.F. Geometrical percolation threshold of overlapping ellipsoids. *Phys. Review E*, 1995, **1** (52), P. 819–828.

NANOSYSTEMS: PHYSICS, CHEMISTRY, MATHEMATICS, 2019, 10 (6), P. 674–680

The influence of wet milling of aluminum and aluminum alloys powder screenings on the characteristics of the aluminum-based pastes

A. V. Egorov[1], D. A. Kozlov[2], Yu. B. Mamaeva[3], A. K. Petrov[3], A. V. Garshev[1,2], P. V. Evdokimov[1,2],
Ya. Yu. Filippov[1], N. K. Orlov[1], V. I. Putlayev[1,2], A. V. Chetvertukhin[3], I. Yu. Mikhailov[4],
S. V. Polyakov[5], A. A. Fedyanin[3]

[1] Lomonosov Moscow State University, Faculty of Chemistry, Leninskie gory, 1, building 3, Moscow, 119991, Russia

[2] Lomonosov Moscow State University, Faculty of Materials Science,
Leninskie gory, 1, building 73, Moscow, 119991, Russia

[3] Lomonosov Moscow State University, Faculty of Physics, Leninskie gory, 1, building 2, Moscow, 119991, Russia

[4] LLC Light Materials and Technologies Institute, Leninskiy prospect, 6/21, Moscow, 119049, Russia

[5] JSC Russian Aluminium Management, Vasilisy Kozhinoi str., 1, Moscow, 121096, Russia

garshev@inorg.chem.msu.ru, egorov@kge.msu.ru, chetvertukhin@nanolab.phys.msu.ru, ivan.mikhaylov@rusal.com

PACS 62.20.Qp **DOI 10.17586/2220-8054-2019-10-6-674-680**

The milling of aluminum powders in non-aqueous solvents is used in the production of high-quality pigment pastes of flake shapes with thickness from some microns to hundreds of nanometers. In Russia, such pigments are not produced at a large scale, however, spherical powders made from aluminum and its alloys are manufactured. Starting the production of pigments from screenings of powder production will not only solve the problem of fine fractions disposal, but also reduce the cost of the target fractions powders. The fraction of powders with an average d50 of less than $\sim$20 μm should be disposed. In this research, by varying the laboratory conditions, the parameters for milling screenings of A8 aluminum powder, AK9ch and 1201 aluminum alloys were selected. The milling was performed in non-aqueous solvents: a highly refined commercial petroleum solvent and liquid paraffin oil. The prospects of using wet milling for the manufacture of pigment pastes from alloys has been demonstrated including average thicknesses of the flakes about 40–80 nm. Thus, it has been demonstrated that wet and bead grindings lead to thinning of metal powder particles to thicknesses of less than 100 nm.

Keywords: aluminum alloy, screenings of powder productions, wet milling.

Received: 12 August 2019

Revised: 30 November 2019

1. Introduction

Spherical-shaped aluminum particle powders are used as powders and pastes in the production of blowing agents for autoclaved aerated concrete and pigments for paints. In the first case, the powder is milled in ball mills, by introducing an oiling additive and by blowing a nitrogen-oxygen mixture with a controlled oxygen content through a mill. In the manufacture of pigment pastes, the powder is milled in a non-aqueous solvent using an oiling additive. By varying the conditions and the milling medium, pigment pastes for various purposes are obtained. Thus, depending on the location of the aluminum powder flakes in the surface layer of the paint coating (pigment flotation), as well as on the aspect ratio of the pigment particle, the reflective properties of the coating (“metallic” effect, graininess, irisation) and its mechanical properties (adhesion, strength, abrasion, hiding power) change significantly. Varnish-and-paint coatings even with the aluminum pigment content of 18% are capable of reflecting up to 70% of infrared radiation and can be used for energy-saving purposes. A promising area for aluminum-containing pigment application is the production of varnish-and-paint materials for the automotive industry (paints with a “metallic” effect) and printing (can & coin type of paints for metallic parts of labels (brochures, posters, coatings on plastics, etc.) for which the numerical value of D50 for flakes and discs is in the range from 10 to 35 μm [1]. The growing production of aluminum powders by the “atomization” method [2] has made it possible to consider the screenings from “atomized” powders as the source of aluminum instead of the aluminum foil. This have given rise to the development of a technology for the production of a number of pigments with a “metallic” effect with new consumer properties. Thus, an experimental study was conducted in [3] aimed at determining the optimal milling parameters for producing pigment pastes from aluminum during wet milling. Obtaining flakes from spherical aluminum particles requires a special approach during milling and this process is described by the two-stage model: at the first stage of milling, the material absorbs energy required for the formation of disc-shaped plate-like particles from the initial spherical ones and at the second stage, the portion of energy is required for the milling of disc-shaped plates into smaller ones with irregular shapes.

There are different methods of manufacturing aluminum plate-like particles, such as stamping, dry and wet milling in ball mills, the use of attritors, and vibration milling [4–6]. When using stamping milling, aluminum powder is abraded with a hammer under an aerobic atmosphere, the powder moves continuously with an air stream and then the fractionation takes place. However, this method is not widespread because of its explosiveness. Horizontal ball mill is used more often in the production of plate-shaped aluminum flakes, as it is more suitable for large-scale production and allows one to achieve good dispersion of the resulting aluminum product. Wet milling is most often used to produce paints and inks; organic solvents are used as a milling medium. The following factors influence the milling process: the size of the milling media, the number of intermediate stops during milling, the amount of oiling additive. The advantages of wet milling are [7]: reduction of particle agglomeration compared to dry milling; no loss of ground material; there is no risk of spontaneous oxidation of small particles; air purification devices are not required; heat transfer is improved.

Today, this technology is widely used in various industries [8, 9]: varnish-and-paint, chemical, pharmacological, fertilizer production, food production, paper manufacturing, bioengineering, nanotechnology and ceramic production. Ball and bead mills are widely used in laboratory modeling of the wet milling process. The use of bead wet milling allows one to obtain a product with a smaller particle size compared with milling in ball mills. Bead mills of both horizontal [7, 8] and vertical design [9] are used. In a horizontal bead mill, in continuous operation, the suspension of the product being milled is pumped through the milling chamber. The running of the mill rotor makes the beads move, which, in turn, crushes the particles of a material. At the end of the work, the suspension of material is drained from the mill. Unlike a ball mill, which is filled with $\sim$ 40 vol.% of balls and crushed material, the filling of a bead mill with milling media reaches 85% by volume and the rest space is filled with crushed material suspended in a solvent. The milling bodies are separated from the crushed powder using a sieve cartridge or slot; the size of this slot does not exceed the half of the milling body size. The milling chamber as well as the rotor can also be cooled during the milling process by a special circuit which is necessary for temperature sensitive materials, since most of the energy transferred for the milling is transformed to heat. It should be noted that extremely high milling energy intensities are characteristic for bead mills in comparison with ball mills. For this reason, due to the various mechanical properties of the alloys, it is viable to carry out milling both in a bead mill and a ball mill when producing pigment pastes from screenings of A8-grade aluminum powders, AK9ch and 1201 alloys.

2. Experimental part

In this work, the screenings of the A8-grade aluminum, AK9ch and 1201 aluminum alloys were used, which were obtained by separation of the powders produced by gas atomization technique under nitrogen atmosphere with a small amount of oxygen for passivation. The powders of the alloys were obtained at Volgograd aluminum factory (United Company RUSAL). The extraction of the fractions from the screenings of the aluminum powders and aluminum-based alloys was performed on the standard equipment for the obtaining of the Company's products with the average d50 value of $\sim$2 μm and $\sim$5 μm, respectively.

The powders and the milling products were studied by scanning electron microscopy (SEM) and X-ray spectral microanalysis by the LEO SUPRA 50 VP instrument (Zeiss, Germany) equipped with energy-dispersive detector X-MAX 80 and INCA software (Oxford Inst., United Kingdom). The samples were analyzed at an acceleration voltage up to 20keV at the magnification of up to $\times$10000 using the "in point" spectra collecting mode when analyzing chemical composition of the materials after milling, and "in area" mode when analyzing chemical composition of the starting powders. The elemental composition package was calculated in semi-automated regime using INCA Energy+ software program (Oxford Inst., United Kingdom).

X-ray diffraction (XRD) patterns were collected using a Rigaku D/MAX 2500 diffractometer ($\theta/2\theta$ Bragg-Brentano reflection geometry) with a scintillation counter. All the measurements were performed with CuK$\alpha_{1,2}$ radiation generated on a rotating Cu anode (50 kV, 250 mA) and monochromatized by a curved graphite [002] monochromator placed at the reflected beam. The XRD patterns were collected in the 5–90° 2θ range with a 0.02° step and at least 0.5 s/step. To reduce the undesirable background intensity, all samples were investigated on monocrystalline Si holders oriented by [510].

The particle-size distribution in the starting alloy powders and milling products was analyzed by static light scattering using laser analyzer of particle sizes Analyzette 22 (Fritsch, Germany) with ultrasound treatment.

The milling of the powders was performed in a horizontal mill of an original construction (LLC "Technocenter", Russia) in the crushing cylinder with the diameter of 210 mm, and in a bead mill 01-HD (Union Process, USA) equipped with a pin shaft. The milling in the bead mill was performed by addition of 80 g aluminum powder or aluminum alloy; 1600 g of steel balls with the diameter of 1 mm; 160 g of paraffin oil and 8 g of an oiling additive to the milling chamber. The rotation frequency of the pin shaft was 500 rpm, the milling chamber was forcedly cooled with water of ambient-temperature. The test samples were collected at 10, 30, 60, 90, 120, 180, 240, and 300 minutes after milling initiation.

In a horizontal mill of the original construction (LLC "Technocenter", Russia), the milling was performed by addition of 150–250 ml of aluminum or aluminum alloy powder with a bulk density from 0.4 to 0.7 g/cm^3, 1500–2400 ml of steel balls with the diameter of 5 mm, 900–1350 ml of paraffin oil or a highly refined commercial petroleum solvent with a distillation temperature of 180–230 $^\circ$C, and up to 3 vol.% of an oiling additive to the crushing cylinder. The rotation frequency of the crushing cylinder was varied from 65 to 95 rpm. The cylinder was cooled forcedly with water of an ambient temperature. The test samples were collected at 24, 40, and 60 hours after the starting of the milling.

Using the milling products, the colorings were obtained, for which the values of the flop index (FI) were determined. The measurements were performed using BYK-mac-i spectrophotometer (BYK Gardner GmbH, Germany). The colorings were made on the 100×140 mm cards ISISTEM (Ideale Sistema LTD U.K, United Kingdom) and LENETA (Leneta Company, USA). For this, the mixtures of varnish, solidifier and the milling products were prepared. The content of the milling products in mixtures was varied from 5 to 50 vol.%. The mixture was applied onto the cards as a layer with a fixed-thickness in the range from 9 to 50 μm using a rod applicator.

3. Results and discussion

The results of the studying of the initial powders by scanning electron microscopy and static light scattering, have proved the attribution of the aluminum and aluminum-based alloys powders to the products with the average particle size of $\sim$2 μm and 5 μm, respectively. The SEM image (Fig. 1) shows the A8-grade aluminum alloy with the average particle size of $\sim$2 μm, and according to static light scattering the d10, d50, and d90 values for this product are 300 nm, 1.6 μm, 3.4 μm, respectively. Moreover, the fraction of nanosized particles does not exceed a few percent. Fig. 2 contains the SEM image of A8-grade aluminum powders with the average particle size of $\sim$5 μm, and the static light scattering for this product reveals the d10, d50, and d90 values of 2.4 μm, 5.6 μm, and 12.6 μm, respectively. According to the EDX microanalysis, the chemical composition of the AK9ch and 1201 aluminum alloy powders satisfies the requirements of GOST 4784-97.

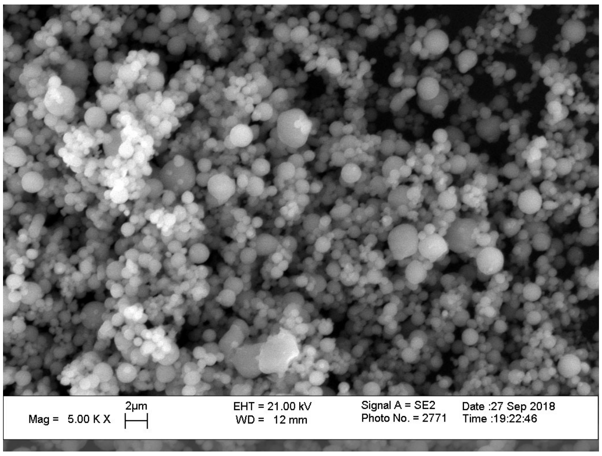

FIG. 1. SEM image of the A8-grade aluminum powder with the average particle size of $\sim$2 μm

For the milling of the A8-grade aluminum powder with the average particle size of $\sim$2 μm as well as of $\sim$5 μm in the ball mill under optimal values of the milling parameters, the maximal d50 values for the products are achieved after the milling during the period from 24 to 48 hours and are equal to 8.5 μm for the A8-grade aluminum powder with the particle size of $\sim$2 μm, and 10.7 μm for for the A8-grade aluminum powder with the particle size of $\sim$5 μm. With increased milling time, the d50 values decrease – after milling for 60 hours, the d50 have reduced to 6.7 μm and 9.2 μm, respectively. The results of the SEM analysis of the A8-grade aluminum powder (the average particle size is $\sim$5 μm) after the milling during 60 hours in the ball mill are presented in Fig. 3. According to static light scattering, the d10, d50, and d90 values for this sample are 2.8, 9.2, and 19.1 μm, respectively. When the A8-grade aluminum powders were milled in the bead mill, the maximum d50 values for the obtained products were achieved after milling for 90–120 minutes and are equal to 7.9 μm for the A8-grade aluminum powder with the particle size of $\sim$2 μm, and 10.2 μm for the powder with the particle size of $\sim$5 μm. A decrease in the d50 values exceeding 1 μm at long milling times has not been observed.

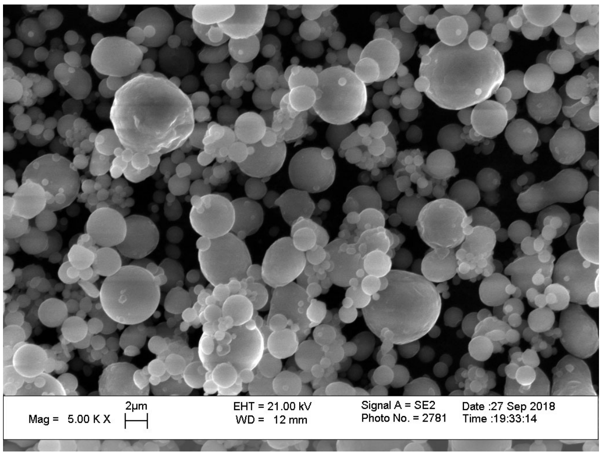

FIG. 2. SEM image of the A8-grade aluminum powder with the average particle size of $\sim$5 μm

According to SEM, the particle thicknesses after wet grinding do not exceed hundreds of nanometers, which leads to the unique optical properties of paints based on the obtained powders.

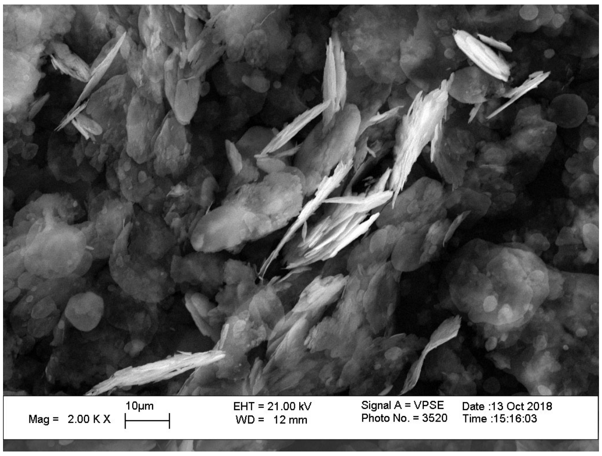

FIG. 3. SEM image of the A8-grade aluminum powder with the average particle size of $\sim$ 5 μm after milling in the ball mill

For the milling of 1201 alloy powder with the average particle size of $\sim$5 μm, under the optimal values of milling parameters, the maximum d50 value is achieved after the milling for 24 hours and is equal to 9.3 μm. With an increase in the milling time, the d50 value for the products decreases – after the milling for 60 hours it was reduced to 4.9 μm.

The AK9ch alloy powder with the average particle size of $\sim$ 5μm failed to be milled in the ball mill under variation of different milling parameters. When milled in the bead mill, the maximal d50 value for the same powders was achieved after milling for 300 minutes and is equal to 9.2 μm (the values were measured after milling for 10, 30, 60, 90, 120, 180, 240 and 300 minutes). The SEM image of the milling product obtained from AK9ch alloy powder with the average particle size of $\sim$5 μm after the milling during 300 minutes in the bead mill is presented in Fig. 4. According to static light scattering, the values of d10, d50, d90 for this sample are 3.4, 9.2, and 17.0 μm, respectively.

The typical appearance of the coloring obtained using aluminum and aluminum-based alloys powder milling products is shown in Fig. 5. This coloring was obtained on the base of milling products prepared from AK9ch alloy with the average particle size of $\sim$5 μm ground in a bead mill for 300 minutes. The flop index (FI) was calculated during studying of light reflection on the coloring:

$$FI = \frac{2.69 \cdot (L_{15} - L_{110}) \cdot 1.11}{L_{45} \cdot 0.86}$$

where L – the lightness parameter, the value of which is varied from 0 – the reflection from the darkest color, to 100 – the reflection from the white standard, L_{15}, L_{45}, L_{110} – the values of L_* obtained at the observation angles of 15°,

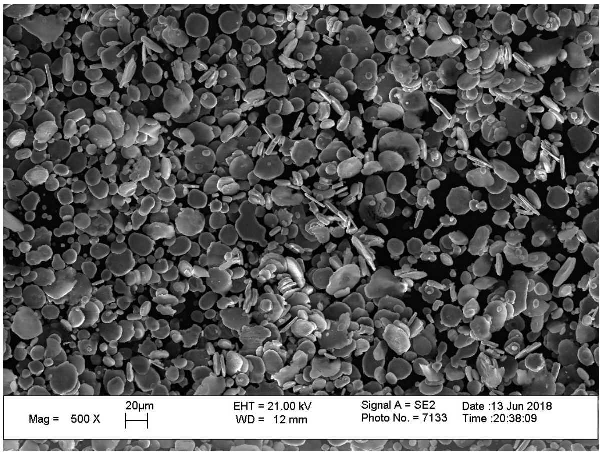

FIG. 4. SEM image of the AK9ch alloy powder with the average particle size of $\sim$5 μm after milling in the bead mill

45°, 110° respectively. The observation angle is measured from the direction of specular reflection towards the normal to the sample surface. For all the pigments with the "metallic" effect the value of FI exceeds 0, but for the most of the modern pigments this parameter ranges from 7 to 19 units. The maximum FI values for the samples based on milling products obtained in ball mills have been observed when the products were milled during 48 hours. Thus, for the milling products obtained from A8-grade aluminum with the average particle diameter of $\sim$5 μm, the maximum FI value is 15.0 units, and for the milling products obtained 1201 aluminum alloy, with the average particle size of $\sim$5 μm, the FI is 13.2.

FIG. 5. The typical appearance of the coloring (the coloring prepared using the milling products of AK9ch alloy powder with the average particle size of $\sim$5 μm)

The milling in a bead mill also allows to obtain the product for the preparation of coloring of materials with the FI corresponding to pigments with the "metallic" effect. Thus, for the milling products obtained from A8-grade aluminum with an average particle size of $\sim$2 μm, the FI is 15.0 units, for products obtained from the A8-grade aluminum with an average particle size of 5 μm, the FI is 10.0 units. And in case of the milling products obtained from AK9ch alloy with an average of $\sim$5 μm, the FI is 15.7. These values correspond to the current FI values for pigments with the "metallic" effect.

The achievement of such values of the flop index is possible due to the fact that under the selected milling conditions, the thickness of aluminum flakes is less than 100 nm, which is confirmed by scanning electron microscopy (Fig. 6) and crystallite sizes calculated according to X-ray diffraction data.

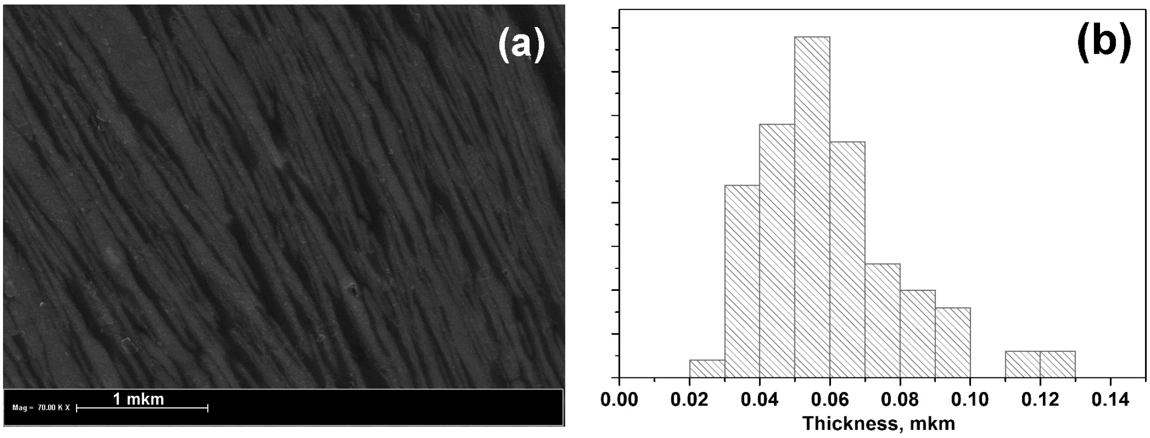

FIG. 6. SEM image of A8 flakes (wet milling) in resin after polishing – (a) and thickness size distribution of the individual flakes – (b)

According to X-ray diffraction data (Fig. 7), the crystallite sizes calculated by the Scherrer formula after bead milling are 83±9 nm and 80±4 nm for A8 and AK9 respectively. Wet milling results in smaller crystallite sizes – 65±4 nm and 43±2 nm for the A8 and AK9 alloys respectively.

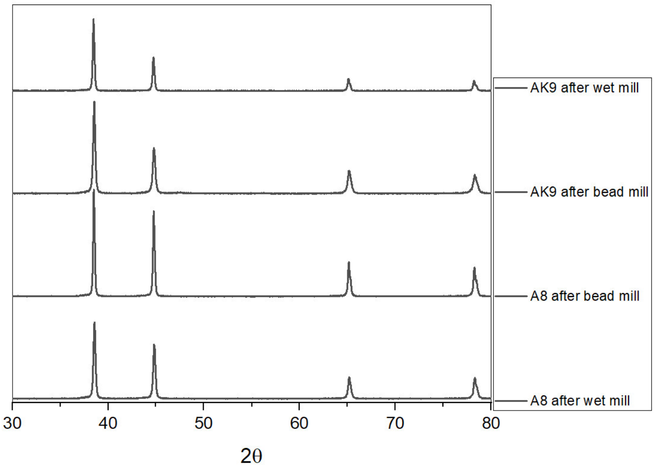

FIG. 7. XRD patterns of A8 and AK9 samples after wet and bead milling

4. Conclusions

The milling of screenings of aluminum powders and aluminum-based alloys using horizontal ball and bead mills can be used for obtaining of pigments and pigment pastes possessing "metallic" effect with the parameters corresponding to the industrially manufactured pastes. The prospects of using a wet milling technique for the manufacture of pigment pastes from alloys has been demonstrated including average thicknesses of the flakes about 40–80 nm. Thus it has been demonstrated that wet and bead grindings lead to thinning of metal powder particles to thickness less than 100 nm. The milling of alloys powders is reasonable to perform in bead mills exhibiting higher striking energy in comparison with ball mills.

Acknowledgment

This work was performed in Lomonosov Moscow state University, the General contractor of the R&D studies, within of the Contract No PMSh-218-2017/01 dated 09.02.2017 at the financial support of Ministry of Education and Science of the Russian Federation according to the Agreement No 075-11-2018-196 dated 28.04.2017 (internal contract number 03.G25.31.0248). The equipment purchased within the Moscow State University Development Program was used in the present work.

References

[1] Bosch W., Cuddemi A. Optimisation of the shear stability of aluminium pigmented waterborne basecoats. *Progress in Organic Coatings*, 2002, **44**(3), P. 249–257.

[2] Garshev A.V., Kozlov D.A., Evdokimov P.V., Filippov Ya. Yu., Orlov N.K., Putlyaev V.I., Chetvertukhin A.V., Petrov A.K. Analysis of Aluminum Alloy Powders for Additive Manufacturing Fabricated by Atomization. *Inorganic Materials: Applied Research*, 2019, **10**(4), P. 901–905.

[3] Svěrák T., Bulejko P., Krištof O., Kalivoda J., Horský J. Covering ability of aluminum pigments prepared by milling processes. *Powder Technology*, 2017, **305**(1), P. 396–404.

[4] Seong-Hyeon Hong, Dong-Won Lee, Byoung-Kee Kim. Manufacturing of aluminum flake powder from foil scrap by dry ball milling process. *Journal of Materials Processing Technology*, 2000, **100**(1-3), P. 105–109.

[5] Watanabe R., Hashimoto H., Lee G.G. Computer Simulation of Milling Ball Motion in Mechanical Alloying. *Materials Transactions*, JIM, 1995, **36**(2), P. 102–109.

[6] Seong-Hyeon Hong, Byoung-Kee Kim. Effects of lifter bars on the ball motion and aluminum foil milling in tumbler ball mill. *Materials Letters*, **57**(2), P. 275–279.

[7] Hoffl K. *Zerkleinernngs- und Klassiermaschinen*. Springer-Verlag, Berlin, Heidelberg, New York, Tokyo, 1986, 275 p.

[8] Pahl M.H. Zerkleinerungstechnik. Verlag TÜV Rheinland, Köln, 1991, P. 283–317.

[9] Kwade A., Schwedes J. Wet Comminution in Stirred Media Mills. *KONA Powder and Particle Journal*, 1997, **15**, P. 91–101.

NANOSYSTEMS: PHYSICS, CHEMISTRY, MATHEMATICS, 2019, 10 (6), P. 681–685

SILD synthesis of the efficient and stable electrocatalyst based on CoO–NiO solid solution toward hydrogen production

I. A. Kodintsev[1], K. D. Martinson[1], A. A. Lobinsky[2], V. I. Popkov[1]

[1]Ioffe Institute, 194021 Saint Petersburg, Russia
[2]Saint Petersburg State University, Peterhof, 198504 Saint Petersburg, Russia
i.a.kod@mail.ru

PACS 73.61.r, 81.15.z, 82.65.+r **DOI 10.17586/2220-8054-2019-10-6-681-685**

Currently, nanocrystalline NiO is well known as one of the best non-noble metal electrode material with low overpotential (OP) but mediocre stability. On the contrary, CoO has remarkable stability but the high values of OP. In this work, a method is proposed to achieve the stability of nickel oxide-based electrode materials while maintaining a low OP via the synthesis of a nanocrystalline CoO–NiO solid solution. Nanocrystals of CoO–NiO solid solution were synthesized by successive ionic layer deposition (SILD). XRD, SEM, and EDX analysis show that the CoO–NiO sample consists of 3 – 5 nm isometric crystallites of the solid solution mentioned above and Ni/Co ratio is equal to 45.4 % / 54.6 % at. Electrochemical investigation of the nanocrystalline CoO–NiO solution as electrode material shows OP values of -240 mV at a current density (CD) of 10 mA/cm^2, Tafel slope values of 78 mV/dec for hydrogen production from water-ethanol solution (10 % vol.) and high cyclic stability – only 3 mV degradation at 10 mA/cm^2 after 100 cycles of cyclic voltammetry. Thus, it was shown that the synthesis of a solid solution within the proposed approach makes it possible to maintain the high electrocatalytic properties inherent in NiO, but with high stability in a wide range of overpotential and in the high cyclic load inherent in CoO.

Keywords: nickel oxide, cobalt oxide, successive ionic layer deposition, hydrogen evolution, electrocatalytic reforming.

Received: 25 July 2019

Revised: 25 November 2019

1. Introduction

The environmental pollution and growing energy crises have stimulated the development of clean electrochemical energy conversation and storage technologies [1,2] . Hydrogen has been regarded as one of the cleanest energy carriers for such purposes. Among the methods of hydrogen production is steam reforming [3,4], biological processes [5], photoelectrolysis [6,7], water electrolysis [8,9] and electrochemical reforming [10,11]. The last one is the most interesting due to the clean and low-temperature process and the use of renewable organic sources (alcohols, carbohydrates, and others). Composites with Pt, Ir and Ru exhibit the highest activity for hydrogen evolution reaction (HER), but it cannot be largely used in electrochemical reforming because of their rarity and high cost [12]. Therefore, durable, high-active and low-cost catalysts from transition elements have been attracted considerable attention since the last decade. These catalysts include sulfides [13,14], phosphides [15,16], nitrides [17,18] and oxides [19,20] of Mo, Co, Fe, V, Ni and other elements.

Nickel and cobalt oxides are typically used for hydrogen evolution reactions, but they are not ideal HER catalysts due to the low stability of NiO and high overpotential of CoO [21–23] . In this paper, we proposed a way to avoid the disadvantages of each oxide by synthesizing nanocrystals of CoO–NiO solid solution by successive ionic layer deposition (SILD). The SILD method is one of the layer-by-layer synthesis methods based on successive and multiple treatments of the substrate in a salt solution that leads to the formation of insoluble nanolayers of the new compound upon interaction on the surface [24–26]. This method is suitable for the coating of most surfaces, even with irregular shapes and sizes, and it's allowed to precision control of multilayer thickness by changing the number of treatment cycles. The SILD method provides a simple and effective way for the creation of metal oxides composites for HER electrodes.

2. Experimental

Nickel plates with a size 5 × 25 mm were used for electrochemical investigation, and monocrystalline silicon plates with the orientation of $\langle 100\rangle$ and a size 5×20 mm were used for characterization by physicochemical methods. Before synthesis, both nickel and silicon plates were treated in acetone for 10 minutes into the ultrasonic bath. Then, nickel plates were treated for 15 minutes in aq. 6 M HCl, then rinsed several times with deionized water and dried on the air at 80 °C for 30 minutes. Silicon plates were treated for 15 minutes in concentrated HF, for 20 minutes in diluted KOH solution with pH = 9.0, and finally were dried on the air at 80 °C for 30 minutes.

CoO–NiO solid solution was synthesized on the nickel and silicon plates by SILD method. As precursors were used the solution containing 0.01 M $Ni(CH_3COO)_2$ and 0.01 M $Co(CH_3COO)_2$ and the solution of NaOH with pH = 9. During the synthesis, the substrates were immersed for 30 seconds into the solution of Ni and Co salts, then into distilled water, NaOH solution, and distilled water again. Such treatment considered as one SILD cycle, which has been repeated several times. The synthesis of pure CoO and NiO samples was carried out according to the techniques previously described in the works [23, 24], so no additional physicochemical analysis was used to characterize synthesis products.

X-ray phase analysis was performed on a Rigaku SmartLab 3 X-ray powder diffractometer; phase analysis of the composition was performed using the ICDD PDF-2 powder database. The average crystallite size (coherent-scattering regions) was calculated from the broadening of X-ray diffraction lines using the Scherrer formula. Elemental analysis and morphology of the synthesized sample were studied by energy dispersive X-ray analysis (EDX) and scanning electron microscopy (SEM) using Tescan Vega 3 SBH scanning electron microscope equipped with an Oxford INCA x-act X-ray microanalysis device.

Electrochemical properties of CoO–NiO solid solution for electrochemical reforming were investigated using potentiostat Elins P-45X and a three-electrode cell. Nickel plate with nanocomposite film deposited via the layer-by-layer method was used as a working electrode, the Ag/AgCl electrode was used as reference electrode and a platinum foil was used as a counter electrode. All measurements have been carried out at atmospheric pressure and room temperature in 1 M KOH solution with 10 % (by volume) ethanol as the electrolyte. The voltammogram was made at a 5 mV/s sweep rate with IR compensation (1.3Ω). The electrochemical stability of the electrode materials was characterized via standard cyclic voltammetry technique carried out for 100 cycles.

3. Results and discussions

Figure 1 shows the result of the XRD investigation of the CoO–NiO sample obtained by the SILD method.

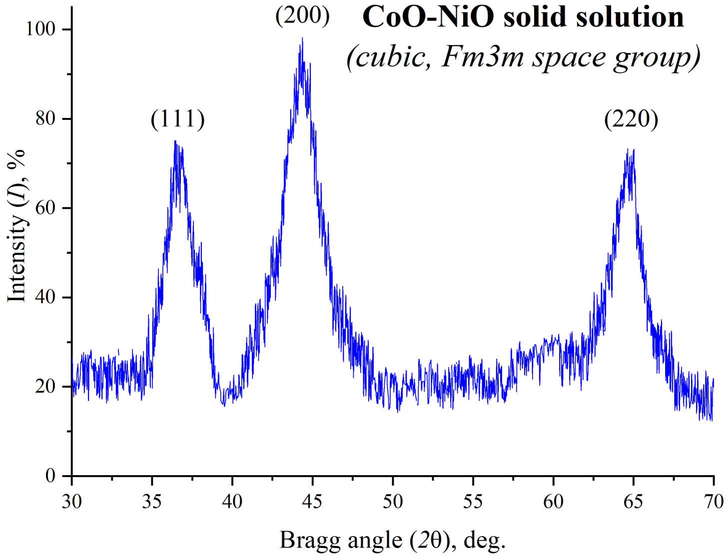

FIG. 1. XRD pattern of the synthesized nanocrystals of CoO–NiO solid solution

The X-ray diffractogram shows three intense diffuse reflections at 36.8°, 44.3°, and 64.6° Bragg angles, which correspond to the crystallographic directions of (111), (200) and (220) into the cubic structure of cobalt (II) / nickel (II) oxide (space group *Fm3m*, structural type of NaCl). The X-ray diffraction lines are strongly broadened, which indicates a small crystallite size – the calculation of the average size of the coherent scattering regions, according to the Scherrer formula, gives a 3 – 5 nm value depending on the chosen crystallographic direction. There is no noticeable difference in the broadening of diffraction lines for various reflections, which indicates that the morphology of the obtained nanocrystals is close to isometric. Due to the significant broadening of the X-ray diffraction lines, an exact determination of the cubic unit cell parameter is impossible; the estimated value of the parameter $a = b = c$, determined by the Rietveld method, is 4.045(5) Å. In this case, the observed shift of the X-ray diffraction lines toward large angles is slightly higher than might be expected for the CoO–NiO solid solution, which indicates a high defectiveness of the obtained nanocrystals and the presence of a large number of vacancies in their structure. Thus, according to the results of X-ray diffractometry, it was found that the obtained substance is a single-phase isometric nanocrystals of a cubic solid solution of CoO–NiO, which are weakly crystallized and characterized by an imperfect structure.

SEM images (Fig. 2) also show that obtained nanocomposite of CoO–NiO consists of ultrafine isometric crystallites – there is no noticeable anisotropy in the morphology of individual nanocrystals. Thus obtained electrode material is a film several microns thick, which consists of ultrafine nanocrystals mentioned above. The EDX analysis shows that Ni/Co ratio in synthesized nanocrystals is equal to 45.4 % / 54.6 %, so main components (CoO and NiO) are in solid solution in an almost equal molar ratio.

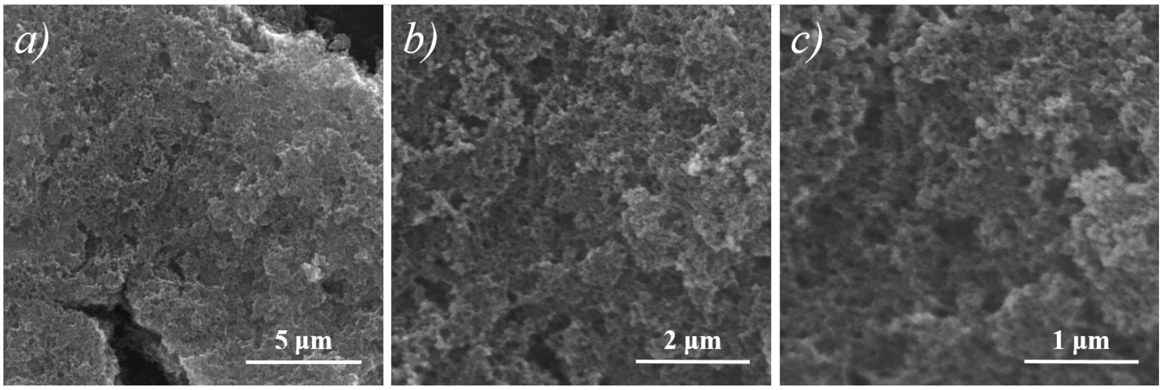

FIG. 2. SEM images of the synthesized nanocrystals of CoO–NiO solid solution at various magnifications (a–c)

The electrocatalytic properties of the CoO–NiO solid solution in the form of thin film on the nickel substrate, as an electrode for hydrogen evolution reaction, were studied by linear voltammetry methods at a constant potential sweep speed and by chronoamperometry. The voltammetry results are presented in Fig. 3. The overpotential value for pure CoO, pure NiO and CoO–NiO solid solution samples was determined and it reaches, respectively, −277, −233, and −240 mV at a current density of 10 mA/cm^2. These results indicate that the absolute value of overpotential for pure nickel oxide (−233 mV) is significantly lower than for pure cobalt oxide (−277 mV). But when considering a CoO–NiO solid solution, the absolute value of the overpotential increases slightly (to −240 mV) and is closer to pure nickel oxide (−233 mV), so the CoO–NiO solid solution still seems to be a promising electrocatalyst.

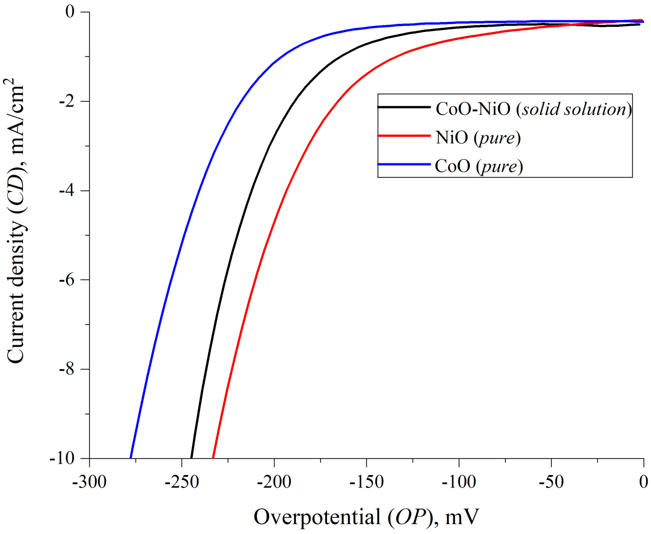

FIG. 3. Polarization curves of CoO–NiO solid solution, and pure NiO and CoO

The Tafel slope was also calculated (Fig. 4) from the measured current-voltage curves. It is an important microkinetic characteristic of the catalyst, which shows its efficiency over a wide range of overpotentials. The Tafel slope for CoO–NiO solid solution, pure NiO, and CoO samples was 78, 94, and 76 mV/dec, respectively. Thus, the Tafel slope for the CoO–NiO solid solution (78 mV/dec) is low and very close to that for pure cobalt oxide (76 mV/dec), which characterizes the synthesized material as stable and effective for electrodes working in a wide range of overpotential values. The Tafel slope for pure nickel oxide (94 mV/dec) is much higher in comparison with the substances considered and indicates its low functional prospects as a material base for electrocatalytic hydrogen evolution.

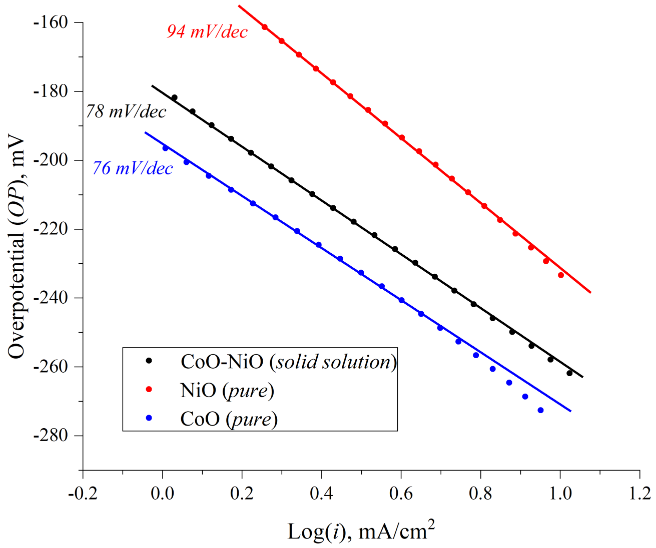

FIG. 4. The Tafel slope of CoO–NiO solid solution, and pure NiO and CoO

For CoO–NiO solid solution and pure NiO and CoO samples, cyclic stability was measured after 100 charge-discharge cycles (Fig. 5).

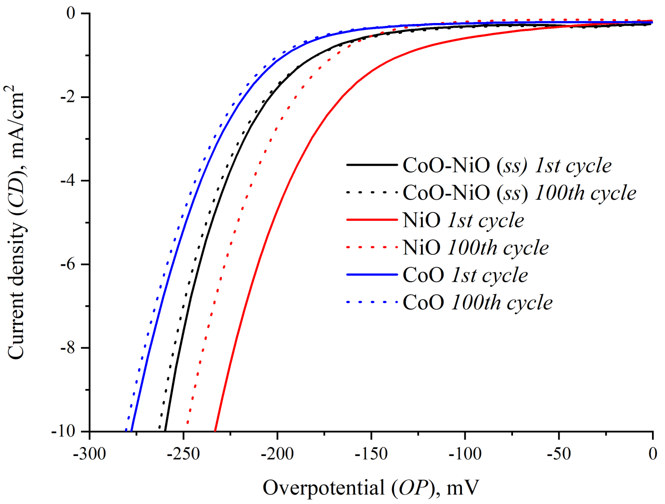

FIG. 5. Cyclic stability of CoO–NiO solid solution, and pure NiO and CoO after 100 charge-discharge cycles

As one can see, the cyclic stability of the CoO–NiO solid solution is at the level of pure CoO and much better than for pure NiO: the electrode degradation for both CoO–NiO and CoO is only 3 mV, while for pure nickel oxide, it is higher than 15 mV. Thus, the inclusion of cobalt into the composition of nickel oxide just slightly increases the overpotential of hydrogen evolution for this catalyst, but it noticeably decreases the Tafel slope as compared with pure nickel oxide, which promotes their best microkinetic characteristics as well as decrease electrode degradation after 100 cycles of cyclic voltammetry.

4. Conclusion

Nanocrystalline CoO–NiO solid solution was synthesized by successive ionic layer deposition. XRD and SEM analysis show that the sample consists of 3 – 5 nm isometric crystallites. EDX investigation confirmed the Ni/Co ratio equal to 45.4 % / 54.6 %. Electrochemical investigation of the CoO–NiO-based electrode shows overpotential values of -240 mV at a current density of 10 mA/cm^2 and Tafel slope values of 78 mV/dec for hydrogen evolution from water-ethanol solution (10 % vol.). And finally, it was shown that synthesized CoO–NiO solid solution is much more stable, then pure NiO in cyclic voltammetry (3 mV vs 15 mV electrode degradation after 100 cycles). Thus, nanocrystalline CoO–NiO solid solution synthesized by the SILD method could be used as an effective and stable electrode material for hydrogen production via electrocatalytic reforming.

References

[1] Lefevre M., Proietti E., Jaouen F., Dodelet J.P. Iron-based catalysts with improved oxygen reduction activity in polymer electrolyte fuel cells. *Science*, 2009, **324**, P. 71–74.

[2] Joya K.S., Joya Y.F., Ocakoglu K., van de Krol R. Water-splitting catalysis and solar fuel devices: artificial leaves on the move. *Angew. Chem.*, 2013, **52**, 10426.

[3] Adeniyi A.G., Ighalo J.O. A review of steam reforming of glycerol. *Chemical Papers*, 2019, **73**, P. 2619–2635.

[4] Iulianelli A., Liguori S., Wilcox J., Basile A. Advances on methane steam reforming to produce hydrogen through membrane reactors technology: A review. *Catalysis Reviews*, 2016, **58**, P. 1–35.

[5] Mishra P., Singh L., et al. NiO and CoO nanoparticles mediated biological hydrogen production: Effect of Ni/Co oxide NPs-ratio. *Bioresource Technology Reports*, 2019, **5**, P. 364–368.

[6] Juodkazis K., Juodkazyte J., et al. Photoelectrolysis of water: Solar hydrogen–achievements and perspectives. *Optic Express*, 2010, **18**, 147.

[7] Jia J., Seitz L.C., et al. Solar water splitting by photovoltaic-electrolysis with a solar-to-hydrogen efficiency over 30 %. *Nature Communications*, 2016, **7**, 13237.

[8] Rashid M., Al Mesfer M.K., Naseem H., Danish M. Hydrogen production by water electrolysis: a review of alkaline water electrolysis, PEM water electrolysis and high temperature water electrolysis. *IJEAT*, 2015, **4**, 2249–8958.

[9] Ogawa T., Takeuchi M., Kajikawa Y. Analysis of trends and emerging technologies in water electrolysis research based on a computational method: a comparison with fuel cell research. *Sustainability*, 2018, **10**, 478.

[10] Kodintsev I.A., Martinson K.D., Lobinsky A.A., Popkov V.I. Successive ionic layer deposition of Co-doped Cu(OH)$_2$ nanorods as electrode material for electrocatalytic reforming of ethanol. *Nanosystems: Physics, Chemistry, Mathematics*, 2019, **10** (5), P. 573–578.

[11] Dmitriev D.S., Popkov V.I. Layer by layer synthesis of zinc-iron layered hydroxy sulfate for electrocatalytic hydrogen evolution from ethanol in alkali media. *Nanosystems: Physics, Chemistry, Mathematics*, 2019, **10** (4), P. 480–487.

[12] Wu. G., Zelenay P. Nanostructured nonprecious metal catalysts for oxygen reduction reaction. *Acc. Chem. Res.*, 2013, **46**, 1878.

[13] Staszak-Jirkovsky J., Malliakas C.D., et al. Design of active and stable Co-Mo-S$_x$ chalcogens as pH-universal catalysts for the hydrogen evolution reaction. *Nat. Mater.*, 2016, **15**, P. 197–204.

[14] Yuan J., Wu J., et al. Facile synthesis of single crystal vanadium disulfide nanosheets by chemical vapor deposition for efficient hydrogen evolution reaction. *Adv. Mater.*, 2015, **27**, P. 5605–5609.

[15] Popczun E.J., Read C.G., et al. Highly active electrocatalysis of the hydrogen evolution reaction by cobalt phosphide nanoparticles. *Angew. Chem.*, 2014, **53**, P. 5427–5430.

[16] Xu Y., Wu R., et al. Anion-exchange synthesis of nanoporous FeP nanosheets as electrocatalysts for hydrogen evolution reaction. *Chem. Commun.*, 2013, **49**, P. 6656–6658.

[17] Kozejova M., Latyshev V., et al. Evaluation of hydrogen evolution reaction activity of molybdenum nitride thin films on their nitrogen content. *Electrochim. Acta*, 2019, **315**, P. 9–16.

[18] Chebanenko M.I., Zakharova N.V., Lobinsky A.A., Popkov V.I. Ultrasonic-assisted exfoliation of graphitic carbon nitride and its electrocatalytic performance in process of ethanol reforming. *Semiconductors*, 2019, **53** (16), P. 28–33.

[19] Guo S., Zhang S., Wu L., Sun S. Co/CoO nanoparticles assembled on graphene for electrochemical reduction of oxygen. *Angew. Chem. Int. Ed. Engl.*, 2012, **51**, P. 11770–11773.

[20] Xu Y.-F., Gao M.-R., et al. Nickel/nickel(II) oxide nanoparticles anchored onto cobalt(IV) diselenide nanobelts for the electrochemical production of hydrogen. *Angew. Chem.*, 2013, **52**, P. 8546–8550.

[21] Danilovic N., Subbaraman R., et al. Enhancing the alkaline hydrogen evolution reaction activity through the bifunctionality of Ni(OH)$_2$/metal catalysts. *Angew. Chem.*, 2012, **51**, P. 12495–12498.

[22] Lobinsky A.A., Tolstoy V.P., Gulina L.B. A novel oxidation-reduction route for successive ionic layer deposition of NiO$_{1+x}\cdot n$H$_2$O nanolayers and their capacitive performance. *Mater. Res. Bull.*, 2016, **76**, P. 229–234.

[23] Lobinsky A.A., Tolstoy V.P. Red-ox reactions in aqueous solutions of Co(OAc)$_2$ and K$_2$S$_2$O$_8$ and synthesis of CoOOH nanolayers by the SILD method. *Nanosystems: Phys. Chem. Math.*, 2015, **6**, P. 843–849.

[24] Tolstoy V.P. Successive ionic layer deposition. The use in nanotechnology. *Russ. Chem. Rev.*, 2006, **75**, 161.

[25] Popkov V.I., Tolstoy V.P. Peroxide route to the synthesis of ultrafine CeO$_2$–Fe$_2$O$_3$ nanocomposite via successive ionic layer deposition. *Heliyon*, 2019, **5** (3), e01443.

[26] Popkov V.I., Tolstoy V.P., Omarov S.O., Nevedomskiy V.N. Enhancement of acidic-basic properties of silica by modification with CeO$_2$–Fe$_2$O$_3$ nanoparticles via successive ionic layer deposition. *Applied Surface Science*, 2019, **473**, P. 313—17.

NANOSYSTEMS: PHYSICS, CHEMISTRY, MATHEMATICS, 2019, 10 (6), P. 686–693

Effect of doping with 'se' on structural, optical, electrical and thermoelectric properties of multilayers of $Bi_2Te_{2.7}Se_{0.3}$ / Sb_2Te_3 to enhance thermoelectric performance

M. Kumari, Y. C. Sharma

Department of Physics, Vivekananda Global University, jagatpura, Jaipur-303012, Rajasthan, India

mjmanisha209@gmail.com

DOI 10.17586/2220-8054-2019-10-6-686-693

Selenium is known to be a semiconductor with many applications, and when it is doped in some chemical compounds, it changes the electrical properties of that compound which directly affect its thermoelectric performance. The present work is to synthesized multilayers of $Bi_2Te_{2.7}Se_{0.3}$ / Sb_2Te_3 by e-beam evaporation technique on glass substrate at room temperature. Prepared thin films were characterized by XRD and also study their electrical, optical and thermoelectrical properties to enhance the thermoelectric performance of Thermoelectric (TE) devices.

Keywords: thermoelectric, $Bi_2Te_{2.7}Se_{0.3}$, Sb_2Te_3, Figure of merit (ZT).

Received: 8 November 2019

Revised: 1 December 2019

1. Introduction

Thermoelectrics is a promising area for the conversion of any type of waste heat into electricity and suitable for power generation. The initial applications of thermoelectric materials was in spacecraft such as in Cassini, Voyager, and New Horizons [1,2]. But now they have many other applications, such as in microcoolers and generators, in CCD technologies, and in infrared detectors. The unique property of thermoelectric devices for conversion of environmental waste heat introduced the elegant concept of harvesting energy from body. The source of energy from a body is thermal energy, which can be utilized and converted into self-powered wearable device [3]. To make a body-wearable device, the heat exchange from hot side to cold side is limited due to large inrefficient thermal resistances [4]. It should be remember that the material used for body-wearable device should have low thermal conductivity. Generally TE devices are not practically applicable, due to their low efficiency. Much research has been done in this field to increase the thermoelectric efficiency. The thermoelectric efficiency is directly dependent on a dimensionless quantity known as Figure of merit (ZT). Higher ZT values of lead to large thermoelectric efficiency. ZT directly depends on electrical conductivity and Seebeck coefficient and inversely proportional to thermal conductivity. The formula for figure of merit ZT= $S^2\sigma T/k$, where S is Seebeck coefficient, σ is electrical conductivity and k is thermal conductivity and T is absolute temperature. Much research has been done to increase the value of electrical conductivity and Seebeck coefficient by selecting an appropriate material. Bi_2Te_3 is most promising thermoelectric material showing good thermoelectric properties at room temperature, which can be used for many applications. Recent research on n-type Bi_2Te_3 alloys showing high ZT using nanostructuring [5–7], nonoelusions [8], texturing [9] and point defect engineering [10]. In many researches, it was found that n-type Bi_2Te_3 compounds have been shown high value of ZT but still they are not suitable for practical applications such as harvesting body heat due to non-optimized properties at room temperature. So, high value of ZT of a material with optimizing transport property at room temperature is required. To satisfy the above requirement recent researches are focused on decreasing lattice thermal conductivity by preparing superlattice structures. Recent enhancements have been done by Venkatasubramanian by fabricating superlattice structures of Bi_2Te_3 / Sb_2Te_3 with high figure of merit 2.4. For body heat harvesting applications, high value of σ and S with relatively low value of K is required at room temperature. So, as it is known that bismuth telluride has been shown to possess the best thermoelectric properties at room temperature and when it is doped with Sb, Se or with some other element it becomes an efficient thermoelectric material. Doping is a very common technique for the improvement in thermoelectric properties by increasing electrical conductivity and decreasing thermal conductivity as doping increased electron-phonon scattering. It has been reported that doping of elements like C, Sn, Pb, O, S, Se can increase the thermoelectric properties of Bi_2Te_3 [11–16]. Superlattice structures are focused on either a multilayered hetrojunction arrangement or by doping in one of the material to form a series of homojunctions [17]. It has been observed that appropriate amount of doping into a superlattice structure can make high performance thermoelectric module and can also develop new properties [18]. Thus, the present work is focused on the synthesis of multilayered $Bi_2Te_{2.7}Se_{0.3}$ / Sb_2Te_3 structures to fulfill the above requirement.

2. Experimental details

All the samples single layer $Bi_2Te_{2.7}Se_{0.3}$ and Sb_2Te_3 (50 nm) each, their bilayer $Bi_2Te_{2.7}Se_{0.3}$–Sb_2Te_3 (103 nm), 5 layers of thickness (510 nm) and 10 layers of total thickness (1024 nm) are fabricated on clean glass substrate by e-beam evaporation technique. The thickness of the films was measured from quartz crystal thickness monitor of vacuum coating unit. The $Bi_2Te_{2.7}Se_{0.3}$ and Sb_2Te_3 are purchased in the powder form from Sigma Company with 99.99% purity. Substrate were cleaned with acetone and dried at room temperature. All the thin films are deposited in a vacuum chamber under the pressure of $\sim 10^{-6}$ Pa with rate of evaporation for $Bi_2Te_{2.7}Se_{0.3}$ was ~2Å/Sec. and for Sb_2Te_3 is ~10Å/Sec. Structural properties are analyzed by XRD in Banasthali Vidyapeeth, Banasthali. The electrical properties like hall measurement, Carrier concentration, mobility, conductivity, sheet resistance and I–V measured were carried out through four probe method in MNIT, Jaipur. The optical properties were measured by LAMBDA 750 (Perkin Elmer) in MNIT, Jaipur to determine the band gap of the samples.

3. Results and discussion. Structural properties

3.1. X-RAY Diffraction (XRD)

The Xrd pattern of multilayers of $Bi_2Te_{2.7}Se_{0.3}$ / Sb_2Te_3 of different thicknesses from ~(50–1000 nm) has been shown in Fig. 1. The main peaks observed in single layer $Bi_2Te_{2.7}Se_{0.3}$ are at 23.46°, 28.28° and 41.05°. There is no peak observed in Sb_2Te_3 which confirms its non- crystalline or amorphous nature. As thicknesses of the samples increases more number of peaks is generated at angles 50.44°, 64.86° and 66.20°, which cannot be observed in single layer $Bi_2Te_{2.7}Se_{0.3}$. The intensity of the peaks is increased, which confirms that crystallinity of the thin films increases as number of alternate layer increases. The Xrd patterns of the multilayer structure of $Bi_2Te_{2.7}Se_{0.3}$ / Sb_2Te_3 are well matched with Xrd pattern in paper of [19].

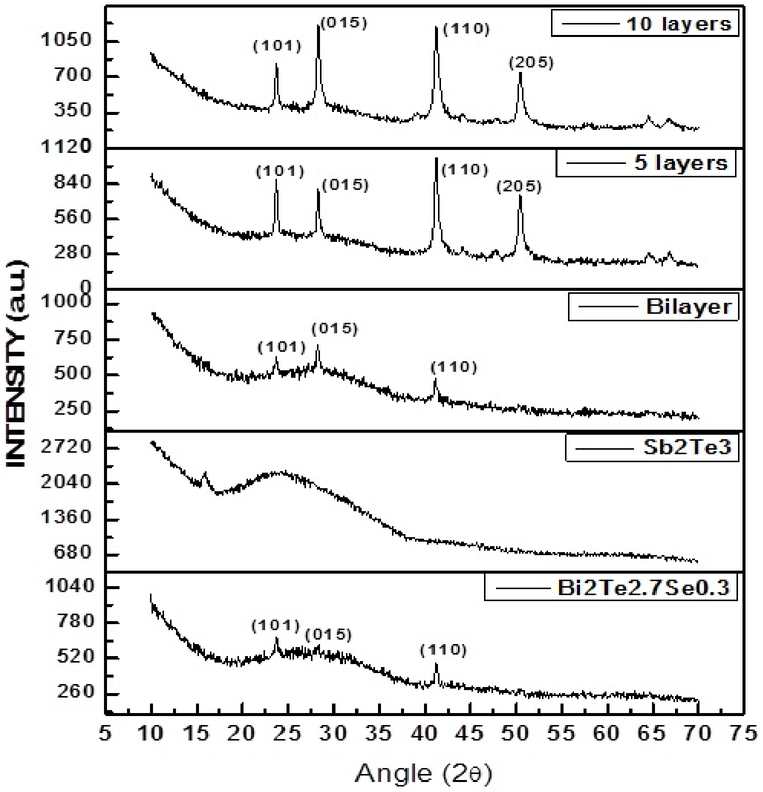

FIG. 1. XRD pattern of multilayers of $Bi_2Te_{2.7}Se_{0.3}$ / Sb_2Te_3 at room temperature

3.1.1. Grain Size. The grain size of the samples of different thicknesses can be calculated using Scherer's formula:

$$D = \frac{k\lambda}{\beta \cos\theta} \tag{1}$$

The calculated structural parameters Full width at half maxima (FWHM), Grain size (D), microstrain (ε), and dislocation density (δ) for alternate layers of $Bi_2Te_{2.7}Se_{0.3}$ / Sb_2Te_3 of various thicknesses ranging from (50–1000 nm) for (0 1 5) orientation have been shown in Table 1.

TABLE 1. The calculated structural parameters, Full width at half maxima (FWHM), Grain size (D), microstrain (ε), and dislocation density (δ) for alternate layers of $Bi_2Te_{2.7}Se_{0.3}$ / Sb_2Te_3 for (0 1 5) orientation

Samples	FWHM β^0	Grain Size(D) (nm)	Strain ($\varepsilon \cdot 10^{-4}$) (lines^{-2}m^{-4})	Dislocation density ($\delta \cdot 10^{13}$) (lines/m^2)
$Bi_2Te_{2.7}Se_{0.3}$ (50 nm)	0.2172	37.76	9.18	70.13
Sb_2Te_3(53 nm)	0.492	16.29	21.26	376.84
Bilayer (103 nm)	0.1855	44.28	7.84	51.00
5 layers (510 nm)	0.2052	39.94	8.67	62.68
10 layers (1024 nm)	0.2879	28.47	12.17	123.37

Where D is the grain size, k is the shape factor (0.94), λ is the wave length of X-ray source (1.5406 Å), θ is the Bragg's angle and β is full width at half maxima.

3.1.2. Microstrain. The microstrain (ε) is developed in thin films is the root mean square of variations in lattice parameters. It can be calculated from the relation:

$$\varepsilon = \frac{\beta \cos\theta}{4} \tag{2}$$

3.1.3. Dislocation density. Dislocation in Xrd is an imperfection in crystal which occurs due to misregistry of lattice in one part with another part of the lattice [17]. The dislocation density (δ) is the length of dislocation lines per unit volume of crystal and it can be determined by the relation:

$$\delta = \frac{1}{D^2} \tag{3}$$

3.2. Scanning Electron Microscopy (SEM)

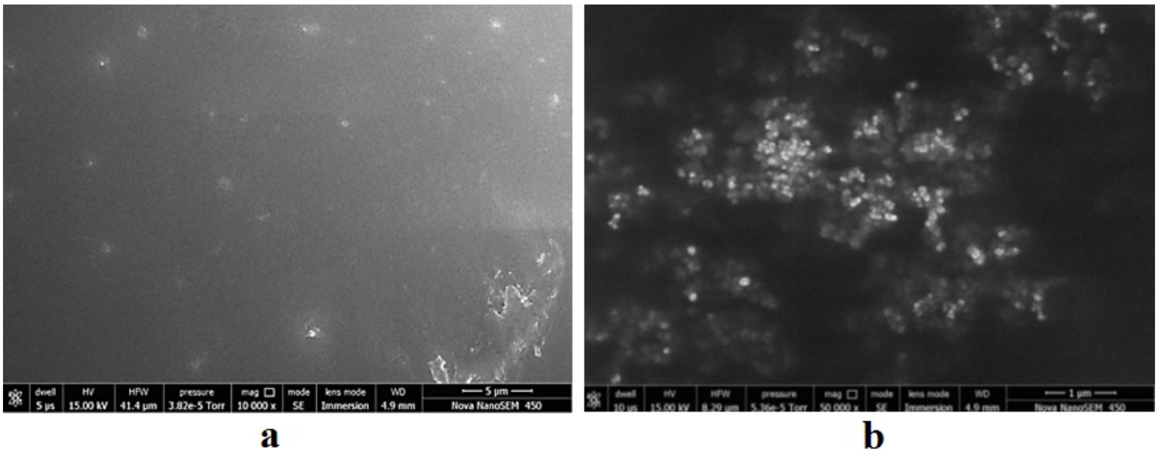

FIG. 2. SEM images of (a) $Bi_2Te_{2.7}Se_{0.3}$ (b) Sb_2Te_3

The SEM images of single layer of $Bi_2Te_{2.7}Se_{0.3}$ and Sb_2Te_3 are shown in Fig. 2. The average grain size from SEM analysis for $Bi_2Te_{2.7}Se_{0.3}$ and Sb_2Te_3 sample is ∼44 nm and 20 nm. It was observed that crystallinity and grain size increase from single layer $Bi_2Te_{2.7}Se_{0.3}$ to bilayer. These results are in good agreement with XRD results.

4. Electrical properties

4.1. I–V Measurements

Figure 3 shown the I–V behavior of multilayers of $Bi_2Te_{2.7}Se_{0.3}$ / Sb_2Te_3 at room temperature. The current is flowing through the samples in milliampere range. The graph shows that slope of the curves increase with thicknesses which determine the conductivity of the sample. It is also been observed that single layer $Bi_2Te_{2.7}Se_{0.3}$ and Sb_2Te_3 show almost linear behavior but a nonlinear behavior is observed as thickness increases up to 5 layers. The semiconducting behavior of the curves increases with thickness which shows that decreasing conductivity.

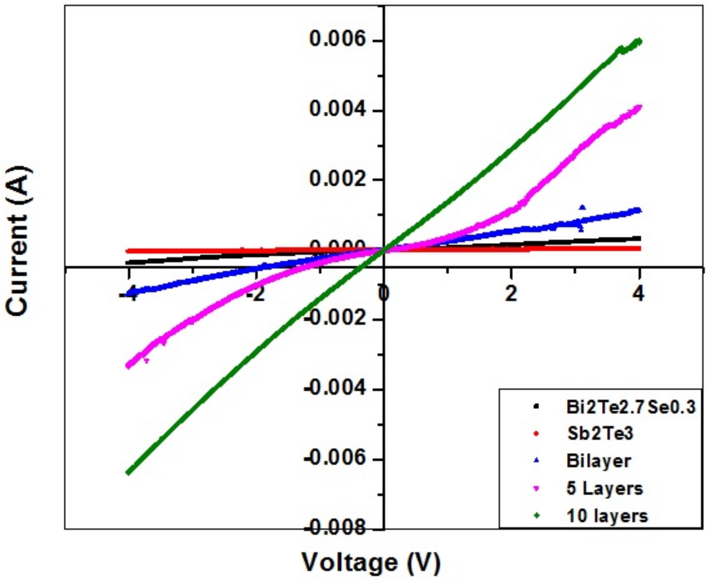

FIG. 3. I–V curves of multilayers of$Bi_2Te_2Se_{0.3}$ / Sb_2Te_3 at room temperatures

4.2. Hall measurements

Table 2 shows the measured Electrical conductivity, Sheet resistance, Bulk carrier concentration, Hall coefficient, mobility and magneto resistance of the Se doped $Bi_2Te_{2.7}Se_{0.3}$, Sb_2Te_3, Bilayer, 5 layers, 10 layers at room temperature. It has been observed that highest electrical conductivity is examined for single layer $Bi_2Te_{2.7}Se_{0.3}$ of 2.43· (10^2 Ω·m)$^{-1}$ and decreases as thickness of alternate layers increases.

TABLE 2. Represents Electrical properties of multilayers of $Bi_2Te_{2.7}Se_{0.3}$ / Sb_2Te_3

Samples	Bulk conc. (10^{21})	Sheet resistance (10^3 Ω)	Conductivity (10^2 Ω·cm)$^{-1}$	Hall coefficient, R_H (10^{-3}cm^3/C)	Mobility, μ (cm^2/V·sec.)	Magneto resistance (10^{-1})
$Bi_2Te_{2.7}Se_{0.3}$	1.38	0.815	2.43	4.58	1.10	0.56
Sb_2Te_3	2.64	1.00	1.87	2.35	4.58	16100
Bilayer	0.67	0.984	0.99	9.23	1.58	1.11
5 layers	0.13	0.207	0.95	3.42	4.30	1.93
10 layers	0.12	0.152	0.64	2.53	5.77	0.50

In order to examine the electronic transport properties, Bulk carrier concentration (n), mobility (μ) and Hall coefficient (R_H) were measured at room temperature. The sign of Hall coefficient was positive for all the samples. It shows that main electrical charge carriers are hole and showing p-type semiconducting behavior. The maximum value of hall coefficient 9.23·(10^{-3} cm^3/C) is found for bilayer sample but decreases as thickness of the sample was further increases. A high value of carrier concentration of (10^{21}) is achieved for all the samples and decrease with thickness. Mobility increases as the number of alternate layers increases. Maximum mobility 5.77 (cm^2/V·sec.) and minimum carrier concentration $0.12 \cdot 10^{21}$ is found to be for 10-layered sample.

Magneto resistance is also an important parameter to study in the field of thermoelectricity which is the tendency of material to change its electrical resistance on the application of eternal magnetic field. In multilayer system tunnel junctions are formed that's why the term giant magnetoresistance (GMR) is used. A high GMR is achieved for single layered Sb_2Te_3 which shows that maximum change in resistance is observed for Sb_2Te_3 on the application external magnetic field.

5. Optical properties

In optical properties, absorbance spectra of all the samples with different thickness were recorded using UV-VIS-NIR double beam spectrometer in the range of (200–1100) nm. Fig. 4 show the optical absorption spectra of single layer $Bi_2Te_{2.7}Se_{0.3}$, Sb_2Te_3 and Bilayer sample. It is obvious that absorption increases with thickness. But, as the thickness increases to 5 or 10 layers, the absorbance pattern was not clearly observed. Because as thickness of the sample is large, the absorbance is greater and only some part of the light will be transmitted through the sample. It is clearly observed from the graph that low absorbance is found in 300–350 nm region which lies in visible region. For all the three samples maximum absorbance was found only at one position which confirms the uniformity of the sample.

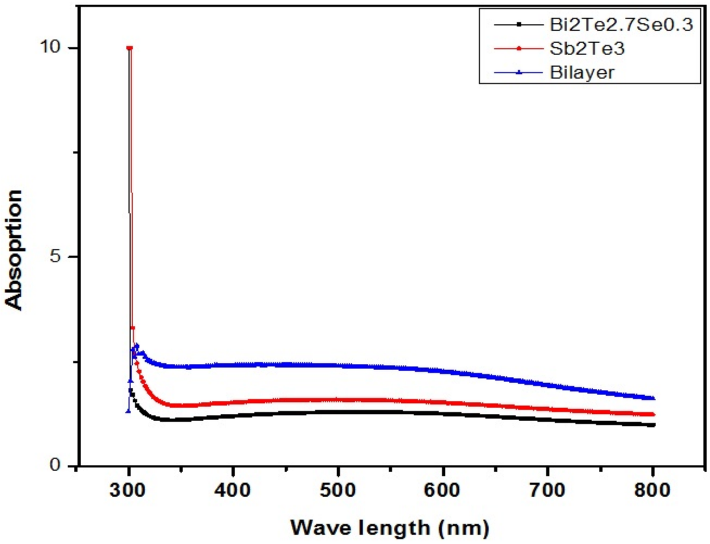

FIG. 4. Show the optical absorption spectra of $Bi_2Te_{2.7}Se_{0.3}$, Sb_2Te_3 and Bilayer sample

The absorption coefficient (α) is determined from transmittance measurements using relation [20]:

$$\alpha = \frac{2.303}{d} \log_{10} \frac{1}{T} \tag{4}$$

where T is transmittance and d is the thickness of the film.

The electronic transition between valence band and conduction band can also be calculated from absorption coefficient using:

$$\alpha = A(h\nu - E_g)^p \tag{5}$$

where A is constant, E_g is the optical band gap, $h\nu$ is incident photon energy and P has discrete values like $\frac{1}{2}$, $\frac{3}{2}$, $\frac{4}{2}$,... etc., depending upon the transition. For direct and allowed transition $P = \frac{1}{2}$, in direct but forbidden case $P = \frac{3}{2}$, and for indirect and allowed transition $P = 2$ and for forbidden case it will be 2 or more. The band gap is determined by extrapolation on x-axis in curve between $(\alpha h\nu)^2$ and $h\nu$. The optical band gap has been determined for different thickness shown in Fig. 5. It has been shown that band gap increases with thickness up to the bilayer and then decreases for 5-layered sample. The graphs show the direct and allowed transitions. These values of band gaps E_g for $Bi_2Te_{2.7}Se_{0.3}$, Sb_2Te_3. Bilayer and layers are 1.34, 1.72, 1.56, 1.22 eV. The variation in band gaps is due to variation in grain size and dislocation density. As dislocation density is high resulting in high band gap of a semiconductor because presence the separation distance of dislocations are greater than interatomic distance [21]. The results are in good agreement with the results of XRD shown in Table 2.

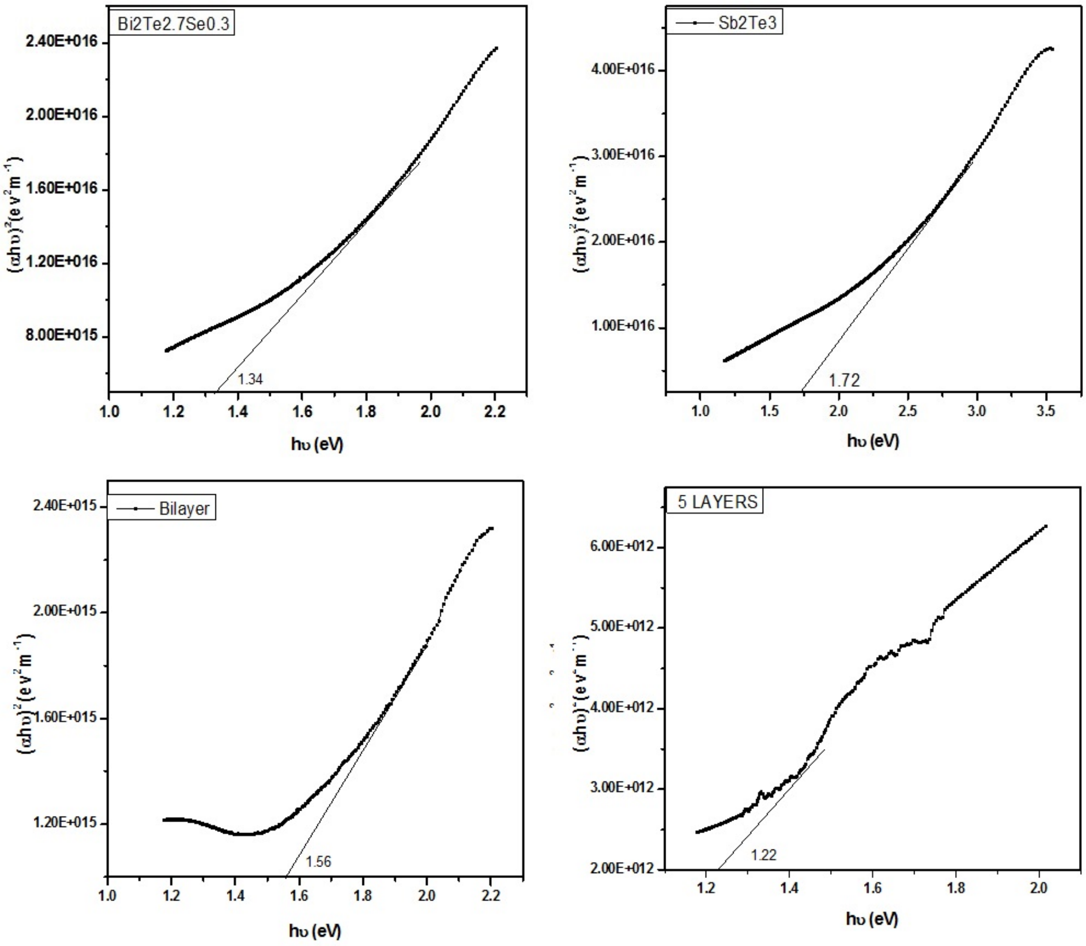

FIG. 5. Band gaps of $Bi_2Te_{2.7}Se_{0.3}$–Sb_2Te_3 thin films

5.1. Thermoelectric Properties

TABLE 3. Represents the Thermoelectrical properties of multilayers of Bi_2Te_3–Sb_2Te_3

Sample details	Seebeck coefficient S (μV/K)	Resistivity ρ ($\mu\Omega\cdot$m)	Power factor ($10^{-3}\cdot$W/m$\cdot$K^2)
$Bi_2Te_{2.7}Se_{0.3}$	−87	41.15	0.183
Sb_2Te_3	210	53.4	0.825
Bilayer	238	101.0	0.560
5 layers	167	105.2	0.265
10 layers	123	156.2	0.096

In thermoelectric measurements, Seebeck coefficients of the samples were measured at room temperature. The Seebeck coefficient, resistivity and power factor of the samples are shown in Table 3. The negative value of Seebeck coefficient for single layer $Bi_2Te_{2.7}Se_{0.3}$ shows n-type charge carrier and positive values for other samples show p-type charge carriers. The results have been shown that maximum Seebeck coefficient is achieved for bilayer sample but Power factor is maximum for Sb_2Te_3. The variations in Seebeck coefficient and power factor are shown in Fig. 6.

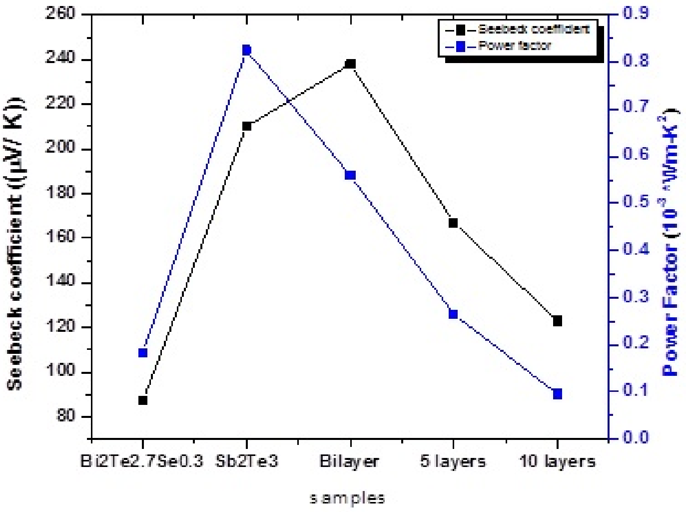

FIG. 6. Seebeck coefficient and power factor of $Bi_2Te_{2.7}Se_{0.3}$–Sb_2Te_3 thin films

6. Conclusion

The multilayered thin films of $Bi_2Te_{2.7}Se_{0.3}$ / Sb_2Te_3 variable thickness from (50–1000) nm were deposited on glass substrate at room temperature by using e-beam evaporation technique. The effect of thickness on structural, electrical and optical properties was studied. XRD studies indicates that the single layer $Bi_2Te_{2.7}Se_{0.3}$ thin film showed polycrystalline nature with preferred orientation along (0 1 5) plane, whereas the single layer Sb_2Te_3 show non crystalline or amorphous nature. Also, as the number of layers increases, the intensity of the planes also increases, which shows that crystallinity increases with thickness. The grain size also increases from single layer to bilayer, but after that, it decreases as the number of layers further increases. SEM analysis shows that single layer $Bi_2Te_{2.7}Se_{0.3}$ and Sb_2Te_3 have average grain size around 44 nm and 20 nm respectively. Results of I–V curve shows that slope increases with thickness and in electrical properties conductivity and charge carrier concentration decreases, whereas mobility increases with thickness. The optical properties show that absorption of all the samples were near visible region and optical transition was found to be direct and allowed. The energy band gap varies with thickness and lies between (1.34–1.72) eV. The maximum band gap was found for Sb_2Te_3. In thermoelectric measurements, the maximum Seebeck was found for Bilayer sample, but the power factor was maximum for single layer Sb_2Te_3.

References

[1] Nozariasbmarz A., Krasinski J.S., Vashaee D., N-Type Bismuth Telluride Nanocomposite Materials Optimization for Thermoelectric Generators in Wearable Applications. *Materials*, 2019, **12**(9), P. 1529.

[2] Schmidt G.R., Sutliff T.J., Dudzinksi L.A. Radioisotope Power: A Key Technology for Deep Space Exploration. In: Singh N., editor. Radioisotopes-Applications in Physical Science. InTech, London, UK, 2011. p. 419.

[3] Bell L.E. Cooling, Heating, Generating Power, and Recovering Waste Heat with Thermoelectric Systems. *Science*, 2008, **321**, P. 1457.

[4] Suarez F., Nozariasbmarz A., Vashaee D., Öztürk M.C. Designing thermoelectric generators for self-powered wearable electronics. *Energy Environment Science*, 2016, **9**, P. 2099–2113.

[5] Yan X., Poudel B., Ma Y., Liu W.S., Joshi G., Wang H., Lan Y.C., Wang D.Z., Chen G., Ren Z.F. Experimental studies on anisotropic thermoelectric properties and structures of n-type $Bi_2Te_{2.7}Se_{0.3}$. *Nano Lett.*, 2010, **10**, P. 3373.

[6] Liu W.S., Zhang Q., Lan Y., Chen S., Yan X., Zhang Q., Wang H., Wang D., Chen G., Ren Z. Thermoelectric Property Studies on Cu-Doped n-type $Cu_xBi_2Te_{2.7}Se_{0.3}$ nanocomposites. *Adv. Energy Mater*, 2011, **1**, P. 577.

[7] Hong M., Chasapis T.C., Chen Z.G., Yang L., Kanatzidis M.G., Snyder G.J., Zou J. n-type $Bi_2Te_{3-x}Se_x$ Nanoplates with Enhanced Thermoelectric Efficiency Driven by Wide Frequency Phonon Scatterings and Synergistic Carrier Scatterings. *ACS Nano*, 2016, **10**, P. 4719.

[8] Song S., Wang J., Xu B., Lei X., Jiang H., Jin Y., Zhang Q., Ren Z. Thermoelectric properties of n-type $Bi_2Te_{2.7}Se_{0.3}$ with addition of nano-ZnO:Al particles. *Material Research Express*, 2014, **1**, P. 035901.

[9] Hu L.P., Liu X.H., Xie H.H., Shen J.J., Zhu T.J., Zhao X.B. Improving thermoelectric properties of n-type bismuth–telluride-based alloys by deformation-induced lattice defects and texture enhancement. *Acta Mater.*, 2012, **60**, P. 4431.

[10] Hu L., Zhu T., Liu X., Zhao X. Point Defect Engineering of High-Performance Bismuth-Telluride-Based Thermoelectric Materials. *Adv. Funct. Mater.*, 2014, **24**, P. 5211–5218.

[11] Tortoich R., Choi J.W. Inkjet. Printing of Carbon Nanotubes. *Nanomaterials*, 2013, **3**(3), P. 453.

[12] Fukuda K., Someya T. Recent Progress in the Development of Printed Thin Film Transistors and Circuits with High Resolution Printing Technology. *Advanced Materials*, 2016, **29**, P. 1–22.

[13] Morgan K.A. et al. *Tuneable sputtered films by doping for wearable and flexible thermoelectrics*. Presented at Materials Research Society Fall, Boston, USA, 2017.

[14] Zhou Y., Li L., Tan Q., Li J.-F. Thermoelectric properties of Pb-doped bismuth telluride thin films deposited by magnetron sputtering. *Journal of Alloys and Compounds*, 2014, **590**, P. 362.

[15] Fan P. et al. Low-cost flexible thin film thermoelectric generator on zinc based thermoelectric materials. *Applied Physics Letters*, 2015, **106**, P. 073.

[16] Zheng S.H. et al. Using high thermal stability flexible thin film thermoelectric generator at moderate temperature. *Applied Physics Letters*, 2018, **112**, P. 163.

[17] Albuquerque E.L., Michael Cottam, Surface Plasmon- and Phonon-Polaritons. In book: Polaritons in Periodic and Quasiperiodic Structures, P. 65–87.

[18] Il-Ho Kim, Soon-Mok Choi, Won-Seon Seo, Dong-Ik Cheong, Hyung Kang. Thermoelectric properties of cu-dispersed $Bi_2Te_{2.7}Se_{0.3}$ nanocomposites, 18th international conference on composite materials, Korea.

[19] Sathyamoorthy R., Dheepa J. Structural characterization of thermally evaporated Bi_2Te_3 thin films. *Journal of Physics and Chemistry of Solids*, 2007, **68**, P. 111.

[20] Dheepa J., Sathyamoorthy R., Subbarayan A. Optical properties of thermally evaporated Bi_2Te_3 thin films. *Journal of Crystal Growth*, 2005, **274**, P. 100–105.

[21] Deshmukh G.D., Patil S.M., Patil S.S., Pawar P.H. Effect of Film Thickness on Structural and Optical Properties of Bi_2Te_3 Thin Films. *Journal of Chemical, Biological and Physical Sciences*. 2015, **5**, P. 2769.

NANOSYSTEMS: PHYSICS, CHEMISTRY, MATHEMATICS, 2019, 10 (6), P. 694–700

Facile combustion synthesis of $TbFeO_3$ nanocrystals with hexagonal and orthorhombic structure

K. D. Martinson[1], V. A. Ivanov[2], M. I. Chebanenko[1], V. V. Panchuk[3], V. G. Semenov[3], V. I. Popkov[1]

[1]Ioffe Institute, Politeknicheskaya St., 26, St. Petersburg, 194021, Russia

[2]Saint Petersburg State Institute of Technology, Moskovsky prospect 26, Saint Petersburg, 190013, Russia

[3]Saint Petersburg State University, Peterhof, 198504 Saint Petersburg, Russia

martinsonkirill@mail.ru

PACS 61.46.+w, 75.50.Bb, 75.60.-d **DOI 10.17586/2220-8054-2019-10-6-694-700**

In this research, the formation process of nanocrystalline terbium orthoferrite ($TbFeO_3$) obtained via a solution combustion technique was studied using powder X-ray diffractometry, scanning electron microscopy, ^{57}Fe Mössbauer spectroscopy, N_2 adsorption analysis, and FTIR spectroscopy. It was shown that glycine-nitrate combustion method permits one to obtain $TbFeO_3$ of three different modifications: orthorhombic o-$TbFeO_3$ (Pbnm), hexagonal h-$TbFeO_3$ ($P6_3$/mmc) and amorphous am-$TbFeO_3$. It was found that the average crystallite sizes of orthorhombic and hexagonal $TbFeO_3$ were 29±3 and 15±2 nm, respectively. The formation mechanism of different structural forms of terbium orthoferrite was investigated on the basis of nanopowders morphology, specific surface areas, average pore sizes, and crystallite sizes.

Keywords: nanocrystals, rare earths, orthoferrites, terbium orthoferrite, $TbFeO_3$, phase formation, polymorphism.

Received: 12 October 2019

Revised: 4 December 2019

1. Introduction

During the last few decades, there has been an increased interest in the study of ferrites with various compositions due to a large number of areas of their practical application [1–3]. Unique structural and electromagnetic parameters allow the use of these type substances in the production of microwave ceramics, magnetically recoverable catalysts, magnetic devices, etc. [4–6]. Among a large number of rare-earth metal orthoferrites, terbium ferrite ($TbFeO_3$) stands out, due to its antiferromagnetic and ferroelectric properties [7]. Despite the fact that compounds of this class were actively studied for more than a decade, the discovery of new areas of use for nanostructured multiferroics in the case of which the electromagnetic properties differ significantly is an important and urgent task is to study the processes of their formation [8]. Furthermore, the discovery of the existence of metastable paramagnetic modification in a number of compounds of the type $RFeO_3$ leaves open the question of their controllable and phase-pure production [9].

Currently, terbium orthoferrite was successfully obtained in two different modifications with an orthorhombic and hexagonal structure. However, a metastable hexagonal structure was obtained only in the form of thin films and in this work, it was obtained for the first time in its bulk form via the solution combustion method. The complexity of its preparation lies in the nature of the polymorphism of terbium orthoferrite and related to the ratio of its ionic radii. According to the data presented in [10, 11], it is known that, under certain conditions, it is possible to obtain a metastable hexagonal modification of yttrium and holmium orthoferrites, due to a number of factors such as small crystallite size and inter-pore space.

The orthorhombic modification of terbium orthoferrite is a distorted perovskite-like structure Fe^{3+} cations, which are in an octahedral oxygen environment, and the Tb^{3+} cation is located in the distorted trigonal prism of O^{2-} anions. It is known from the literature that there are two types of directions of rotation of the oxygen octahedra of the rhombic structure of rare-earth metal orthoferrites that correspond to the space groups Pnma or Pbnm [12]. It should be noted that the latter type of structure is almost never encountered. The rhombic modification of o-$TbFeO_3$ is thermodynamically stable over the entire temperature range of the compound. The hexagonal modification of terbium orthoferrite corresponds to a more deformed perovskite-like structure and corresponds to the unit cell h-$TbFeO_3$ ($P6_3$/mmc) which consists of FeO_5 trigonal pyramids and yttrium Tb atom planes. Besides that, each terbium atom is in the octahedron, the structure of which is tightly packed oxygen atoms with four additional oxygen atoms along the axis c with a significant distance from the terbium atom. This explains the metastable nature of the hexagonal modification, in which case the Fe^{3+} cation is located in the center of a trigonal bipyramid.

In this work, terbium orthoferrite was obtained by the solution combustion method at various Red/Ox ratios using glycine as a fuel and a chelating agent (G/N = 0.2–1.4). The choice of this synthesis technique was made because the solution combustion method has already shown its effectiveness in obtaining metastable hexagonal modifications of rare-earth element orthoferrites of the $RFeO_3$ type [10, 11]. All obtained terbium orthoferrite powders were investigated by a complex of physicochemical methods, including determination of chemical composition, morphology, and structure.

2. Experimental

Nanocrystalline terbium orthoferrite was obtained by the glycine-nitrate combustion method using glycine as fuel at different G/N ratios in the initial mixture (G/N = 0.2–1.4) using the technology described in detail in [13, 14]. The reaction solution was prepared using nitrates of terbium ($Tb(NO_3)_3{\cdot}6H_2O$) (puris.), iron ($Fe(NO_3)_3{\cdot}9H_2O$) (puris.) and glycine ($C_2H_5NO_2$) (puris.) dissolved in 40 ml of distilled water and heated to 50 ° C. The redox ratio was calculated in such a way as to differ from the stoichiometry of the reaction in steps of 0.2:

$$G/N = \frac{n_{Gly}}{n_{NO_3^-}}$$

n_{Gly} – glycine amount of mole, $n_{NO_3^-}$ – nitrate groups amount of mole. It should be noted that in the case of a significant deviation from the stoichiometry of the reaction, a number of foreign substances (C, CO, N_2O, NO, NO_2) may form, in which case, it is difficult to accurately equalize the reaction. In this regard, the calculations were performed based on the formation of terbium orthoferrite with a stoichiometric ratio of glycine to nitrate-groups:

$$3Tb(NO_3)_3 + 3Fe(NO_3)_3 + 10C_2H_5NO_2 \rightarrow 3TbFeO_3 + 20CO_2 + 14N_2 + 25\,H_2O$$

The reaction solution thus prepared was mixed until the starting components were completely dissolved and heated until the water was almost completely removed and the self-ignition point was reached and as a result, brown powders were formed. Obtained samples were thermally treated in a muffle furnace at a temperature of 500 ° C for 2 hours to remove impurity organics and mechanically milled in a mortar.

The elemental analysis and morphology of the synthesized compositions were studied by scanning electron microscopy and energy dispersive x-ray analysis using a scanning electron microscope *Tescan Vega 3 SBH* equipped with an *Oxford INCA* x-act x-rat spectral microanalysis.

Powder X-ray diffraction analysis was performed using the method of powder x-ray diffraction on *Rigaku SmartLab 3* powder diffractometer using monochromatic CuKα radiation and *ICDD PDF-2* powder database. The average crystallite size (coherent scattering area) was determined from X-ray diffraction lines broadening using Scherrer equation:

$$D = \frac{k\lambda}{\beta\cos\theta}$$

where k is the crystal shape factor (assumed to be 0.94 in the isometric approximation), λ is the X-ray emission wavelength (CuK$_\alpha$, $\lambda = 0.15406$ nm), β is the diffraction maximum broadening with considering instrumental error (in radians), θ is the diffraction peak position (Bragg angle).

Absorption spectra of the samples and the presence of impurity organics were determined by FTIR spectroscopy on *Shimadzu IRTracer-100* in the range from 500 to 3800 cm^{-1} in absorption mode.

The state of Fe atoms in obtained compositions has been studied using Mössbauer spectrometer Wissel (Germany). Measurements have been made in absorption geometry at room temperature. Isomer shift has been evaluated with respect to α-Fe. Information about phase composition has been obtained by comparing the Mössbauer parameters of iron atom state recorded in the experiment with the data of other studies presented within literature.

The specific surface of the obtained compositions was studied using a low-temperature nitrogen (N_2) sorption-desorption method. The isotherms of all synthesized samples were obtained at the temperature of liquid nitrogen (77 K) using a *Micrometrics ASAP 2020* analyzer after vacuum degassing at 300 ° C for 5 h.

3. Results and discussion

According to energy-dispersive X-ray spectroscopy data the obtained samples correspond in their chemical composition to terbium orthoferrite ($TbFeO_3$) with a ratio of terbium atoms are close equal to 50%/50% (Fig. 1,a).

The largest deviation from the stoichiometric composition ($\approx 1\%$) is observed for the samples obtained at a ratio of G/N = 0.4 and 1.0, which lies within the error of the determination method used. The results of scanning electron microscopy demonstrate the effect of the Red/Ox ratio on the morphology of the synthesized $TbFeO_3$ powders (Fig. 1,b-h). The data obtained indicate that, with a slight deviation from stoichiometry (G/N = 0.4 and 0.8), agglomerates several microns in size consisting of nanometer-sized particles are formed. In their appearance, they resemble agglomerates of other orthoferrites obtained by solution combustion [15]. With a significant deficiency (G/N $<$ 0.4) and excess glycine (G/N $>$ 0.8), the formation of amorphous structures without pronounced differences is observed.

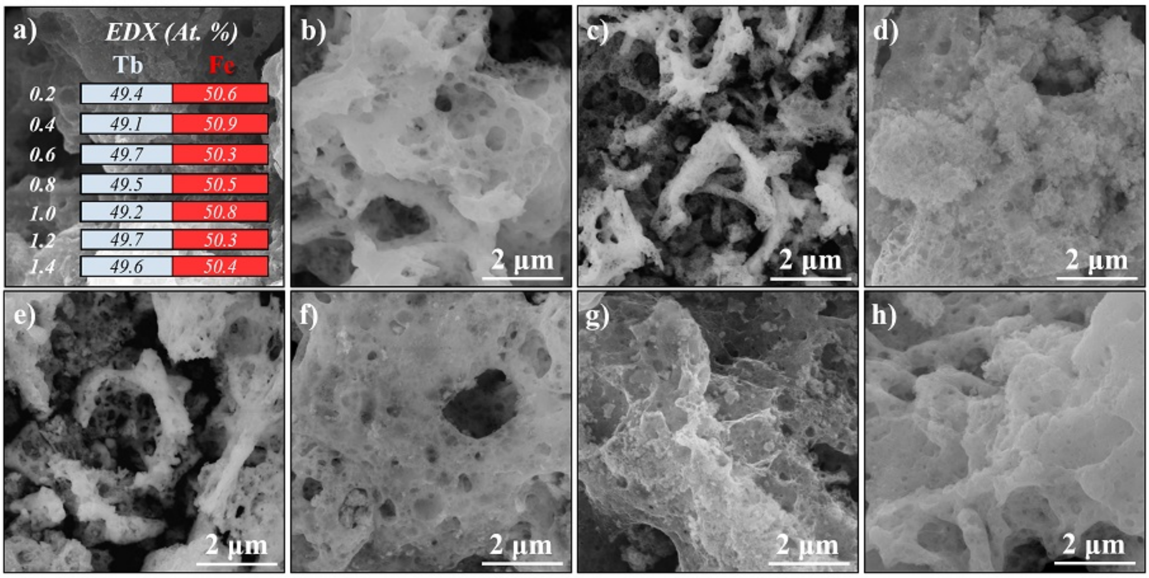

FIG. 1. EDX results (a) and SEM images of glycine-nitrate combustion products, synthesized at the following G/N ratio: 0.2 (b), 0.4 (c), 0.6 (d), 0.8 (e), 1.0 (f), 1.2 (g) and 1.4 (h)

The most unusual sample appears to be obtained with a stoichiometric ratio of glycine to nitrogen in nitrates (G/N $<$ 0.6) in the agglomerates of which there are no large numbers of voids which are usually formed as a result of abundant gas evolution during the self-ignition process. In addition, the obtained images clearly demonstrate that this sample consists of loose nanostructured compositions. This feature is most likely related to the shift of the maximum point of the real combustion temperature, which was repeatedly mentioned in a number of other works [16, 17].

The results of the X-ray powder diffraction analysis show that the formation of terbium orthoferrite begins with a glycine-nitrate ratio of G/N = 0.4 (Fig. 2).

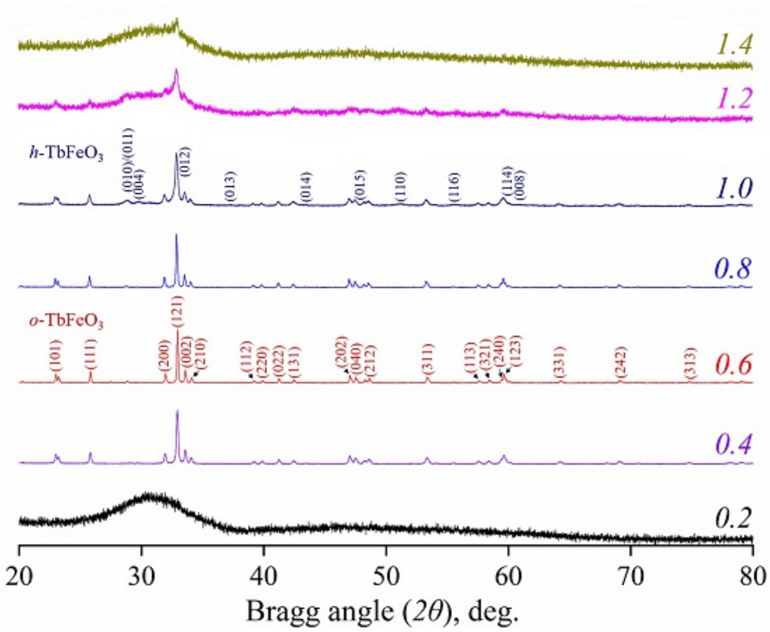

FIG. 2. PXRD pattern of $TbFeO_3$-based nanopowders synthesized at different G/N ratio

It should be noted that the redox environment of the reaction solution significantly affects the phase composition of the resulting compositions. For example, the orthorhombic modification of terbium orthoferrite o-$TbFeO_3$ is formed in a wide range of G/N ratios from 0.4 to 1.2. In the case of a transition to the region of a significant excess of fuel

(G/N = 1.0–1.4), the appearance of hexagonal terbium orthoferrite h-TbFeO$_3$ and amorphous terbium orthoferrite am-TbFeO$_3$ was observed. The appearance of metastable hexagonal modification is associated with the peculiarities of the process of its formation, namely, the thickness of the inter-pore space, the size of the resulting particles, and the combustion mode. All these factors are directly affected by the selected glycine to nitrate ratio, which was described in detail in [10, 12]. In this case, a similar situation is observed and the formation of metastable hexagonal modification occurs exclusively in areas of a significant excess of glycine, the conditions in which correspond to those necessary for its formation. In the region with a significant lack of fuel (G/N = 0.2), the formation of terbium hexagonal orthoferrite does not occur. The average crystallite sizes of orthorhombic and hexagonal TbFeO$_3$ are 29±3 and 15± nm, respectively.

The results of Mössbauer spectroscopy indicate the presence of three main components in the spectra of the synthesized samples – two doublets and one sextet (Fig. 3).

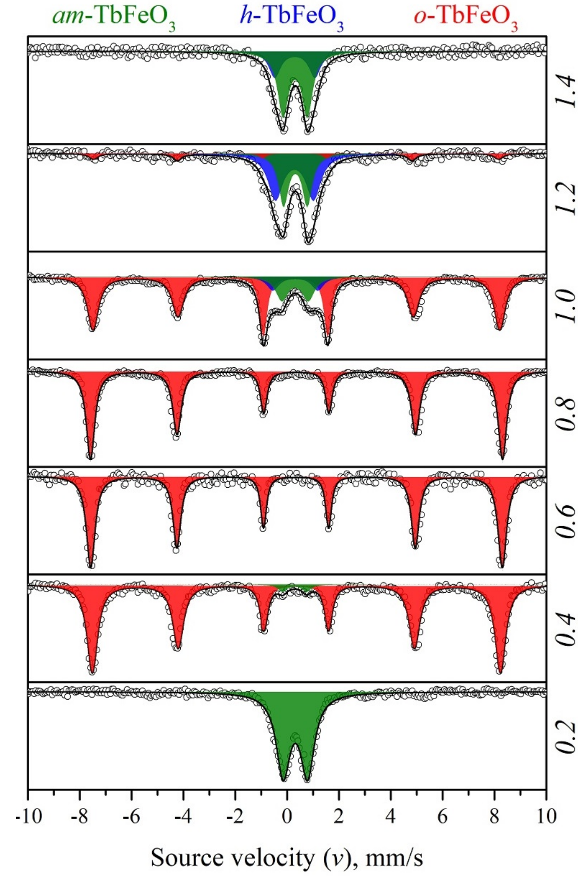

FIG. 3. ^{57}Fe Mössbauer spectra of TbFeO$_3$-based nanopowders synthesized at different G/N ratio

These components according to the value of the isomeric shift (*IS* = 0.306–0.349 mm/s) correspond to the presence of iron atoms in the oxidation state of 3+. A sextet with zero quadrupole splitting refers to the position of the Fe^{3+} cation in the oxygen octahedron [FeO$_6$] in the perovskite-like structure of holmium orthoferrite and, according to the value of hyperfine magnetic splitting (H_{eff} = 48.987 T), agrees well with the results of other studies [18–20]. The remaining two doublets have close values of the isomeric shift – 0.313 and 0.306 mm/s, but differ greatly in the magnitude of the quadrupole splitting – 0.948 and 1.600 mm/s, correspondingly. In accordance with our previous study [10], these two components of the Mössbauer spectra can be attributed to the amorphous (*am*-TbFeO$_3$) and hexagonal (h-TbFeO$_3$) forms of terbium orthoferrite, correspondently. The Mössbauer characteristics of various modifications of terbium orthoferrite are given in Table 1. Thus, the results of ^{57}Fe Mössbauer spectroscopy fully confirm the data of X-ray diffraction.

According to the results of FTIR spectroscopy of the synthesized samples (Fig. 4), the amount of substances adsorbed on the surface of terbium orthoferrite directly depends on the glycine to nitrate ratio.

TABLE 1. Mössbauer characteristics of the different $TbFeO_3$ modifications

Terbium orthoferrite modification	Isomer shift (*IS*), mm/s		Quadrupole splitting (QS), mm/s		Effective magnetic field (H_{eff}), T	
	This work	Literature	This work	Literature	This work	Literature
am-$TbFeO_3$	0.313(19)	0.30 [19]	0.948(52)	1.18 [19]	—	—
h-$TbFeO_3$	0.306(13)	0.29 [19]	1.600(86)	2.13 [19]	—	—
o-$TbFeO_3$	0.349(11)	0.357 [20]	~ 0	0.007 [20]	48.987(91)	49.9 [18]

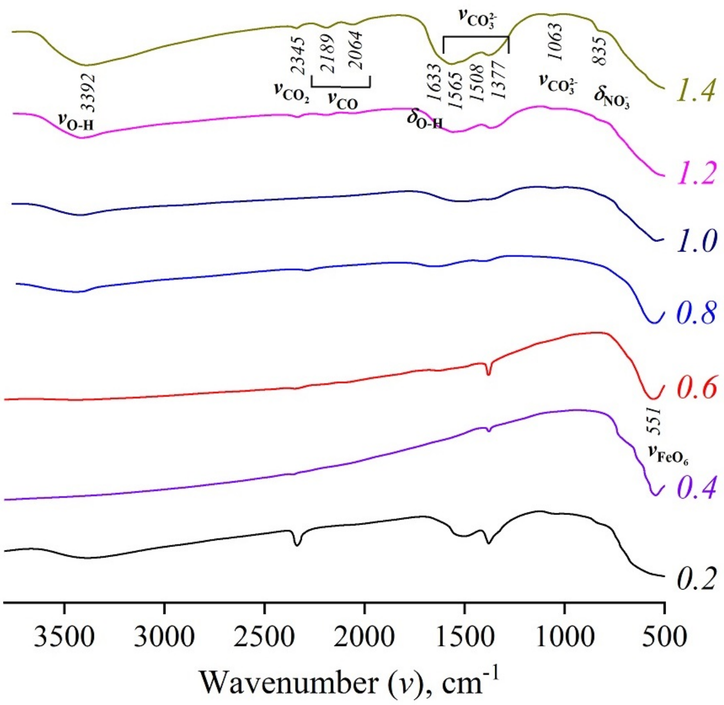

FIG. 4. FTIR spectra of $TbFeO_3$-based nanopowders synthesized at different G/N ratio

The samples obtained with a significant shortage and excess fuel (G/N = 0.2 and 0.4) are characterized by the presence of a large amount of sorbed water whose absorption bands are observed in the region of 3400 cm^{-1} and correspond to asymmetric vibrations of the O-H bond in H_2O molecules. Besides, several absorption bands in the region between 1500 and 1350 cm^{-1} correspond to symmetric and asymmetric stretching vibrations of the C–O bond in the carbonate group CO_3^{2-} and are most noticeable in the samples obtained with the ratio G/N = 1.2 and 1.4, which, in turn, corresponds to the region of the presence of the maximum percentage of hexagonal modification. The presence of a large number of carbonate groups is most likely due to the active interaction of the obtained powders with carbon dioxide (CO_2), which is one of the main gaseous combustion products. It should also be noted the presence of absorption bands in the region from 2190 to 2060 cm^{-1} correspond to vibrations of the C–O bond in carbon monoxide, which is also a product obtained during combustion. In addition, the presence of the absorption band peaked at 550 cm^{-1} that corresponds to stretching vibrations of the Fe–O bond on the octahedron [FeO_6] of terbium orthoferrite confirms X-ray diffraction data.

The most important parameter that determines the possibility of forming a metastable hexagonal modification is the size of the inter-pore space and specific surface area. The determination of these parameters for terbium orthoferrite samples obtained at various glycine-nitrate ratios was carried out on the basis of the results of measuring the low-temperature (77 K) adsorption-desorption of nitrogen N_2 by the surface of the sample (Fig. 5).

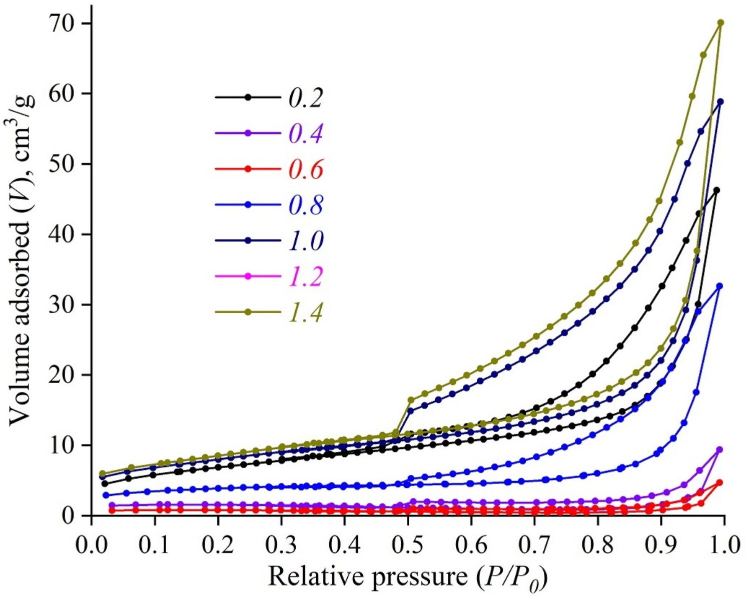

FIG. 5. N_2 adsorption-desorption isotherms of $TbFeO_3$-based nanopowders synthesized at different G/N ratio

An analysis of the data presented indicates that the obtained isotherms correspond to H2 type (with the exception of the sample synthesized at a ratio of $G/N = 0.6$) according to the IUPAC classification, which is typical for substances with a porous structure.

The specific surface value determined with the multi-point BET (Brunauer – Emmett – Teller) method is shown in Fig. 6.

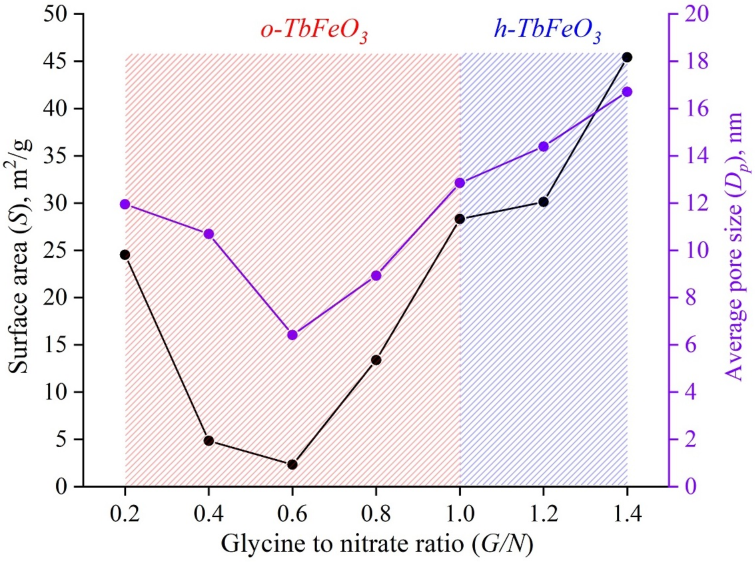

FIG. 6. Surface area vs average pore size of $TbFeO_3$-based nanopowders depending on the G/N ratio

According to the data obtained, the total porosity of the samples ranges from 0.073 cm^3/g to 0.003 cm^3/g and is due to the presence of pores with diameters of 6–17 nm depending on the glycine-nitrate ratio used (Fig. 6). These values are strictly correlated with crystallite sizes of terbium hexagonal orthoferrite, which may indicate the stabilization of this structural form due to the spatial limitations of inter-pore space. Thus the porous structure of the obtained compositions plays a decisive role in the formation of terbium orthoferrite nanocrystals with a hexagonal and orthorhombic structure, which is a distinctive feature of phase formation in systems based on rare-earth orthoferrites [10].

4. Conclusions

In the present paper, our investigation of the process for terbium orthoferrite formation under solution combustion conditions using glycine as a fuel has been completed. It has been shown that at glycine-nitrate G/N ratios ranging from 0.4 to 0.8, the orthorhombic terbium orthoferrite (o-$TbFeO_3$) is formed with a particle size of 29±3 nm. Upon reaching a point of a significant excess of glycine ($G/N > 1.0$) and, as a result, the appearance of a large number of carbonate groups from the combustion products and the average pore size about 13–17 nm, the formation of amorphous am-$TbFeO_3$ and hexagonal h-$TbFeO_3$ ($P6_3/mmc$) is observed. The maximum percentage of hexagonal modification is observed for the sample obtained at a ratio of G/N = 1.2 and is equal to 27%.

Acknowledgment

This study was financially supported by the Russian Foundation for Basic Research (project no. 18-03-00414) and partially performed using the equipment of the Engineering Center of St. Petersburg State Institute of Technology (Technical University).

References

[1] Berezhnaya M.V., Perov N.S., Almjasheva O.V., Mittova V.O., Nguyen A.T., Mittova I.Ya., Druzhinina L.V., Alekhina Yu.A. Synthesis and Magnetic Properties of Barium-Doped Nanocrystal Lanthanum Orthoferrite. *Russian Journal of General Chemistry*, 2019, **89**(3), P. 480–485.

[2] Martinson K.D., Koziritskaya S.S., Panteleev I.B., Popkov V.I. Low coercivity microwave ceramics based on LiZnMn orthoferrite synthesized via glycine-nitrate combustion. *Nanosystems: Physics, Chemistry, Mathematics*, 2019, **10**, P. 313–317.

[3] Lomanova N.A., Tomkovich M.V., Osipov A.V., Ugolkov V.L., Danilovich D.P., Panchuk V.V., Semenov V.G., Gusarov V.V. Formation of $Bi_{1-x}Ca_xFeO_{3-\delta}$ Nanocrystals via Glycine-Nitrate Combustion. *Russian Journal of General Chemistry*, 2019, **89**(9), P. 1843–1850.

[4] Durán A., Moxca L., Borbón–Núñez H.A., Tiznado H., Romo-Herrera J.M., Ostos C., Arnache O., Siqueiros J.M. The role of the interface on magnetic properties for $YFeO_3$@Al_2O_3 core-shell structure. SN Applied Sciences, 2019, **1**, P. 1331.

[5] Martinson K.D., Kondrashkova I.S., Omarov S.O., Sladkovskiy D.A., Kiselev A.S., Kiseleva T.Yu., Popkov V.I. Magnetically recoverable catalyst based on porous nanocrystalline $HoFeO_3$ for process of n-hexane conversion. Advanced Powder Technology, 2019, https://doi.org/10.1016/j.apt.2019.10.033 (in print)

[6] Proskurina O.V., Abiev R.S., Danilovich D.P., Panchuk V.V., Semenov V.G., Nevedomsky V.N., Gusarov V.V. Formation of nanocrystalline $BiFeO_3$ during heat treatment of hydroxides co-precipitated in an impinging-jets microreactor. Chemical Engineering & Processing: Process Intensification, 2019, **143**, P. 107598.

[7] Gupta P., Mahapatra P.K., Choudhary R.N.P. $TbFeO_3$ ceramic: an exciting colossal dielectric with ferroelectric properties. *Physica Status Solidi*, 2019, P. 1900236.

[8] Park B.G., Kim S.B., Lee H.J., Jeong Y.H. Magnetic properties of the orthoferrites $TbFeO_3$ and $ErFeO_3$. *Journal of the Korean Physical Society*, 2008, **53**, P. 758–762.

[9] Akbasheva A.R., Semisalova A.S., Perov N.S., Kaul A.R. Weak ferromagnetism in hexagonal orthoferrites $RFeO_3$ (R = Lu, Er-Tb). Applied Physics Letters, 2011, **99**, P. 122502.

[10] Popkov V.I., Almjasheva O.V., Nevedomskiy V.N., Panchuk V.V., Semenov V.G., Gusarov V.V. Effect of spatial constraints on the phase evolution of $YFeO_3$-based nanopowders under heat treatment of glycine-nitrate combustion products. Ceramics International, 2018, **44**, P. 20906–20912.

[11] Kondrashkova I.S., Martinson K.D., Zakharova N.V., Popkov V.I. Synthesis of nanocrystalline $HoFeO_3$ photocatalyst via heat treatment of products of glycine-nitrate combustion. *Russian Journal of General Chemistry*, 2018, **88**, P. 2465–2471.

[12] Ismael M., Elhaddad E., Taffa D.H., Wark M. Synthesis of Phase Pure Hexagonal $YFeO_3$ Perovskite as Efficient Visible Light Active Photocatalyst. *Catalysts*, 2017, **7**(11), P. 326.

[13] Martinson K.D., Cherepkova I.A., Panteleev I.B., Popkov V.I. Single-step solution-combustion synthesis of magnetically soft $NiFe_2O_4$ nanopowders with controllable parameters. *International Journal of Self-propagating High-temperature Synthesis*, 2019, **28**, P. 266–270.

[14] Martinson K.D., Panteleev I.B., Shevchik A.P., Popkov V.I. Effect of Red/Ox ratio on the structure and magnetic behavior of $Li_{0.5}Fe_{2.5}O_4$ nanocrystals synthesized by solution combustion approach. *Letters on Materials*, 2019, **9**, P. 475–479.

[15] Tugova E., Yastrebova S., Karpov O., Smith R. $NdFeO_3$ nanocrystals under glycine nitrate combustion formation. *Journal of Crystal Growth*, 2017, **467**, P. 88–92.

[16] Wu A., Shen H., Xu J., Jiang L., Luo L., Yuan S., Cao S., Zhang H. Preparation and magnetic properties of $RFeO_3$ nanocrystalline powders. *Journal of Sol-gel Science and Technology*, 2011, **59**, P. 158–163.

[17] Martinson K.D., Cherepkova I.A., Sokolov V.V. Formation of Cobalt Orthoferrite Nanoparticles during the burning of glycine-nitrate and their magnetic properties. *Glass Physics and Chemistry*, 2018, **44**, P. 21–25.

[18] Nikolaev O., Hall I., Barlio S.N., Guretskii S. A Mössbauer study of temperature-driven spin-reorientation transitions in $TbFeO_3$. *Journal of physics: condensed matter*, 1994, **6**, P. 3793–3799.

[19] Downie L.J., Goff R.J., Kockelmann W., Forder S.D., Parker J.E., Morrison F.D., Lightfoot P. Structural and electrical properties of the hexagonal orthoferrites $MFeO_3$ (M = Y, Yb, In). *Journal of Solid State Chemistry*, 2012, **190**, P. 52–60.

[20] Mathur S., Veith M., Rapalaviciute R., Shen H., Goya G.F., Martins Filho W.L., Berquo T.S. Molecule derived synthesis of nanocrystalline $YFeO_3$ and investigations on its weak ferromagnetic behavior. *Chemistry of Materials*, 2004, **16**, P. 1906–1913.

NANOSYSTEMS: PHYSICS, CHEMISTRY, MATHEMATICS, 2019, 10 (6), P. 701–710

The effect of carbon nanotube on the structure of H–NS protein DNA complex: molecular dynamics approach

Najmeh Mahdavipour, Mohammad Reza Bozorgmehr*, Mohammad Momen-Heravi

Department of Chemistry, Mashhad Branch, Islamic Azad University, Mashhad, Iran

*bozorgmehr@mshdiau.ac.ir, mr_bozorgmehr@yahoo.com

DOI 10.17586/2220-8054-2019-10-6-701-710

Most of the experimental biophysical and biochemical observations of proteins are in dilute solutions, while inside the cell is a crowded environment.The effect of crowding on the structure and activity of biomolecules is not completely clear. In this work, molecular dynamics simulation was used to study the effect of single walled carbon nanotube (SWCNT) on the H–NS protein in the presence and absence of double-stranded nucleic acid. The values of root mean square deviation (RMSD) and its distribution, radius of gyration (Rg) and its distribution and root mean square fluctuation (RMSF) were calculated. Changes in the secondary structure of the H–NS were also calculated. The contributions of each residue of H–NS in free energy of binding between H–NS and DNA were calculated. The results indicate that the SWCNT unfolds the structure of the H–NS. In terms of contribution of residues in secondary structures, in the presence of a SWCNT, the sheet secondary structure of the H–NS changes more than helices secondary structure. In the triple system, which includes H–NS, SWCNT and DNA; Ala-1, Arg-3, Lys-6, Lys-17, Arg-24, Lys-30, Lys-31, Lys-38 and Lys-46 residues have a favorable effect on the interaction of the H–NS with the DNA.

Keywords: crowding, MMPBSA, secondary structure, contact map.

Received: 21 October 2019

Revised: 23 November 2019

1. Introduction

In cellular environments, a large number of compounds, such as proteins, saccharides, lipids, DNA, RNA, ions, etc., coexist [1, 2]. The concentration range of biomolecules in the cell is between 40 and 500 gL^{-1} [3, 4]. This concentration range is equivalent to occupying 20 to 40 percent of the cell volume. Therefore, inside the cell is a crowded environment. However, most biochemical *in vitro* studies are carried out in dilute solution [5]. In the case of parameters such as temperature, pressure, and pH, the change of parameters can be such as to reflect the physiological behavior of the cell environment, but this is not true about the effect of crowding. The effect of crowding on the structure and activity of biomolecules is not completely clear. On the other hand, the understanding of this effect leads to a better understanding of the behavior of biomolecules in the cell's environment. In order to mimic molecular crowding *in vitro*, various materials are used in the laboratory. Alcohols [6], polymers [7], and carbon nanotubes [8] are among the materials used in this field. Substances used as a crowding agent should have features such as chemically inert, high solubility in water, and varied in size. Except for high solubility in water, carbon nanotubes are suitable for other criteria. Carbon nanotubes are biocompatible because they have carbon; on the other hand, they can have a wide variety in terms of length and diameter. Also, single-walled carbon nanotubes (SWCNT) have great applications in drug delivery [9] and providing biosensors [10] due to their unique structural features.

H–NS are DNA-binding proteins which can cause condense DNA *invivo* and *in vitro* [11]; it does this as eukaryotic histones. The H–NS protein has two domains, which are interacting with the DNA in the C-terminal domain. Protein H–NS has been shown to bind to DNA with 47 residues at its C-terminus, and digest the protein during this process [11]. The binding domain of H–NS protein has a unique three-dimensional structure that is not similar to other DNA-binding proteins. The DNA-binding domain of H–NS protein has two beta-sheetsand two-alphahelices. Due to the presence of six lysine residues and two arginine residues in the binding domain of H–NS, this region of the protein has a positive charge. H–NS has a binding affinity with all types of DNA, but its binding affinity to double-stranded DNA is more pronounced [12]. Two mechanisms for the binding of H–NS to DNA have been proposed [13]: (i) via specific binding, in which H–NS binds to an AT-rich region of DNA; (ii) non-specific binding, in which the H–NS can bind over the whole DNA.

Although being crowded *in vivo*, biomolecules maintain their structure and activity; however, crowing under *in vitro* conditions causes changes in the structure and function of the biomolecules. How the structure of proteins in the presence of crowding factors is changed is not fully understood. Here, the structure of H–NS protein and its interaction with double-stranded DNA using molecular dynamics simulation is investigated. This is done in the presence and absence of arm-chair single-wall carbon nanotubes.

2. Molecular dynamics simulation details

Four different simulation boxes were designed. In the first box, the binding domain of H–NS protein with pdb code 1HNS in the protein data bank was placed in the center of the simulation box (denoted as *protein* system). In the second box,the H–NS was placed along with the four arm-chair SWCNTs (5, 5) (denoted as *protein-SWCNT* system). The H–NS was placed in the center of the box and the SWCNTs were randomly placed. In the third box,the H–NS and the DNA were placed (denoted as *protein-DNA* system) (see Table 1). The DNA structure was taken from the protein databank with code 4QJU. In this structure, the protein is also existed with nucleic acid that the protein is removed using the PyMol software [14]. In the fourth box, the H–NS, DNA and four SWCNTs were placed (denoted as *protein-SWCNT-DNA* system). All designated boxes are filled with water type TIP3P [15]. Sodium and chloride ions were used to neutralize the design systems.

TABLE 1. Overview of studied system and simulation details

System	Number of water molecules	Number of NA ion(s)	Number of Cl ion(s)
Protein	3891	0	1
Protein-SWCNT	5064	0	1
Protein-DNA	15895	39	0
Protein-SWCNT-DNA system	15664	39	0

All molecular dynamics simulations were performed with Gromacs package version 5.1.25.2.1 [16] and OPLS-AA/Lall atomforce field. Because the force field parameters for SWCNT are not present in the default version of the Gromacs software,the structure of this compound was optimized by using of B3LYP density functional method with the basis function of 6-31G*. To control the optimization, frequency calculations were performed and virtual frequencies were not observed. All *ab initio* calculations were done by GAMESS software package [17]. To eliminate the primary kinetic energy in each of the simulation boxes and inappropriate contacts between the atoms, energy minimization was done using steepest descent method [18]. Each simulation box achieved two-stage equilibrium in NVT and NPT ensemble. At this stage,the time of equilibration was considered 5 ns with time step 0.002 ps. Finally, molecular dynamics was performed by solving equations of motion for 100 ns with the 2 fs time step. The PME algorithm was used to calculate electrostatic interactions [19]. LINCS algorithm [20] was employed to fix the chemical bonds between the atoms of the protein and SETTLE algorithm [21] in the case of water molecules. To fix a constant temperature (298 K) and pressure (1 bar) during the simulations, systems components were coupled with V-rescaleand Nose-Hoover thermostat [22] respectively, in each of equilibration steps and molecular dynamics simulations.

3. Results and discussion

One way to examine the stability of a structure in molecular dynamics simulation is to calculate root mean square deviation (RMSD). The RMSD is defined as:

$$RMSD(t_1, t_2) = \left[\frac{1}{M} \sum_{i=1}^{N} m_i \left\| r_i(t_1) - r_i(t_2) \right\| \right]^{1/2}, \tag{1}$$

where r_i is the atomic position at time t and $M = \sum_{i=1}^{N} m_i$. The Cα-RMSD values of the H–NS protein were calculated in the designated systems. The result is shown in Fig/ A1 of the Appendix. The stability of H–NS structure in systems *protein* and *protein-SWCNT-DNA* is similar,while H–NS in system *protein-DNA* has the lowest stability. For a better comparison between structural stability in different systems, the probability distribution of the RMSD value was calculated. The result is shown in Fig. 1.

According to the figure, in the *protein-SWCNT-DNA* system with the most crowding H–NS is similar to H–NS in system *protein*. Also, SWCNT alone and nucleic acid alone cause instability of the H–NS structure. Another factor that can determine the activity and stability of the protein structure is compression of the conformation [23]. We used the radius of gyration (*Rg*)to indicate the compression of the protein structure. The *Rg* value of protein is calculated

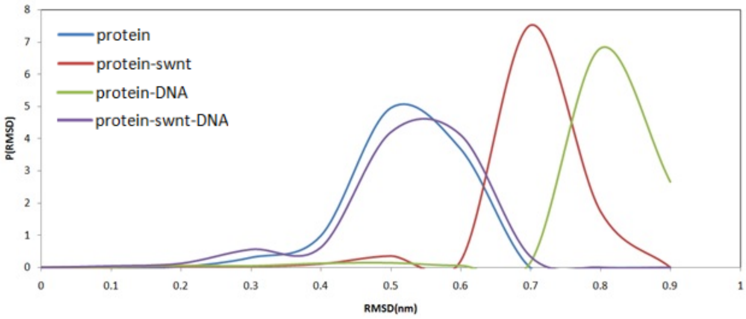

FIG. 1. The probability distribution of the RMSD in systems: *protein*, *protein-SWCNT*, *protein-DNA* and *protein-SWCNT-DNA*

using following relation:

$$R_g = \left(\frac{\sum_i \left\| r_i \right\|^2 m_i}{\sum_i m_i} \right)^{\frac{1}{2}}, \tag{2}$$

where m_i is the atomic mass of i and r_i the atomic position of i relative to the center of the molecule [24]. The R_g of H–NS were calculated in the designed systems. The result is shown in Fig. A2 of the Appendix. The probability distribution of the R_g value was calculated, also. The result is shown in Fig. 2.

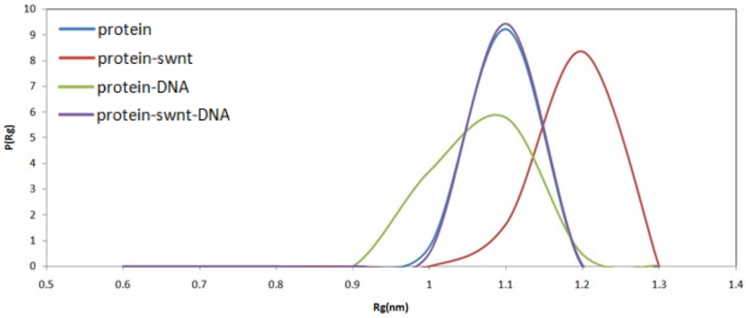

FIG. 2. The probability distribution of the R_g in systems: *protein*, *protein-SWCNT*, *protein-DNA* and *protein-SWCNT-DNA*

Regarding the figure, it can be seen that the SWCNT has caused the H–NS structure to unfold. Since the SWCNT has a hydrophobic nature, it is expected to change the structure of the protein by changing the hydrophobic interactions. In other systems, the average of R_g is almost equal. The similarity between H–NS in systems *protein* and *protein-SWCNT-DNA* is significant. The root mean square fluctuation (RMSF) values of H–NS sequences are calculated in different systems and shown in Fig. 3.

RMSF is a measure of the flexibility of protein's residues [25]. It is observed at the N-terminal of the H–NS, where the fluctuations are greater, especially in the case of the *protein-SWCNT-DNA* system. Also, in the middle region of the H–NS, the Arg-24 residue in the *protein-SWCNT-DNA* system has a high flexibility. Given the fact that this residue is in the random coil region of H–NS, and its side chain is larger than any other residue, this result is logical. To further examine the changes in the residues in the secondary structure of the H–NS in different studied systems, the secondary structure of the H–NS was calculated in each of the designed systems. The results are shown in Fig. 4.

The secondary structure of the H–NS, along with solvent accessible surface area for its residue, was obtained from polyview-2d software [26]. To determine the secondary structures shown in Fig. 4, a sample structure from molecular trajectory is required. The free energy landscape analysis (FEL) method was used for sampling [27].

There are three steps in the free energy analysis method: first, calculate the root-mean-square-deviation (RMSD) and the H–NS's radius of gyration (R_g); second, calculate the probability of the presence of H–NS's conformations in each of the values calculated for the RMSD and R_g; third, calculate the free energy based on the probability values calculated in the second step. The results of the FEL analysis are reported in two-dimensional form in Fig. A3 through A6 and in 3D in Figs. A7 to A10 in the Appendix. Regarding these figures, a minimum free energy region was

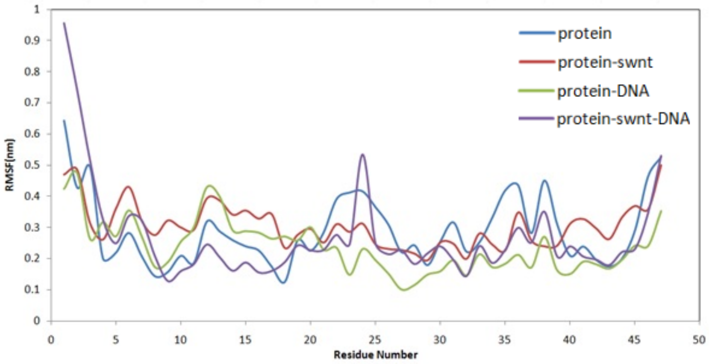

FIG. 3. Average RMSF values for each residue of H–NS during simulation in each system

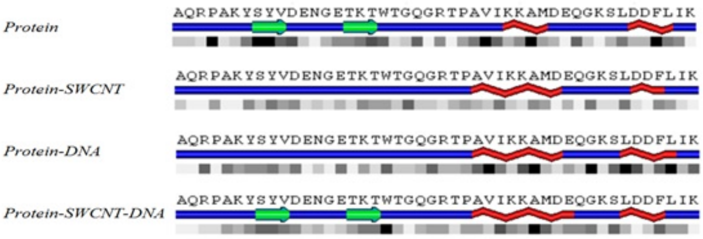

FIG. 4. The secondary structure of the H–NS, along with the solvent accessible surface area for its residues. 🟥 Helix; 🟩 β strand; 🟦 coil; ▨ Dark: completely buried, bright: completely exposed

sampled. Fig. 4A is obtained from the free energy sampling. As can be seen in Fig. 4A, in the secondary structure of H–NS in systems *protein* and *protein-SWCNT-DNA* there are two helices and two sheets. In the secondary structure of H–NS, in systems *protein-SWCNT* and *protein-DNA*, the two sheets structures have disappeared. The first sheet consists of Ser-8, Tyr-9 and Val-10 residues. Considering the aromatic ring of Tyr-9 and the structure of two other amino acids, this sheet has a hydrophobic nature. The second sheet is composed of Thr-16, Lys-17 and Thr-18 amino acids. Therefore, the second sheet that is deleted in systems *protein-SWCNT* and *protein-DNA* has a polar nature. In system *protein-SWCNT-DNA*, the first size of first helix is larger than the first helix in the system *protein*. On the other hand, the size of the second helix in both systems is approximately equal. It is also observed that in system *protein-SWCNT-DNA*, the first sheet has been folded into the H–NS interior, while in the *protein* system the solvent accessible surface area of first sheet is increased. The contact map was used to check the change in the tertiary structure of the H–NS. Fig. 5 shows the contact map and the contact difference maps of the structures of the H–NS in *designed* system.

In Fig. 5, in the lower triangle of the diagram the black dots indicate the common contacts and the pink dots show the contacts that are present in the H–NS in *protein* system, but absent in the H–NS in *protein-SWCNT* system. The green dots indicate the contacts that are present in the H–NS in *protein-SWCNT* system, but absent in the H–NS in *protein* system. In the upper triangle of the diagram, the differences between the structures are indicated by the intensity of the red and blue colors. The regions in blue color show the contacts that are not altered and those in the red color show the difference between the two structures. The greater the number of red dots in Fig. 5 shows that the SWCNT alone have had a greater effect on the tertiary structure of H–NS. On the other hand, the distribution pattern of red spots is different in Fig. 5, which shows how the SWCNT effects on the tertiary structure differ in the presence and absence of DNA. The Kollman et al. method was used [28, 29] used to determine the contribution of each residue of H–NS in free energy of binding between H–NS and DNA. In this method, the free energy is obtained by:

$$G = E_{bnd} + E_{el} + E_{vdW} + G_{pol} + G_{np} - TS, \tag{3}$$

where G_{pol} and G_{np} are polar and nonpolar solvation free energies, which were obtained from the generalized Born and solvent accessible surface methods, respectively and E_{bnd}, E_{el} and E_{vdW} are the MM energies (bonding, bending, and dihedral), electrostatic energy and van der Waals interactions, respectively. The last term in Eq. 3, in which S is entropy and T is temperature, is obtained from the normal mode (NM) analysis. The contribution of each of the H–NS's residues in the free energy of binding of H–NS to the DNA in designed system is shown in Fig. 6.

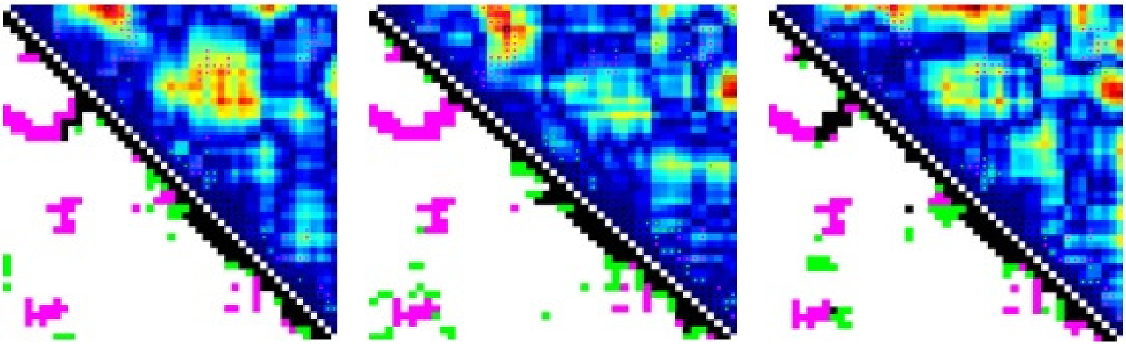

(a) (b) (c)

FIG. 5. The contact map (lower triangle) and the contact difference maps (upper triangle) of the A) structures of the H–NS in *protein* system and H–NS in *protein-SWCNT* system B) the structures of the H–NS in *protein* system and H–NS in *protein-DNA* system C) the structures of the H–NS in *protein* system and H–NS in *protein-SWCNT-DNA* system. The colors used are described in the text

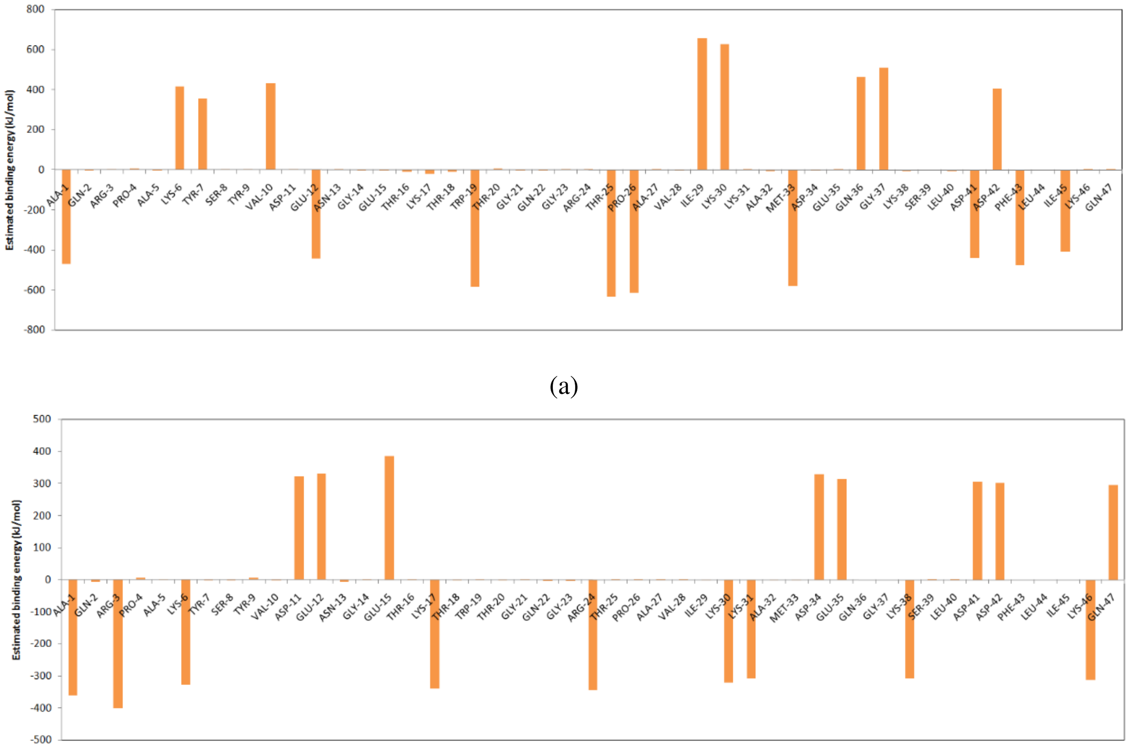

(a)

(b)

FIG. 6. The contribution of each of the H–NS's residues in the free energy of binding of H–NS to the DNA in A) *protein-DNA B)protein-SWCNT-DNA*

Comparison of A and B in Fig. 6 shows that in both systems eight residues have positive free energy (unfavorable effect) in H–NS binding to DNA, and nine amino acids have negative free energy (favorable effect). In system *protein-DNA*, residues that have an unfavorable effect on H–NS binding to the DNA are Lys-6, Tyr-7, Val-10, Ile-29, Lys-30, Gln-36, Gly-37 and Asp42. Also, in this system, residues that have a favorable effect on H–NS binding to the DNA are: Ala-1, Glu-12, Trp-19, Thr-25, Pro-26, Met-38, Asp-41, Phe-43 and Ile-45. In system *protein-SWCNT-DNA*, residues that have an unfavorable effect on H–NS binding to the DNA are Asp-11, Glu-12, Glu-15, Asp-34, Glu-35, Asp-41, Asp-42 and Gln-47. In this system, residues that have favorable effect onH–NS binding to the DNA are Ala-1, Arg-3, Lys-6, Lys-17, Arg-24, Lys-30, Lys-31, Lys-38 and Lys-46. It is observed that the SWCNT has affected the interaction of H–NS with DNA by changing the position of charged residues. In the absence of a SWCNT, it also seems that the H–NS interacts more strongly with hydrophobic interactions with DNA, while in the presence of SWCNT the H–NS interacts with the DNA by electrostatic interactions.

4. Conclusion

The effect of single walled arm-chair carbon nanotube (5, 5) on H–NS protein was studied by molecular dynamics simulation. The calculations were carried out in the presence and absence of double-stranded nucleic acid. In the secondary structure of the H–NS, the beta sheets of the protein were influenced by the SWCNT more than their helices. In a triple system that contains H–NS, DNA and SWCNT, and is more crowded, the structure of the H–NS is more similar to that of the dilute solution. The interactions between protein and nucleic acid and the binding energies of the residues involved were obtained. The results indicate that the nanotube has altered the interaction between protein and nucleic acid. The results are consistent with experimental observations [30].

References

[1] Ellis R.J. Macromolecular crowding: an important but neglected aspect of the intracellular environment. *Current opinion in structural biology*, 2001, **11** (1), P. 114–119.

[2] Miyoshi D., Sugimoto N. Molecular crowding effects on structure and stability of DNA. *Biochimie*, 2008, **90** (7), P. 1040–1051.

[3] Srere P.A. Protein crystals as a model for mitochondrial matrix proteins. *Trends in Biochemical Sciences*, 1981, **6**, P. 4–7.

[4] Zimmerman S.B., Minton A.P. Macromolecular crowding: biochemical, biophysical, and physiological consequences. *Annual review of biophysics and biomolecular structure*, 1993, **22** (1), P. 27–65.

[5] Ellis R.J. Macromolecular crowding: obvious but underappreciated. *Trends in biochemical sciences*, 2001, **26** (10), P. 597–604.

[6] Doghaei A.V., Housaindokht M.R., Bozorgmehr M. Molecular crowding effects on conformation and stability of G-quadruplex DNA structure: Insights from molecular dynamics simulation. *Journal of theoretical biology*, 2015, **364**, P. 103–112.

[7] Jiao M., et al. Attractive protein-polymer interactions markedly alter the effect of macromolecular crowding on protein association equilibria. *Biophysical journal*, 2010, **99** (3), P. 914–923.

[8] Xu M., et al. Alignment control of carbon nanotube forest from random to nearly perfectly aligned by utilizing the crowding effect. *ACS Nano*, 2012, **6** (7), P. 5837–5844.

[9] Bianco A., Kostarelos K., Prato M. Applications of carbon nanotubes in drug delivery. *Current opinion in chemical biology*, 2005, **9** (6), P. 674–679.

[10] Tlmaciu C.-M., Morris M.C. Carbon nanotube biosensors. *Frontiers in chemistry*, 2015, **3**, P. 59.

[11] Atlung T., Ingmer H. HNS: a modulator of environmentally regulated gene expression. *Molecular microbiology*, 1997, **24** (1), P. 7–17.

[12] Falconl M., et al. Proteins from the prokaryotic nucleoid: primary and quaternary structure of the 15kD Escherichia coli DNA binding protein HNS. *Molecular microbiology*, 1988, **2** (3), P. 323–329.

[13] Tupper A.E., et al. The chromatinassociated protein HNS alters DNA topology in vitro. *The EMBO journal*, 1994, **13** (1), P. 258–268.

[14] DeLano W., The PyMOL Molecular Graphics System. DeLano Scientific; Palo Alto, CA: 2002. `URL: http://www.pymol.org`.

[15] Price D.J., Brooks C.L. III. A modified TIP3P water potential for simulation with Ewald summation. *The Journal of chemical physics*, 2004, **121** (20), P. 10096–10103.

[16] Van Der Spoel D., et al. GROMACS: fast, flexible, and free. *Journal of computational chemistry*, 2005, **26** (16), P. 1701–1718.

[17] Schmidt M.W., et al. General atomic and molecular electronic structure system. *Journal of computational chemistry*, 1993, **14** (11), P. 1347–1363.

[18] Luenberger D.G., Ye Y. *Linear and nonlinear programming*, **2**, 1984, Springer.

[19] Essmann U., et al. A smooth particle mesh Ewald method. *The Journal of chemical physics*, 1995, **103** (19), P. 8577–8593.

[20] Hess B., et al. LINCS: a linear constraint solver for molecular simulations. *Journal of computational chemistry*, 1997, **18** (12), P. 1463–1472.

[21] Miyamoto S., Kollman P.A. Settle: An analytical version of the SHAKE and RATTLE algorithm for rigid water models. *Journal of computational chemistry*, 1992, **13** (8), P. 952–962.

[22] Bussi G., Donadio D., Parrinello M. Canonical sampling through velocity rescaling. *The Journal of chemical physics*, 2007, **126** (1), P. 014101.

[23] Ghaderi S., Bozorgmehr M.R., Morsali A. Structure study and predict the function of the diphtheria toxin in different pH levels (Acidic-Basic-Natural) using molecular dynamics simulations. *Entomology and Applied Science Letters*, 2017, **3** (4), P. 49–56.

[24] Honarparvar B., Skelton A.A. Molecular dynamics simulation and conformational analysis of some catalytically active peptides. *J. Mol. Model.*, 2015, **21** (4), P. 100.

[25] Housaindokht M.R., Bozorgmehr M.R., Monhemi H. Structural behavior of Candida antarctica lipase B in water and supercritical carbon dioxide: A molecular dynamic simulation study. *The Journal of Supercritical Fluids*, 2012, **63**, P. 180–186.

[26] Porollo A.A., Adamczak R., Meller J. POLYVIEW: a flexible visualization tool for structural and functional annotations of proteins. *Bioinformatics*, 2004, **20** (15), P. 2460–2462.

[27] Lei H., et al. Folding free-energy landscape of villin headpiece subdomain from molecular dynamics simulations. *Proceedings of the National Academy of Sciences*, 2007, **104** (12), P. 4925–4930.

[28] Kumari R., et al. g_mmpbsa–a GROMACS tool for high-throughput MM-PBSA calculations. *Journal of chemical information and modeling*, 2014, **54** (7), P. 1951–1962.

[29] Kollman P.A., et al. Calculating structures and free energies of complex molecules: combining molecular mechanics and continuum models. *Accounts of chemical research*, 2000, **33** (12), P. 889–897.

[30] Nii D., et al. Selective binding of single-stranded DNA-binding proteins onto DNA molecules adsorbed on single-walled carbon nanotubes. *Colloids and Surfaces B: Biointerfaces*, 2014, **121**, P. 325–330.

Appendix

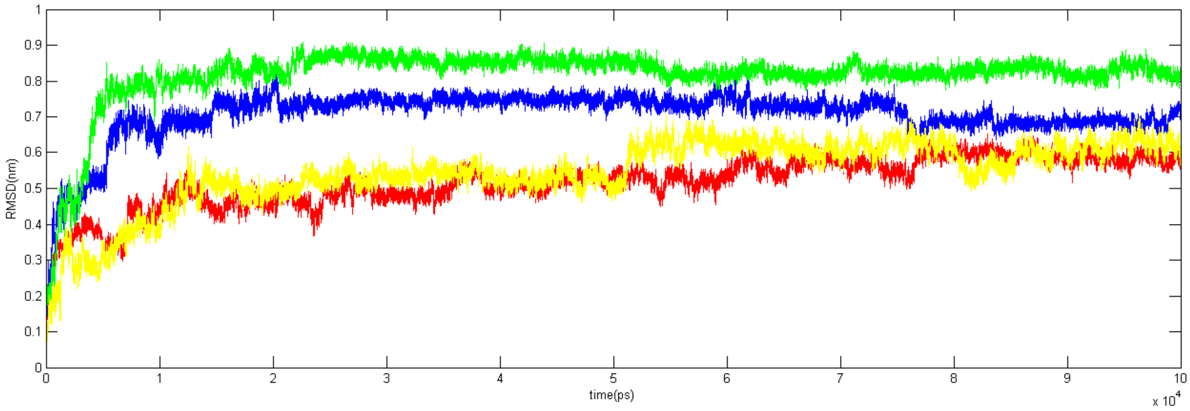

FIG. A1. The Cα-RMSD (nm) of H–NS vs. time (ps). Red: *protein*; blue: *protein-SWCNT*; green: *protein-DNA*; yellow: *protein-SWCNT-DNA*

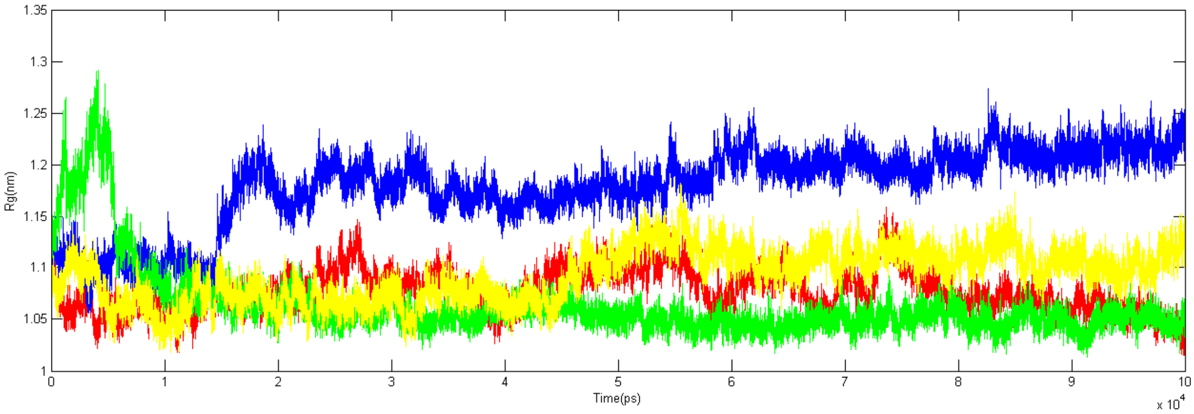

FIG. A2. The R_g (nm) of H–NS vs. time (ps). Red: *protein*; blue: *protein-SWCNT*; green: *protein-DNA*; yellow: *protein-SWCNT-DNA*

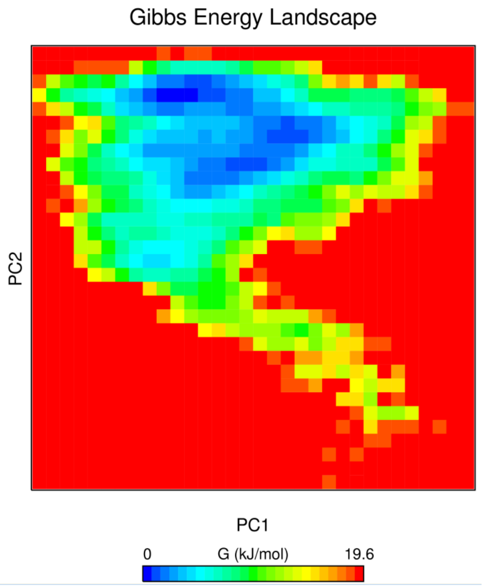

FIG. A3. 2D Free Energy Landscape of the *protein* simulated system

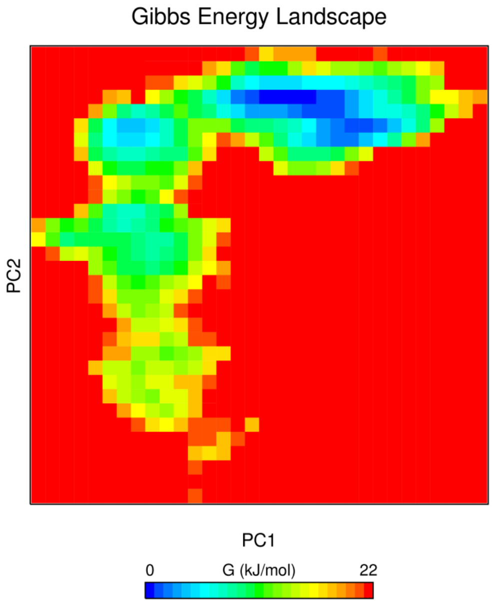

FIG. A4. 2D Free Energy Landscape of the *protein-SWCNT* simulated system

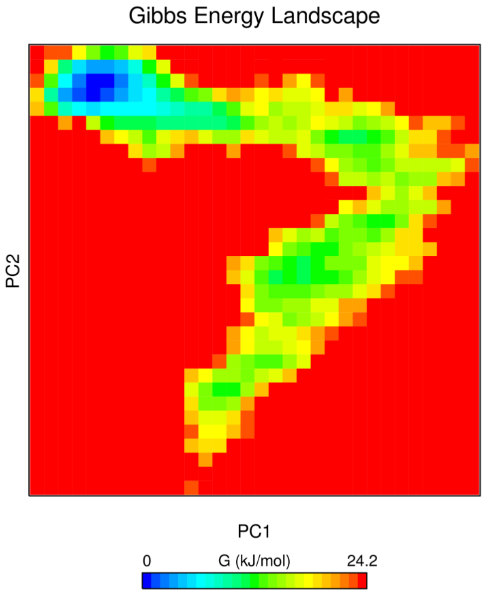

FIG. A5. 2D Free Energy Landscape of the *protein-DNA* simulated system

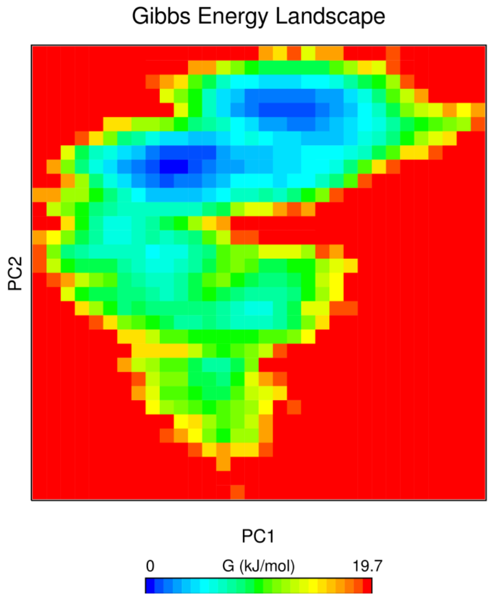

FIG. A6. 2D Free Energy Landscape of the *protein-SWCNT-DNA* simulated system

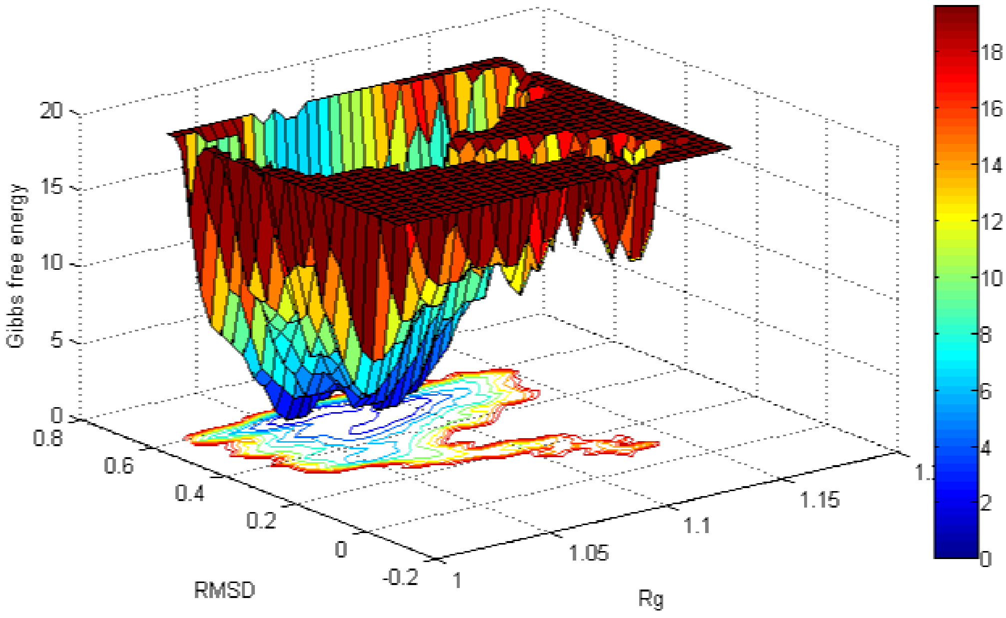

FIG. A7. 3D Free Energy Landscape of the *protein* simulated system

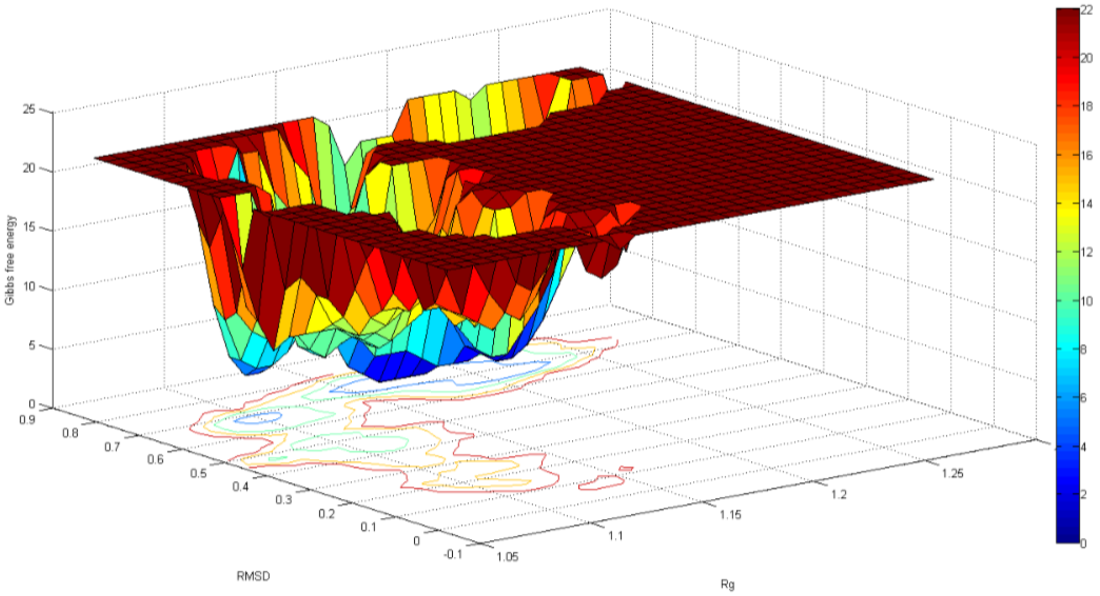

FIG. A8. 3D Free Energy Landscape of the *protein-SWCNT* simulated system

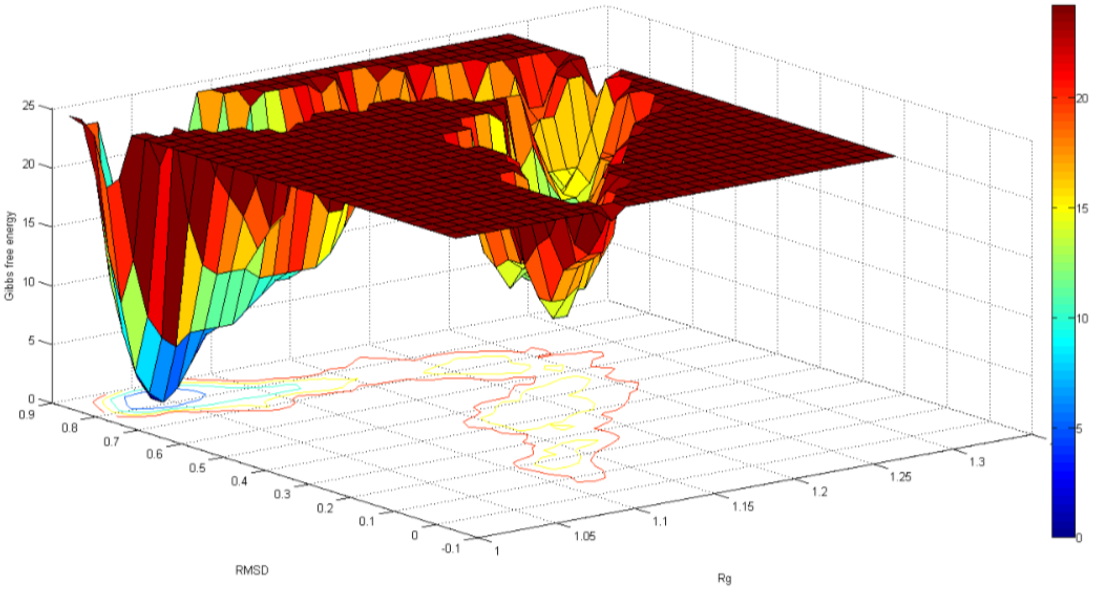

FIG. A9. 3D Free Energy Landscape of the *protein-DNA* simulated system

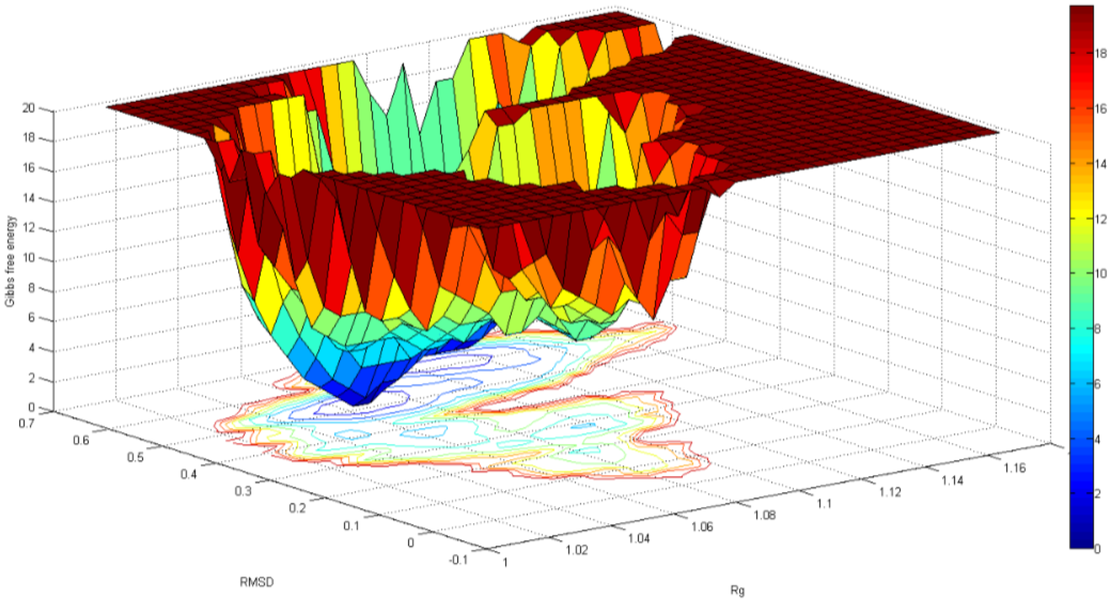

FIG. A10. 3D Free Energy Landscape of the *protein-SWCNT-DNA* simulated system

NANOSYSTEMS: PHYSICS, CHEMISTRY, MATHEMATICS, 2019, 10 (6), P. 711–719

A comparative study of the effect of solvents on the optical, structural and morphological properties of ZnO–GO nanocomposites synthesized by sol-gel method

Sudha Maurya*[1], Sandhya Pillai[2]

Department of Nanotechnology, Christian College of Engineering and Technology,
Bhilai, Durg, Chhattisgarh, India
*sudhamaurya1911@gmail.com

DOI 10.17586/2220-8054-2019-10-6-711-719

Zinc Oxide-Graphene Oxide (ZnO–GO) nanocomposites were prepared using solvents polyvinylpyrrolidone (PVP) and N-Methyl-2 Pyrrolidone (NMP) by sol-gel technique and their optical, structural and morphological properties were investigated. X-ray Diffraction (XRD) studies show the presence of planes of GO and ZnO confirming the formation of composites. The particle sizes were calculated using Scherrer's formula and were found to be in the nanometer range. Scanning Electron Microscopy (SEM) images show the formation of layered structures dispersed non-uniformly over clusters of particles. Energy Dispersive X-Ray (EDX) spectra confirm the presence of carbon, zinc and oxygen in the composites. The optical absorbance of ZnO–GO synthesized using PVP was higher than ZnO–GO with NMP with the absorption edge shifting to shorter wavelength in the presence of NMP. The band gap values were found to be in the range of 2.7–3.0 eV. The band gap of ZnO–GO synthesized using NMP was higher than ZnO–GO synthesized using PVP.

Keywords: GO, ZnO, ZnO–GO Nanocomposite, PVP, NMP.

Received: 2 November 2019

Revised: 30 November 2019

1. Introduction

Zinc Oxide (ZnO), a wide band gap II–VI semiconductor has been a subject of extensive research owing to its numerous interesting properties, making it a desirable material for application in conductive oxide [1], solar cell [2], display and sensors [3, 4], and photocatalysis [5, 6]. However, pure ZnO suffers from weak photo response [7], fast recombination of electron-hole pairs [8] and low operating speed.

GO is a layer of graphene functionalized with oxygen-containing moieties, such as hydroxyl (OH), carbonyl (C=O) and alkoxy (C–O–C) groups. It possesses unique properties that are different from graphene due to the existence of various oxygenated functional groups on the surface of GO. Graphene Oxide (GO) has attracted researchers due to its high surface area, high mobility of charge carriers and excellent stability. Hybrid of GO and ZnO (nanocomposites) can offer better prospects to enhance the photoresponsivity, stability and flexibility of ZnO for various applications [9, 10].

ZnO can be prepared by different means, of which the sol-gel is a popular method because of its low cost, reliability, reproducibility, simplicity. The choice of solvents used for reaction and capping the particles affects the shape and size of the composites [11]. Although there have been several reports on the synthesis of these composites using different solvents, a comparative study of the effect of solvents on the properties of the composites have not been presented to date. In the present work ZnO–GO nanocomposites were prepared using two polymer solvents – PVP and NMP. There are reports that a polymer matrix is useful in the formation of nanoparticles as it possesses the properties of the host polymer as well as the guest nanoparticles [12]. The polymers can also help in easier shaping and formation of the composite materials. PVP is a good surface stabilizer, growth modifier and particle disperser [13]. It also inhibits agglomeration by steric effect [14]. NMP is a 5 member ring compound containing nitrogen. It has high dissolving power and high purity. It can dissolve organic and inorganic compounds well or even better than chlorofluorocarbon (CFC) solvents. This paper presents the structural, morphological and optical characterization of ZnO–GO nanocomposites prepared using PVP and NMP as capping agents.

2. Experimental techniques

2.1. Synthesis of Zinc Oxide (ZnO)

ZnO nanoparticles were synthesized by sol gel method. The appropriate quantity of Zinc acetate was dissolved in deionized water and mixed with an equal quantity of aqueous 0.05 M NaOH solution slowly with continuous stirring at 50 °C. The reaction mixture was maintained at this temperature for 2 hours and then cooled to room temperature. The resultant precipitate was centrifuged and then washed with deionized water and dried at room temperature.

2.2. Synthesis of Graphene Oxide (GO)

Graphene oxide (GO) was synthesized using modified Hummers method from pure graphite powder [15]. First, 108 ml of sulphuric acid (H_2SO_4) and 12 ml of phosphoric acid (H_3PO_4) (volume ratio 9:1) were mixed and stirred using ultrasonic bath (53 KHz, 80 W) for several minutes. 0.9 g of graphite powder was added into the solution under stirring condition. The mixture was ultrasonicated for an hour and then kept in an ice bath keeping the temperature at approximately 5 °C. Then, 5.28 g of potassium permanganate ($KMnO_4$) was then added slowly into the solution. This mixture was stirred under ultrasonic irradiation for 6 hours until the solution became dark green and thereafter was magnetically stirred for 1 hr after removing from the icebath. To eliminate excess of $KMnO_4$, 2.7 ml of hydrogen peroxide (H_2O_2) was dropped slowly and stirred for 10 minutes. On adding hydrogen peroxide, the residual $KMnO_4$ and MnO_2 was reduced to soluble salts. The solution was cooled and 20 ml of hydrochloric acid (HCl) and 60 ml of deionized water (DIW) was added and centrifuged for 7 minutes.The suspension was filtered using high quality Whatman filter paper The residue obtained after decantation w washed with HCl and DIW for 3 times to remove the metal ions. The filtrate was again mixed with DIW several times so as to remove any other impurities and then ultrasonicated for 1 hr to obtain dispersion of GO. The washed GO solution was dried using oven at 90 °C for 24 hours to produce the GO powder.

2.3. Synthesis of ZnO–GO nanocomposites

ZnO–GO nanocomposites were synthesized with two different ratios of ZnO to GO – namely $ZnO_{0.5}$–$GO_{0.5}$ and $ZnO_{0.7}$–$GO_{0.3}$. 0.5 g graphene oxide and 0.1 g PVP/NMP was dispersed in 500 ml deionised water to form graphene oxide solution. 0.5 g ZnO nanoparticles were added into graphene oxide solution and the mixture was stirred at room temperature for 2 hrs. The resultant precipitate was filtered and thoroughly washed with deionized water to remove impurities and dried at 80 ° C for 5 hrs to obtain $ZnO_{0.5}$–$GO_{0.5}$ nanocomposites. $ZnO_{0.7}$–$GO_{0.3}$ nanocomposites were also synthesized using the above method.

FIG. 1. ZnO–GO nanocomposites

2.4. Characterization Methods

XRD studies were performed at NIT Raipur using PANalytical 3KW X'pert powder – Multifunctional X-ray diffractometer, SEM and EDX studies were also carried out at NIT Raipur using ZEISS EVO 18 Scanning Electron Microscope and INCA 250 EDS with X-MAX 20 nm detector. Optical absorbance spectral studies were done using ELICO-SL210 UV-VIS spectrophotometer.

3. Results and discussion

3.1. Absorbance spectra

Fig. 2(a) depicts the optical absorbance spectra of $ZnO_{0.5}$–$GO_{0.5}$–$PVP_{0.1}$ and $ZnO_{0.5}$–$GO_{0.5}$–$NMP_{0.1}$ while Fig. 2(b) shows the absorbance spectra of $ZnO_{0.7}$–$GO_{0.3}$–$PVP_{0.1}$ and $ZnO_{0.7}$–$GO_{0.3}$–$NMP_{0.1}$ nanocomposites. The absorption edge in these composites is around 420 nm for those prepared with PVP while in the case of composites

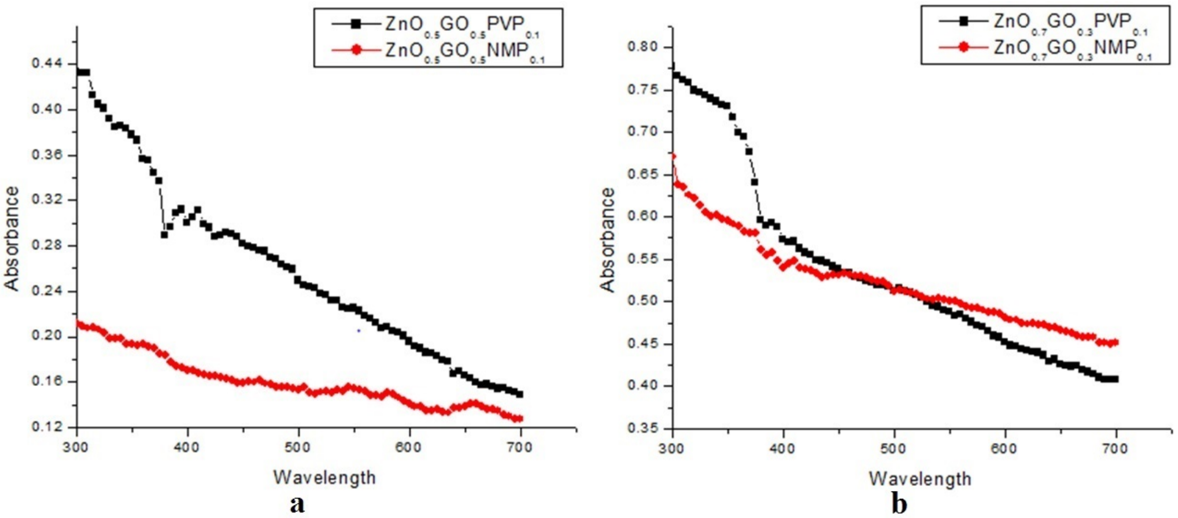

a b

FIG. 2. (a)Absorbance spectra of $ZnO_{0.5}$–$GO_{0.5}$–$PVP_{0.1}$ and $ZnO_{0.5}$–$GO_{0.5}$–$NMP_{0.1}$ Nanocomposites; (b)Absorbance spectra of $ZnO_{0.7}$–$GO_{0.3}$–$PVP_{0.1}$ and $ZnO_{0.7}$–$GO_{0.3}$–$NMP_{0.1}$ Nanocomposites

prepared with NMP, the absorption edge shifts to shorter wavelength around 400 nm. This is in agreement with other reports on the absorption edge of GO–ZnO composites [8, 16]. Tauc's plots (plot between $(\alpha hv)^2$ vs hv where α is the absorption coefficient) were used to determine the band gap of the material from the absorbance data. Fig. 3(a) represents the Tauc's plot of $ZnO_{0.5}$–$GO_{0.5}$–$PVP_{0.1}$ and $ZnO_{0.5}$–$GO_{0.5}$–$NMP_{0.1}$ and Fig. 3(b) shows the Tauc's plot of $ZnO_{0.7}$–$GO_{0.3}$–$PVP_{0.1}$ and $ZnO_{0.7}$–$GO_{0.3}$–$NMP_{0.1}$. The corresponding values of band gap are presented in Table 1 and are found to be in the range between 2.7 and 3.0 eV. The band gap values of composites prepared with NMP are higher than those with PVP.

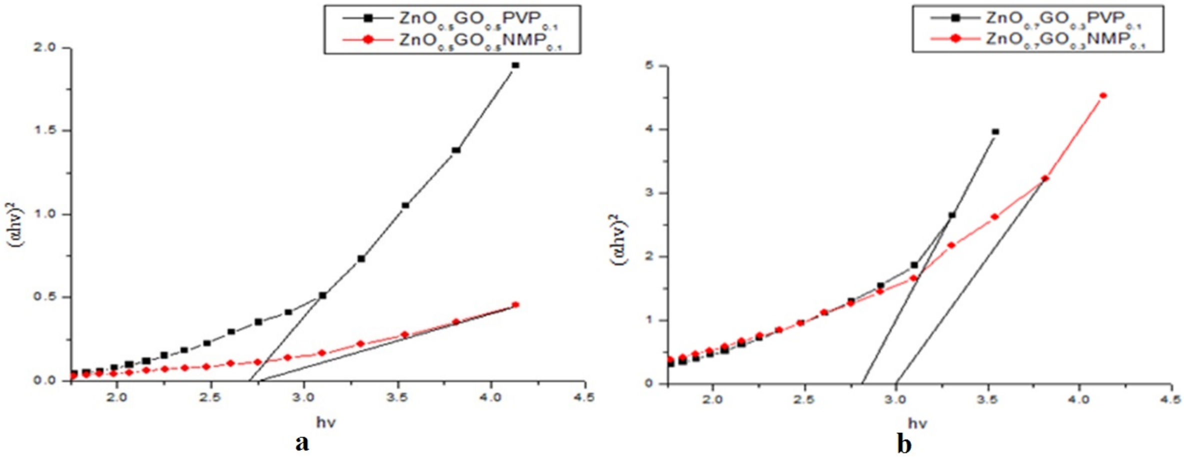

a b

FIG. 3. (a)Tauc's plot of $ZnO_{0.5}$–$GO_{0.5}$–$PVP_{0.1}$ and $ZnO_{0.5}$–$GO_{0.5}$–$NMP_{0.1}$ Nanocomposites; (b)Tauc's plot of $ZnO_{0.7}$–$GO_{0.3}$–$PVP_{0.1}$ and $ZnO_{0.7}$–$GO_{0.3}$–$NMP_{0.1}$ Nanocomposites

3.2. XRD Studies

Figure 4(a) and 4(b) represent the X-ray diffractograms of $ZnO_{0.5}$–$GO_{0.5}$–$PVP_{0.1}$ and $ZnO_{0.5}$–$GO_{0.5}$–$NMP_{0.1}$ and the corresponding data are presented in Tables 2 and 3 respectively. The assignments of the different peaks were made by comparison with JCPDS data of GO and JCPDS data 36-1451 of ZnO and calculation of lattice constants, which showed agreement with the reported values. In both the cases, maximum intensity corresponds to the (100) plane of ZnO. The other prominent planes corresponding to ZnO are (002), (101), (102), (110), (103), (200), (004) which have been observed in both the cases. Diffraction line (002) of GO is also observed.

TABLE 1. Band Gap values of ZnO–GO Nanocomposites

S No.	**Sample**	**Band Gap (eV)**
1	$ZnO_{0.5}GO_{0.5}PVP_{0.1}$	2.7
2	$ZnO_{0.5}GO_{0.5}NMP_{0.1}$	2.75
3	$ZnO_{0.7}GO_{0.3}PVP_{0.1}$	2.8
4	$ZnO_{0.7}GO_{0.3}NMP_{0.1}$	3.0

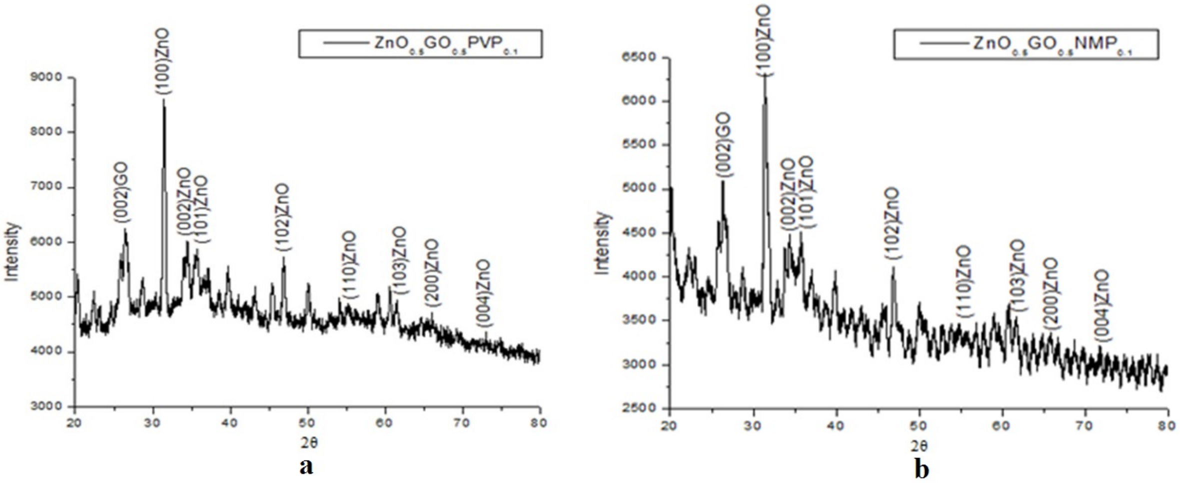

FIG. 4. (a)X-ray diffractogramof $ZnO_{0.5}$–$GO_{0.5}$–$PVP_{0.1}$ Nanocomposites; (b)X-ray diffractogram of $ZnO_{0.5}$–$GO_{0.5}$–$NMP_{0.1}$ Nanocomposites

TABLE 2. XRD data of $ZnO_{0.5}$–$GO_{0.5}$–$PV_{0.1}$ Nanocomposites

d Value(A^0)		**Relative Intensity**		**hkl**	**Lattice Constant c (A^0)**	
(Obs)	**(Rep)**	**(Obs)**	**(Rep)**		**(Obs)**	**(Rep)**
3.3714	3.3608	–	–	(002)GO	–	–
2.8392	2.8143	100	57	(100)ZnO	$a = 3.278$	$a = 3.25, c = 5.207$
2.6031	2.6033	70	44	(002)ZnO	$c = 5.206$	$a = 3.25, c = 5.207$
2.5104	2.4759	68.24	100	(101)ZnO	$a = 3.308, c = 5.206$	$a = 3.25, c = 5.207$
1.9347	1.9111	66.69	23	(102)ZnO	$a = 3.339, c = 5.206$	$a = 3.25, c = 5.207$
1.6327	1.6247	55.52	32	(110)ZnO	$a = 3.265$	$a = 3.25, c = 5.207$
1.5054	1.4771	57.58	29	(103)ZnO	$a = 3.49, c = 5.206$	$a = 3.25, c = 5.207$
1.4125	1.4072	54.78	4	(200)ZnO	$a = 3.262$	$a = 3.25, c = 5.207$
1.2941	1.3017	50.70	2	(004)ZnO	$c = 5.176$	$a = 3.25, c = 5.207$

Fig. 5(a) and 5(b) represent the X-ray diffractograms of $ZnO_{0.7}$–$GO_{0.3}$–$PVP_{0.1}$and $ZnO_{0.7}$–$GO_{0.3}$–$NMP_{0.1}$ and the corresponding data are presented in Tables 4 and 5 respectively. The diffraction lines observed with $ZnO_{0.7}$–$GO_{0.3}$ are quite different from the lines observed in the case of $ZnO_{0.5}$–$GO_{0.5}$. The maximum intensity peak in both $ZnO_{0.7}$–$GO_{0.3}$–$PVP_{0.1}$ and $ZnO_{0.7}$–$GO_{0.3}$–$NMP_{0.1}$ composites is (002) plane of ZnO. The other planes observed are (100), (101), (102), (110) of ZnO and (002) plane of GO. The presence of diffraction lines of both GO and ZnO confirms the formation of the nanocomposites. The existence of only one GO peak may be due to the partial reduction of the GO to Graphene sheet [15].

The particle sizes were calculated using the Debye–Scherrer's formula (D=0.94λ/ß$_{1/2}\cos\theta$) and the corresponding values are presented in Table 6. The average particle sizes were found to be in the nanometer range.

TABLE 3. XRD data of $ZnO_{0.5}$–$GO_{0.5}$–$NMP_{0.1}$ Nanocomposites

d Value(A^0)		**Relative Intensity**		**hkl**	**Lattice Constant (A^0)**	
(Obs)	**(Rep)**	**(Obs)**	**(Rep)**		**(Obs)**	**(Rep)**
3.3846	3.3608	–	–	(002)GO	–	–
2.8462	2.8143	100	57	(100)ZnO	$a = 3.286$	$a = 3.25, c = 5.207$
2.5992	2.6033	70.93	44	(002)ZnO	$c = 5.198$	$a = 3.25, c = 5.207$
2.5104	2.4759	71.29	100	(101)ZnO	$a = 3.31, c = 5.198$	$a = 3.25, c = 5.207$
1.9347	1.9111	65.01	23	(102)ZnO	$a = 3.345, c = 5.198$	$a = 3.25, c = 5.207$
1.6168	1.6247	55.03	32	(110)ZnO	$a = 3.233$	$a = 3.25, c = 5.207$
1.5008	1.4771	56.17	29	(103)ZnO	$a = 3.466, c = 5.198$	$a = 3.25, c = 5.207$
1.417	1.4072	53.35	4	(200)ZnO	$a = 3.272$	$a = 3.25, c = 5.207$
1.2986	1.3017	49.47	2	(004)ZnO	$c = 5.194$	$a = 3.25, c = 5.207$

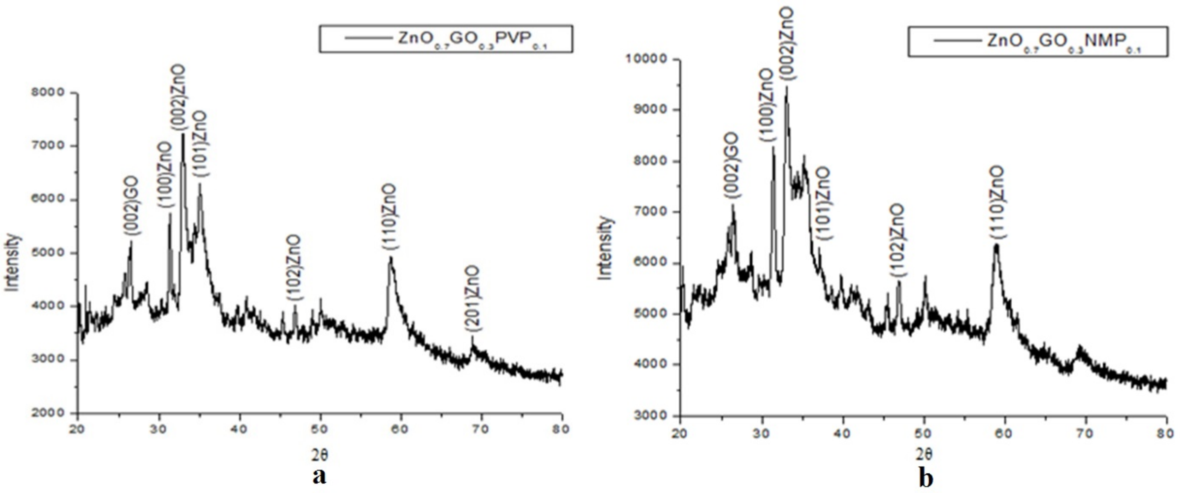

FIG. 5. (a)X-ray diffractogram of $ZnO_{0.7}$–$GO_{0.3}$–$PVP_{0.1}$ Nanocomposites; (b)X-ray diffractogramof $ZnO_{0.7}$–$GO_{0.3}$–$NMP_{0.1}$ Nanocomposites

TABLE 4. XRD data of $ZnO_{0.7}$–$GO_{0.3}$–$PVP_{0.1}$ Nanocomposites

d Value(A^0)		**Relative Intensity**		**hkl**	**Lattice Constant (A^0)**	
(Obs)	**(Rep)**	**(Obs)**	**(Rep)**		**(Obs)**	**(Rep)**
3.3583	3.3608	–	–	(002)GO	–	–
2.8485	2.8143	79.52	57	(100)ZnO	$a = 3.289$	$a = 3.25, c = 5.207$
2.7116	2.6033	100	44	(002)ZnO	$c = 5.423$	$a = 3.25, c = 5.207$
2.554	2.4759	87.14	100	(101)ZnO	$a = 3.289, c = 5.768$	$a = 3.25, c = 5.207$
1.9347	1.9111	55.58	23	(102)ZnO	$a = 3.289, c = 5.272$	$a = 3.25, c = 5.207$
1.5724	1.6247	68.22	32	(110)ZnO	$a = 3.144$	$a = 3.25, c = 5.207$

TABLE 5. XRD data of $ZnO_{0.7}$–$GO_{0.3}$–$NMP_{0.1}$ Nanocomposites

d Value(A^0)		Relative Intensity		hkl	Lattice Constant (A^0)	
(Obs)	(Rep)	(Obs)	(Rep)		(Obs)	(Rep)
3.3681	3.3608	–	–	(002)GO	–	–
2.8392	2.8143	87.63	57	(100)ZnO	$a = 3.278$	$a = 3.25, c = 5.207$
2.7095	2.6033	100	44	(002)ZnO	$c = 5.419$	$a = 3.25, c = 5.207$
2.4804	2.4759	67.96	100	(101)ZnO	$a = 3.278, c = 5.099$	$a = 3.25, c = 5.207$
1.9326	1.9111	59.97	23	(102)ZnO	$a = 3.278, c = 5.276$	$a = 3.25, c = 5.207$
1.6554	1.6247	53.88	32	(110)ZnO	$a = 3.31$	$a = 3.25, c = 5.207$

TABLE 6. Particle sizes of ZnO–GO Nanocomposites

S No.	Sample	Particle size (nm)
1	$ZnO_{0.5}GO_{0.5}PVP_{0.1}$	9.55
2	$ZnO_{0.5}GO_{0.5}NMP_{0.1}$	6.48
3	$ZnO_{0.7}GO_{0.3}PVP_{0.1}$	7.6
4	$ZnO_{0.7}GO_{0.3}NMP_{0.1}$	6.55

3.3. SEM Studies

The SEM micrographs of the $ZnO_{0.5}$–$GO_{0.5}$–$PVP_{0.1}$, $ZnO_{0.5}$–$GO_{0.5}$–$NMP_{0.1}$, $ZnO_{0.7}$–$GO_{0.3}$–$PVP_{0.1}$ and $ZnO_{0.7}$–$GO_{0.3}$–$NMP_{0.1}$ at a magnification of 50KX are shown in Fig. 6(a), 6(b), 7(a) and 7(b) respectively. A layered structure consisting of a mixture of sheets and rods along with small clusters of particles distributed on the surface of GO is seen in all the cases, confirming the interaction between ZnO and GO. The distribution of sheets and rods is on the surface of GO in the case of ZnO–GO–NMP composites in comparison to ZnO–GO–PVP composites. The images suggest that the formation of sheets and rods of ZnO prevent the stacking of graphene sheets and contribute to the electron transfer between ZnO rods and GO.

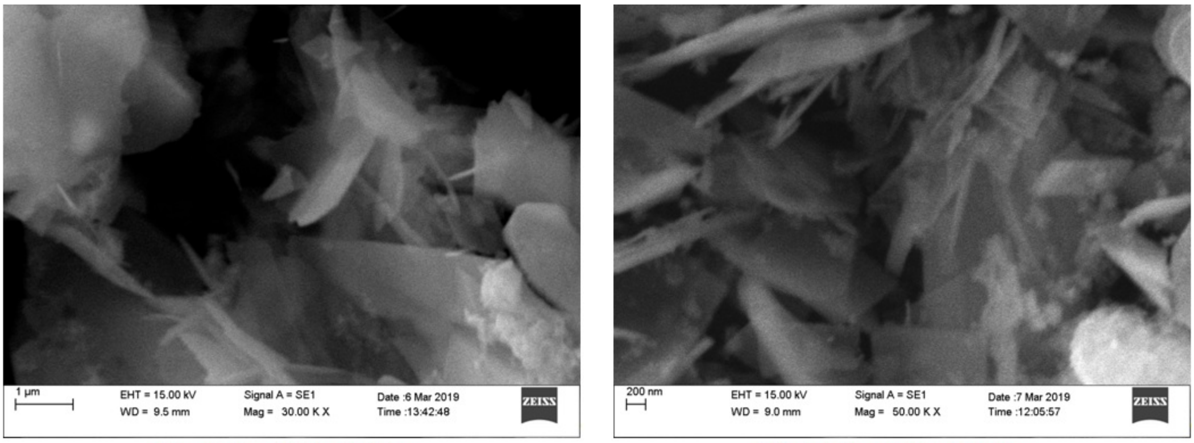

(a) $ZnO_{0.5}$-$GO_{0.5}$-$PVP_{0.1}$ (b) $ZnO_{0.5}$-$GO_{0.5}$-$NMP_{0.1}$

FIG. 6. SEM image of (a) $ZnO_{0.5}$–$GO_{0.5}$–$PVP_{0.1}$ Nanocomposites and (b) $ZnO_{0.5}$–$GO_{0.5}$–$NMP_{0.1}$ Nanocomposites

3.4. EDX Studies

Figures 8(a), 8(b), 9(a) and 9(b) represent the EDX spectra of $ZnO_{0.5}$–$GO_{0.5}$–$PVP_{0.1}$, $ZnO_{0.5}$–$GO_{0.5}$–$NMP_{0.1}$, $ZnO_{0.7}$–$GO_{0.3}$–$PVP_{0.1}$ and $ZnO_{0.7}$–$GO_{0.3}$–$NMP_{0.1}$ respectively. The presence of C, Zn and O is detected in all the cases confirming the formation of the nanocomposites. In the case of the ZnO–GO composites prepared in the presence of NMP, the C content is higher in comparison to the composite prepared in the presence of PVP. PVP is a

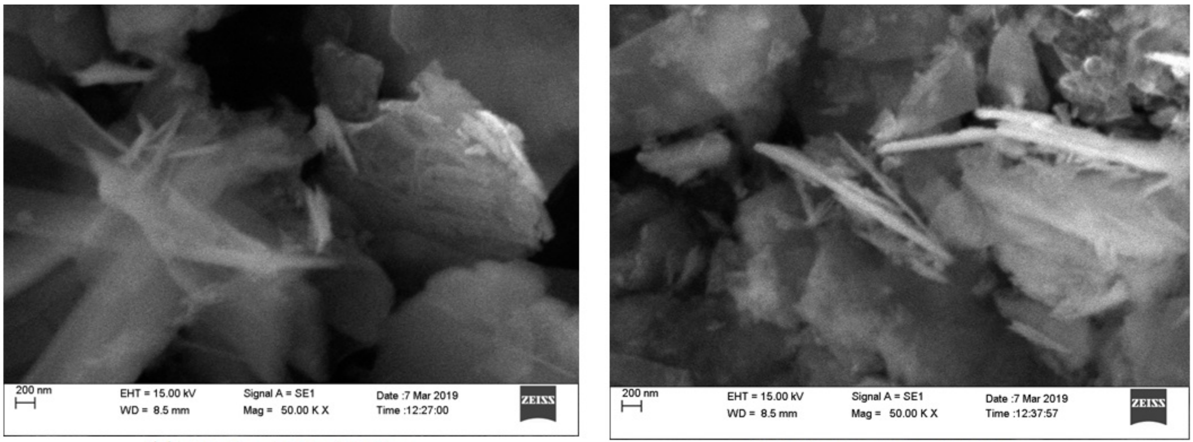

(a) $ZnO_{0.7}$-$GO_{0.3}$-$PVP_{0.1}$ (b) $ZnO_{0.7}$-$GO_{0.3}$-$NMP_{0.1}$

FIG. 7. SEM image of (a) $ZnO_{0.7}$–$GO_{0.3}$–$PVP_{0.1}$ Nanocomposites and (b) $ZnO_{0.7}$–$GO_{0.3}$–$NMP_{0.1}$ Nanocomposites

known surface stabilizing water soluble polymer effective in solubilization of Carbon materials [8], thereby resulting in the decreased percentage of Carbon atoms in these composites.

Element	Weight%	Atomic%
C K	11.50	19.84
O K	53.28	69.00
Zn K	35.22	11.17

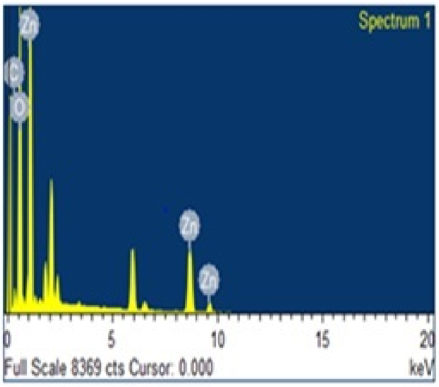

a

Element	Weight%	Atomic%
C K	28.64	40.84
O K	50.07	53.59
Zn K	21.29	5.58

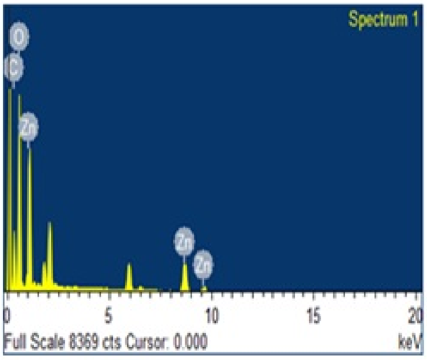

b

FIG. 8. EDX spectra of (a) $ZnO_{0.5}$–$GO_{0.5}$–$PVP_{0.1}$ Nanocomposites and (b) $ZnO_{0.5}$–$GO_{0.5}$–$NMP_{0.1}$ Nanocomposites

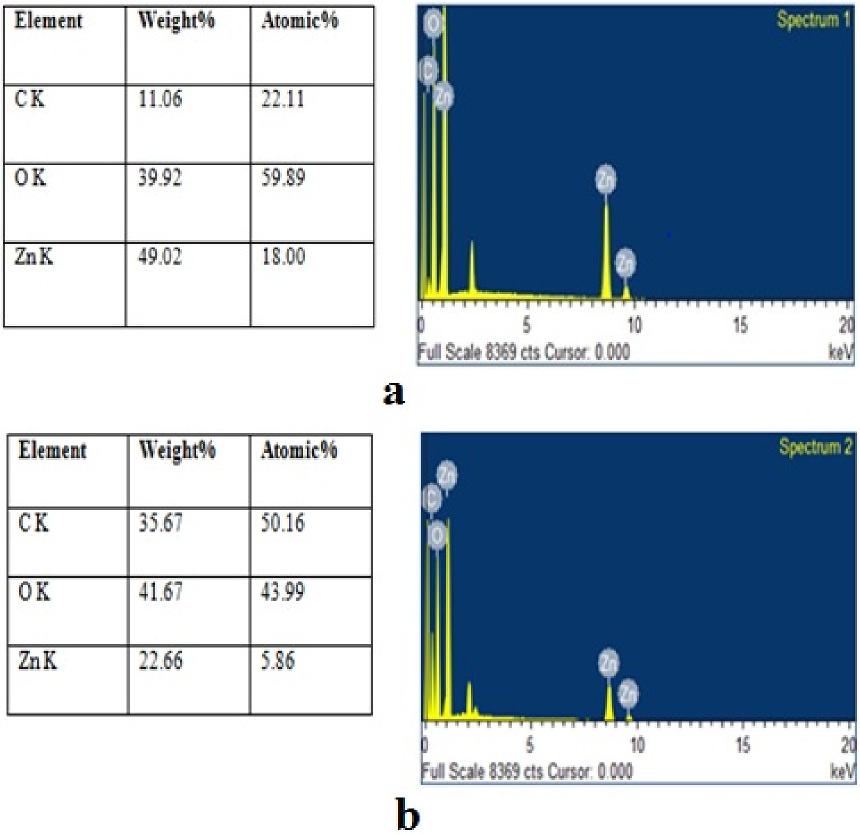

Element	Weight%	Atomic%
CK	11.06	22.11
OK	39.92	59.89
ZnK	49.02	18.00

Element	Weight%	Atomic%
CK	35.67	50.16
OK	41.67	43.99
ZnK	22.66	5.86

FIG. 9. EDX spectra of (a) $ZnO_{0.7}$–$GO_{0.3}$–$PVP_{0.1}$ Nanocomposites and (b) $ZnO_{0.7}$–$GO_{0.3}$–$NMP_{0.1}$ Nanocomposites

3.5. Conclusion

ZnO–GO nanocomposites were synthesized successfully using PVP and NMP as solvents by the sol-gel technique. The structural properties investigated using XRD studies showed the presence of planes of both GO and ZnO confirming the formation of composites. The particle sizes determined from XRD were found to be in nano range. A layered structure comprising of sheets and rods anda non-uniform distribution of agglomerating particles was observed from SEM micrographs. EDX spectra showed reflections of Carbon, Zinc and Oxygen in the composites. ZnO–GO synthesized using PVP showed higher absorbance in comparison toZnO–GO with NMP. A shift in absorption edge to shorter wavelength in the presence of NMP was also observed. The band gap values were found to range from 2.7–3.0 eV with the band gap of ZnO–GO with NMP showing a higher value than ZnO–GO with PVP. It is quite clear from our observations that the optical band gaps of the nanocomposites are affected by varying the solvents. However, a marked difference in the structure of the composites is not observed by the presence of different solvents.

Acknowledgment

The authors are thankful to Mr. Suresh Dua and Mr. Vinod Kumar Ingole of NIT Raipur for XRD, SEM and EDX studies.

References

[1] Muslih E.Y., Kim K.H. Preparation of Zinc Oxide (ZnO) Thin Film as Transparent Conductive Oxide (TCO) from Zinc Complex Compound on Thin Film Solar Cells: A Study of O_2 Effect on Annealing Process. *IOP Conf. Series: Materials Science and Engineering*, 2017, **214**, P. 012001.

[2] Law M., Greene L.E., Johnson J.C., Saykally R. and Yang P.D. Nanowire Dye-Sensitized Solar Cells, *Nature Materials*, 2005, **4**, P. 455.

[3] Al-Fandi M., Oweis R., Albiss B.A., AlZoubi T., M-Ali Al-Akhras, Qutaish H., Khwailah H., Al-Hattami S., Al-Shawwa E. A prototype Ultraviolet Light Sensor based on ZnO Nanoparticles/Graphene Oxide Nanocomposite Using Low Temperature Hydrothermal Method, International Conference on Advanced Materials (ICAM 2015). *IOP Publishing IOP Conf. Series: Materials Science and Engineering*, 2015, **92**. P. 012009.

[4] Wan Q., Li Q.H., Chen Y.J., Wang T.H., He X.L., Li J.P., Lin C.L. Fabrication and ethanol sensing characteristics of ZnO nanowire gas sensors. *Appl. Phys.Lett.*, 2017, **84**, P. 3654.

[5] Seyed A. Hosseini, ShabnamBabaei.Graphene Oxide/Zinc Oxide (GO/ZnO) Nanocomposite as a Superior Photocatalyst for Degradation of Methylene Blue (MB)-Process Modeling by Response Surface Methodology (RSM). *J. Braz. Chem. Soc.*, 2017, **28**(2), P. 299–307.

[6] Kant S., Kumar A. A comparative analysis of structural, optical and photocatalytic properties of ZnO and Ni doped ZnOnanospheres prepared by sol-gel method. *Adv. Mater. Lett.*, 2012, **3**, P. 350–354.

[7] Shao D., Qin L., Sawyer S. High Responsivity, Bandpass Near-UV Photodetector Fabricated From PVA-In_2O_3 Nanoparticles on a GaN Substrate. *Photonics J IEEE*, 2012, **4**(3), P. 715–720.

[8] Labhane P.K., Patle L.B., Huse V.R., Sonawane G.H., Sonawane S.H. Synthesis of reduced graphene oxide sheets decorated by zinc oxide-nanoparticles: Crystallographic, optical, morphological and photocatalytic study. *Chemical Physics Letters*, 2016, **661**, P. 13–19.

[9] Maira B. Moreno-Trejo, Yolanda Agapito-Navarro, Uriel Marquez-Lamas, Tania Lara Ceniceros, Jose Bonilla-Cruz, Margarita Sanchez-Domínguez. Preparation of Zinc Oxide Nanostructures and Hybrid Graphene/Zinc Oxide nanomaterials by a polysaccharide aqueous-based method, Third US-Mexico Meeting Advances in Polymer Science and XXVII SPM National Congress Nuevo Vallarta, December 2014 MACROMEX 2014.

[10] Dongzhi Zhang, Jingjing Liu, Bokai Xia. Layer-by-Layer Self-Assembly of Zinc Oxide/Graphene Oxide Hybrid Toward Ultrasensitive Humidity Sensing. *IEEE Electron Device Letters*, 2016, **37**(7).

[11] Phindile B. Khoza, Makwena J. Moloto, Lucky M. Sikhwivhilu.The Effect of Solvents, Acetone, Water, and Ethanol, on the Morphological and Optical Properties of ZnO Nanoparticles Prepared by Microwave. *Journal of Nanotechnology*, 2012, **2012**, Article ID 195106, 6 pages.

[12] Ibrahim Mustapha Alibe, Khamirul Amin Matori, Hj Ab Aziz Sidek, Yazid Yaakob, Umer Rashid, Ali Mustapha Alibe, Mohd Ha?z Mohd Zaid, Salisu Nasir, Maharaz Mohammed Nasir. Effects of polyvinylpyrrolidone on structural and optical properties of willemite semiconductor nanoparticles by polymer thermal treatment method. *Journal of Thermal Analysis and Calorimetry*, 2019, **136**, P. 2249–2268.

[13] Kallum M. Koczkur, Stefanos Mourdikoudis, Lakshminarayana Polavarapu, Sara E. Skrabalak. Polyvinylpyrrolidone (PVP) in nanoparticle synthesis. *Dalton transactions*, 2015, **41**.

[14] Shingo Tachikawa, Atsushi Noguchi, Takeharu Tsuge, Masahiko Hara, Osamu Odawara, Hiroyuki Wada. Optical Properties of ZnO Nanoparticles Capped with Polymers, **Materials**, 2011, **4**, P. 1132–1143.

[15] Zaaba N.I., Foo K.L., Hashim U., Tan S.J., Wei-Wen Liu, Voon C.H. Synthesis of Graphene Oxide using Modified Hummers Method: Solvent Influence. *Procedia Engineering*, 2017, **184**, P. 469–47.

[16] Gayathri S., Jayabal P., Kottaisamy M., Ramakrishnan V. Synthesis of ZnO decorated graphene nanocomposite for enhanced photocatalytic properties. *Journal of Applied Physics*, 2014, **115**, P. 173504.

NANOSYSTEMS: PHYSICS, CHEMISTRY, MATHEMATICS, 2019, 10 (6), P. 720–724

Methodology of analyzing the InSb semiconductor quantum dots parameters

A. I. Mikhailov, V. F. Kabanov, M. V. Gavrikov

Saratov State University, Department of Nanoand Biomedical Technologies,
Astrakhanskaya, 83, Saratov, 410012, Russia

maks.gavrikov.96@gmail.com

DOI 10.17586/2220-8054-2019-10-6-720-724

The investigation of indium antimonide quantum dots has been carried out by the methods of differential normalized tunnel current-voltage characteristics, electron microscopy, particle size analysis and spectral dependence of the absorption coefficient. Qualitatively and quantitatively consistent measurement results were obtained with an error less than 15 %. It is concluded that the analysis of normalized differential tunnel current-voltage characteristics is an effective method of express-analysis that can be used in investigation of quantum-sized objects properties.

Keywords: quantum dots, indium antimonide, differential tunnel current-voltage characteristics, energy spectrum.

Received: 12 September 2019

Revised: 1 November 2019

1. Introduction

In recent decades,semiconductor quantum dots (QDs) have caused great interest among researchers after the discovery of their quantum-size optical and electronic properties. The practical application of QD includes nanoelectronics, optoelectronics (displays, photovoltaics, light sources), visualization of biological objects, sensors, and etc. [1–6].

Indium antimonide (InSb) QDs causes particular interest due to the unique properties of indium antimonide: ultra-high electron mobility (up to 78000 cm^{2}V^{-1}s^{-1}), direct and narrow (0.18 eV) band gap, small effective masses ofconduction electrons($0.013m_0$, m_0 – mass of a free electron) [7] and large de Broglie wavelength of electrons – up to 55 nm.

The obtaining of various technologies has allowed us to solve problems of physical modeling of electronic processes in QD, investigate the influence of composition and structure on their properties and their interaction during segregation. This is especially important for colloidal QD, in which the crystalline and electronic structures are determined by self-organized nucleation during chemical synthesis, not forced, as during epitaxial growth.

The aim of this work is to develop and substantiate the methodology forinvestigation of InSbquantum dots electrophysical properties.

2. Samples obtaining technologies

Colloid synthesis of InSb QDs was carried out in anhydrous oleylamine using indium chloride $InCl_3$ and antimony tris [bis(trimethylsilyl)amide]($Sb[N(Si–(Me)_3)_2]_3$) as precursors according to the technique [8]. An additional modification of the technique was that a mixture of acetate and indium chloride in the ratio 4:1 was used as the indium precursor. The halide in this system is necessary for the reaction, and the addition of acetate allows to minimize the aggregation processes. QD were transferred from a colloidal solution to the glass substrates with indium – tin oxide (ITO) layer by self-organization of ensembles on the surface with subsequent controlled evaporation of the solvent and control of the layer parameters by optical constants control methods.

3. Research methods

The obtained samples were examined by scanning tunnel microscopy (STM) using SOLVER Nano, a laser particle size analyzer using Zetasizer Nano ZS, scanning electron microscopy (SEM) using a MIRA 2 LMU autoemission scanning electron microscope.

For more complete analysis of electrophysical properties of the obtained film samples with QD, in particular, the electronic spectrum, the STM technique was used. The studies were carried out using an SPM SOLVER Nano scanning probe microscope. Before measuring the tunnel I–V characteristic of an individual particle, we scanned the film surface by STM method in the stabilized – current mode of measurements. After analyzing the STM image of the macrosample surface, we chose no less than 10 points for recording the I–V characteristics. We automatically recorded no less than 10 I–V characteristics per point. The measurements were carried out at currents ranging from

10^{-11} to 10^{-9} A and at voltages from 0 to 2 V. Taking into account the reproducibility of the result of measurements, we selected points with stable characteristics, after which we averaged the obtained characteristics.

Tunneling CVC were measured between the probe and the ITO-deposited layer of InSb QDs. The characteristic size of the QDs was 10 – 20 nm, the distance between the probe and the QD was about 1 – 2 nm. The radius of the probe is determined mainly not by the macroscopic radius of curvature of the tip, but by its atomic structure, i.e. at the tip of the probe there is a high probability of one protruding atom or a small cluster of atoms (few nm) [9]. The stabilizer used in the synthesis of QDs does not allow them to aggregate among themselves and separates them. These two facts allow us to say that the current will mainly be determined by the flow of electrons from a single quantum-sized particle to nanoscale "protrusion" on the probe.

To analyze the experimental tunnel current-voltage characteristics, we used the method of normalized differential current-voltage characteristics $(dI/dV)/(I/V)$ as the dependence on the voltage V. In addition, as shown in [6, 10], this method can be used for analysis of conductivity mechanisms of obtained structures, calculations of their parameters and other important electronic processes.

4. Model representations and results

It is known that quantum-size effects in nanoparticles can be observed under the necessary conditions:

1) characteristic size of nanoparticle should be about the de Broglie wavelength (quantization of the energy spectrum of QD);
2) interval between discrete levels $\varepsilon_{i+1} - \varepsilon_i$ must be at least $3 \div 4$ of kT value (for example, about $4kT$, which corresponds to 0.1 eV at room temperature).

The electron energy in QD can be represented as a three-dimensional infinitely deep potential well and if we use the QD cube-shaped model with the edge a, the position of the energy spectrum levels can be represented this way [11]:

$$\varepsilon_i = \frac{(\pi\hbar)^2}{2m^*} \cdot \frac{1}{a^2} \cdot \left(l^2 + m^2 + n^2\right), \tag{1}$$

here $l, m, n = 1, 2, 3, \ldots$ are natural numbers corresponding to the QD level numbers; m^* is the electron effective mass, and a is the characteristic size of the QD (cube edge).

The electron energies calculated by formula (1) for the first three allowed levels in an InSb QD are shown in Fig. 1. In the calculations, we used the electron effective mass in the conduction band of InSb $m^* \sim 0.013m_0$, where m_0 is the free electron mass.

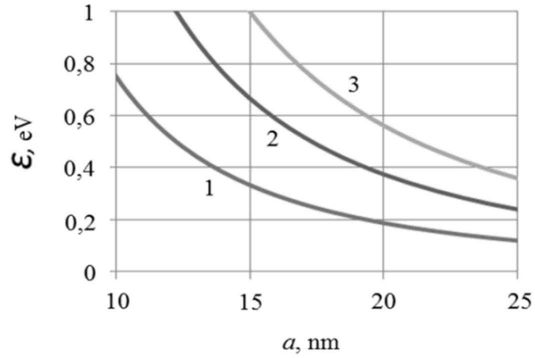

FIG. 1. Calculated electron energies of the first three allowed energy levels (1,2,3) in an InSb QD as a function of the characteristic QD size a (using the "cubic" QD model)

Realization of the necessary conditions for observing quantum-size effects is possible with characteristic sizes of InSb nanoparticles less than 30 nm (de Broglie wavelength is about 55 nm, interval between discrete levels $\varepsilon_2 - \varepsilon_1$ is morethan 0.1 eV). In this case, in the range of variable sizes of QD from 10 to 30 nm, the energy gap $\varepsilon_{c1} - \varepsilon_{v1}$ will vary from 0.3 to 1.0 eV considering the width of the band gapof bulk material (and the position of maximum absorption coefficient will vary from 1.2 to 4.1 μm). This allows us to reasonably assume the possibility of a significant effect of the characteristic size of the InSb QD on their optical and electrical properties overa wide range.

In this research, the normalized differential tunnel current-voltage characteristics were examined and analyzedata negative bias potential on the substrate relative to the probe. In this case, electrons tunnelfrom the ITO electrode to the probe of the tunnel microscope through the discrete levels of the QD. The discrete energy spectrum of conduction electrons of a quantum-size object definesthe peaks on the normalized differential I–V characteristic (Fig. 2(a) they are indicated by arrows). The experimentally obtained values of the applied voltage on the peaks were set in accordance with the calculated values of the electron energy levels of the QD (Fig. 2(b)). That way we determined the range of characteristic sizes of QD, which were compared with the available results. A schematic representation of the band structure with the corresponding energy levels when the potential on the substrate changes relative to the probe is presented in [12].

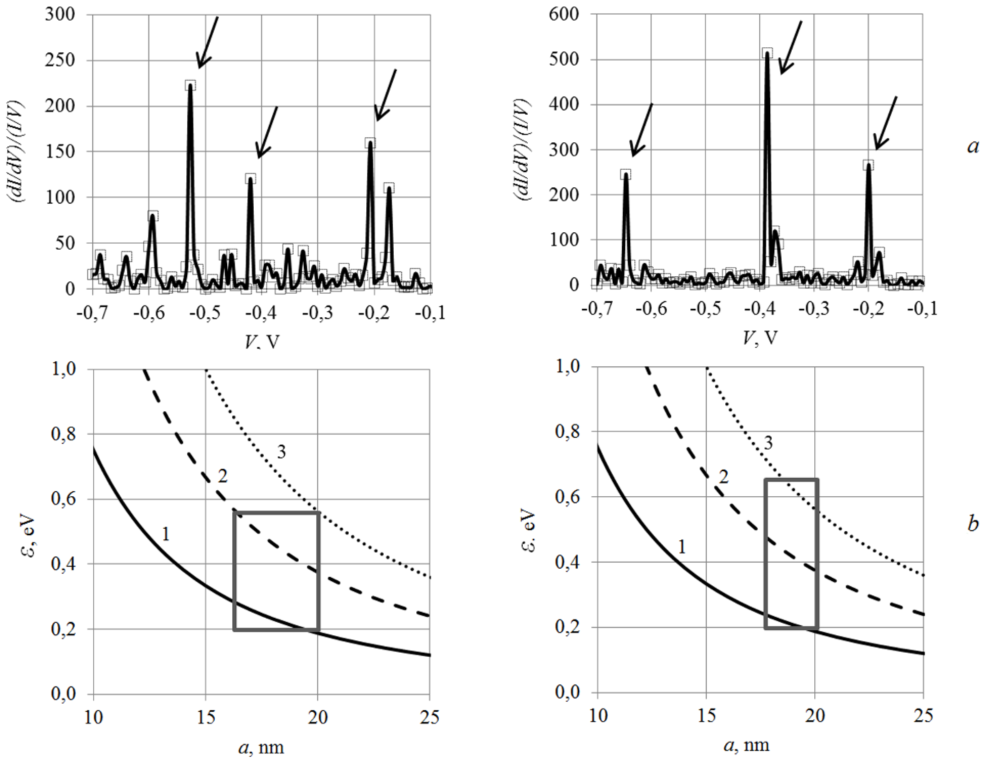

FIG. 2. (a) – typical normalized differential tunnel I–V characteristic of InSb QD samples; (b) – accordance with calculated levels of the energy spectrum. 1,2,3 – calculated electron energies of the first three allowed energy levels

This methodallow us to estimate the characteristic sizes of QD in the range from 16 to 20 nm with the measurement errors of the peak positions less than $2kT$.

To confirm the validity of obtained results, particle size analysis, spectral analysis and direct measurements using SEM were performed.

Spectral analysis of the obtained QD was performed in the range of 1.5 – 5 μm. Typical dependence of the absorption coefficient α on the wavelength is presented in Fig. 3

Size estimation of nanoparticles by the position of the maximum on the spectral dependence using the model of the QD cubic form showed characteristic values in the range of 14 – 17 nm.

The results of particle size investigation, using a laser particle size analyzer, is shown in Fig. 4. The obtained results were in the range of 17 – 22 nm.

To clarify the validity of these estimates, direct measurements were made using SEM. The results presented in Fig. 5 show good agreement with the estimated QDs sizes.

5. Conclusions

Thus, it can be concluded that the analysis of normalized differential tunnel current-voltage characteristics is an effective method of express-analysis that can be used in investigation of quantum-sized objects properties, in particular, InSb quantum dots.

Size estimates of samples were obtained using different approaches (particle size analysis, analysis of the spectral dependence of the absorption coefficient, analysis by the method of differential normalized tunnel current-voltage characteristics and direct measurements using SEM) demonstrate qualitatively and quantitatively agreed results with an error less than 15 %.

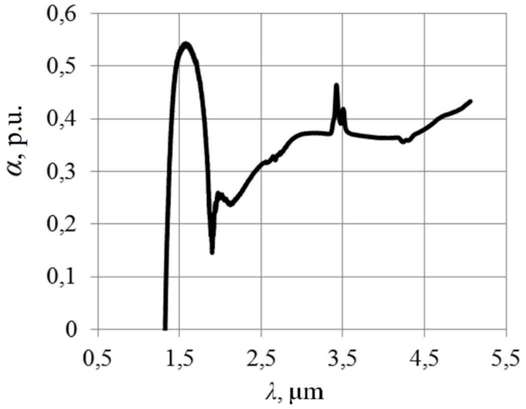

FIG. 3. Typical spectral dependence of the absorption coefficient of InSb QD

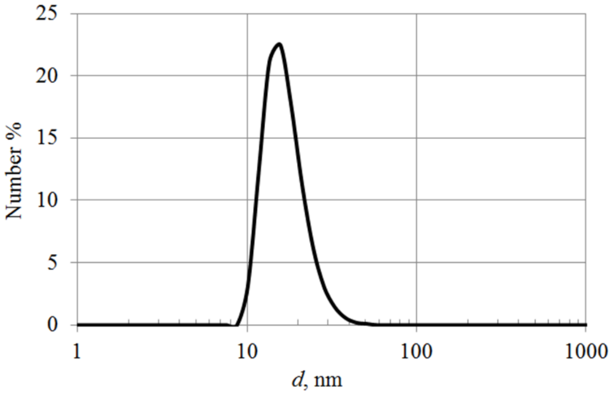

FIG. 4. InSb QD size estimating using a laser particle size analyzer

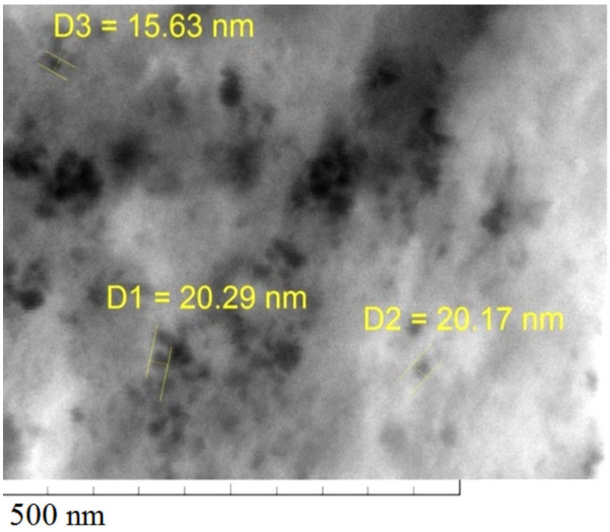

FIG. 5. Typical SEM images of InSb QDs

Acknowledgements

This work was supported by grants from the Russian Foundation for Basic Research Projects No. 19-07-00087 and No. 19-07-00086.

References

[1] Reiss P., Carriere M., et al. Synthesis of Semiconductor Nanocrystals, Focusing on Nontoxic and Earth-Abundant Materials. *Chem. Rev.*, 2016, **116** (18), P. 10731–10819.

[2] Yoffe A.D. Semiconductor quantum dots and related systems: Electronic, optical, luminescence and related properties of low dimensional systems. *Advances in Physics*, 2010, **50** (1), P. 1–208.

[3] Algar W.R., Tavares A.J., Krull U.J. Beyond labels: A review of the application of quantum dots as integrated components of assays, bioprobes, and biosensors utilizing optical transduction. *Analytica Chimica Acta*, 2010, **673** (1), P. 1–25.

[4] Brichkin S.B., Razumov V.F. Colloidal quantum dots: synthesis, properties and applications. *Russ. Chem. Rev.*, 2016, **85** (12), P. 1297–1312.

[5] Li N., Zhang X., Chen S., Hou X. Synthesis and Characterization of CdS Nanoparticles in the Presence of Oleic Acid as Solvent and Stabilizer. *Journal of Physics and Chemistry of Solids*, 2011, **72** (11), P. 1195–1198.

[6] Mikhailov A.I., Kabanov V.F., et al. Methodology of analyzing the A2B6 semiconductor quantum dots parameters. *Nanosystems: Physics, Chemistry, Mathematics*, 2018, **9** (4), P. 464–467.

[7] Abautret J., Perez J.P., et al. Characterization of midwave infrared InSb avalanche photodiode. *J. Appl. Phys.*, 2015, **117** (24), 244502 (1–6).

[8] Liu W., Chang A.Y., Schaller R.D., Talapin D.V. Colloidal InSb Nanocrystals. *J. Am. Chem. Soc.*, 2012, **134** (50), P. 20258–20261.

[9] Mironov V.L. *Principles of Scanning Probe Microscopy*. Tekhnosfera, Moscow, 2009, 110 p.

[10] Mikhailov A.I., Kabanov V.F., Zhukov N.D. Peculiarities of field electron emission from submicron protrusions on a rough InSb surface. *Technical Physics Letters*, 2015, **41** (11), P. 1065–1067.

[11] Dragunov V.P., Neizwestny I.G., Gridchin V.A. *Fundamentals of nanoelectronics*. Fizmatkniga, Moscow, 2006, 496 p.

[12] Mikhailov A.I., Kabanov V.F., et al. Electronic Properties of A2B6 Quantum Dots Incorporated into LangmuirBlodgett Films. *Bulletin of the Russian Academy of Sciences: Physics*, 2017, **81** (12), P. 1472–1475.

NANOSYSTEMS: PHYSICS, CHEMISTRY, MATHEMATICS, 2019, 10 (6), P. 725–732

Experimental evaluation of chemical resistance of steatite products towards aluminum-based melts

N. K. Orlov[1], D. A. Kozlov[1], S. A. Tikhonova[1], A. A. Tikhonov[1], A. V. Garshev[1,2,*], P. V. Evdokimov[1,2],
V. I. Putlayev[1,2], A. A. Vasyakov[3], A. V. Chetvertukhin[3], A. K. Petrov[3], I. Yu. Mikhailov[4],
S. V. Polyakov[5], A. A. Fedyanin[3]

[1]Faculty of materials science, Lomonosov Moscow State University, Moscow, Russia

[2]Faculty of Chemistry, Lomonosov Moscow State University, Moscow, Russia

[3]Faculty of Physics, Lomonosov Moscow State University, Moscow, Russia

[4]LLC Light Materials and Technologies Institute, Moscow, Russia

[5]JSC Russian Aluminium Management, Moscow, Russia

nicolasorlov174@gmail.com, kozlov@inorg.chem.msu.ru, *garshev@inorg.chem.msu.ru,
vasyakov@nanolab.phys.msu.ru, chetvertukhin@nanolab.phys.msu.ru, Ivan.Mikhaylov@rusal.com,
fedyanin@nanolab.phys.msu.ru

PACS 65.40.-b, 81.20.-n, 81.40.Gh, 61.25.Mv **DOI 10.17586/2220-8054-2019-10-6-725-732**

The processes taking place with a spray unit during aluminum dispersion have been analyzed. It has been shown that the major process which occurs in a nipple during aluminum flowing is the reduction of silicon with aluminum and, also, with magnesium from the melt (in case when aluminum-magnesium or magnesium-containing alloys are used). The reduction of silicon results in the formation of nanoscale particles with crystalline size 20–50 nm and leads to the degradation of the nipple material, which is accompanied by its cracking and the formation of nanoscale channels and the flow of melt into the material through these channels. This phenomenon leads to the rupture and/or blockage of the nipple.

Keywords: aluminum alloys, steatite, steatite nipple, AK7 alloy.

Received: 14 August 2019

Revised: 30 November 2019

1. Introduction

Primary aluminum production is one of the most labor- and energy-intensive processes. Nevertheless, these expenses are compensated by the high demand for the resulting metal, which is ensured by the convenience of using aluminum and its alloys in aircraft and rocketry, in the production of gas blowing agents and pigments [1]. Moreover, powders based on aluminum and its alloys obtained from primary aluminum and the relevant ligatures are widely used in the manufacture of metallic parts by selective laser fusion [2], and the mechanical characteristics of the resulting products are as good as of the cast parts [3]. In many cases, an intermediate technological product is the powder consisting of particles no larger than 100 microns in size, which is produced by the dispersion of molten aluminum and aluminum-based alloys under high pressure by a small diameter nozzle [1]. This method is notable for its simplicity and effectiveness. However, the nozzle material (for example, ceramics based on steatite — a natural mineral based on talc, magnesite, and chlorite [4]) is prone to a gradual loss of its initial properties due to the reaction with the flowing melt.

2. Materials and methods

Steatite nipples were made by molding a mixture of pre-ground steatite and liquid glass. After molding, the nipples were dried in a muffle furnace at a temperature of 270 °C, and then they were again immersed into liquid glass and kept at the same temperature. Then the nipples were held at a temperature of 600 °C.

To study the interaction of steatite nipples with aluminum melt, the small nipple samples in an AK7ch alloy melt were isothermally treated for 6, 12, 24, and 48 hours at temperatures of 700 °C and 850 °C. The experiments were carried out in a Nabertherm N7/H resistance muffle furnace under air atmosphere. Then the nipple samples were taken out of the furnace and cooled to a room temperature in the air.

In addition, to verify the possibility of interaction of the aluminum melt with the nipple material, the annealing of the nipple material crushed in the mortar with AK7ch alloy powder was performed. The experiment was carried out in an STA 409 PC Luxx thermal analyzer (Netzsch, Germany) under an argon flow (150 ml/min) with preliminary air evacuation.

The studying of the nipple after aluminum dispersion was carried out using a sample obtained from the factory of aluminum powder production. To determine the composition of the reaction layer, the samples were poured into Struers SpeciFix-20 epoxy resin and ground using a Struers DAP-V grinding-polishing machine (Struers, Germany) in accordance with the guidelines [8].

X-ray phase analysis was carried out on a Rigaku D/Max-2500 instrument (Rigaku, Japan) with a mounted rotating anode. In the course of the experiment, CuK$\alpha_{1,2}$ radiation was used; the experiment was conducted in a reflection mode. The samples were applied onto zero-background silicon cuvettes; the data was collected in the range of angles of 5-90 $^\circ$ 2θ with an increment of 0.02 $^\circ$ 2θ and the signal accumulation time of 0.5 s. The obtained X-ray patterns were analyzed using WinXPOW software with the ICDD PDF-2 database.

Thermal analysis combined with the evolved gas mass spectrometry, was conducted using STA 409 PC Luxx thermal analyzer (Netzsch, Germany) with vertical loading of samples and an Aëolos QMS 403 C quadrupole mass spectrometer (Netzsch, Germany) with heating of the inlet capillary system. The experiments were carried out in alundum crucibles in the temperature range from 40 °C to 1200 °C with the heating rate of 10 °C/min under an air atmosphere. The weight of the samples did not exceed 100 mg.

To obtain microscopic images, the pre-polished samples were examined using a LEO SUPRA 50 VP scanning electron microscope (Zeiss, Germany) using an X-MAX 80 energy dispersive detector (OxfordInst., United Kingdom). The accelerating voltage was set as 20 keV, the data was collected in the mapping mode with a signal accumulation time of 30 minutes. To calculate the elemental composition, the INCA Oxford software package was used in semi-automatic mode. Optical images of the specimens were obtained using an Olympus BX41 optical microscope.

3. Results and discussion

To study the change in the elemental composition during the interaction of the nipple material with the aluminum melt, the samples obtained during isothermal treatment in the furnace were studied by EDX microanalysis. According to the obtained data, the initial nipple contained about 3% Na, 0.6% K, 7% Al, 14% Si, 8% Mg, 0.06% Ti, and 5% Fe (atomic %). It should be noted that the nipple is made from the natural mineral steatite with the addition of liquid glass, and therefore its composition is significantly different from the point of the analysis.

Thermal analysis (Fig. 1) of the nipple material showed a mass loss of 11% with the release of CO_2 and H_2O continuing up to 930 °C. The loss of water up to 200 °C corresponds to the removal of adsorbed water, whereas the loss of water in the range from 400 to 930 °C corresponds to the decomposition of clinochlore and muscovite. The release of CO_2 may correspond to the decomposition of the same clinochlor and muscovite with substituted hydroxy groups into carbonate ones. This substitution does not cause the change in the phase composition due to the structural features of aluminosilicates and this is the reason why the X-ray phase analysis results show the presence of hydroxide forms.

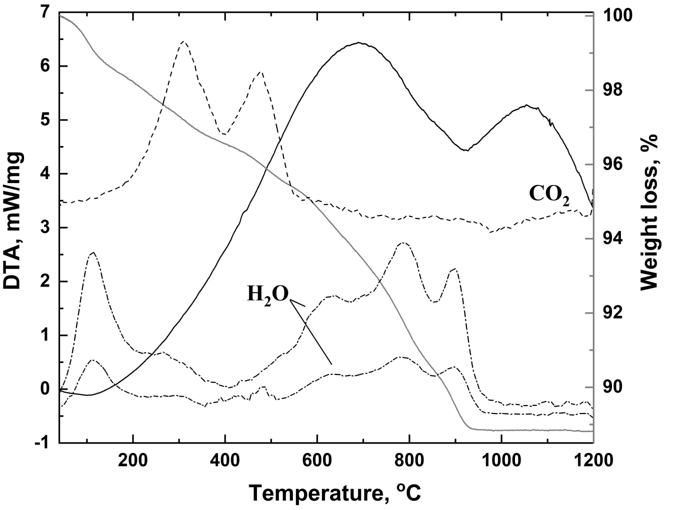

FIG. 1. Thermal analysis of the steatite nipple (1 – differential thermal analysis, 2 – the sample mass loss curve, 3 – the mass spectrum of H_2O^+ and OH^+ions, 4 – the mass spectrum of CO_2^+ions)

According to the X-ray diffraction patterns obtained from the powders of the initial nipple and the nipple annealed in the presence of aluminum (Fig. 2), the steatite nipple consists of crystalline aluminosilicates: muscovite and clinochlore (according to the database of crystal structures, ICDD cards 7–42 and 12–242, respectively). X-ray phase analysis of the samples after annealing at 700 °C for 48 hours showed that muscovite remains as the predominant phase, whereas clinochlore decomposes (the intensity of its main reflections decreases markedly at 12.5 and 25.1°2θ) without the formation of new crystalline phases. After the annealing at 850 °C for 48 hours, muscovite is also present in the sample, but new phases also appear: forsterite (Mg_2SiO_4), nepheline ($NaAlSiO_4$) and cristobalite (SiO_2) (according to the database of crystal structures, ICDD, cards 34-189 and 35 424 and 76-941, respectively).

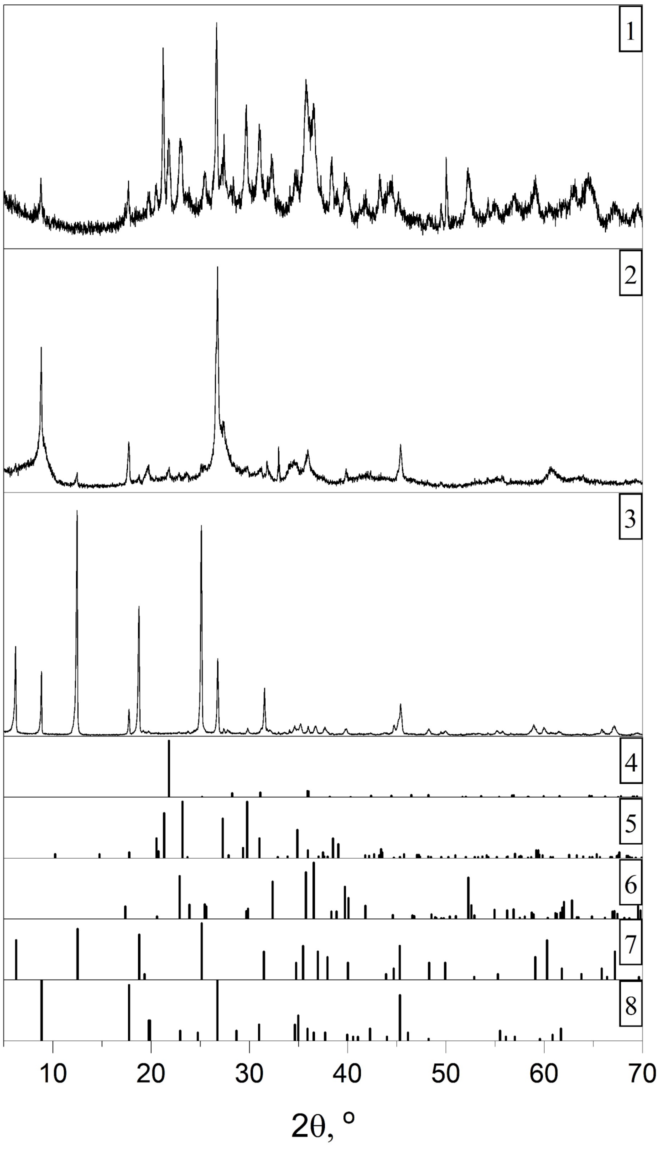

FIG. 2. X-ray phase analysis of the nipple material (1 – X-ray diffraction pattern of the nipple after isothermal treatment at 850°C during 48 hours; 2 – X-ray diffraction pattern of the nipple after isothermal treatment at 700°C during 48 hours, 3 – X-ray diffraction pattern of the initial nipple; 4 – the positions of cristobalite reflections, SiO_2 ICDD [76-941], 5 – the positions of nepheline reflections $NaAlSiO_4$ ICDD [35-424], 6 – the positions of forsterite reflections Mg_2SiO_4 ICDD [34-189], 7 – the positions of clinochlore reflections $(Mg,Al)_6(Si,Al)_4O_{10}(OH)_8$ ICDD [12-242], 8 – the positions of muscovite reflections, $(K,Na)(Al,Mg,Fe)_2(Si,Al)_4O_{10}(OH)_2$ ICDD [7-42])

Thus, according to the data of thermal and X-ray phase analysis, we can conclude that during the exploitation of steatite nipples at the melting temperatures of aluminum and its alloys (650 °C–900 °C), a noticeable degradation of the material occurs with a change in the phase composition of the nipple.

Fig. 3 shows the SEM image and the elements distribution maps of Al, Mg, and Si at the boundary of the nipple sample with the melt after holding at 700 °C for 6 hours. Besides the region of aluminum metal (Al map) and the nipple region (Mg and O maps), a region containing elevated concentrations of magnesium, aluminum, and oxygen was also found at the melt boundary. Probably, this accumulation of magnesium at the melt boundary is caused by the oxidation-reduction (redox) reactions on the surface of the nipple, which is presumably accompanied by the oxidation of magnesium metal from the melt and the reduction of iron and silicate ions to nanosized Fe or Si impurities: 4Almelt + 3SiO2 = 2Al2O3 + 3Simelt

$$4\mathrm{Al}_{melt} + 3\mathrm{SiO}_2 = 2\mathrm{Al}_2\mathrm{O}_3 + 3\mathrm{Si}_{melt}, \tag{1}$$

$$2\mathrm{Mg}_{melt} + \mathrm{SiO}_2 \rightarrow 2\mathrm{MgO} + \mathrm{Si}_{melt}, \tag{2}$$

$$2\mathrm{Fe}^{3+} + 3\mathrm{Mg}_{melt} \rightarrow 3\mathrm{Mg}^{2+} + 2\mathrm{Fe}_{melt}. \tag{3}$$

It should be noted, that these areas contain no other elements presented in the original nipple. Therefore, the probable reaction product may be either MgO, magnesium silicate or magnesium aluminate.

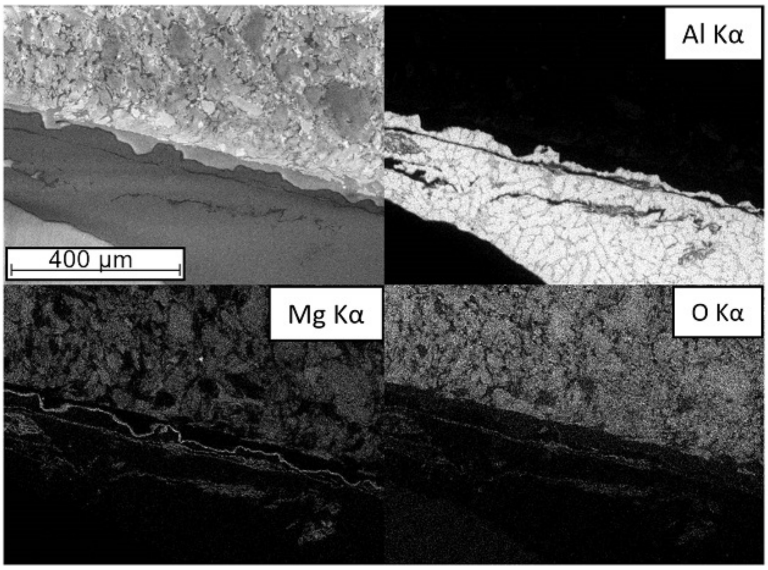

FIG. 3. SEM image in backscattered electrons and the elemental distribution map in the sample obtained during isothermal treatment of steatite in the melt at 700°C over 6 hours

The emergence of a magnesium-containing layer is observed on all samples obtained as a result of the interaction of the nipple with aluminum melt. According to the EDX results, the areas of aluminum penetration into the body of the nipple appear with an increase in the isothermal treatment time to 24 hours. The sizes of these areas increase with increasing isothermal treatment time up to 48 hours. Thus, Fig. 4 shows the SEM image of a sample obtained as a result of the interaction of the nipple with the melt at 700 °C for 48 hours.

According to EDX data, aluminum presents not only in the metal layer near the boundary, but also penetrates into the body of the nipple (the dark region in the SEM image in Fig. 4). In addition, at the boundary of the region of aluminum penetration into the nipple body, a pronounced concentration of sodium is observed, which is caused by the diffusion of sodium ions from the boundary with the melt. This diffusion is probably due to the negative gradient of the chemical potential caused by the redox reactions. It is likely that the interaction of the aluminum melt with the nipple material leads to the reduction of silicates to silicon accompanied by the oxidation of aluminum:

$$6\mathrm{Al}_{liq} + 4\mathrm{SiO}_3^{2-} \rightarrow 3\mathrm{Al}_2\mathrm{O}_4^{2-} + 4\mathrm{Si}_{liq}, \tag{4}$$

$$4\mathrm{Al}_{liq} + 3\mathrm{SiO}_2 \rightarrow 2\mathrm{Al}_2\mathrm{O}_3 + 3\mathrm{Si}_{liq}. \tag{5}$$

It is worth noting that an increase in the temperature and the treatment time of the nipple in the metal melt leads to an increase in the area of aluminum penetration. This is probably caused by the lowering of the melt viscosity with temperature increase, which results in the penetration of the melt into smaller channels, up to nanoscale ones. On the other hand, the reduction of nanosized silicon leads to the cracking of the ceramic material causing its degradation and an increase in the porosity of the channels.

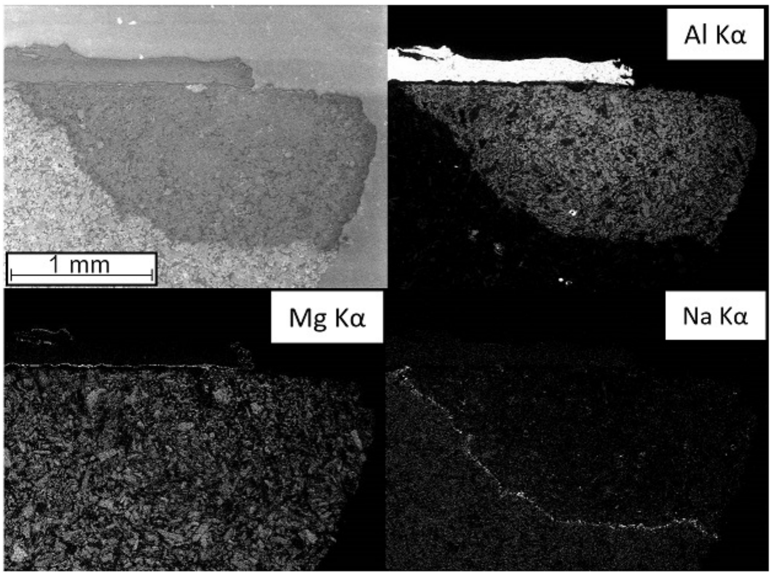

FIG. 4. SEM image in backscattered electrons and the elemental distribution map in the sample obtained during isothermal treatment of steatite in the melt at 700°C during 48 hours

In the samples obtained under isothermal treatment at 850 °C, the magnesium-containing layer does not form, apparently, due to the instability of the products of the magnesium layer at the given temperature. In this case, aluminum penetrates into the nipple to a much greater depth, which is related to an increase in the yield strength of the AK7ch alloy.

Figure 5 shows the SEM and element distribution maps of Al, Mg, and Si at the boundary between the nipple sample and the melt after exposure at 850 ° C for 24 hours. The greater penetration of aluminum into the body of the nipple is confirmed by the intense Al signal (Al map) from the entire nipple region (Mg map). It is also worth noting that at a given time of isothermal treatment an oxygen signal is present from the entire aluminum region indicating the complete oxidation of aluminum under these conditions.

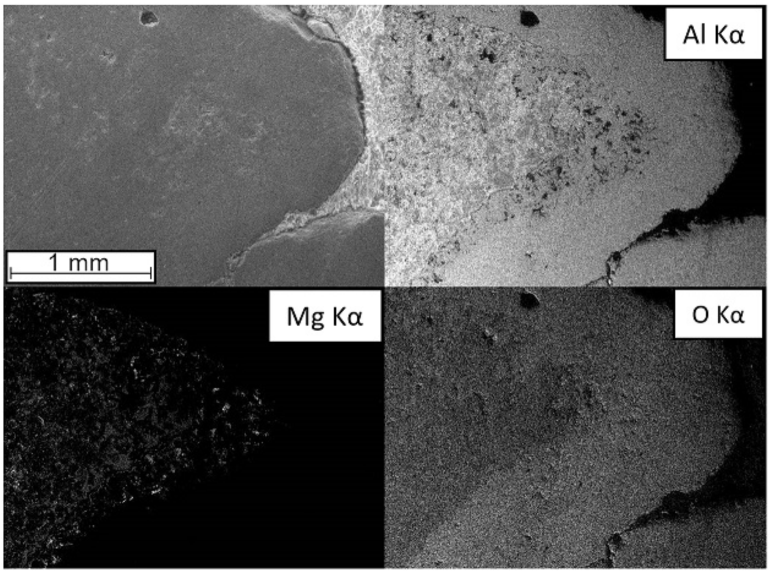

FIG. 5. SEM image in backscattered electrons and the elemental distribution map in the sample obtained during isothermal treatment of steatite in the melt at 850 °C for 24 hours

According to the EDX data, the accumulation of individual elements (Na and Mg) and the penetration of aluminum into the body of the nipple can be explained by the occurrence of the redox reactions at the boundary of the nipple with the melt: the oxidation of metallic magnesium and aluminum from the melt and the reduction of iron and

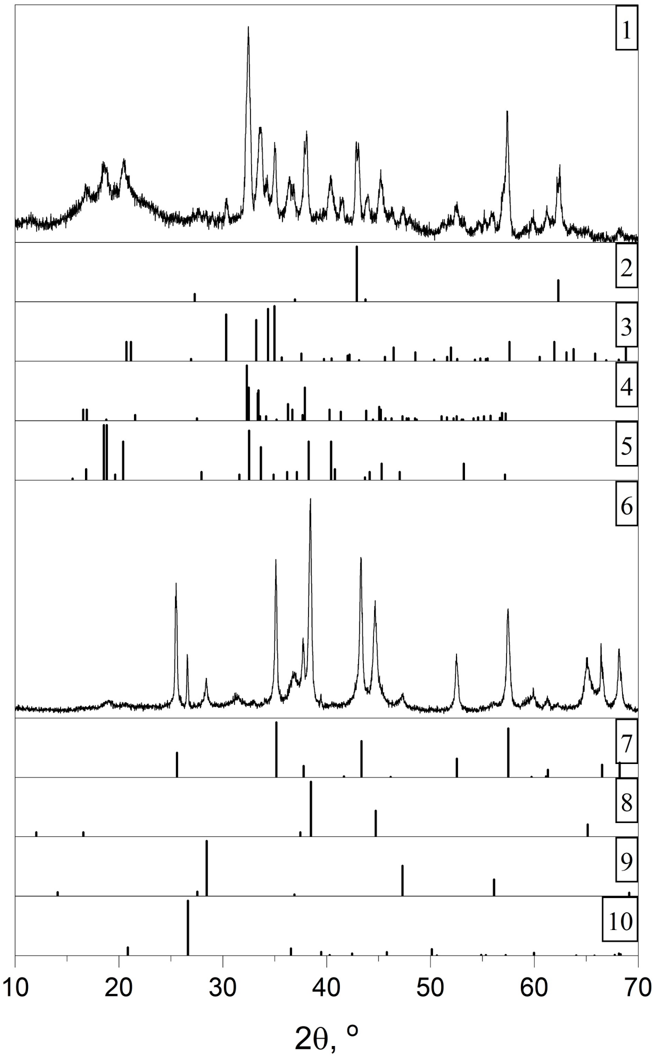

FIG. 6. X-ray phase analysis of the nipple after interaction with the aluminum melt at 850 °C during 12 hours (1 – X-ray diffraction pattern of the region of Na accumulation; 2 – the positions of MgO reflections, ICDD [45-946]; 3 – the positions of $NaAlO_2$ reflections, ICDD [331200]; 4 – the positions of thermonatrite $Na_2CO_3 \cdot H_2O$ reflections, ICDD [8-448], 5 – the positions of $Na_2Al_2O_4 \cdot 6H_2O$ reflections, ICDD [29-1165], 6 – X-ray diffraction pattern of the nipple; 7 – the positions of corundum Al_2O_3 reflections, ICDD [46-1212]; 8 – the positions of Al reflections, ICDD [4787], 9 – the positions of silicon reflections Si, ICDD [27-1402], 10 – the positions of SiO_2 reflections, ICDD [79-1906])

silicates. Thus, we can assume the following mechanism of slag formation: aluminum melt, when flowing through a steatite nipple, partially reduces silicates, transforming into aluminum oxide and aluminates and settles on the walls of the nipple. In turn, at low temperatures, in addition to aluminum oxidation, the reduction of silicates and iron ions by magnesium occurs, leading to the formation of a magnesium-containing layer on the surface of the nipple.

Figure 6 shows the results of XRD analysis of nipple samples after interaction with aluminum melt. The following aluminum-containing phases can be distinguished in the diffraction pattern obtained from the contact area of metallic aluminum with a nipple: metallic aluminum and corundum, and silicon-containing phases – quartz and silicon. The presence of these phases confirms the previously proposed slag formation mechanism (4), according to which, aluminum is oxidized near the surface of the nipple due to the reduction of silicates. The upper X-ray pattern (Fig. 6) corresponds to the boundary of aluminum penetration into the nipple material. According to the results of X-ray phase analysis, after cooling in the air, $Na_2Al_2O_4 \cdot 6H_2O$, $Na_2CO_3 \cdot H_2O$ and $NaAlO_2$ phases with a high sodium content are present in this region of the sample confirming the enrichment of this region with sodium which was proved by EDX

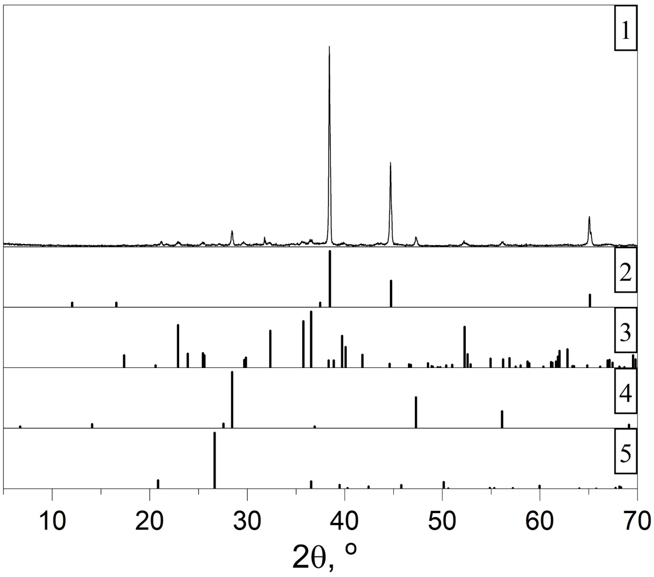

FIG. 7. X-ray phase analysis of the nipple material after grinding with aluminum powder and annealing at 1200 °C (1 – X-ray pattern of the obtained powder; 2 – the positions of Al reflections, ICDD [4787]; 3 – the positions of forsterite, Mg_2SiO_4, reflections, ICDD [34-189]; 4 – the positions of Si reflections [27-1402], 5 – the positions of quartz, SiO_2, reflections, ICDD [79-1906])

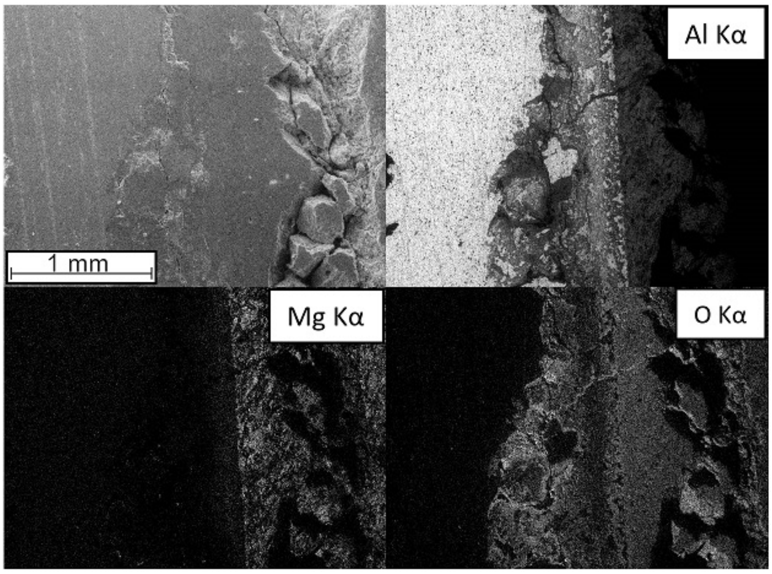

FIG. 8. SEM image in backscattered electrons and elemental distribution maps in the nipple sample obtained from the manufacturer

microanalysis. According to X-ray diffraction data (Fig. 6), the crystallite size of formed silicon crystallites calculated by the Scherrer formula is 21±3 nm, whereas main aluminum-containing phase corundum has characteristic sizes of crystallites of about 44±3 nm.

XRD analysis of the sample of aluminum and steatite after annealing in argon confirmed the assumption that silicon is reduced by magnesium and aluminum. The X-ray diffraction pattern shows peaks of pure silicon with crystallites sizes about 100 nm, which were absent in the initial steatite (Fig. 7).

The results of EDX analysis of the nipples after experiments on the aluminum dispersion show a similar picture (Fig. 8).

The sample contains 4 regions that differ in composition. The first region corresponds to the metallic aluminum located near the boundary of the nipple and the melt. Aluminum and oxygen are present in the second region indicating that the formation of slag occurs due to the oxidation of aluminum metal on the surface of the nipple. In the third region, Al, Si, and O are detected corresponding to the penetration of aluminum into the body of the nipple. It is between the second and third regions where the initial boundary between the nipple and the melt passes, which is confirmed by the even shape of the boundary and the absence of magnesium in the second region. The fourth region corresponds to the nipple material which did not interact with aluminum. Thus, the distribution of elements in the nipple sample confirms the previously proposed mechanism of slag formation on the surface of the nipple as a result of its interaction with the aluminum melt.

4. Conclusions

In summary, it was shown that the most probable reason for slag formation on the surface of steatite nipples caused by the interaction with the aluminum melt is the aluminum oxidation accompanied by the aluminum penetration into the body of the nipple. During the reduction of silicon in the steatite by aluminum melt, the nanoscale particles with crystalline size of 20–50 nm are formed rather than the monolithic layer of the reduction products. Thus reduction process leads to degradation of the nipple material, which is accompanied by its cracking. In this case, the nipple failure can be caused not only by a decrease in the effective diameter of the nipple as a result of the aluminum oxide growth on the inner surface of the nipple, but also by the mechanical instability of the nipple caused both by the removal of gaseous water and carbon dioxide during the nipple heating to the operating temperature and by the degradation of the material during its chemical reduction with molten aluminum.

Acknowledgment

The work was carried out in the organization of the Lead Executor of R&D (Lomonosov Moscow State University) under the Agreement No. PSh-218-2017/ 01 dated 02.09.2017 with financial support from the Ministry of Education and Science of the Russian Federation under Agreement No. 075-11-2018-196 dated 04.28.2017 (internal contract number 03.G25.31.0248).

References

[1] Gopienko V.G., Osipov B.R., Nazarov B.P., Ryumin V.M., Volkov I.V., Yasakov N.I. *Production and application of aluminum powders and fine powders*. Moscow, 1980, 67 p.

[2] Garshev A.V., Kozlov D.A., Evdokimov P. V., Filippov Y.Y., Orlov N.K., Putlyaev V.I., Chetvertukhin A.V., Petrov A.K. Analysis of Aluminum Alloy Powders for Additive Manufacturing Fabricated by Atomization. *Inorg. Mater. Appl. Res.*, 2019, **10**, P. 901–905.

[3] Kempen L., Thijs L., Van Humbeeck J., Kruth J.-P. Mechanical properties of $AlSi_{10}Mg$ produced by Selective Laser Melting. *Phys. Procedia*, 2012, **39**, P. 439–446.

[4] Bhavan I., Lines C. *Indian Minerals Yearbook* 2015 Vol. III- Mineral Reviews, Indian Bureau of Mines, Nagpur, 2015, 50 p.

[5] Kuksa A.V., Molkov A.V., Gubanov A.V., Linkov S.V. *Melt metals spraying jet*, RU2321475, 2007.

[6] Arkhipov V.A., Evsevleev M.J., Zhukov A.S., Zmanovskij S.V., Konovalenko A.I., Litvinov A.V. *Nozzle for melted metals spraying*, RU2554257, 2014.

[7] Kabatsov M.V., Lagutkin S.V. *Device for producing metal distribution by melt melt*, RU133032, 2013.

[8] Bjerregaard L., Geels K., Ottesen B., Rueckert M. *Metalog Guide*, Richard Larsen A/S, Rodovre, 1992, 115 p.

NANOSYSTEMS: PHYSICS, CHEMISTRY, MATHEMATICS, 2019, 10 (6), P. 733–739

Effect of heterogeneous inclusions on the formation of TiO_2 nanocrystals in hydrothermal conditions

V. V. Zlobin[1], A. A. Krasilin[2], O. V. Almjasheva[1,2]

[1]Saint Petersburg Electrotechnical University “LETI”, Professor Popov St. 5, Saint Petersburg, 197376, Russia
[2]Ioffe Institute, Politekhnicheskaya St. 26, Saint Petersburg, 194021, Russia

zvv1210@yandex.ru, ikrasilin@mail.ioffe.ru, almjasheva@mail.ru

PACS 81.07.Wx **DOI 10.17586/2220-8054-2019-10-6-733-739**

The effects of heterogeneous impurities on the process of titanium dioxide nanoparticle formation during hydrothermal synthesis and photocatalytic properties of synthesized particles were studied. Pre-formed TiO_2 nanoparticles of anatase and rutile modifications were used as the heterogeneous impurity. It is shown that the heterogeneous impurities may be considered neither as geometric constraints precluding the crystallization, nor as crystallization centers.

Keywords: nanoparticles, titanium dioxide, anatase, rutile, hydrothermal synthesis.

Received: 24 September 2019

Revised: 18 November 2019

1. Introduction

Currently, titanium dioxide is of significant interest, both as an object of fundamental research [1–4] and material for various practical applications [5–23]. Nanosized powders of titanium dioxide are used in metallurgy [5, 6], electronics [7–9], polymer industry [10, 11], photovoltaics [12–15], and biomedicine [16, 17]. Another important area for nanocrystalline titanium dioxide is photocatalysis [13, 18–23]. Since the properties of TiO_2 nanoparticles strongly depend on phase composition, morphology and surface structure, many scientific papers focus on formation mechanism and design of various titanium oxide nanocrystals [1, 18–29].

Despite great number of papers on the effect of formation conditions on the obtained structure and properties of titanium dioxide nanoparticles, there is still uncertainty in the mechanisms of various modifications formation and their stability ranges. The thermodynamically stable TiO_2 modification (for macro-sized particles) is that with rutile structure. However, nanocrystals of titanium dioxide anatase modification are predominantly formed as a result of the soft chemistry synthesis [1, 4, 18, 24, 26, 28–31]. The transformation of anatase into rutile only takes place upon additional thermal treatment accompanied by crystal growth [32–35].

It is also unclear, which TiO_2 modification is the most active photocatalyst, how an amorphous component influences the catalytic properties of titanium oxide, which ratio of the amorphous and different crystalline phases is to be chosen for maximum catalytic activity [22, 26, 29, 30, 35–37].

The studies [38–40] demonstrated that the structural and morphological characteristics of nanoparticles being formed may be changed by introducing a heterogeneous impurity to act either as geometrical constraints or as crystal-nucleating centers providing the phases’ structural continuity. Therefore, it is of interest to study the effect of a heterogeneous impurity on the process of titanium dioxide nanoparticles formation during hydrothermal synthesis and also on the particles’ photocatalytic properties.

2. Experimental section

Pre-formed nanocrystalline titanium dioxide particles of rutile and anatase structure were used as the nanosized particles introduced into the reaction medium during nanocrystalline TiO_2 synthesis.

The titanium dioxide nanocrystals of rutile and anatase structure were obtained under hydrothermal conditions by dehydration of hydrated titanium dioxide ($TiO_2 \cdot nH_2O$) derivedby precipitation from a dilute solution of titanium tetrachloride (high pure 12-3, TU 6-09-2118-77) using an ammonium hydroxide solution (reagent-grade, GOST 3760-79).

The effect of impurity phases on the titanium dioxide crystallization process was studied by precipitating $TiO_2 \cdot nH_2O$ from $TiCl_4$ dilute solution in a suspension of pre-formed titanium dioxide nanoparticles of various structures, using ammonium hydroxide solution, with subsequent hydrothermal treatment.

The hydrothermal treatment was conducted at 250 °C and $P = 70$ MPa. PTFE liners with the reagents were placed into steel autoclaves and loaded into an oven. Upon completion of isothermal exposure at specified temperatures, the oven was switched off, and the autoclaves and the oven were left to cool. The accuracy of the isothermal exposure temperature control was $\pm 5^\circ$. The hydrothermal treatment time was recorded by duration of the autoclaves' isothermal exposure in the oven. The synthesis products were rinsed with distilled water and dried at a temperature of 90 °C. The duration of the hydrothermal treatment at the oven temperature of 250 °C varied from 15 min to 4 hours. Distilled water was used as the hydrothermal fluid.

To determine the samples' elemental composition, we carried out energy dispersive X-ray spectroscopy (EDS) on FEI Quanta 200 scanning electron microscope with EDAX analyzer.

The phase analysis was carried out by x-ray diffraction, using Rigaku Smart Lab 3 X-ray powder diffractometer. The phase identification was performed by comparing the obtained diffractograms with ICDD database cards. The rutile to anatase ratio was calculated by formula proposed in [41]. The crystallites' dimensions were assessed by X-ray diffraction line broadening, using Scherrer formula. The crystallite size distribution was determined by XRD profile analysis, with the use of Rigaku Smart Lab 3 and Maud software packages.

Photocatalytic activity of the obtained compositions was studied under HPX-2000-HP-DUV xenon source radiation with a nominal power of 75 W. The weighed sample powder was dispersed in distilled water with ultrasonication during 30 minutes. Then 1.9 ml of the suspension was transferred into a standard PMMA cell which then was placed into a spectrometer compartment. The cell content was mixed throughout the experiment using a magnetic stirrer and thermally controlled at 25 °C. 75 μl of 400 mg/l crystal violet water solution was added to the suspension. The obtained mixture was held for 30 min in a dark place to take account of the possible dye adsorption, and then irradiated for 2 hours. The change in the dye concentration was calculated by reduction in the absorption peak intensity. Commercial titanium dioxide Degussa P25 powder was used as reference material.

3. Results and discussion

The titanium dioxide nanoparticles pre-formed in hydrothermal conditions were TiO_2 of rutile (Fig. 1, curve *1*) and anatase (Fig. 1, curve *2*) structure with a crystallite size of about 10 and 15 nm, respectively. Based on the XRD line nature of the TiO_2 rutile sample (Fig. 1, curve *1*), it can be concluded that a part of titanium dioxide is in X-ray amorphous state.

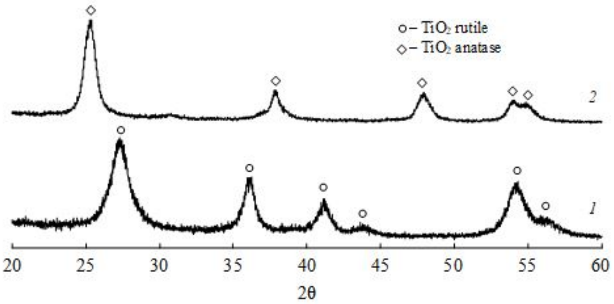

FIG. 1. X-ray diffractograms of the pre-formed nanocrystals: *1* – TiO_2 (rutile); *2* – TiO_2 (anatase)

According to X-ray diffraction data, the samples' X-ray diffractograms obtained after hydrated titanium dioxide precipitation in the suspension of nanoparticles demonstrated X-ray peaks corresponding to TiO_2 crystalline phases, in the suspension of which the hydrated titanium dioxide precipitation was carried out (Fig. 2, curves *1* and *2*).

For the reference material, hydrated titanium dioxide was used, which was obtained by precipitating from titanium tetrachloride dilute solution, in accordance with a method identical to that for obtaining the compositions. The X-ray diffractogram shown in Fig. 2, curve *1*, indicates that $TiO_2 \cdot nH_2O$ obtained as a result of the precipitation is in X-ray amorphous state. Based on the data of X-ray diffraction analysis of hydrated titanium dioxide obtained by precipitation with no impurities and of $TiO_2 \cdot nH_2O$ precipitated in the suspension of TiO_2 nanoparticles of various modifications (curve *1* and curves *2* and *3*, respectively), it can be supposed that the latter is likely to be not all-crystalline and that a part of the substance is likely to be in X-ray amorphous state. Based on the elemental analysis data, it can be concluded that impurity elements, the presence of which may arise out of the precipitation method, such as Cl^- ions, are absent.

Figure 3 shows x-ray diffractograms for the samples obtained as a result of hydrothermal treatment at 250 °C for 0.5 h, as an example.

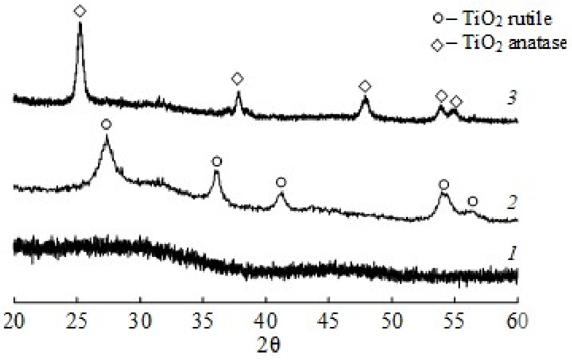

FIG. 2. X-ray diffractograms of the initial compositions: *1* – $TiO_2 \cdot nH_2O$; *2* – TiO_2(rutile)–$TiO_2 \cdot nH_2O$; *3* – TiO_2(anatase)–$TiO_2 \cdot nH_2O$

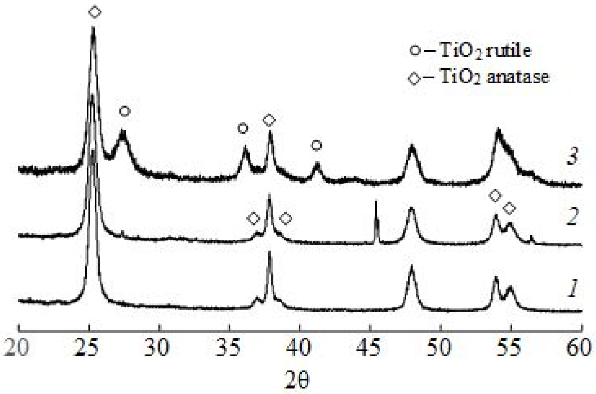

FIG. 3. X-ray diffractograms for the samples obtained as a result of hydrothermal treatment at 250 °C for 0.5 h. *1* – $TiO_2 \cdot nH_2O$; *2* – TiO_2(anatase)–$TiO_2 \cdot nH_2O$; *3* – TiO_2(rutile)–$TiO_2 \cdot nH_2O$

The X-ray diffractograms both of the samples with no heterogeneous impurity (Fig. 3, curve *1*) and of the samples obtained by precipitation in the suspension of titanium oxide nanoparticles of various structural modifications, after hydrothermal treatment (Fig. 3, curves *2* and *3*) demonstrated X-ray peaks corresponding to TiO_2 anatase modification. The increase in the isothermal exposure period for all the samples led to increased intensity of anatase peaks, however, for the system TiO_2(rutile)–$TiO_2 \cdot nH_2O$, the intensity of reflexes corresponding to TiO_2-rutile only changed insignificantly. Only reduction in the X-ray peak broadening was observed, which may indicate increase in the crystallite dimensions.

Based on the X-ray diffraction data, crystallization degrees and crystallite dimensions were plotted against the duration of isothermal exposure (Fig. 4–5).

As it is seen from Fig. 4, at the hydrothermal treatment initial stage, during the first 30 minutes, a rather intensive anatase formation is observed: the anatase fraction in the system increases from 0.2 to ~ 0.75 mol.%. This can likely be explained by TiO_2 (anatase) particle crystallization from the amorphous phase. In this case, the nature of change in the crystalline modification fraction corresponds to that of crystallization of titanium dioxide with no impurities. The size of crystallites of titanium dioxide formed is systematically smaller than that of crystallites in the system TiO_2(anatase)–$TiO_2 \cdot nH_2O$. Moreover, the dependence between the size of titanium dioxide crystallites obtained with no heterogeneous impurities and the isothermal exposure duration is monotonic. While in the system "TiO_2(anatase)–$TiO_2 \cdot nH_2O$", the initial stage of crystallization is accompanied by reduction in the mean size of anatase crystallites (Fig. 4(b), curve *2*). It is likely that in the case of crystallization from the amorphous phase the size of particles formed is much smaller than that of anatase particles already introduced as the heterogeneous impurity (see Fig. 4(b), curve *1*), which leads to a reduction in the crystallite mean size. During the subsequent hydrothermal treatment of the reaction system, phase formation mechanism is changed, which leads to slowing down of the crystallization rate. And the anatase crystallite growth is due to the processes of crystallization of the remaining amorphous phase on the

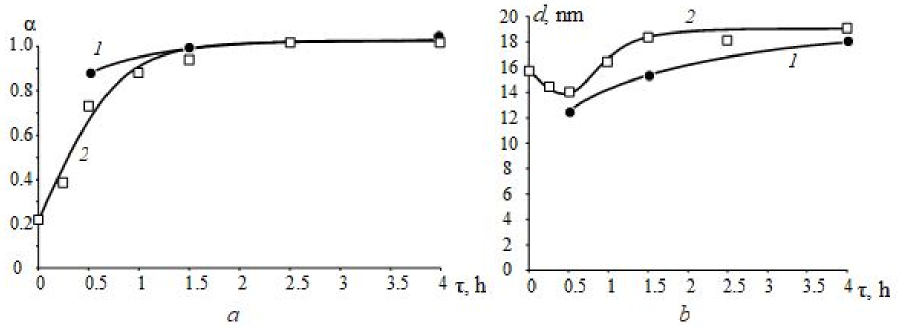

FIG. 4. Crystalline phase (TiO_2-anatase) fraction (a) and anatase crystallite dimensions (b) as a function of the duration of $TiO_2 \cdot nH_2O$ hydrothermal treatment (curves *1*) and of the composition of TiO_2(anatase)–$TiO_2 \cdot nH_2O$ (curves *2*)

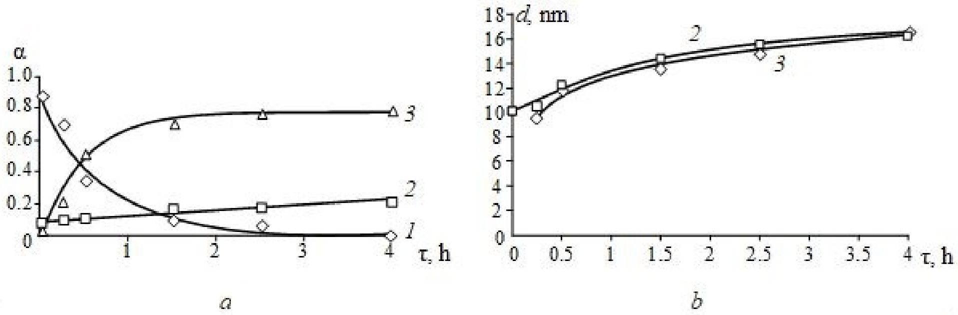

FIG. 5. Amorphous and crystalline phase (TiO_2-anatase, rutile) fraction (a) and anatase crystallite mean size (b) as a function of the duration of the composition TiO_2(rutile)–$TiO_2 \cdot nH_2O$ hydrothermal treatment at a temperature of 250 °C: *1* – amorphous fraction; *2* – TiO_2 with rutile structure; *3* – TiO_2 with anatase structure

anatase particles surface, which, in its turn, leads to systematically larger crystallite sizes in the system TiO_2(anatase)–$TiO_2 \cdot nH_2O$ as compared to crystallites formed as a result of hydrothermal treatment of $TiO_2 \cdot nH_2O$.

As a result of hydrothermal treatment of the composition obtained by precipitating $TiO_2 \cdot nH_2O$ in the suspension of rutile nanoparticles, peaks corresponding to anatase structure titanium dioxide appear in the X-ray diffractograms (Fig. 3, curve *3*). Increase in the hydrothermal treatment duration leads to increased anatase peak intensity. However, increase in the fraction of rutile structure TiO_2 phase is very insignificant (Fig. 5(a)).

From the relationship of anatase crystalline phase fraction and change in the mean size of anatase crystallites formed as a result of hydrothermal treatment (Fig. 5) and also the data of TiO_2 crystallization process analysis shown in Fig. 4(a), curve *1*, it is seen that in this case, anatase is also formed at the initial stage from the amorphous phase due to the process of nucleation. And, judging by mild correlation with the change in the fraction of crystalline titanium dioxide with rutile structure, the X-ray amorphous component probably contained in the heterogeneous impurity (Fig. 1, curve *2*) is also crystallized primarily as anatase structural modification.

Thus, it can be concluded that the use of a heterogeneous impurity of the studied composition and particle size has almost no effect on the process of phase formation in the TiO_2–H_2O system. This is likely due to the fact that the distance between the introduced nanoparticles significantly exceeds the size of TiO_2 critical nucleus [42]. Thus, the heterogeneous impurities may be considered neither as geometric constraints precluding the crystallization, as it was the case for Al_2O_3 [39,43] or Cr_2O_3 [44], nor as crystallization centers.

On the one hand, the absence of any effect of titanium dioxide nanoparticles of various structural modifications on the phase composition of $TiO_2 \cdot nH_2O$ formed as a result of dehydration under hydrothermal conditions may be associated with significant difference in the sizes of titanium dioxide critical nucleus and of crystallites introduced as the heterogeneous impurity. On the other hand, clusters are likely to be formed during the precipitation of $TiO_2 \cdot nH_2O$ from the titanium tetrachloride solution, and the arrangement of titanium and oxygen atoms in the clusters is similar to anatase structural elements [43,44]. And at the hydrothermal treatment stage, the anatase-like clusters grow together following the accommodative mechanism, as it was proposed in [43].

The results of photocatalytic properties assessment for samples synthesized by hydrothermal treatment of compositions obtained by $TiO_2 \cdot nH_2O$ precipitation in the suspension of anatase and rutile nanoparticles are presented in Fig. 6.

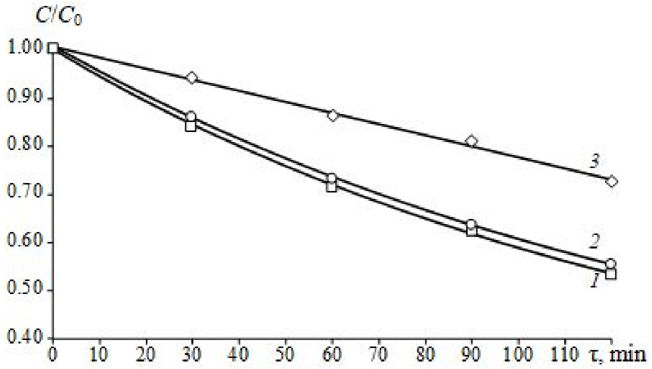

FIG. 6. Coloring agent relative concentration change as a function of UV-exposure time: *1* – commercial material TiO_2 (P25 Degussa), *2* – sample obtained by hydrothermal treatment of TiO_2(anatase)–$TiO_2 \cdot nH_2O$, *3* – sample obtained by hydrothermal treatment of TiO_2(rutile)–$TiO_2 \cdot nH_2O$

The analysis of relationships presented in Fig. 6 allows concluding that the sample composed only of the anatase modification (Fig. 6, curve *2*) demonstrates characteristics comparable to that of the commercial material (Fig. 6, curve *1*). While even an insignificant quantity of rutile titanium dioxide leads to remarkable reduction in the system photocatalytic activity (Fig. 6, curve *3*). On one hand, the results agree with literature data, e.g., [26, 45], indicating that the anatase modification of titanium dioxide exhibits higher catalytic properties than rutile one. However, the reference material P25 Degussa that, according to [36], consists of a mixture of anatase, rutile and in some cases amorphous TiO_2, demonstrates almost equal photocatalytic properties than the anatase sample. Based on the obtained results, it can be supposed that the determining influence on titanium dioxide photocatalytic activity is produced by an interface between various TiO_2 modifications formed during the material synthesis. In case of the precipitation method used, the particles of anatase and rutile are likely to be in pinpoint contact that has no effect on the obtained system properties, and the method for obtaining P25 Degussa, i.e. pyrolysis of titanium tetrachloride, allows for more active superficial contact of anatase and rutile.

4. Conclusions

Thus, based on the obtained data, it can be concluded that to control the formation process of titanium dioxide of any structural modification, we need to vary the conditions of $TiO_2 \cdot nH_2O$ precipitation from the solution, alter the chemical composition of precursors [25, 27–31], or precipitation procedures [47, 48].

Acknowledgements

The authors express their gratitude to V. V. Gusarov for the attention he paid to the work. X-ray diffraction was performed using the equipment of the Engineering Center Saint Petersburg State Institute of Technology. This study was financially supported by the Russian Science Foundation (project No. 16-13-10252).

References

[1] Savinkina E.V., Kuz'micheva G.M., et al. Synthesis and morphology of anatase and η-TiO_2 nanoparticles. *Inorganic Materials*, 2011, **47** (5), P. 489–494.

[2] Hanaor D.A.H. Sorrell C.C. Review of the anatase to rutile phase transformation. *Journal of Materials Science*, 2011, **46** (4), P. 855–874.

[3] Esmaeilzadeh J., Ghashghaie S., et al. Effect of dispersant on chain formation capability of TiO_2 nanoparticles under low frequency electric fields for NO_2 gas sensing applications. *Journal of the European Ceramic Society*, 2014, **34** (5), P. 1201–1208.

[4] Rahiminezhad-Soltani M., Saberyan K., Shahri F., Simchi A. Formation mechanism of TiO_2 nanoparticles in H_2O-assisted atmospheric pressure CVS process. *Powder Technology*, 2011, **209** (1–3), P. 15–24.

[5] Kumar C.A.V., Rajadurai J.S. Influence of rutile (TiO_2) content on wear and microhardness characteristics of aluminium-based hybrid composites synthesized by powder metallurgy. *Transactions of Nonferrous Metals Society of China*, 2016, **26** (1), P. 63–73.

[6] Chougule A.B., Patil P.M., Umasankar V. Enhancement of hardness property of AA2219 by varying TiO_2 percentage as a reinforcement. *Materials Today: Proceedings*, 2018, **5** (2, Part 2), P. 7628–7634.

[7] Lü X., Yang W., et al. Enhanced electron transport in Nb-doped TiO_2 nanoparticles via pressure-Induced phase transitions. *Journal of the American Chemical Society*, 2014, **136** (1), P. 419–426.

[8] Huang Y., Zhang J. The electrical behaviors of anatase titanium dioxide (TiO_2) nanoparticles under high pressure. *Solid State Communications*, 2019, **287**, P. 1–6.

[9] Shen L., Zhang X., et al. Design and tailoring of a three dimensional TiO_2-graphene-carbon nanotube nanocomposite for fast lithium storage. *The Journal of Physical Chemistry Letters*, 2011, **2** (24), 3096.

[10] Tian C. Internal influences of hydrolysis conditions on rutile TiO_2 pigment production via short sulfate process. *Materials Research Bulletin*, 2018, **103**, P. 83–88.

[11] Sun M., Liu F., Shi H. Han E. A study on water absorption in freestanding polyurethane films filled with nano-TiO_2 pigments by capacitance measurements. *Acta Metallurgica Sinica (English Letters)*, 2009, **22** (1), P. 27–34.

[12] Vildanova M.F., Kozlov S.S., et al. Niobium-doped titanium dioxide nanoparticles for electron transport layers in perovskite solar cells. *Nanosystems: Physics, Chemistry, Mathematics*, 2017, **8** (4), P. 540–545.

[13] Haffad S., Kiprono K.K. Interfacial structure and electronic properties of TiO_2/ZnO/TiO_2 for photocatalytic and photovoltaic applications: A theoretical study. *Surface Science*, 2019, **686**, P. 10–16.

[14] Wan J., Tao L., et al. A facile method to produce TiO_2 nanorods for high-efficiency dye solar cells. *Journal of Power Sources*, 2019, **438**, 227012.

[15] Marandi M., Goudarzi Z., Moradi L. Synthesis of randomly directed inclined TiO_2 nanorods on the nanocrystalline TiO_2 layers and their optimized application in dye sensitized solar cells. *Journal of Alloys and Compounds*, 2017, **711**, P. 603–610.

[16] Lamberti A., Pirri C.F. TiO_2 nanotube array as biocompatible electrode in view of implantable supercapacitors. *Journal of Energy Storage*, 2016, **8**, P. 193–197.

[17] Katahira K., Mifune N., Komotori J. Generation of biocompatible TiO_2 layer using atmospheric pressure plasma-assisted fine particle peening. *CIRP Annals*, 2017. **66** (1), P. 515–518.

[18] Kolen'ko Y.V., Garshev A.V., et al. Photocatalytic activity of sol-gel derived titania converted into nanocrystalline powders by supercritical drying. *Journal of Photochemistry and Photobiology A: Chemistry*, 2005, **172**, P. 19–26.

[19] Cabrera-Reina A., Martínez-Piernas A.B., et al. TiO_2 photocatalysis under natural solar radiation for the degradation of the carbapenem antibiotics imipenem and meropenem in aqueous solutions at pilot plant scale. *Water Research*, 2019, **166**, 115037.

[20] Vorontsov, A.V., Kozlov, D. V., Smirniotis, P. G., Parmon, V. N. TiO_2 photocatalytic oxidation: II. Gas-phase processes. *Kinetics and Catalysis*, 2005, **46** (3), P. 422–436.

[21] Humayun M., Raziq F., Khan A., Luo W. Modification strategies of TiO_2 for potential applications in photocatalysis: a critical review. *Green Chemistry Letters and Reviews*, 2018, **11** (2), P. 86–102.

[22] Savinkina E.V., Obolenskaya L.N., et al. A new η-itania-based photocatalyst. *Doklady Physical Chemistry*, 2011, **441** (1), P. 224–226.

[23] Savinkina E.V., Obolenskaya L.N., et al. Effects of peroxo precursors and annealing temperature on properties and photocatalytic activity of nanoscale titania. *Journal of Materials Research*, 2018, **33** (10), P. 1422–1432.

[24] Rahiminezhad-Soltani M., Saberyan K., Shahri F., Simchi A. Formation mechanism of TiO_2 nanoparticles in H_2O-assisted atmospheric pressure CVS process. *Powder Technology*, 2011, **209** (1–3), P. 15–24.

[25] Machida M, Kobayashi M., Suzuki Y., Abe H. Facile synthesis of > 99 % phase-pure brookite TiO_2 by hydrothermal conversion from Mg_2TiO_4. *Ceramics International*, 2018. **44** (14), P. 17562–17565.

[26] Allen N.S., Mahdjoub N., et al. The effect of crystalline phase (anatase, brookite and rutile) and size on the photocatalytic activity of calcined polymorphic titanium dioxide (TiO_2). *Polymer Degradation and Stability*, 2018, **150**, P. 31–36.

[27] Leal J.H., Cantu Y., Gonzalez D.F., Parsons J.G. Brookite and anatase nanomaterial polymorphs of TiO_2 synthesized from $TiCl_3$. *Inorganic Chemistry Communications*, 2017, **84**, P. 28–32.

[28] de Mendona V.R., Lopes O.F., et al. Insights into formation of anatase TiO_2 nanoparticles from peroxo titanium complex degradation under microwave-assisted hydrothermal treatment. *Ceramics International*, 2019, **45** (17, Part B), P. 22998–23006.

[29] Macwan D.P., Dave P.N., Chaturvedi S. A review on nano-TiO_2 sol–gel type syntheses and its applications. *Journal of Materials Science*, 2011, **46** (11), P. 3669–3686.

[30] Kaifeng Yu K., Ling M., Liang J., Liang C. Formation of TiO_2 hollow spheres through nanoscale Kirkendall effect and their lithium storage and photocatalytic properties. *Chemical Physics*, 2019, **517**, P. 222–227.

[31] Wang C.-C., Ying J.Y. Sol-gel synthesis and hydrothermal processing of anatase and rutile titania nanocrystals. *Chemistry of Materials*, 1999, **11** (19), P. 3113–3120.

[32] Ding X.-Z., Liu X.-H. Correlation between anatase-to-rutile transformation and grain growth in nanocrystalline titania powders. *Journal of Materials Research*, 1998, **13** (9), P. 2556–2559.

[33] Gribb A.A., Banfield J.F. Particle size effects on transformation kinetics and phase stability in nanocrystalline TiO_2. *American Mineralogist*, 1997, **82**, P. 717–728.

[34] Yang J., Gao M., et al. Hysteretic phase transformation of two-dimensional TiO_2. *Materials Letters*, 2018, **232**, P. 171–174.

[35] Wang Y., Zhang W., et al. Fabrication of TiO_2(B)/anatase heterophase junctions in nanowires *via* a surface-preferred phase transformation process for enhanced photocatalytic activity. *Chinese Journal of Catalysis*, 2018, **39** (9), P. 1500–1510.

[36] Ohtani B., Prieto-Mahaney O.O., Li D., Abe R. What is Degussa (Evonik) P25? Crystalline composition analysis, reconstruction from isolated pure particles and photocatalytic activity test. *Journal of Photochemistry and Photobiology A: Chemistry*, 2010, **216** (2–3), P. 179–182.

[37] Ohno T., Sarukawa K., Matsumura M. Photocatalytic Activities of Pure Rutile Particles Isolated from TiO_2 Powder by Dissolving the Anatase Component in HF Solution. *The Journal of Physical Chemistry B*, 2001, **105**, P. 2417–2420.

[38] Yorov Kh.E., Sipyagina N.A., et al. SiO_2–TiO_2 binary aerogels: Synthesis in new supercritical fluids and study of thermal stability. *Russian Journal of Inorganic Chemistry*, 2016, **61** (11), P. 1339–1346

[39] Almjashev O.V., Gusarov V.V. Effect of ZrO_2 nanocrystals on the stabilization of the amorphous state of alumina and silica in the ZrO_2–Al_2O_3 and ZrO_2–SiO_2 systems. *Glass Physics and Chemistry*, 2006, **32** (2), P. 162–166.

[40] Gusarov V.V. Malkov A.A., Malygin A.A., Suvorov S.A. Formations of aluminum titanate in compositions with a high level of spatial and structural conjugation of components. *Russian Journal of General Chemistry*, 1994, **64** (4), P. 554–557. (in Russian)

[41] Spurr R.A., Myers H. Quantitative Analysis of Anatase-Rutile Mixtures with an X-Ray Diffractometer. *Analytical Chemistry*, 1957, **29** (5), P. 760–762.

[42] Almjasheva O.V. Formation and structural transformations of nanoparticles in the TiO_2–H_2O system. *Nanosystems: Physics, Chemistry, Mathematics*, 2016, **7** (6), P. 1031–1049.

[43] Al'myashev O.V., Gusarov V.V. Features of the phase formation in the nanocomposites. *Russian Journal of General Chemistry*, 2010, **80** (3), P. 385–390

[44] Almjasheva O.V. Formation of oxide nanocrystals and nanocomposites in hydrothermal conditions, structure and properties of materials on their basis. Abstract of dissertation for the degree of Doctor of Sciences, 2018, 44 p. (in Russian)

[45] Almjasheva O.V., Gusarov V.V. Metastable clusters and aggregative nucleation mechanism. *Nanosystems: Physics, Chemistry, Mathematics*, 2014, **5** (3), P. 405–417.

[46] Lebedev V.A., Kozlov D.A., et al. The amorphous phase in titania and its influence on photocatalytic properties. *Applied Catalysis B: Environmental*, 2016, **195**, P. 39–47.

[47] Proskurina O.V., Nogovitsin I.V., et al. Formation of $BiFeO_3$ nanoparticles using impinging jets microreactor. *Russian Journal of General Chemistry*, 2018, **88** (10), P. 2139–2143.

[48] Abiev R.S., Almyasheva O.V., Izotova S.G., Gusarov V.V. Synthesis of cobalt ferrite nanoparticles by means of confined impinging-jets reactors. *Journal of Chemical Technology and Applications*, 2017, **1** (1), P. 7–13.

NANOSYSTEMS:

PHYSICS, CHEMISTRY, MATHEMATICS

INFORMATION FOR AUTHORS

The journal publishes research articles and reviews, and also short scientific papers (letters) which are unpublished and have not been accepted for publication in other magazines. Articles should be submitted in English. All articles are reviewed, then if necessary come back to the author to completion.

The journal is indexed in Web of Science Core Collection (Emerging Sources Citation Index), Chemical Abstract Service of the American Chemical Society, Zentralblatt MATH and in Russian Scientific Citation Index.

Author should submit the following materials:

1. Article file in English, containing article title, the initials and the surname of the authors, Institute (University), postal address, the electronic address, the summary, keywords, MSC or PACS index, article text, the list of references.
2. Files with illustrations, files with tables.
3. The covering letter in English containing the article information (article name, MSC or PACS index, keywords, the summary, the literature) and about all authors (the surname, names, the full name of places of work, the mailing address with the postal code, contact phone number with a city code, the electronic address).
4. The expert judgement on possibility of publication of the article in open press (for authors from Russia).

Authors can submit a paper and the corresponding files to the following addresses: nanojournal.ifmo@gmail.com, popov1955@gmail.com.

Text requirements

Articles should be prepared with using of text editors MS Word or LaTex (preferable). It is necessary to submit source file (LaTex) and a pdf copy. In the name of files the English alphabet is used. The recommended size of short communications (letters) is 4-6 pages, research articles– 6-15 pages, reviews – 30 pages.

Recommendations for text in MS Word:

Formulas should be written using Math Type. Figures and tables with captions should be inserted in the text. Additionally, authors present separate files for all figures and Word files of tables.

Recommendations for text in LaTex:

Please, use standard LaTex without macros and additional style files. The list of references should be included in the main LaTex file. Source LaTex file of the paper with the corresponding pdf file and files of figures should be submitted.

References in the article text are given in square brackets. The list of references should be prepared in accordance with the following samples:

[1] Surname N. *Book Title*. Nauka Publishing House, Saint Petersburg, 2000, 281 pp.
[2] Surname N., Surname N. Paper title. *Journal Name*, 2010, **1** (5), P. 17-23.
[3] Surname N., Surname N. Lecture title. In: Abstracts/Proceedings of the Conference, Place and Date, 2000, P. 17-23.
[4] Surname N., Surname N. Paper title, 2000, URL: http://books.ifmo.ru/ntv.
[5] Surname N., Surname N. Patent Name. Patent No. 11111, 2010, Bul. No. 33, 5 pp.
[6] Surname N., Surname N. Thesis Title. Thesis for full doctor degree in math. and physics, Saint Petersburg, 2000, 105 pp.

Requirements to illustrations

Illustrations should be submitted as separate black-and-white files. Formats of files – jpeg, eps, tiff.

NANOSYSTEMS:

PHYSICS, CHEMISTRY, MATHEMATICS

Журнал зарегистрирован
Федеральной службой по надзору в сфере связи, информационных технологий и массовых коммуникаций
(свидетельство ПИ № ФС 77 - 49048 от 22.03.2012 г.)
ISSN 2220-8054

Учредитель: федеральное государственное автономное образовательное учреждение высшего образования
«Санкт-Петербургский национальный исследовательский университет информационных технологий, механики и оптики»

Издатель: федеральное государственное автономное образовательное учреждение высшего образования
«Санкт-Петербургский национальный исследовательский университет информационных технологий, механики и оптики»

Отпечатано в Учреждении «Университетские телекоммуникации»
Адрес: 197101, Санкт-Петербург, Кронверкский пр., 49

Подписка на журнал НФХМ
На первое полугодие 2020 года подписка осуществляется через
ОАО Агентство «Роспечать»
Подписной индекс 57385 в каталоге «Издания органов научно-технической информации»